UNIVERSITAT DE BARCELONA

Department d'Astronomia i Meteorologia

Moving Groups as imprints of the non-axisymmetric components of the Milky Way

Memòria presentada per

M. Teresa Antoja Castelltort

per optar al grau de

Doctor per la Universitat de Barcelona

Barcelona, Març 2010

UNIVERSITAT DE BARCELONA

Department d'Astronomia i Meteorologia

PROGRAMA DE DOCTORAT EN FÍSICA

Moving Groups as imprints of the non-axisymmetric components of the Milky Way

Memòria presentada per M. Teresa Antoja Castelltort per optar al grau de

Doctor per la Universitat de Barcelona

Barcelona, Març 2010

DIRECTORS DE LA TESI

Dra. Francesca Figueras Siñol

Dr. Octavio Valenzuela Tijerino

Als meus pares.

Agraïments

En primer lloc vull agrair a tots aquells que han contribuït en la planificació, realització i discussió d'aquesta tesi. He tingut la sort de comptar amb dos codirectors que es complementaven perfectament i que m'han guiat i supervisat pel camí observacional i per les simulacions. Dono les gràcies a la meva codirectora de tesi, la Dra. Francesca Figueras, perquè em va iniciar en l'estudi dels grup mòbils ara fa ja uns quants anys. D'ella he après moltes coses i en valoro especialment que sempre està al dia. També li agraeixo la confiança que ha tingut en les meves possibilitats i tot el que m'ha escoltat a nivell personal. D'altra banda, també dono les gràcies al meu codirector Dr. Octavio Valenzuela pel seu rigor i sobretot el seu gran entusiasme. Ell ha fet que aquest estudi ampliés els seus horitzons. El seu suport anímic i el seu punt crític han estat providencials.

Moltes altres persones m'han ajudat a tirar endavant aquest projecte. Especialment agraeixo a la Dra. Barbara Pichardo. Els seus braços oberts (i els seus braços espirals) han estat claus en el desenvolupament d'aquesta tesi. Moltes gràcies també al Dr. Edmundo Moreno que ha realitzat part dels codis utilitzats en aquesta tesi i amb el que sempre hi he trobat molta afinitat. En especial agrairé també a totes les persones que he conegut i han estat amb mi a Mèxic. Allà hi he viscut una de les millors experiències de la meva vida gràcies a moltes d'elles. També vull agrair al Dr. Jordi Torra que va col·laborar amb nosaltres a l'inici de la tesi. Igualment al Dr. David Fernández que va dirigir part d'aquest treball i sobretot que em va donar suport personal en tot moment. Moltes gràcies a la Dra. Mercè Romero que en aquests últims mesos ha esdevingut una col·laboradora molt disposada. Els seus ànims han estat providencials moltes vegades. Vull reconèixer també l'ajuda de Dr. Claus Fabricius en la supervisió del text i el seu interès, i al Kike Herrero que ha fet la meravellosa fotografia de la Via Làctia que apareix en portada.

És difícil mencionar totes les persones que han donat suport i s'han interessat per aquest treball. Voldria recordar-me especialment de tots els meus companys de despatx que d'alguna manera o altra m'han donat ajut i ànims. Aquests han estat Juan Carlos, Jordi P., Javi, Aidan i Eva. També vull agrair als meus companys i amics de llicenciatura i doctorat amb els que tant camí he compartit. Moltes gràcies

també al Gaby, Dani i Jordi V. Amb ells hem solucionat molts problemes informàtics i altres de personals. I a les Maries que m'han escoltat en tants assajos de la mateixa presentació! D'altra banda, vull agrair a la resta del meu equip i a les persones del Departament de Astronomia i Meteorologia. Gràcies en especial als amics que hi he fet. Tots ells m'han acompanyat en el meu dia a dia de treball. No vull oblidar-me tampoc de totes les persones externes a la matèria que sempre s'han interessat pel que estava fent i que m'aclaparen a preguntes sobre ciència. Aquests són especialment el meu avi Tomàs, en Pau, la Laia V. i els meus cosins Anna i Ramon.

Per a mi ha estat molt important el suport i la comprensió de tots els meus amics, aquells que sempre hi són. En Jordi, la Marta, la Jorgina, en Pau, la Eva, la Laia, en Joan i la Judith. No es pot descriure tot el que he viscut amb ells. Gràcies també al Fede per allò que hem compartit a Mèxic i pel que ha fet per mi, sempre tan mal correspost. Al Julio li agraeixo la seva alegria i ajuda entre altres. També a les meves companyes de jazz i als amics de l'esplai i dels "Padres". Ignasi, Sílvia, Jordi F.,... i en especial a tots aquells que han ajudat al meu pare. La llista seria molt llarga.

A la meva germana Gemma li agraeixo la entesa i tot allò que només una germana et pot donar. Ella sempre ha compartit amb mi alegries i preocupacions. També ha col·laborat en aquesta tesi ajudant-me en el disseny de la portada. Gràcies també a tota la resta de família entre ells els meus avis Teresa, Tomàs i Faustí. També a l'Alberto i la Merçè, que ara ja són de la meva família.

Ja acabant, vull donar les gràcies als meus pares, a qui dedico aquest treball. Ells han aconseguit amb esforç i part de sacrifici que el pogués realitzar preocupant-me de poques coses. Gràcies per això i per mil coses més. A ells els dec tot.

Finalment, les meves gràcies infinites a l'Oscar. D'ell en trec total l'alegria, companyia, tranquil·litat i amor necessaris per tirar endavant. Gràcies per tots els plats que has fregat últimament.

Resum en català

Antecedents

Fa 400 anys que Galileo Galilei va realitzar la primera observació amb telescopi que mostrà que la banda lluminosa que travessa el cel està formada per moltes estrelles. Just acabem de commemorar aquest aconteixement i altres de les seves observacions en l'Any Internacional de l'Astronomia 2009. Des d'aquella primera observació de la Via Làctia (en anglès Milky Way, MW), la comprensió de la Galàxia ha millorat tant pel que fa a la seva estructura a gran escala com, en més detall, al nostre entorn dins el disc Galàctic. D'altra banda, els avenços en astronomia extragalàctica i cosmologia estan cada vegada més connectats a l'astronomia Galàctica, col·locant la MW en un context plenament cosmològic. Tot just comencem a entendre alguns aspectes del seu procés de formació (e.g. Freeman & Bland-Hawthorn 2002).

Durant les dues últimes dècades, l'estudi de la MW ha experimentat aquest progrés extraordinari gràcies a l'arribada d'observacions de gran qualitat, millors models i mètodes, i a l'ús de potent maquinari de càlcul (e.g. Turon et al. 2008). Entre les noves troballes, s'ha demostrat que la nostra galàxia té diversos components estructurals no-axisimètrics. Els més rellevants són la barra Galàctica i els braços espirals. En particular, l'entorn solar (una esfera d'uns 200 pc de radi al voltant del Sol) ha pogut ser estudiat en detall entre altres gràcies a les posicions i velocitats estel·lars determinades per la missió Hipparcos. Tot i que és una regió molt petita comparada amb l'extensió total de la Galàxia, l'entorn solar ha esdevingut de gran valor pel que fa a la informació d'alguns processos que tenen lloc a la MW, especialment per la precissió de les dades disponibles en aquesta regió. En particular, la riquesa de la cinemàtica o la complexa distribució de composicions químiques estel·lars de l'entorn solar poden constituir un conjunt d'empremtes i fòssils de diversos processos Galàctics.

L'enfoc clàssic de l'estudi de la cinemàtica en l'entorn solar ha estat normalment lligat a la determinació de la funció de distribució de velocitats utilitzant models simples com l'el·lipsoide de Schwarzschild i la seva caracterització mitjançant la desviació del vèrtex o, en general, els moments d'ordre n. No obstant, les observacions han mostrat que el camp de velocitats en l'entorn solar mostra una gran complexitat. Una de les característiques més intrigants és l'existència dels grups mòbils. Aquests són corrents estel·lars que creuen la regió al voltant del Sol i que es

veuen com a sobredensitats en l'espai de velocitats. La distribució de velocitats de les estrelles veïnes no és suau i presenta diversos d'aquests grups mòbils.

L'estudi dels grups mòbils estel·lars de l'entorn solar té una llarga tradició en el camp de l'astronomia Galàctica (vegeu el Capítol 2 per a un resum històric), des del descobriment dels grups mòbils de les Pleiades, Hyades i Ursa Major (Mädler 1846, Proctor 1869). Després d'aquests treballs pioners, Eggen va continuar l'estudi dels grups mòbils intentant caracteritzar exhaustivament per primer cop les seves propietats (Eggen 1996b i les referències a l'interior). Com que aquestes estructures comparteixen la seva cinemàtica amb certs cúmuls estel·lars, aquests primers estudis es centraven en la hipòtesi que els grups mòbils eren el resultat de la dispersió de cúmuls.

L'arribada de les dades astromètriques de la missió Hipparcos va comportar la confirmació definitiva de l'existència dels grups mòbils. No obstant, quan van ser possibles els primers intents d'evaluar l'estat evolutiu i composició química dels membres dels grups mòbils, es va veure que les estrelles en un cert grup semblaven tenir un rang molt ampli d'edats, metal·licitats i distribucions semblants a les observades per a la mostra sencera. Des de llavors, s'ha realitzat una quantitat de treball considerable per intentar explicar l'origen dels grups mòbils a resultes d'aquests nous indicis.

En aquests moments, l'origen d'aquestes estructures cinemàtiques no està ni molt menys comprès, tot i que fa més de 140 anys que van ser descobertes (vegeu el Capítol 2 per una visió més àmplia de les teories sobre el seu origen). Actualment es consideren vàries possibilitats. Com es va proposar primerament, els grups mòbils poden ser el resultat de processors interns en el disc com ara dispersió de cúmuls. Alternativament, podrien ser deguts als efectes dinàmics induïts pels components no-axisimètric de la MW (braços espirals i barra). També s'ha proposat que alguns d'ells siguin remanents d'acrecions passades, mentre que d'altres podrien ser deguts a efectes dinàmics externs sobre el disc causats per fenòmens d'interacció. Tot i que inicialment es van considerar mútuament excloents, tots aquests mecanismes són naturals en els models actuals de formació de galàxies. La combinació d'algunes d'aquestes propostes es converteix en un escenari complex però fascinant. A més, podent ser fòssils d'aquests processos dinàmics, sigui el que sigui, els grups mòbils poden proporcionar claus sobre característiques importants de la Galàxia i sobre els mecanismes dinàmics que hi tenen lloc.

Recentment, la hipòtesi que els grups mòbils són deguts a efectes cinemàtics dels components no-axisimètrics de la Galàxia ha guanyat popularitat. Això ha estat en part perquè s'ha trobat consistència entre un dels grups mòbils i els efectes de les ressonàncies de la barra. Segons aquesta hipòtesi, les ressonàncies i l'estructura orbital induïdes per la barra o els braços espirals poden causar sobredensitats en la distribució de velocitats. En altres paraules, un grup mòbil seria un grup d'estrelles que creua l'entorn solar seguint un cert tipus d'òrbites sota la influència

de la barra o dels braços espirals. En aquest cas, una motivacío addicional s'afegeix al repte de desxifrar l'enigma sobre l'origen dels grups mòbils: si es prova que aquestes estructures cinemàtiques depenen de les característiques de la barra i dels braços espirals de la MW, es podrien convertir en una eina molt útil per entendre l'estructura a gran escala i la dinàmica de la MW en el seu present i també en el seu passat. En efecte, alguns estudis s'han aventurat a utilitzar alguns grups mòbils observats per restringir paràmetres com la velocitat de rotació de la barra o algunes característiques dels braços espirals. Degut a la poca informació que hi ha sobre algunes de les característiques dels components no-axisimètrics, la possibilitat de restringir-les utilitzant els grups mòbils és molt prometedora i ens ajudaria a complementar altres mètodes.

Objectius de la tesi i metodologia

S'ha demostrat ja els efectes dels components no-axisimètrics poden crear grups cinemàtics en la distribució local de velocitats. L'evidència més rellevant és la demostració que els efectes de les ressonàncies de la barra Galàctica poden produir grups cinemàtics semblants al grup observat d'Hercules. Però malgrat l'esforç d'aquests estudis recents, l'origen ressonant o dinàmic dels grups mòbils no ha estat provat de manera definitiva per a cap estructura cinemàtica observada en particular. De fet, diferents origens plausibles coexisteixen per certs grups. A més, hi ha una llarga llista de qüestions obertes que són intens tema de debat o que encara no s'han abordat. Aquests són alguns exemples de aspectes no resolts:

- Quina és la contribució dels braços espirals a l'estructura cinemàtica en l'entorn solar?
- Quin es el poder de la barra per induir grups de baix moment angular com Artcurus?
- És possible recuperar empremtes particulars de la barra i els braços espirals quan els dos components no-axisimètric actuen a la vegada? O la combinació d'aquests components crea grups cinemàtics addicionals?
- Com podem assegurar que un grup en particular és degut a l'efecte de la barra o dels braços espirals?
- Són tots els grups mòbils de l'entorn solar deguts als efectes dels braços espirals i la barra?
- Quines són les capacitats d'aquestes empremtes per restringir les propietats de la barra i els braços espirals? Quines propietats poden ser restringides i quines no?
- Quin és exactament el mecanisme dinàmic que crea els grups mòbils? Són grups d'òrbites caòtiques o sobredensitats al voltat d'òrbites periòdiques?
- Com alterarà l'evolució Galàctica aquesta interpretació de l'origen dels grups mòbils i la seva capacitat de restringir les propietats de la MW?

Totes aquestes preguntes sense resposta demostren que es requereix més investigació. En aquesta tesi pretenem donar resposta a alguna d'elles.

La tesi estudia l'origen dels grups mòbils amb particular èmfasi a la possibilitat que els grups mòbils siguin empremtes dels components no-axisimètrics de la MW. Així, les podrem utilitzar per restringir l'estructura a gran escala de la nostra Galàxia. Els objectius particulars d'aquesta investigació són:

1. Analitzar i caracteritzar els grups mòbils observats, establint una perspectiva observacional al seu origen.

2. Explorar fins a quin punt podem utilitzar les empremtes cinemàtiques per restringir l'estructura a gran escala de la MW i la seva evolució recent.

Per conduir la recerca en aquesta tesi, hem escollit dos enfocs diferents: una metodologia observacional i una de teòrica. Per una banda, portem a terme un anàlisi d'una mostra observacional, compilada de diferents catàlegs, utilitzant tècniques estadístiques multiescala per tal de controlar el soroll de Poisson. Per altra banda, realitzem simulacions de partícules test en un potencial flexible de la MW, consistent amb diverses restriccions observacionals recents, per tal d'explorar l'espai de fases disponible per la distribució local d'estrelles.

En ambdós enfocs volem analitzar i caracteritzar les estructures cinemàtiques, és a dir establir la seva forma, mida, significància estadística, i en alguns casos, la seva edat i composició química. Això requereix la utilització de tècniques estadístiques robustes específiques. A més, la comparació entre les distribucions observades i les simulades requereix la utilització del mateix mètode estadístic robust. Nosaltres utilitzem la tècnica anomenada Wavelet Denoising (WD), que ens permet obtenir funcions de distribució via un tractament de suavitzat/filtratge a diferents escales que elimina el soroll de Poisson. El WD s'ha utilitzat en altres branques de l'astrofísica, però no s'havia utilitzat en aquest tema en particular.

L'enfoc observacional ha estat motivat per dos contribucions importants que han proporcionat nou material per complementar les dades astromètriques de Hipparcos i Tycho: i) les dades de velocitats radials de CORAVEL per un nombre significant d'estrelles de tipus espectral tardà pertanyents al catàleg d'Hipparcos (Nordström et al. 2004 per les estrelles nanes i Famaey et al. 2005 per les estrelles gegants) i ii) el cens uvby–β d'estrelles FGK nanes, que ha permès la derivació d'edats i metal·licitats (Nordström et al. 2004). A més, dades d'estrelles OBA (Asiain et al. 1999a, Torra et al. 2000) i nanes M (Reid et al. 2002, Bochanski et al. 2005) completen aquesta mostra extensa. La mostra compilada constitueix un compendi de més de 24000 estrelles amb les millors dades astromètriques i fotomètriques disponibles per l'entorn solar. Hem aplicat la tècnica multiescala de WD a aquesta mostra per caracteritzar i analitzar els grups mòbils en l'espai U–V–$edat$–$[Fe/H]$. Aquest anàlisi observacional estableix les restriccions per un subsegüent estudi de l'origen dels grups mòbils. Aquest treball també ha requerit un rigurós tractament dels errors i restriccions observacionals i els biaixos de la mostra.

L'enfoc teòric d'aquesta tesi es realitza mitjançant integracions numèriques d'òrbites de partícules test distribuïdes en un disc, sota la influència d'un potencial de la MW. Hem aprofitat el model de potencial PM04–MW (Pichardo et al. 2003b, 2004), que és un model específic per la MW, consistent amb diverses restriccions observacionals recents. Aquest model consisteix en una part axisimètrica, i una barra i dos braços espirals com a part no-axisimètrica. Aquest nou model és molt flexible per ser adaptat a les observacions i està construït directament d'una distribució realista de massa 3D, a partir de la qual es deriven el potencial gravitacional i les forces. Al nostre coneixement, l'estudi de l'efecte d'un model de distribució de massa, i en particular d'aquest nou model, en la distribució de velocitats local que s'aborda en aquest treball no s'ha realitzat mai anteriorment. Un altre aspecte important d'aquesta tesi és que utilitzem una gran varietat de condicions inicials, temps i procediments d'integració. Aquests pretenen representar estrelles que han nascut en diferents moments i amb diferents condicions cinemàtiques, com les que hi ha en l'entorn solar, i han estat dissenyats per ser consistents amb alguns aspectes de l'evolució Galàctica. Per realitzar aquesta tesi, s'ha requerit un estudi exhaustiu del model i de les condicions inicials de les partícules test. Amb aquestes simulacions obtenim la distribució cinemàtica induïda, no només a l'entorn solar, sinó en altres posicions del disc. Les distribucions obtingudes també són tractades mitjançant la tècnica multiescala del WD, com en la mostra observacional. Aquesta metodologia ens permet evaluar el paper de components no-axisimètrics realistes de la MW, la barra i els braços espirals, en la formació dels grups mòbils del disc. Explorem l'espai de paràmetres del model PM04–MW utilitzant diferents simulacions per tal d'evaluar els efectes de cada característica particular dels braços espirals o la barra en les distribucions de velocitat. Finalment, també utilitzem un mètode per establir la regularitat de les òrbites en les estructures cinemàtiques que són creades en les simulacions de partícules test.

Resultats i conclusions

Com a resultats del treball observacional d'aquesta tesi hem trobat els següents. Les estructures cinemàtiques més dominants en el pla U–V són les branques de Sirius, Coma Berenices, Hyades-Pleiades i Hercules. Del gran rang d'edats i metal·licitats dins d'aquestes branques, refusem els models que expliquen els grups mòbils com a remanents de cúmuls estel·lars. La branca d'Hercules és més rellevant a la regió de radis galactocèntrics interiors. També en la regió propera al Sol en comparació a la zona que s'allunya en direcció a la rotació Galàctica. Per Hyades-Pleiades, Coma Berenices i Sirius, com més negativa és la component V de la branca, més gran és la seva metal·licitat mitja. La branca d'Hercules no segueix aquest comportament i té una dispersió de metal·licitat més gran que la resta.

El nostre treball amb simulacions ha mostrat els següents resultats. La barra Galàctica i

els braços espirals creen fortes empremtes cinemàtiques. El braccos poblen la regió cinemàtica d'Hercules i no únicament la barra tal i com tradicionalment es creu. Els braços també indueixen branques cinemàtiques lleugerament inclinades que s'assemblen a les branques observades. Els grups a baix moment angular com Arcturus poden tenir un origen relacionat amb la barra quan actua sobre un disc relativament calent, la qual cosa introdueix una nova perspectiva en la interpretació d'aquests grups diferent de la del seu origen extragalàctic. En les nostres simulacions on els braços espirals i la barra actuen a la vegada, empremtes individuals de cada component poden ser encara identificades en les distribucions de velocitat finals.

L'anàlisi de la mostra observacional i de les simulacions indica que és factible que alguns dels grups mòbils observats en l'entorn solar tinguin un origen dinàmic relacionat amb els efectes provocats pels braços espirals i la barra. L'enfoc que hem realitzat amb les simulacions de partícules test demostra que els components no-axisimètrics de la Galàxia que són consistents amb vàries restriccions observacionals provoquen unes empremtes fortes en la cinemàtica estel·lar local. Aquestes empremtes bàsicament són sensibles a l'orientació i velocitat dels braços espirals i de la barra. Aquest fet l'hem confirmat amb l'estudi de la regularitat de les òrbites en el pla U–V. Per altra banda, la força dels components no-axisimètrics, el temps d'exposició a aquests components, o les característiques dels discs utilitzats per traçar la funció de distribució a l'espai de fases, com la dispersió de la velocitat, influencien en la manera que els grups cinemàtics són poblats. La dependència dels grups cinemàtics estel·lars en l'estructura i dinàmica del model i en les condicions inicials dels nostres experiments proven que els grups cinemàtics poden aportar importants restriccions als components no-axisimètrics de la MW.

En el cas dels braços espirals, existeix molta ambigüitat observacional, per exemple, en la seva velocitat de rotació, la força, la orientació, el número de braços o el seu temps de vida. Les fortes empremtes dels braços auto-gravitants en les distribucions de velocitat al radi solar i la sensibilitat dels nostres resultats a les propietats dels braços indiquen que es pot utilitzar la cinemàtica per a restringir aquesta incertesa actual. Trobem empremtes fortes, però diferents quan els braços espirals són de llarga o de curta durada. Al nostre coneixement, els efectes dels braços auto-gravitants en la distribució de velocitats no s'havia estudiat fins ara. Per altra banda, trobem diferències significants entre els efectes produïts per braços auto-gravitants o per un model de braços derivat de l'aproximació de braços altament enrollats (en anglès Tight-winding Approximation, TWA). Això és degut a les diferències importants que hi ha entre la forma del camp de forces d'un model TWA i d'un derivat d'una distribució de masses. També hem vist que els braços auto-gravitants creen estructures més fortes comparades amb les creades pels braços TWA. Aquest fet pot ajudar a investigar si els braços de la MW són febles i àltament enrotllats com els TWA o són forts i auto-gravitants.

Pel que fa a la barra de la MW, la seva orientació respecte el Sol està actualment força ben

restringida. Contràriament, la seva velocitat de rotació ha estat determinada utilitzant mètodes independents que han obtingut resultats similars, però encara tenen molta incertesa. Els grups cinemàtics poden ajudar definitivament tant en la seva determinació com en la restricció de propietats de la recentment descoberta barra llarga de la MW. Només s'han observat diferències menors quan utilitzem el model de quadrupol o el de la barra prolata quan tenen amplituds de força similars i els discs no són molt calents. Per tant, podem concloure que contràriament al cas dels braços espirals, on hi ha importants diferències entre els models, sembla més difícil poder discriminar entre els dos models de barra. No obstant, hem observat que els perfils de les forces són, en efecte, molt diferents en les regions interiors al disc i en la mateixa barra. Com que quan utilitzem condicionals inicials més calentes apareixen òrbites que tenen unes excursions radials més grans, que fins i tot poden entrar dins la barra, esperem resultats més acurats quan utilitzem la barra prolata, que és un model més realista en aquestes regions. El model de barra quadrupol és probablement només una bona aproximació a radis grans.

Hi ha alguns exemples de resultats força reveladors en el nostre estudi mitjançant simulacions. Primer, els braços espirals i la barra poden influir en regions del pla U–V inesperades pel que fa a especulacions d'altres estudis. Per exemple els braços espirals, i no la barra exclusivament, poden poblar la regió del grup mòbil d'Hercules. És important que aquest grup mòbil pugui ajudar a restringir tant els braços espirals com la barra. També observem que les branques observades i els grups mòbils en la part central del pla U–V poden ser resultat dels braços espirals, però també influenciades per la barra. Segon, la bimodalitat provocada per la barra podria explicar l'existència del grup Hyades-Pleiades. Això podria canviar les restriccions en la velocitat de rotació de la barra, obtinguda sovint de l'ajust al grup mòbil d'Hercules.

Finalment, la possibiltat que els grups cinemàtics de baix moment angular puguin ser influenciats i, en efecte, causats per les resonàncies de la barra introdueix una nova perspectiva en la recent interpretació del seu origen extragalàctic. Tot i que la nostra mostra observacional no inclou grups de baix moment angular, altres estudis observacionals han suggerit a patir amb les abundàncies químiques estel·lars que Arcturus té un origen dinàmic en el disc. Les nostres simulacions han demostrat aquest fet, relacionant-lo amb la influència de la barra. És molt prometedor que grups cinemàtics com el d'Arcturus puguin restringir les propietats de la barra, com la seva velocitat de rotació o la seva orientació. A més, com que les estrelles d'aquestes estructures cinemàtiques poden venir de radis molt interns, poden aportar informació sobre els processos que tenen lloc a les regions centrals de la Galàxia o prop de la mateixa barra. Si finalment es prova que són grups cinemàtics transitoris, també podrien aportar infomació sobre l'evolució temporal de la MW. A més, el grup mòbil d'Hercules també podria ser consistent amb algun d'aquest grups transitoris.

En les simulacions on s'hi inclouen tant la barra com els braços espirals, empremtes indivi-

duals de la barra i dels braços es poden encara identificar en les distribucions finals de velocitats al llarg del radi solar. El detall de les empremtes depèn dels paràmetres particulars del model i de la posició estudiada sobre el disc. Això demostra que els nostres estudis amb només braços espirals o només barra són vàlids per estudiar els efectes de cada component i poden ser utilitzats per restringir les característiques de la barra i dels braços espirals. A més, com que en el cas on hi tenim els dos components les estructures poden distorsionar-se amb el temps, podríem obtenir límits temporals en l'acció conjunta dels components. El manteniment d'almenys algunes propietats orbitals de la barra o dels braços espirals donen suport a la viabilitat de la hipòtesi que els grups mòbils són deguts a l'estructura orbital i les ressonàncies dels components no-axisimètrics de la MW.

Concloent, aquesta tesi ha comportat anàlisi estadística de dades (tècniques multiescala), explotació científica de catàlegs astronòmics (cinemàtica, edats fotomètriques, metal·licitats), tractament rigurós d'errors observacionals i biaixos, dinàmica Galàctica, models analítics del potencial de la MW, simulacions amb partícules test, programació i execució de simulacions en sistemes multiprocessadors, i coneixement dels errors esperats i simuladors de la missió Gaia. Tot aquest sistema de tècniques i metodologies ens col·loquen en un bon punt de partida per assumir el repte de Gaia en la propera dècada.

Abstract

It has been shown that the effects of the bar and the spiral arms of the MW can induce kinematic groups in the local stellar velocity distribution. The aims of this thesis are: i) to characterise the observed moving groups, establishing observational insights into their origin, and ii) to explore to what extent we can use the kinematic imprints to constrain the large-scale structure of the MW and its recent evolution. To undertake the observational study we have applied the wavelet denoising technique to a compendium of kinematic, age and $[Fe/H]$ data for more than 24000 stars of the solar neighbourhood. We find that the dominant kinematic structures in the U–V plane are the branches of Sirius, Coma Berenices, Hyades-Pleiades and Hercules. From the large spread of ages and metallicities inside them, we refuse the models that relate their origin to cluster disruption. The Hercules branch is more conspicuous in the region of inner galactocentric radius, and for a region near the Sun in comparison to a region that is located further in the direction of rotation. For Hyades-Pleiades, Coma Berenices and Sirius the more negative the V component, the higher the mean metallicity. The Hercules branch does not follow this correlation and has a higher metallicity dispersion. On the other hand, we have performed test particle simulations in a flexible MW potential that is consistent with several observational constraints in order to explore the phase space available to the local stellar distribution. Our results show that the bar and the spiral arms create strong kinematic imprints on the velocity distributions. When the spiral arms and the bar act together, individual imprints of each component can be still identified in the final velocity distributions. The spiral arms crowd the kinematic region of Hercules and not only the bar, as traditionally believed. The arms also induce slightly tilted kinematic branches that resemble some of the observed ones. The low angular momentum moving groups such as Arcturus can have an origin related to the bar acting on a relatively hot stellar disc, which introduces a new perspective on the interpretation of its extragalactic origin. We find that the induced stellar kinematics groups depend on the structure and dynamics of the model and on the initial conditions of our experiments. We discuss if it is currently possible to use the stellar phase space groups as constraints to the large-scale structure and evolution of the MW.

The author was supported by the Predoctoral Fellowships of IEEC and Generalitat de Catalunya FI, and by the LENAC mobility program. This thesis has been carried out at the Departament d'Astronomia i Meteorologia (Universiat de Barcelona) and the Instituto de Astronomía (Universidad Nacional Autónoma de México). This study was supported by the CICYT under contracts AYA2003-07736 and AYA2006-15623-C02-02, by MEC contracts ESP2006-13855-C02-01 and AYA2009-14648-C02-01, grants CONACyT 60354 and 50720, and UNAM PAPIIT IN1 19708. The simulations were run at the HP CP 4000 cluster (KanBalam) in the DGSCA/ UNAM and at the CATON cluster (Sol) at the DAM/UB.

Contents

List of abbreviations

1D	One-dimensional
2D	Two-dimensional
3D	Three-dimensional
Λ-CDM	Lambda Cold Dark Matter
DF	Distribution Function
GC	Galactic Centre
IC	Initial Conditions
ILR	Inner Lindblad Resonance
LSR	Local Standard of Rest
MW	Milky Way
OLR	Outer Lindblad Resonance
RSR	Regional Standard of Rest
TWA	Tight-winding Approximation
WT	Wavelet Transform
WD	Wavelet Denoising

List of associated publications

- **Origin and evolution of moving groups I: Characterization in the observational kinematic-age-metallicity space**

  Antoja, T.; Figueras, F.; Fernández, D.; Torra, J. 2008, A&A, 490, 135

  http://adsabs.harvard.edu/abs/2008A%26A...490..135A

- **Stellar Kinematic Constraints on Galactic Structure Models Revisited: Bar and Spiral Arm Resonances**

  Antoja, T.; Valenzuela, O.; Pichardo, B.; Moreno, E.; Figueras, F.; Fernández, D. 2009, ApJ, 700, 78

  http://adsabs.harvard.edu/abs/2009ApJ...700L..78A

- **Dominant mechanisms in the evolution of the kinematic structures**

  Antoja, T.; Figueras, F.; Fernández, D. Highlights of Spanish Astrophysics IV, Ed. Figueras, F., Girart, J.M., Hernńdez, M., Jordi, C., Springer, 2007

- **Wavelet transform to characterise moving groups: observations versus dynamic effects**

  Antoja, T.; Figueras, F.; Fernández, D., Astronomical data analysis IV, ed. C. Surace, Edition on internet, 2006

- **Origin of the Moving Groups and their Contribution to the Determination of the Large-scale Galactic Potential**

  Antoja, T.; Fernández, D.; Figueras, F.; Moreno, E.; Pichardo, B.; Torra, J.; Valenzuela, O., Highlights of Spanish Astrophysics V, J.Gorgas, L.J. Goicoechea, J. I. Gonzalez-Serrano, J.M. Diego (in press), 2009

- **Midiendo la Via Lactea con Gaia**

  Antoja, T.; Torra, J.; Figueras, F.; Jordi, C., Revista Española de Física, 23, 3, 18, 2009

- **Connecting Moving Groups to the Bar and Spiral Arms of the Milky Way**

  Antoja, T.; Valenzuela, O.; Figueras, F.; Pichardo, B.; Moreno, E., IAU Highlights of Astronomy, XXVII IAU General Assembly, 2009

Part I

INTRODUCTION

Chapter 1

General introduction

1.1 Background

It is 400 years since Galileo Galilei performed the first telescope observation which showed that the luminous band that crosses our sky is made of numerous stars. We have just commemorated this and his other early telescope observations through celebrating the International Year of Astronomy 2009. Since that first observation of the Milky Way (MW), our understanding of the Galaxy has improved considerably regarding both its large-scale structure and, in more detail, our neighbourhood within the disc. Additionally, the advances in extragalactic astronomy and cosmology are becoming ever more connected to Galactic astronomy, setting the MW in a full cosmological scenario. We are now beginning to understand some aspects of its process of formation (e.g. Freeman & Bland-Hawthorn 2002).

In the last two decades the study of the MW has experienced outstanding progress owing to the advent of high-quality observations, better models and methods, and the use of powerful computation facilities (e.g. Turon et al. 2008). Among the new findings, it has been shown that the Galaxy has several non-axisymmetric structural components. The most relevant are the Galactic bar and the spiral arms. In particular, the solar neighbourhood (a sphere of about 200 pc around the Sun) has been studied in depth thanks to the stellar positions and velocities that were determined by the Hipparcos mission. Despite being an extremely tiny region compared to the whole extension of the Galaxy, the solar neighbourhood has proved to be of great value. Due to the high precision of the data in this region, this region has provided us with important information regarding some processes that take place in the MW. The rich kinematics or the complex stellar chemical distribution in the solar neighbourhood may constitute a set of imprints and fossils left after several Galactic processes.

The classic approach to studying the kinematics of the solar neighbourhood has been linked to the determination of the velocity distribution function using simple models such as the Schwarzschild ellipsoid and its characterisation through the vertex deviation or, in general, the moments of order n. However, the observations have revealed that the velocity field of the solar neighbourhood exhibits a high degree of complexity. One of the most intriguing features of the velocity distribution is the existence of moving groups. These are stellar streams crossing the region around the Sun which are seen as overdensities in the velocity space. The distribution of neighbouring stars in the velocity space is far from being smooth and includes several of these moving groups.

The study of stellar moving groups in the solar neighbourhood has a long tradition in Galactic astronomy (see Chapter 2 for a historical overview), going back to the discovery of the Pleiades, Hyades and Ursa Major groups (Mädler 1846, Proctor 1869). After this pioneering work, the study of moving groups continued with Eggen, who first tried to provide a thorough characterisation of their properties (Eggen 1996b and references therein). Since these structures shared their kinematics with certain stellar clusters, these first studies worked exhaustively on the hypothesis that moving groups were a result of the dispersion of clusters.

The advent of Hipparcos astrometric data led to the definitive confirmation of the existence of moving groups. However, once the first attempts to evaluate the evolutionary state and the chemical composition of the members of moving groups were made, the stars in a given group seemed to show a very wide range of ages and metallicities, and distributions similar to those observed for the whole sample under study. Since then, a considerable amount of work has been performed in an attempt to explain the origin of the moving groups in keeping with these new findings.

At present, the origin of these kinematic structures is far from completely understood although it is more than 140 years since they were discovered (see Chapter 2 for a comprehensive review of the theories of their origin). Nowadays, several possibilities are considered. As first proposed, moving groups could be the result of internal disc processes such as stellar cluster disruption. Alternatively, they could be due to the induced dynamical effects of the non-axisymmetric components of the MW (i.e. spiral arms and bar). It has been proposed that some moving groups are remnants of past accretion events, whereas others could be due to external dynamical effects on the disc resulting from interaction events. Although they were initially considered mutually exclusive, all such mechanisms are present in current galaxy formation models. A combination of some of these ideas is a complex but fascinating scenario. Moreover, since they may be fossils of these dynamical processes, whatever they are, the moving groups could provide clues about important characteristics of the Galaxy and about some dynamical mechanisms that occur in it.

Recently, the hypothesis that moving groups are due to the induced kinematic effects of the non-axisymmetric components of the Galaxy has gained popularity. This is partially because of the consistency of one of the observed moving groups in the solar neighbourhood with the effects of the Galactic bar resonances. According to this hypothesis, the orbital structure that is induced by the bar or the spiral arms and their resonances could cause overdensities in the velocity distribution. In other words, a moving group would be a group of stars that crosses the solar neighbourhood following a certain type of orbit under the influence of the bar and/or the spiral arms. Here, there is additional motivation apart from the challenge of unravelling the enigma of the origin of moving groups. If this kind of kinematic structure is shown to depend on the characteristics of the bar and the spiral arms of the MW, it may prove very useful for our understanding of the large-scale structure and dynamics of the MW in its present and also its past form. Indeed, some studies have already ventured as far as using some observed moving groups to constrain parameters such as the bar pattern speed or certain characteristics of the spiral arms. The possibility of constraining the properties of the bar and the spiral arms of the MW using moving groups is very promising as a complement to other methods because of the lack of information about some characteristics of these non-axisymmetric components.

1.2 Thesis aims and methodology

It has already been shown that the effects of the non-axisymmetric components can induce kinematic groups in the local stellar velocity distribution. The most compelling evidence is the demonstration that the effects of the Galactic bar resonances can trigger a kinematic group similar to the observed Hercules group. But despite the efforts made in these recent studies, the resonant or dynamical origin of the moving groups has not been proved for any particular observed kinematic structure. In fact different plausible origins coexist for certain groups. Moreover, there is a long list of unresolved questions that are still a matter of debate or that have not yet been addressed. These are some examples:

- What is the spiral arm contribution to the kinematic structure in the solar neighbourhood?
- Which is the power of the bar to induce moving groups of low angular momentum such as the observed Arcturus?
- Is it possible to recover particular imprints of the bar and the spiral arms when the two non-axisymmetric components act together? Or does the combination of these two components create additional kinematic groups?
- How can we assure that one particular group is due to a given effect of the bar or the spiral arms?

- Are all the observed moving groups at the solar neighbourhood induced by effects of the spiral arms and the Galactic bar?
- What are the capabilities of these imprints to constrain the properties of the bar and the spiral arms? What properties can be constrained and what can not?
- Which is exactly the dynamical mechanism that trigger the moving groups? Are they groups of chaotic orbits or overdensities around resonant periodic orbits?
- How does the Galactic evolution alter this interpretation for the origin of the moving groups and their capability to constrain the large-scale structure of the MW?

All these unresolved questions in the field show that further research is required. In this thesis we attempt to answer some of them.

This thesis deals with the origin of the moving groups with particular reference to the possibility that moving groups are imprints of the non-axisymmetric components of the MW (bar and spiral arms) which would mean that they could be used to constrain the large-scale structure of our Galaxy. The specific aims of this research are:

1. To analyse and characterise the observed moving groups, establishing observational insights into their origin.

2. To explore the extent to which we can use the kinematic imprints to constrain the large-scale structure of the MW and its recent evolution

To conduct the research entailed in this thesis, we have chosen two different approaches: an observational and a theoretical methodology. On the one hand, we analyse an observational sample, compiled from several catalogues, using multiscale statistical techniques in order to control the Poisson noise. On the other hand, we perform test particle simulations in a flexible MW potential that is consistent with several observational constraints in order to explore the phase space available to the local stellar distribution.

Both for the observational and simulation approaches we aim to analyse and characterise the kinematic structures, i.e. establish their shape, size or statistical significance, and in some cases their age and chemical composition. This requires the use of robust statistical techniques. Moreover, the comparison between the observed and simulated distributions requires the use of exactly the same robust statistical methods. We use the Wavelet Denoising (WD) technique which allows us to obtain distribution functions via a smoothing/filtering treatment at different scales that eliminates Poisson noise. The WD has been used in other astrophysical topics, but has never been applied to this particular subject.

The observational approach has been motivated by two important observational contributions that have provided new material that complements the Hipparcos and Tycho astrometric

data: i) the CORAVEL radial velocity data for a significant number of late-type stars belonging to the Hipparcos catalogue (Nordström et al. 2004 for dwarf stars and Famaey et al. 2005 for giant stars); and ii) the uvby–β survey of FGK dwarf stars, which has allowed the derivation of ages and metallicities (Nordström et al. 2004). Also, data on OBA-type stars (Asiain et al. 1999a, Torra et al. 2000) and M dwarfs (Reid et al. 2002, Bochanski et al. 2005) complete an extensive sample which is ready to be used for the analysis of the kinematic structures. Therefore, the whole compiled sample constitutes an extensive compendium of the best available astrometric, photometric and spectroscopic data for more than 24000 stars in the solar neighbourhood. We have applied the WD multiscale technique to this sample to characterise and analyse the moving groups in the U–V–age–$[Fe/H]$ space. This observational analysis establishes constraints for the subsequent study of the origin of moving groups. This work has also required rigorous treatment of the observational errors, constraints and sample biases.

The simulation approach is performed using numerical integrations of test particle orbits which are distributed in a disc under a MW potential model. We have taken advantage of the PM04–MW potential model (Pichardo et al. 2003b, 2004) which is a specific model for the MW potential that is consistent with several recent observational constraints. This model consists of an axisymmetric part together with a bar and two spiral arms as non-axisymmetric components. This new model is very flexible to be adapted to observations. It is built directly with a realistic 3D mass distribution from which the gravitational potential and the forces are derived. To our knowledge, the study of the effects of a mass distribution model (and in particular of this new model) on the local velocity distribution which is addressed here has not been considered before. Another important aspect of our study is the use of a great variety of initial conditions and integration times and procedures. These attempt to represent stars that are born at different times and with different kinematic conditions, like those in the solar neighbourhood, and have been designed to be as consistent as possible with some aspects of the Galactic evolution. An exhaustive study of both the model and the test particle initial conditions has been required for this thesis. With these simulations we obtain the induced kinematic distribution not only of the solar neighbourhood but in other positions of the disc. The distributions are also treated with the WD multiscale technique, as the observational sample is. This methodology allows us to evaluate the role of realistic non-axisymmetric components of the MW, namely the spiral arms and the bar, on the formation of moving groups in the disc. We explore the parameter space of the PM04–MW potential model using different simulations in order to evaluate the effects of each particular characteristic of the spiral arms or the bar on the velocity distributions. We also use a method to ascertain the regularity of the particle orbits in the kinematic structures that are created in the test particle simulations.

1.3 Thesis outline

This thesis is structured as follows. After this introductory chapter of Part I, Chapter 2 reviews the observations that led to the discovery of the moving groups, the past and current studies which have attempted to establish their properties and the theories of their origin proposed to date. A brief description of the observational data, statistical methods for data analysis, dynamical models and simulations that have contributed to this field is also offered.

Part II is concerned with the statistical methods that are applied in this thesis to observational and simulation data. In Chapter 3, descriptions of the wavelet transform and the wavelet denoising methods are provided. The particular algorithms and filters used are described. Chapter 4 contains a detailed description and some examples of how these methods work. We also explain what their capabilities and advantages are when compared to other techniques that have been used in this discipline. The chapter ends with a description of the software packages used, the implementation process and the CPU costs of the method.

Part III presents the observational study used in this thesis and deals with the characterisation of the observed moving groups. Chapter 5 presents the observational data that we use, together with their precisions and possible biases. Chapter 6 characterises the structures in the velocity plane in depth, and also gives comparisons between the moving groups for different spectral types and luminosity classes, and different positions on the Galactic disc near the Sun. Then, Chapter 7 and Chapter 8 constitute a first attempt to analyse the age and metallicity distributions of the kinematic groups, respectively. Finally, the main consequences of the observational work are summarised and discussed in Chapter 9.

Part IV is concerned with our test particle simulations. First, Chapter 10 provides a description of the simulation method and the initial conditions. We also present the method for quantifying the regularity of the orbits. This chapter examines the advantages and drawbacks of our simulation methodology as it is compared with other theoretical approaches used in this area. Chapter 11 describes the essential characteristics of the PM04–MW potential model and is also concerned with contrasting this with other widely-used models, with special emphasis on their force fields.

Part V reports the results and conclusions of the test particle simulations. First, Chapter 12 deals with some preliminaries regarding the presentation of the results, by giving more specific details about the simulations and methodology. Chapter 13 examines the kinematic effects induced by the spiral arms while Chapter 14 does the same with the bar. The effects produced on a disc with hotter kinematics are shown separately in Chapter 15 as they deserve special considerations. Finally, Chapter 16 presents the results of the spiral-bar PM04–MW potential model; a model that includes both bar and spiral arms. For all these chapters, we explore

the parameter space of the PM04–MW potential model using different simulations in order to evaluate the effects of each particular characteristic of the spiral arms or the bar on the velocity distributions. We also explore the effects on the disc with different initial conditions. At the end of the main chapters of this part, we summarise and discuss the results.

Finally Part VI summarises the main outcomes of the whole thesis. It brings out the general conclusions and examines the perspectives for future studies of moving groups. At the end of the thesis, we present the bibliography and three appendixes. Appendix A is where we discuss some considerations about the initial conditions. Appendix B contains additional results of our simulations. In Appendix C we speculate about the possible resonance influence on the dark matter particles in the dark disc predicted in recent cosmological simulations of galaxy formation.

1.4 Introductory definitions

The (U, V, W) velocity reference system will be used throughout this thesis. It is centred on a given position on the Galactic plane and moves following the Regional Standard of Rest (RSR). The RSR is defined as the point located at a galactocentric radius R that describes a circular orbit around the centre of the Galaxy with a constant circular speed $V_c(R)$. For the solar neighbourhood this is called the Local Standard of Rest (LSR). U is the radial velocity component, which is positive towards the GC; V is the azimuthal component, positive in the direction of Galactic rotation; and W is the component perpendicular to the plane, positive towards the North Galactic Pole. The velocities with respect this reference system are sometimes called peculiar velocities. A sketch of this velocity reference system in the solar neighbourhood and in other regions of the Galactic plane is shown in Figure 1.1.

The Sun moves with a certain peculiar velocity with respect to the LSR, which is referred to as $(U, V, W)_\odot$. The velocities of the stars around the Sun are often given with respect to the Sun and then they are called heliocentric velocities and despite being confusing, are often also designed as (U, V, W). In the observational part of this thesis (Part III), we use heliocentric velocities as we only work with the velocity distribution near the Sun. In Parts IV and V, as we deal with simulated velocity distributions over the whole Galactic plane, we use peculiar velocities.

Regarding the spatial coordinate systems, we use galactocentric cylindrical coordinates (R,ϕ,z) with the azimuth $\phi > 0$ in the direction of rotation as indicated in Figure 1.1. The origin of ϕ is on the line between the Sun and the GC. In our observational study, the Sun is assumed to be at $\phi = 0°$, $R = R_\odot \equiv 8.5\,\mathrm{kpc}$ and $z = 0$. For the simulations, given the uncertainty

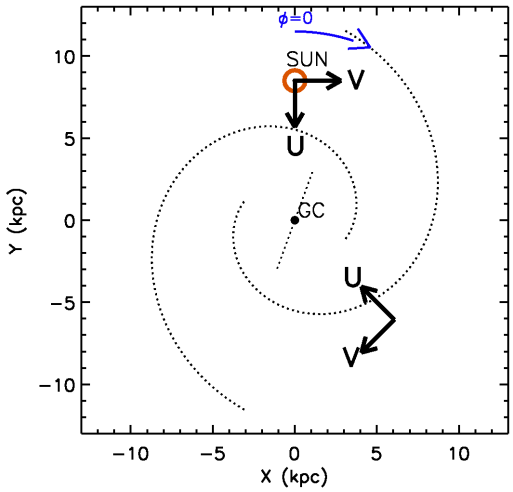

Figure 1.1: **Spatial and kinematic reference systems.** Sketch of the reference systems for the spatial positions and velocities used in this thesis superimposed on a rough sketch of the MW disc.

in the exact orientation of the bar and especially the spiral arms, the position of the simulated Sun with respect to these non-axisymmetric components is variable. Initially, as default, the Sun will also be located as assumed above. The Cartesian galactocentric XY coordinate system is oriented as in Figure 1.1 with the Sun at $X = 0$ and $Y = 8.5\,\mathrm{kpc}$. Occasionally, we use the coordinate η which is centred on the Sun and positive in the direction of Galactic rotation taken e.g. from Asiain et al. (1999a) and that is in fact equivalent to X.

Chapter 2

Historical evolution of the moving groups study and interpretation

In this chapter we review the observations that led to the discovery of the moving groups, the past and current studies devoted to establish their properties and the theories proposed up to now for their origin. A brief description of the observational data, statistical methods for data analysis, dynamical models and simulations that have contributed in this field is also offered. It will be shown how this field is an example of elegant applications of statistical techniques to large samples of data. Also, theoretical works on this subject have involved numerous and varied procedures and modelling which were developed in a parallel manner: analytical approximations, tests particle simulations or N-body simulations. Moreover, the study of the moving groups has progressively been linked to the study of the MW large-scale structure and, more recently, to its formation and evolution. Actually, as it will be seen in this chapter, these kinematic structures, which up to now have been detected only in the solar neighbourhood, have turned out to be a tool to constrain some of the structural characteristics of the MW in its present and past form. However, at the moment the origin of these kinematic structures is far from being completely understood.

The review is done approximately in chronological order and divided in sections which try to group the different stages of the study of the moving groups according to the methods and data used and the theories suggested to explain the origin of moving groups. The chapter tries to describe the more relevant studies for this thesis.

2.1 Discovery of the moving groups

The serendipitous discovery of the first moving group was a consequence of the attempt to determine the solar motion in the 18-19th century. The effect of the Sun's motion would be an apparent divergence of the proper motions of the neighbouring stars which the Sun was moving towards, and convergence of those in the region it was leaving. The German astronomer J.H. von Mädler was one of those who were trying to measure the proper motions of the stars around the Sun in order to deal with this issue. By examining some of these measures, Mädler (1846) determined the region towards which the Sun was moving and, assuming that the orbit of the Sun was circular, he concluded that the central point of the Sun's orbit was located near the Perseus constellation. As the Pleiades open cluster was the brightest one near that region of the sky, he announced that the Pleiades -and with strong probability Alcyone– were the central group of the entire system which the Sun and the other stars were moving around (the "central Sun" theory):

> German: *Entbehren die Schlüsse, welche ich in Vorstehenden, freilich in gedrängtester Kürze, mitgetheilt habe, nicht alles Grundes, so ist hier der Angelpunkt gefunden, um den das gesammte Heer der übrigen Fixsterne seine ungeheuren Bahnen beschreibt.* (English: If the conclusions, which I have only described above in the uttermost brevity, are not unfounded, then the central point which the entire crowd of all other fixed stars move around in their immense orbits has been found.)

Moreover, not only did he notice the uniformity of the proper motions of 11 stars of this cluster but also, more important, he discovered that, among the stars within several degrees in the sky of this group, a large percentage exhibited the same motion. This fact was a confirmation of his theory, as these central stars, expected to be fixed, were just reflecting the Sun's motion[1]. Although his interpretation was wrong –this conception of the Galaxy was quickly refuted by other astronomers–, he had in fact discovered the Pleiades moving group.

It was Proctor (1869) who identified several preferential directions of movement in the solar neighbourhood. He reported the existence of two more prominent *star-drifts* apart from the one of the Pleiades: one in the constellation of Gemini and Cancer (later called Hyades moving group) and another in Leo (later called Sirius moving group)[2]. He wrote in the Proceedings of the Royal Society of London:

[1] Additional bibliography: Loomis, E., *The recent progress of astronomy: especially in the United States*, Arno Press, USA, 1980

[2] Although they were first named as the constellations where they were observed, finally the streams took other names from open clusters or stars that shared the same kinematics: Pleiades (stream 0), Hyades (stream I or Taurus group) and Sirius (stream II or Ursa Major group).

A careful examination of the proper motions of all the fixed stars in the catalogues published by Messrs. Main and Stone (Memoirs of the Royal Astronomical Society, vols. xxviii. and xxxiii) has led me to a somewhat interesting result. I find that in parts of the heavens the stars exhibit a well-marked tendency to drift in a definite direction. In the catalogues of proper motions, owing to the way in which the stars are arranged, this tendency is masked: but when the proper motions are indicated in maps, by affixing to each star a small arrow whose length and direction indicate the magnitude and direction of the star's proper motion, the star-drift (as the phenomenon may be termed) becomes very evident.

Proctor (1869)

After Proctor's discovery, Kapteyn (1905) announced his theory of stellar motions, offering for the first time an explanation for the existence of the two streams found by Proctor (1869). When he examined a catalogue with the proper motions of 3200 stars, he noticed also that they were incompatible with the commonly accepted contemporary assumption that the motions of the stars were randomly distributed. Actually, the observed proper motion distribution could be explained by his theory of *star-streaming* by which all the stars, without exception, move in the two preferential and opposite directions. This was a consequence of two once distinct but now intermingled populations of stars moving relative to one another, with different mean motions relative to the Sun.

At that time, Kapteyn was devoted to study the *sidereal problem*, that is understanding the architecture of the MW system through statistical techniques (star distributions through space as a function of absolute magnitude, spectral type and distance). Proper motions were supposed to be very useful in this study. Among others, they were used to derive the *velocity law* (distribution of velocities). Also, they could be employed as distance indicators, since it was then commonly accepted that larger proper motion was a guide to nearness of the star on the assumption of random stars' motions. The discovery of the invalidity of this premise led him to accept the inadequacy to use stellar motions to solve the sidereal problem. However, as it will be seen in later chapters, nowadays the relevance of the stellar streams in the study of the architecture of the MW –the "modern" sidereal problem– is almost unquestionable.

Like Kapteyn, Eddington (1906) interpreted the streams as two swarms in relative motion and with the movement of the stars in each stream being separately random and following independent Maxwellian velocity distributions. Schwarzschild (1907) gave an alternative interpretation when he found that the observed distribution of velocities could be also explained by a unique ellipsoidal distribution with the proper reference frame and three unequal axes, that is a different velocity dispersion for each direction. However, no dynamical explanation for the later so used "Scwarzschild distribution" was offered at that moment[3].

[3]For a deeper discussion about these studies see (next page):

In his 'Stars, Motions in space and the two-drift theory, A tentative explanation of the "two star streams" in terms of gravitation', Turner (1912) gave possibly the first explanation for the streams related to the orbits of stars moving in a one single global system. According to this study, one stream would comprise stars moving with elliptical orbits that approach the centre of the whole system, and the other one, elliptical orbits leaving the centre. Also Jeans (1922a) discussed the possibility that the streams were due to circular motion in both directions around the centre of the local system, as an integral part of the Galactic system in steady motion. Modern explanations for the moving groups concerning orbits have been proposed recently as well (see Section 2.4), which are not so different to these pioneering studies. Besides, Lindblad (1923, 1925a) studied the idea that the Kapteyn streams were due to encounters of stars with vast local accumulations of matter which produce great deviations from the stars' original paths toward the solar neighbourhood, which perhaps would cause the suggested final streams of opposite rotation.

The preferential or ellipsoidal motion and also the asymmetry of the velocity distribution[4] were in the end explained dynamically thanks to the theory of Galactic rotation of Lindblad (1925b). B. Lindblad showed that the ellipsoidal distribution was a simple consequence of the orbits of stars travelling around the centre of the Galaxy and being not circular but elliptical orbits with different inclinations to the Galactic plane. This can be considered as a pilot usage of the local velocity distribution to explain general features of the Galaxy, namely its rotation. However, the presence of marked streams moving in the direction of the groups of Taurus (Hyades) and Ursa Major (Sirius) still complicated the interpretation of the velocity distribution.

2.2 Disruption of clusters

The coincidence between the two favoured directions of motion and the motion of the well-known clusters, suggested that the clusters were the centre of bigger groups with members scattered all

- Chandrasekhar, S., *Eddington, the most distinguished astrophysicist of his time*, Cambridge University Press, Great Britain, 1983
- Trumpler, J., Weaver, H.F., *Statistical Astronomy*, Dover Publications, USA, 1953
- van der Kruit, P.C., van Berkel K., *The Legacy of J.C. Kapteyn*, Kluwer Academic Publishers, The Netherlands, 2000
- Voigt, H.H., *Karl Schwarzschild: Gesammelte Werke / Collected Works, Volume 1*, Springer, Germany, 1992

[4] The asymmetric drift was deeply studied by Stromberg (1925) using the available radial velocities at that time. He determined that the group motion of several classes of stars was continuously larger along a given axis for higher velocity dispersions of the group, causing an asymmetry in the general velocity distribution. Consequently, the Sun's velocity depended on the class of objects to which it was referred.

Table 2.1: **Velocities of the moving groups.** Mean heliocentric velocities of some moving groups studied by Eggen (1958, 1971, 1996a,b) and references therein.

STREAM	$U(\mathrm{km\,s^{-1}})$	$V(\mathrm{km\,s^{-1}})$	$W(\mathrm{km\,s^{-1}})$
Pleiades(Stream 0)	-12	-21	-10
Hyades (Stream I)	-40	-16	-2
Sirius(Stream II)	15	1	-11
NGC 1901	-26	-10	-1
HR1614	-5	-60	-6
IC 2391	-21	-16	-8
61 Cygni	-80	-53	-6
ζ Herculis	-54	-45	-26
Arcturus	9	-110	-9
Kapteyn's star group	-13	-228	-16

over the sky. For example, Wilson (1932) committed himself to establish the cluster and group members of Taurus (Hyades) finding that stars sharing this motion were spread through the whole sky. Afterwards the dynamics of the *moving clusters*, which were the originators of the streams in the solar vicinity, was explored by many authors. For instance, Jeans (1922b) studied the shapes and rates of expansion of the clusters. Later Bok (1934), motivated by the different picture of the Galaxy at that time, repeated the previous analysis by studying the stability of the clusters subject to tidal forces of the MW as a whole and to the random encounters. This reinforced the disruption of clusters as a plausible origin for the moving groups.

Subsequent to the discovery of the first moving groups (Mädler 1846, Proctor 1869), others were discovered in other regions of the sky. After the mentioned pioneering studies, Olin J. Eggen worked intensively on the establishment of the spatial and kinematic properties of many of these stellar streams in the solar neighbourhood (see Eggen 1996b and references therein). The main moving groups studied by Eggen and their heliocentric velocities are shown in Table 2.1.

Following the previous ideas, Eggen worked on the hypothesis that moving groups are a result of the dispersion of stellar clusters or "cluster evaporation", being the open clusters with similar kinematics the remnants of bigger previous structures. In later studies (e.g. Eggen 1996b), he developed more the argument as follows. The individual stars, after their birth in a cluster, followed isoperiodic orbits and the internal and external forces on the cluster caused small perturbations on the components U, V and W of the velocity, forming a halo of stars around the clusters. He called these expanded clusters *superclusters*. When the perturbations

became stronger, a tube of orbits was generated in the velocity space intersecting the solar neighbourhood. Similarly, Weidemann et al. (1992) suggested the possibility that the Hyades supercluster was formed by the superposition of several similar *needles* (escaped stars from a cluster) generated in the process of cluster evaporation which had been made successively by a common parent giant molecular cloud in a prolonged star formation process.

2.3 The Hipparcos Era and the ages of the moving groups

The advent of Hipparcos astrometric data evidenced the need of using and developing more sophisticated statistical methods to study the moving groups (see also Section 4.3). Such amount of data led to the definitive establishment of the existence of moving groups and to the recognition of substructures within them (Chereul et al. 1998, Asiain et al. 1999a). In addition, together with Dehnen (1998), all these authors attempted for the first time to evaluate the evolutionary state of the members of some moving groups. This was necessary in order to establish their origin and evolution and, in particular, to prove if they were disrupted clusters. Dehnen (1998) used the astrometric data from Hipparcos to derive the velocity distribution only from positions and proper motions using a maximum likelihood algorithm. As this method did not require radial velocities, his sample was very extensive (14369 stars) and had less observational biases. He considered the U–V plane as a superposition of a smooth background distribution with several prominent maxima corresponding to the moving groups. He used subsamples composed of stars with different spectral types using the (B-V) index to study the velocity distribution of old and young stars and found that the red main sequence stars, which were on average older, also presented the maxima, which seemed in contradiction with the hypothesis of the cluster disruption. He also pointed out that the component W of the sample was not rich in kinematic substructure. Besides, according to this author the streams are responsible for the vertex deviation[5] and follow the asymmetric drift relation as a whole.

Once again without radial velocities and as no photometric data were available, Chereul et al. (1998) could only use what they called *palliative* ages which were estimated from absolute magnitudes and colours. Using a procedure based on the wavelet analysis to establish the overdensities in the velocity space and their significance, they showed that the age distribution of the stars in moving groups (with dispersion about $\sigma \sim 6.3$ km s^{-1}) seems to be similar to that observed for their whole sample. By contrast, at smaller scales ($\sigma \sim 3.8$ km s^{-1} and $\sigma \sim 2.4$ km s^{-1}) they found that moving groups are structured in 2 or 3 substructures with ages coherent with the scenario proposed by Weidemann et al. (1992). He therefore suggested that

[5] Angle in the velocity space between the direction pointing from the Sun to the GC and the direction of the major principal axes of the velocity ellipsoid.

the superclusters could have formed due to the random superposition of minor groups.

Using an adaptive kernel and wavelet transform analysis, Skuljan et al. (1999) studied the distribution function in the U–V plane of a sample of 4000 Hipparcos stars with available radial velocities. These authors observed that the distribution function was characterised by a few branches at larger scales than the moving groups that are diagonal, parallel and roughly equidistant. The branches were called Sirius, middle branch, Pleiades branch, which included the Hyades moving group, and Hercules branch. They were seen in both early-type and late-type stars in an attempt to separate young and old stars.

More precise ages, derived using Strömgren photometry, were used by Asiain et al. (1999b) to study young moving groups in the U–V–*age* space with kernel functions. They observed that the velocity dispersion of several substructures within the Pleiades moving group was compatible with that expected for the evolution of a stellar complex as described by Efremov (1988). This conclusion was restricted to groups of stars with ages up to about 1 Gyr as both differential Galactic rotation and disc heating would have dispersed older groups among the field stars.

The previous studies show that the following advances in the characterisation of the moving groups required the availability of two key parameters: radial velocities and precise ages. The first survey of Coravel for dwarfs stars FGK with Strömgren photometry (ages) was published in 2004 (Nordström et al. 2004) (14139 stars). In a preliminary study of the U-V plane of this sample, these authors corroborated the existence of the branches of Skuljan et al. (1999). Famaey et al. (2005) used radial velocity data of Coravel for 6000 Hipparcos KM giant stars. These authors identified the superclusters of Hyades-Pleiades, Sirius and the Hercules stream through a maximum-likelihood method based on a Bayesian approach and imposing a Gaussian distribution for the velocities. More important, they showed that isochrones in the H-R diagram indicated that the stars belonging to the moving groups had a wide range of ages. Furthermore, Famaey et al. (2007, 2008) showed that the distributions of mass, metallicity and age of the stars in some of the streams were incompatible with their being a product of a cluster disruption.

All these observational studies and specially the characterisation of the evolutionary state of the moving groups demanded a different explanation for their origin. Guided by old and contemporary theoretical studies (see Section 2.4), Dehnen (1998) speculated that orbital resonances, probably of the Galactic bar, could be the cause of the existence of most moving groups observed in the solar neighbourhood. However, he was still relating the moving groups to the clusters as he specified that the process may consist of an evolving resonance that traps a cluster as a whole, originally born in a near-circular orbit, and shifted it to its current position in the U–V plane. Besides, Skuljan et al. (1999) suggested that the streams were due to effects of the spiral structure combined with the initial velocities of the stars. Other authors began to use the term *dynamical* or *resonant stream* (e.g. Famaey et al. 2005).

2.4 Dynamical effects of the MW bar and spiral arms

The first new theoretical arguments in favour of a dynamic origin of the moving groups were put forward by Mayor (1970). He interpreted the deviation of the vertex of the velocity distribution and the streams in terms of the perturbation by the spiral density wave of Lin (1971). However, he could still not abandon the idea that the existence of the streams was a consequence of the initial conditions affected later by the perturbation.

On the other hand, Kalnajs (1991) proposed, for the first time after the establishment of a modern vision of the general structure of the MW, a dynamical model to explain the existence of moving groups absolutely not related to the formation and evolution of clusters. He pointed out that they are a consequence of the Sun being near the outer parts of the OLR of the Galactic bar and due to a mechanism similar to the one that forms rings in external galaxies (Buta 1986). He identified the groups of Hyades and Sirius with the stellar orbits that cross near the solar neighbourhood which are closed orbits in the bar's reference system. In particular, the moving group of Hyades was associated to the inner orbits (orientation perpendicular to the bar) while Sirius was related to the external orbits (parallel to the bar). From this link, this author estimated the orientation, intensity and pattern speed of the bar. For instance, assuming a circular velocity of 225 $\mathrm{km\,s^{-1}}$ in the solar circle (8.5 kpc), the bar's pattern speed was 46 $\mathrm{km\,s^{-1}kpc^{-1}}$ (placing the OLR at 8.3 kpc) and it was inclined 56° in the direction of rotation, being the first time that the streams are used to estimate characteristics of the large-scale structure of the MW. Also, according to his model the radial extent of the region where these orbits cross is proportional to the square root of the bar force field.

After the model by Kalnajs (1991), other studies focused on the effects of the bar or the non-axisymmetric components of the MW on the velocities of the solar neighbourhood. For instance, Weinberg (1994) showed that the bar can cause distinctive stellar kinematic signatures with the OLR being near the solar position. Although the location of the OLR in this study ($R \sim 5\,\mathrm{kpc}$) is slightly different from the range of locations which are considered nowadays, he mentioned the interesting point that the kinematic signatures depend on the evolutionary history of the bar and therefore velocity data may be used to probe the evolutionary history as well as the present state of the Galaxy.

Furthermore, the studies of Raboud et. al (1998) and Fux (2000, 2001) focused on the origin of the Hercules structure and its connection to Galactic bar resonances. The Hercules moving group, also called the U anomaly, was identified in the 70s using samples of late spectral type (see Table 2.1) and is a group of stars that move in the direction of the Galactic anti-centre and lags with respect of the LSR[6]. Using the self-consistent numerical models by Fux (1997), they

[6] The existence of a group around the LSR and the Hercules structure is also often called *bimodality*.

showed that the stars of Hercules follow the so called *hot orbits*. These are stars with Jacobi energies[7] larger than the effective potential in its saddle points that can move away of the inner parts of the bar and travel, in an erratic manner, until crossing the corotation circle and finally escape. Afterwards, in Fux (2001), where he used test particle and also N-body simulations, he specified that this stream is due to an overdensity of chaotic orbits near the external regions of the OLR, that at certain bar inclination angles, get a radial movement towards the outer MW.

By contrast, Dehnen (1999, 2000) proposed, through test particle simulations, that the Hercules structure consists of stars that have been scattered by the OLR. In particular, for several pattern speeds and orientations of the bar, a group of unstable chaotic orbits called $x_1 * (2)$ causes the separation of the velocity distribution in two groups, being the one with slower rotation and mean outward radial motion associated to the Hercules moving group. In that study, the low probability of this bimodality being caused by the resonant spiral structure of the MW was also remarked. He argued that the spiral arm perturbation affects mainly stars with epicycles smaller than the inter-arm separation, being the Hercules epicycles substantially larger (of the order of 3 kpc).

The hypothesis of the dynamical origin of these structures have gained popularity partially because of the consistency of the observed Hercules structure with the effects of the Galactic bar resonances. Consequently, steady and transient spiral arms were also proposed to explain the existence of some of these stellar groups similarly as it has been done with the bar. By numerically integrating test particle orbits, De Simone et al. (2004) showed that stochastic spiral density waves can produce kinematic structures. Few but intense transient spirals reproduced structures which are arranged in branches similar to those found by Skuljan et al. (1999). The backward integration of Dehnen (2000) was used also in De Simone et al. (2004) and it allowed him to study particles with different ages in the simulations, which led him to conclude that particles in each simulated branch had a wide range of ages as the observed ones.

Also Quillen & Minchev (2005) developed a method to quantify through orbital numerical integration the velocity distribution function that would result from the existence of families of periodic orbits around the solar neighbourhood due to the spiral structure. They found, for models with the Sun in the outer limits of the ILR 4:1 and for a certain spiral arms orientation, the existence of two periodic orbits in the positions of Coma Berenices and Hyades-Pleiades (considered here as a unique group).

The studies by Chakrabarty (2007) were the first attempt to analyse the kinematic response

[7] In the non-inertial reference frame (moving with the pattern speed of the bar) the potential is independent of time, which gives an integral of motion, the Jacobi integral, defined as $E_J = \frac{1}{2}\mathbf{v'}^2 + \Phi_0 + \Phi_b - \frac{1}{2}|\mathbf{\Omega_P} \times \mathbf{r'}|^2 = \frac{1}{2}\mathbf{v'}^2 + \Phi_{eff}$, with $\mathbf{v'}$ the velocity of the system. The primes show coordinate with respect to the non-inertial reference system.

of the outer parts of Galactic discs to the bar and to the spiral structure acting separately and also simultaneously. Using test particle simulations she showed that the combined effect of a bar and 4 weak spiral arms is necessary to reproduce accurately the five significant moving groups (Hercules, Hyades, Pleiades, Coma Berenices and Sirius) of the solar neighbourhood. However, in that study the spiral arms seem to contribute only in the fine kinematic structure, thus weakening constraints on the MW spiral structure based on the solar neighbourhood kinematics. In her simulations, the Hercules stream was created by scattering off the OLR of the bar and the other moving groups were a consequence of irregular orbits and resonant families. In Chakrabarty & Sideris (2008) they found that their models caused strong chaoticity in the outer parts of the disc, specially when the major resonances of the bar and the spiral overlap.

2.5 Extragalactic imprints

While the dynamic or resonant mechanism was shown to be a plausible explanation for the main moving groups, new completely different mechanisms were proposed. The discovery of the Sagittarius dwarf galaxy still experiencing disruption by the MW (Ibata et al. 1994) and also of the associated tidal debris of this and other dwarfs (Yanny et al. 2000, Martinez-Delgado et al. 2001) provided evidence for the galaxy formation processes in the Λ-CDM cosmogony. But also all these new findings, together with other observations which seem to indicate the presence of kinematic substructure in the halo of the MW (for example the Kapteyn's star group of Table 2.1 that was assigned to the halo by Eggen 1996b), raised the question of whether some of these streams could be found in the solar neighbourhood as debris of disrupted accreted dwarf galaxies and perhaps seen as clumps in the velocity space similar to the moving groups.

In this sense, the study by Helmi & White (1999) was the first to analyse the kinematic signatures of disrupted satellites in a relatively local volume. Using N-body simulations in fixed halo and disc potentials, they characterised the variation of the structures with time and in different points of the orbits in the U–V–W velocity space and in the action-angle space. In the U–V plane, the stars of the same stream showed similarities but also a large velocity range. A distribution with the characteristic shape of a banana in this plane was obtained for some cases and certain positions of the orbit (specially near the apocentre). As the stars with the same progenitors should have similar integrals of motions, the distributions of stars in other spaces began to be explored in order to identify better the streams. With a combination of analytic work and cosmological simulations, it was studied how this debris would appear in the angular momentum space L_z–$L_\perp$, the $E - L_z$ and $E - L$ planes and debris from one satellite were identified when they applied these methods to a group of metal-poor stars selected from several samples (Helmi et al. 1999b, Helmi & de Zeeuw 2000).

More important, hydrodynamical numerical simulations, which had improved considerably at that time, suggested that the debris of satellites whose orbital plane was similar to the one of the disc might have a significant contribution to old stars of the disc of the MW (Abadi et al. 2003). This increased the motivation for searching satellite debris right in the disc, and perhaps nearer the solar neighbourhood.

Additionally, the identification of such debris required a characterisation of the observed kinematic structures in terms of their evolutionary state and their chemical composition (the so-called chemical tagging). In particular, Navarro et al. (2004) reanalysed a sample of stars belonging to the Arcturus group (Table 2.1) and concluded that their similar apocentric radius, common angular momentum, and metal abundance pattern that was compatible with a common brief star formation history, were consistent with having arisen from a past accretion event. As the simulations had shown that the bar's typical induced perturbations were in the range of the 20-50 $\mathrm{km\,s^{-1}}$, they rejected this dynamical origin for Arcturus which has a lag of $\sim 110\,\mathrm{km\,s^{-1}}$.

Later, from the theoretical point of view, several studies have focused again on the identification of this kind of accreted streams from their orbital characteristics. For instance, (Helmi et al. 2006) found that the stars in such streams clustered in the 2D planes of the space of orbital apocentre, pericentre and L_z. Examining the catalogue by Nordström et al. (2004) in this space, they found several new distinctive stellar groups in the solar vicinity with peculiar ages, metallicities and kinematics coherent with being remnants of accreted satellites. The N-body simulations by Villalobos & Helmi (2009) demonstrated again that the stars of a debris of an accreted satellite exhibit a banana shape in the U–V plane, low angular momentum and high eccentricity, whereas the stars of the original disc were concentrated in the centre of this plane. Also using N-body simulations, Gomez & Helmi (2009) have shown that the space of orbital frequencies is suitable for the identification of satellite debris and also for the determination of the accretion time.

In the observational domain, using several observational catalogues, Arifyanto & Fuchs (2006) searched for streams in the e and L_z space, which using the epicycle theory can be approximated by $\sqrt{U^2 + 2V^2}$ and V respectively. With this method, they identified the known moving groups and a new one with possible extragalactic origin. The RAVE data releases were analysed in e.g. Seabroke et al. (2008) and Klement et al. (2008) with a little contradictory results. While the former did not find any evidence for vertical streaming in the solar neighbourhood, the latter identified a previously known stream and a new one of apparently extragalactic origin. Besides, some old and new stellar streams have been identified in the SDSS data from their kinematics ("effective" integrals of motion, angular momentum, eccentricity, and orbital polar angle) and their single peak $[Fe/H]$ distributions which are coherent with progenitors with a well defined star-forming epoch (e.g. Klement et al. 2009).

2.6 New scenarios

New chemical tagging, that is new determinations of detailed chemical abundances from high resolution spectroscopy, has been a key point in trying to disentangle the mechanism originating a certain stream. For instance, Bensby et al. (2007b) found a wide spread in the distributions of age and chemical abundances of the stars in the Hercules stream and concluded that this group was compatible with being a dynamical feature formed by stars from the inner regions of the MW which have been scattered probably by the Galactic bar. Other studies have opened the debate about the origin of some groups with apparently well-known origin. This is the case of the study by Williams et al. (2009) who observed that the stars in the Arcturus moving group have chemical abundances similar to the stars in the disc. From this evidence, they discussed a possible disc-dynamical origin of Arcturus and speculated about the bar 6:1 OLR as the triggering mechanism.

Moreover, the old idea that moving groups are disrupted clusters is still a possible explanation for some groups as other authors have shown recently. First, other minor kinematic structures in the solar neighbourhood such as HR1614 have low chemical and age scattering, and hence do seem to be remnants of a dispersed star-forming event (Feltzing & Holmberg 2000, De Silva et al. 2007). Besides, using images from the Spitzer Space Telescope at intermediate spatial frequencies, aging star complexes distorted by shear were found in other galaxies by Block et al. (2009) and interpreted as azimuthal young star streams for the first time observed in spiral galaxies other than the MW.

The Λ-CDM scenario also offered the possibility of explaining the moving groups as a perturbation in the disc due to events of galaxy satellite accretion. For instance, Quillen et al. (2009) used test particles simulations to study the structures in the velocity distribution of the solar neighbourhood due to the disc perturbation caused by a massive satellite (several times $10^9 M_\odot$) in a tight eccentric orbit. They found that this phenomenon can cause strong structures at low velocities (within 40 $\mathrm{km\,s^{-1}}$ of the LSR) and smaller streams of high velocity mainly with $V > 0$. Second, Minchev et al. (2009) also with test particles simulations and a semi-analytical approach showed that in an unrelaxed disc due to, for instance, a recent merger, the velocity distribution exhibits waves that travel in the direction of V that can be associated to observed moving groups of the low angular momentum. In particular, with their model they try to explain the origin of HR1614, Arcturus and other groups of low angular momentum which were traditionally thought to be extragalactic debris (see Section 2.5). This model predicted more moving groups in the solar neighbourhood and a strong perturbation of the disc $\sim 9\,\mathrm{Gyr}$ ago.

In addition, Minchev et al. (2010) showed with test particle simulations that the growth of the bar in the disc can create two quasi periodic orbits precessing around the families $x_1(1)$ and

$x_1(2)$ that produce streams of low velocity near the solar neighbourhood. Depending on the time formation of the bar and its parameters, their model creates several kinematic structures similar to some observed ones. In particular, to account for the strength of the Pleiades structure they estimated the bar age to be between 1.75 and 2.25 Gyr.

Today moving groups contribute in an important fraction of MW studies. On one hand, the moving groups seem to complicate the determination of the solar motion (Seabroke & Gilmore 2007) and the vertex deviation (Vorobyov & Theis 2008). But on the other hand, they have turned out to be useful in the understanding of the large-scale structure of the MW and also, as recently suggested, of its formation and evolution. To summarise, nowadays several possibilities for the origin of the moving groups are considered:

- Cluster and star complex disruption
- Orbital and resonant effects of the non-axisymmetric structure of the MW (spiral arms and bar): periodic orbits, chaos, precession of periodic orbits, transient spiral structure
- Tidal debris of past accretion events
- External dynamical effects on the disc resulting from interaction events

The origin of each structure is currently far from resolved. Different plausible explanations for the moving groups of low angular momentum and for the ones with low epicyclic energies seem to coexist. A combination of some of these ideas becomes a complex but fascinating scenario.

Part II

MULTISCALE STATISTICAL METHODS

This part is concerned with the statistical methods that are applied in this thesis to observations and simulations. One of the goals of Parts III and V is to analyse the moving groups in the kinematic space or, in general, the N-dimensional space of stellar parameters, using observational and simulated samples. Specifically we aim to characterise these structures establishing their shape, size or statistical significance. This requires the use of robust statistical techniques. Moreover, the comparison between the observed and simulated distributions demands the use of exactly the same robust techniques. The statistical methods that we use for this purpose are the following:

- Wavelet transform (WT): visualising and detecting structures according to their different sizes or scales (Section 3.1).
- Wavelet denoising (WD): obtaining a smooth distribution function from a point distribution via a smoothing/filtering treatment at different scales that deals with the Poisson fluctuations (Section 3.3).

The WD has been used in other astrophysical topics, but has never been applied to this particular subject. A detailed description of these methods can be found in Starck & Bijaoui (1994), Lega et al. (1995), Murtagh et al. (1995), Starck et al. (1998), Starck & Murtagh (2002). Although these methods can be applied to general N-dimensional spaces, the analysis and the visualisation can become very complex. For this reason, in Parts III and V these methods are applied in 2D to different combinations of any two of the variables considered: kinematic parameters, age and metallicity.

In Chapter 3 a description of the method in 2D case is provided. The particular used algorithms and filters are described. In Chapter 4 we detail how these methods work and give some examples. We also explain which are their capabilities and advantages in front other techniques. The chapter finishes by describing the WT and WD software packages used, the implementation process and the CPU costs of the method. For simplicity, sometimes the method will be mathematically formulated for the 1D case.

Chapter 3

Method description

3.1 The wavelet transform

The WT decomposes a function $f(x, y)$ on the basis obtained by translation and dilation of the so-called *mother wavelet* Ψ, which is localised in both physical and frequency space. The method consists of applying the correlation product between the function and the wavelet function:

$$w_a(x, y) = f(x, y) \otimes \Psi\left(\frac{x}{a}, \frac{y}{a}\right) \tag{3.1}$$

where a is the scale parameter and $w_a(x, y)$ the wavelet coefficient. By varying a, a set of 2D data or images corresponding to the wavelet coefficients of the data at given scales are obtained. The integral of the wavelet function is equal to zero and therefore, the WT analyses the overdensities and underdensities of the function, assigning them positive and negative coefficients respectively. A constant function would produce null coefficients. The key point is that the WT is able to discriminate structures as a function of scale, and thus it is well suited for detecting structures at one scale that are embedded within features at a different, larger scale.

The continuous form of the WT calculated in the point (b_i, b_j) is defined as:

$$w_a(b_i, b_j) = \frac{1}{\sqrt{a}} \int_{-\infty}^{\infty} \int_{-\infty}^{\infty} f(x, y) \Psi^*\big(\frac{x - b_i}{a}, \frac{y - b_j}{a}\big)\, dxdy \ . \tag{3.2}$$

For $a = 1$ y $b_i = b_j = 0$, $\Psi\big(\frac{x-b_i}{a}, \frac{y-b_j}{a}\big)$ is the mother wavelet and Ψ^* its complex conjugate.

In practise, if the function $f(x, y)$ is only known in N_p points, the wavelet coefficients are calculated using the wavelet series:

$$w_a(b_i, b_j) = \frac{1}{\sqrt{a}} \sum_{n=1}^{N_p} f_n(x, y) \Psi^*\big(\frac{x - b_i}{a}, \frac{y - b_j}{a}\big) \ . \tag{3.3}$$

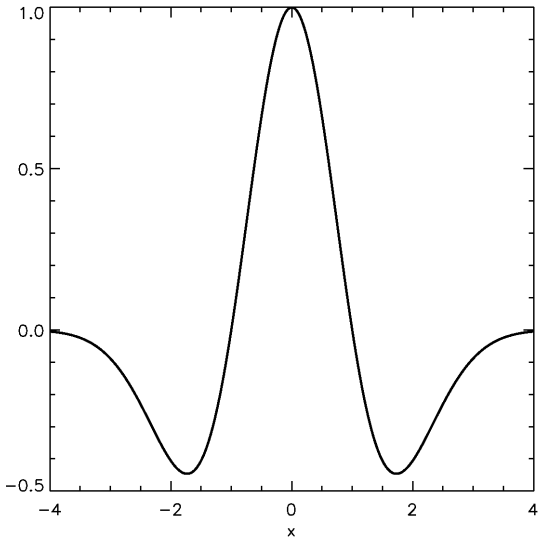

Figure 3.1: **Mexican hat function.**

When the function $f(x, y)$ consists of a distribution of N_p points $(x_n,\ y_n)$ in a plane, as in the case of this thesis, the coefficients are simply:

$$w_a(b_i, b_j) = \frac{1}{\sqrt{a}} \sum_{n=1}^{N_p} \Psi^*\big(\frac{x_n - b_i}{a}, \frac{y_n - b_j}{a}\big) \ . \tag{3.4}$$

There are many families of wavelets depending on the mother wavelet used, which in turn depends on the purpose of the analysis and the function to be analysed. Probably the most common mother wavelet is the *Mexican Hat* or *Hermitan Wavelet* (see Figure 3.1 for the 1D example) which is the second derivative or Laplacian of the Gaussian function:

$$\Psi(x, y) = (2 - x^2 - y^2)e^{\frac{x^2+y^2}{2}} \ . \tag{3.5}$$

The characteristics of the WT detailed here and the use of this mother wavelet, make this transformation suitable for one of the main aims of this study: the statistical analysis of the structures present in a given distribution. Unfortunately, the computation time of the WT described here (e.g. Equations 3.3 or 3.4) is very large, specially if large amounts of data are analysed. This is due to the fact that the wavelet coefficients must be computed for a set of points in a 2D region for every scale and every point. Actually, the complexity of the process is $\mathrm{O}(NN_pJ)$, where N is the total number of points (b_i, b_j) where the WT is carried out, N_p is the total number of points where the original function is known (or the total number of points of a distribution) and J is the desired total number of scales. To solve this, a more optimum WT implementation has been used in this thesis and it is described in Section 3.2.

3.2 The *à trous* algorithm

As seen in Section 3.1, the WT can involve high computation times. To solve this, a discrete WT can be used which evaluates the coefficients in a given scale using the results for previous scales. Specifically, it is possible to define a discrete WT which allows us to compute a discrete set of wavelet coefficients or a scale-related set of "views" of the 2-D function. An example is the *à trous* ("with holes") WT algorithm, that will be used in this study. In this case, the WT performs on a function $c_0(x, y)$ consisting of a grid of pixels with a bin size of Δ. In the case of a set of discrete points, the function $c_0(x, y)$ is first approximated for instance by smoothing the set of points on a grid with a bin size of Δ[1]. With this algorithm, the following decomposition is obtained:

$$c_0(x, y) = \sum_{j=1}^{J} w_j(x, y) + c_J(x, y) \tag{3.6}$$

where j indicates the scale of the WT, the set $(w_1, ..., w_J)$ are the wavelet coefficients and $c_J(x, y)$ is a smooth version of the original signal $c_0(x, y)$.

The algorithm (for simplicity in the 1D case) consists of the following process:

1. The value j is set to 0.

2. A set of band-pass filters h that allows structures to be recognised at each scale is constructed from the so-called *scaling function* $\phi(x)$:

$$\frac{1}{2}\phi\Big(\frac{x}{2}\Big) = \sum_l h(l)\phi(x - l) \tag{3.7}$$

   and the mother wavelet in this case is:

$$\frac{1}{2}\psi\Big(\frac{x}{2}\Big) = \phi(x) - \frac{1}{2}\phi\Big(\frac{x}{2}\Big) \ . \tag{3.8}$$

3. The data $c_j(x)$ is convolved with the discrete filter h to get $c_{j+1}(x)$, involving the data corresponding to certain close points (through l).

$$c_{j+1}(x) = \sum_l h(l)c_j(x + 2^j l) \ . \tag{3.9}$$

   The distance between one involved point and the next adjacent one is 2^j in units of the bin size Δ. This is a process of data smoothing.

[1] This can be carried out for example by simple star counts in a grid (histogram in 2D). For more details see Chapter 4.

4. The WT coefficients are obtained from the difference:

$$w_{j+1}(x) = c_j(x) - c_{j+1}(x) \ . \tag{3.10}$$

5. If the scale j is smaller than the number of total scales or resolution desired J, this value j is increased and step 2 and subsequents are repeated.

6. Finally, when $j = J$ the decomposition of the original function $c_0(x)$ is obtained (Equation 3.6).

For the 2D case, the transformation is applied separately in each dimension:

$$c_{j+1}(x, y) = \sum_l \sum_m h(l)h(m)c_j(x + 2^j l, y + 2^j m) \ . \tag{3.11}$$

The final values $c_J(x, y)$ show the details of $c_0(x, y)$ at scale of size 2^J, in units of the grid bin Δ, as they are built with a smoothing filter of $2^J \times \Delta$ size. Equivalently, the intermediate $c_j(x, y)$ are obtained with a smoothing filter of $2^j \times \Delta$ size. As $w_{j+1} = c_j - c_{j+1}$, the structures detected at each scale $j + 1$ have a size that is approximately between $2^j \times \Delta$ and $2^{j+1} \times \Delta$ or equivalently, $3 \times \Delta \times 2^{j-2}$ for w_j. For more details of the *à trous* WT algorithm see e.g. Starck & Murtagh (2002).

Usually the B_3-Spline as scaling function is used (see Figure 3.2a). In the 1D example it is:

$$\phi(x) = B_3(x) = \frac{1}{12}\big(|x-2|^3 - 4|x-1|^3 + 6|x|^3 - 4|x+1|^3 + |x+2|^3\big) \ . \tag{3.12}$$

From this scaling function and using 3.8, the mother wavelet of Figure 3.2b is obtained. It can be seen that it is very similar to the Mexican hat of Figure 3.1 in its shape and properties. As seen in Section 3.1, this type of mother wavelet are suitable for the statistical analysis of the overdensities (and underdensities) present in a given distribution. Also due to the properties of the B_3-Spline, the transformation is isotropic and thus allows the detection of features with no preferred direction[2]. For all these reasons, in this thesis the *à trous* algorithm for the WT with the B_3-Spline as scaling function is used.

According to 3.12, the left-hand side of Equation 3.7 is now expressed as:

$$\frac{1}{2}\phi\Big(\frac{x}{2}\Big) = \frac{1}{6}\phi(x+2) + \frac{1}{4}\phi(x+1) + \frac{3}{8}\phi(x) + \frac{1}{4}\phi(x-1) + \frac{1}{6}\phi(x-2), \tag{3.13}$$

[2]Note that the isotropy is not defined in non-metric spaces, such as some of the ones used here.

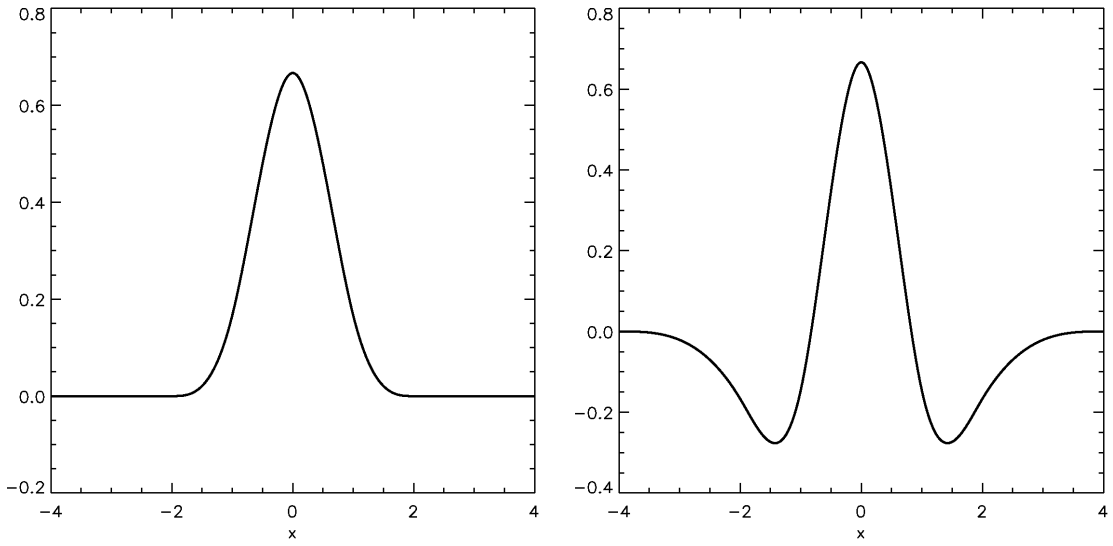

(a) (b)

Figure 3.2: (a): **Scaling function B_3-Spline.** (b): **Mother wavelet obtained from the B_3-Spline.**

Comparing the right-hand side of this equation with the right-hand side of Equation 3.7, it can be seen that the discrete filter h correspond to the coefficients multiplying the function ϕ in Equation 3.13. Applying these filter to $c_0(x)$ (Equation 3.9 with $j = 0$), we have:

$$c_1(x) = \frac{1}{16}c_0(x+2) + \frac{1}{4}c_0(x+1) + \frac{3}{8}c_0(x) + \frac{1}{4}c_0(x-1) + \frac{1}{16}c_0(x-2) \tag{3.14}$$

and in general for any scale $j + 1$:

$$c_{j+1}(x) = \frac{1}{16}c_j(x+2^j\cdot 2) + \frac{1}{4}c_j(x+2^j\cdot 1) + \frac{3}{8}c_j(x) + \frac{1}{4}c_j(x-2^j\cdot 1) + \frac{1}{16}c_j(x-2^j\cdot 2)\ . \tag{3.15}$$

In 2D this leads to a row-by-row convolution with the mask $(1/16, 1/4, 3/8, 1/4, 1/16)$, followed by column-by-column convolution with the same mask. Then, using Equation 3.10, the wavelet coefficients are:

$$w_{j+1}(x) = -\frac{1}{16}c_j(x+2\cdot 2^j) - \frac{1}{4}c_j(x+2^j) + \frac{5}{8}c_j(x) - \frac{1}{4}c_j(x-2^j) - \frac{1}{16}c_j(x-2\cdot 2^j)\ . \tag{3.16}$$

This algorithm has several advantages. First, the complexity of the computation of this WT is $O(NJ)$, where N is the total number of pixels in the grid[3] and J is the total number of scales.

[3]Note that this N is different from N_p which is the number of points where the function $f(x, y)$ is known or the number of points of the initial distribution.

This results in a very low computational cost (see Chapter 4 for exact values of the present application). Finally, this implementation enables us to restore the signal c_0 from the set of wavelet coefficients w easily and without losing any information (Equation 3.6), which is a very useful characteristic of this implementation as it will be shown in Section 3.3.

3.3 The denoising method

The data $c_0(x, y)$ present statistical fluctuations related to the fact that the sample of points is finite[4]. In the case of the function analysed here (number of stars or test particles), the noise in each initial grid point obeys Poisson statistics. These fluctuations are detected as structures (or voids), especially at the smaller scales of the WT. The aims of WD are first to ascertain the significance of the wavelet coefficients $w_j(x, y)$ at each scale and second to filter these coefficients in order to obtain a smooth distribution function through adaptative filtering.

If a model for the noise can be assumed, the probability that a wavelet coefficient $w_j(x, y)$ is significant can be estimated. Then in simple thresholding methods, a detection threshold is defined for each scale and coefficients with higher probability of being due to noise are rejected or set to 0 (e.g. *Multiresolution Hard, Soft and k-Sigma Thresholding*, see Starck et al. 1998 and Starck & Murtagh 2002). Also iterative filterings are often used. But as an alternative, a more sophisticated method is used here: the Wiener-like filtering in the wavelet space, or multiresolution Wiener filtering (Starck & Bijaoui 1994). This allows the treatment of each coefficient significance as a continuous function and therefore the denoising consists of weighting each coefficient according to its significance. This filtering method is detailed in Sect. 3.4.

The WD method allows us to obtain a smooth distribution function by reconstructing the transformed data after denoising or filtering at each scale, which is the key point of the method. Thus, the denoised signal $\widetilde{c}(x, y)$ is obtained by adding the first J denoised scales $\widetilde{w_j}$ $(j = 1, J)$ to the smooth version $c_J(x, y)$:

$$\widetilde{c}(x, y) = \sum_{j=1}^{J} \widetilde{w_j}(x, y) + c_J(x, y) \ . \tag{3.17}$$

The number of scales J which should be used in the WD depends on the image or signal size and will be deeply discussed in Section 4.2. In theory[5], this could be $J = \log_2(N)$, where N is the number of pixels of the grid in its smallest direction, but it is also suggested that, in

[4]This is apart from the error in the data from which the function c_0 is built, e.g. the errors in the velocity components of each star. This observational error is somehow treated in the choice of Δ (see Chapter 4)

[5]See for instance the documentation of the MR software used in our study (Section 4.4).

practice, it is preferable to use a lower value such as $J = \log_2(N)-1$ or $J = \log_2(N)-2$. It seems reasonable to adopt the option of increasing J until no change is observed in the reconstructed denoised signal $\widetilde{c}(x, y)$, i.e. WD up to the scale J, hereafter called $J_{plateau}$, where all signal is found to be significant (noise free).

The multiscale structures that are expected to appear could be very complex. In this sense, the WD offers several advantages. First, the method is more straightforward than other methods used in this field (see Section 4.3 for a comparison with other methods). It offers smoothing with a unique recipe and it does not require additional simulations for the treatment of Poisson fluctuations. Second, it allows an automatic local filtering as the denoising is carried out at several scales. The analysis is not restricted to one specific scale or band-width because all scales are visualised at the same time in the final distribution. Last but not least, this method is more precise than other smoothing methods such as Gaussian smoothing which degrades resolution and is shown to introduce Gaussian features into the distribution (Martínez et al. 2005) and, therefore, is not suitable for the detection of structures that may be far from Gaussian.

3.4 The multiresolution Wiener filtering

This filtering method is originally designed to be applied to Gaussian noise. However as we will see below, it can be adapted to Poisson noise. Due to the properties of the WT, a Gaussian noise in the original signal c_0 is transmitted into Gaussian noise in the wavelet planes. The multiresolution Wiener filtering (Starck & Bijaoui 1994) is used exactly when the measured wavelet coefficients w_j, at a given scale j and a given position, result from a noisy process, with a Gaussian distribution with a mathematical expectation W_j, and a standard deviation σ_j:

$$P(w_j/W_j) = \frac{1}{\sqrt{2\pi}\sigma_j} e^{-\frac{(w_j - W_j)^2}{2\sigma_j^2}} \quad . \tag{3.18}$$

If the noise in the data c_0 is not Gaussian but Poisson noise, as in the present study, the Anscombe transformation (Anscombe 1948)

$$A(c_0) = 2\sqrt{c_0 + 3/8} \tag{3.19}$$

can be applied to turn it into an approximately stationary Gaussian noise with unitary variance under the assumption that the mean value of c_0 is large (approximately > 10, Murtagh, private communication). The counts associated with the structures in our study is expected to be large enough for this condition to hold. Consequently, after the Anscombe transformation is performed, the probability density of the coefficients w_j becomes Gaussian and the multiresolution Wiener filtering can be applied.

The noise standard deviation at each scale σ_j resulting from a Gaussian noise in the original signal with standard deviation equal to 1 are calculated using simulations and the values are tabulated in Starck & Murtagh (2002) (see their Table 2). Then this method assumes that the set of expected coefficients W_j for a given scale also follows a Gaussian distribution, with a null mean, as the wavelet function has null integral, and a standard deviation S_j:

$$P(W_j) = \frac{1}{\sqrt{2\pi}S_j} e^{-\frac{W_j^2}{2S_j^2}} \ . \tag{3.20}$$

Equivalently, the measured coefficients satisfy:

$$P(w_j) = \frac{1}{\sqrt{2\pi}s_j} e^{-\frac{w_j^2}{2s_j^2}} \ . \tag{3.21}$$

where s_j^2 is the variance of w_j. In the algorithm, S_j is locally estimated as $S_j^2 = s_j^2 - \sigma_j^2$. To estimate W_j knowing w_j, Bayes' theorem gives:

$$P(W_j/w_j) = \frac{P(W_j)P(w_j/W_j)}{P(w_j)} = \frac{1}{\sqrt{2\pi}\beta_j} e^{-\frac{(W_j-\alpha_j w_j)^2}{2\beta_j^2}} \tag{3.22}$$

where $\alpha_j = \frac{S_j^2}{S_j^2+\sigma_j^2}$ and $\beta_j^2 = \frac{S_j^2\sigma_j^2}{S_j^2+\sigma_j^2}$. Thus, the probability $P(W_j/w_j)$ follows a Gaussian distribution with a mean $\alpha_j w_j$ and a variance β_j^2. The mathematical expectation of W_j is $\alpha_j w_j$ and consequently the denoised coefficients are computed through a linear filter with a simple multiplication of the coefficients

$$\widetilde{w_j} = \alpha_j w_j \ . \tag{3.23}$$

The complexity of the WD using this filtering method is $\mathrm{O}(NJ)$, where N is the total number of pixels of the grid and J is the number of scales.

This and other algorithms for filtering in the wavelet space were compared in Starck & Bijaoui (1994). Using an image with artificially added noise, they conclude that Wiener-type filtering provided the best results, generally leading to better SNR than the simple hard thresholding. The evaluation of the quality of the restoration was carried out in terms of the correlation coefficient and the mean-square error not only between the original image and the noised image but also between each plane (scale) of the WT. Although it is out of the scope of the present study to investigate exhaustively the different filtering methods, we compared the results obtained using a thresholding and other methods of filtering in the wavelet space with the multiresolution Wiener filtering. We concluded that the latter produces smoother distributions, without additional artifacts.

Chapter 4

Application to the kinematics-age-metallicity space

The aim of this chapter is to recapitulate the essential points of the methods of Chapter 3 and to show the process of their application step by step by an example. This example of application is basically focused on the case of the U–V plane and for this we use the observational sample extensively described in Chapter 5.

4.1 Application of the Wavelet Transform

First of all, the starting point is the set of (U_i,V_i) for each star of the sample (Figure 4.1 with 24190 stars). This first representation of the velocities as a 2D plot looks really confusing, although some structures could be recognised in this plane. In order to study robustly this structures the methods of Chapter 3 must be used. To this end, the function $c_0(x, y)$ ($c_0(U, V)$ in this example) is needed. In the present study, the first smoothing of the data is obtained from simple star counts in a grid (histogram in 2D). The choice of Δ is carried out here depending on the observational errors or the resolution of the data. A value too small would not be coherent with the errors but a too large one would cause too much loss of resolution. The final results do not depend significantly on this choice provided that it is between the mentioned limits. The values $0.5\,\mathrm{km\,s^{-1}}$, 0.01 Gyr and 0.01 dex for velocity, age and metallicity, respectively have been chosen (see Section 5.2).

The initial data for the WT, c_0, is shown in Figure 4.2. This representation of the velocities, despite being better than the one in Figure 4.1 (for example at high densities), is still not defining clear groups neither structures undistinguishable from the noise. Also the effects of the

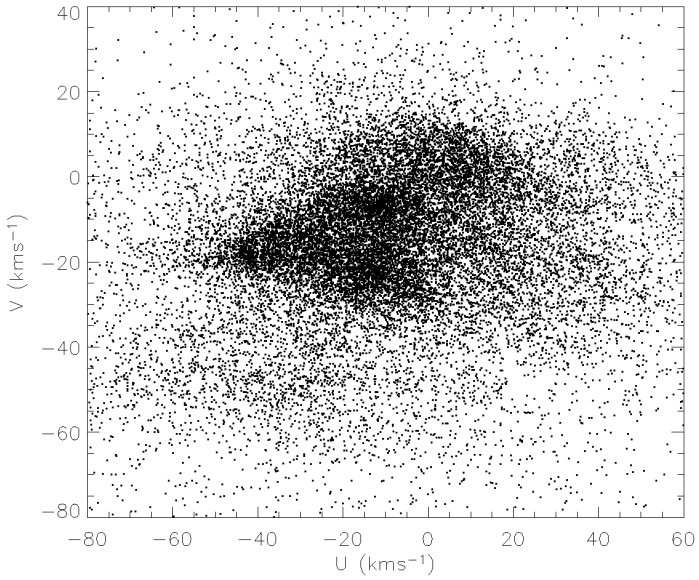

Figure 4.1: **Points in the U–V plane.** Points in the U–V plane for the stars of the observational sample.

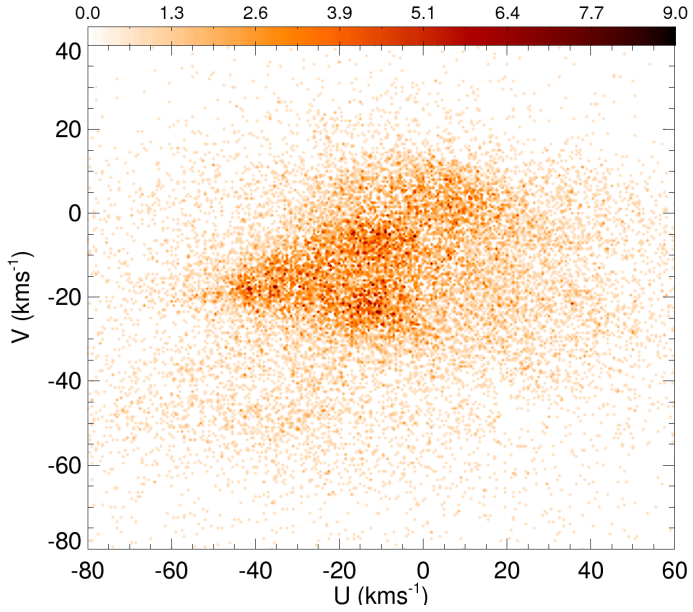

Figure 4.2: **First approximation to the density in the U–V plane.** Initial density signal $c_0(U, V)$ in the U–V plane for the observational sample.

Table 4.1: **Bin & structure sizes.** Value of Δ and size of the structures detected at each smooth plane (c_j) and at each scale of the WT (w_j) for velocities, age and metallicity.

U,V ($\mathrm{km\,s^{-1}}$)				age (Gyr)				$[Fe/H]$ (dex)			
$\Delta = 0.5$				$\Delta = 0.01$				$\Delta = 0.01$			
c_0	0.5			c_0	0.01			c_0	0.01		
c_1	1	w_1	0.75	c_1	0.02	w_1	0.015	c_1	0.02	w_1	0.015
c_2	2	w_2	1.5	c_2	0.04	w_2	0.030	c_2	0.04	w_2	0.030
c_3	4	w_3	3	c_3	0.08	w_3	0.060	c_3	0.08	w_3	0.060
c_4	8	w_4	6	c_4	0.16	w_4	0.120	c_4	0.16	w_4	0.120
c_5	16	w_5	12	c_5	0.32	w_5	0.240	c_5	0.32	w_5	0.240
c_6	32	w_6	24	c_6	0.64	w_6	0.480	c_6	0.64	w_6	0.480
c_7	64	w_7	48	c_7	1.28	w_7	0.960	c_7	1.28	w_7	0.960

discretization in bins is noticed. A continuous and denoised distribution function that would allow the accurate analysis of the structures is required.

The next step before the WD is the application of the WT where the data c_0 is decomposed into the different scales. For 5 scales w_1, w_2, w_3, w_4 and w_5, following Equation 3.10 the decomposition of Figure 4.3 is obtained and the final smooth version c_5 is also shown. Figure 4.4 shows the smooth planes c_i involved in the obtention of each wavelet plane (Equation 3.9): each wavelet plane w_i of Figure 4.3 is obtained from the smooth planes $c_i - c_{i+1}$. Also according to Equation 3.6, the addition of the six planes of this Figure makes Figure 4.2.

As explained in Section 3.2, the sizes of the structures present in each of the planes of the transform can be calculated for a given Δ as $2^j \times \Delta$ for the smooth planes c_j and as $3 \times \Delta \times 2^{j-2}$ for w_j. Table 4.1 shows the size of the structures detected on each smooth plane and on each plane of the WT for the velocities and for the rest of the variables (age and metallicity).

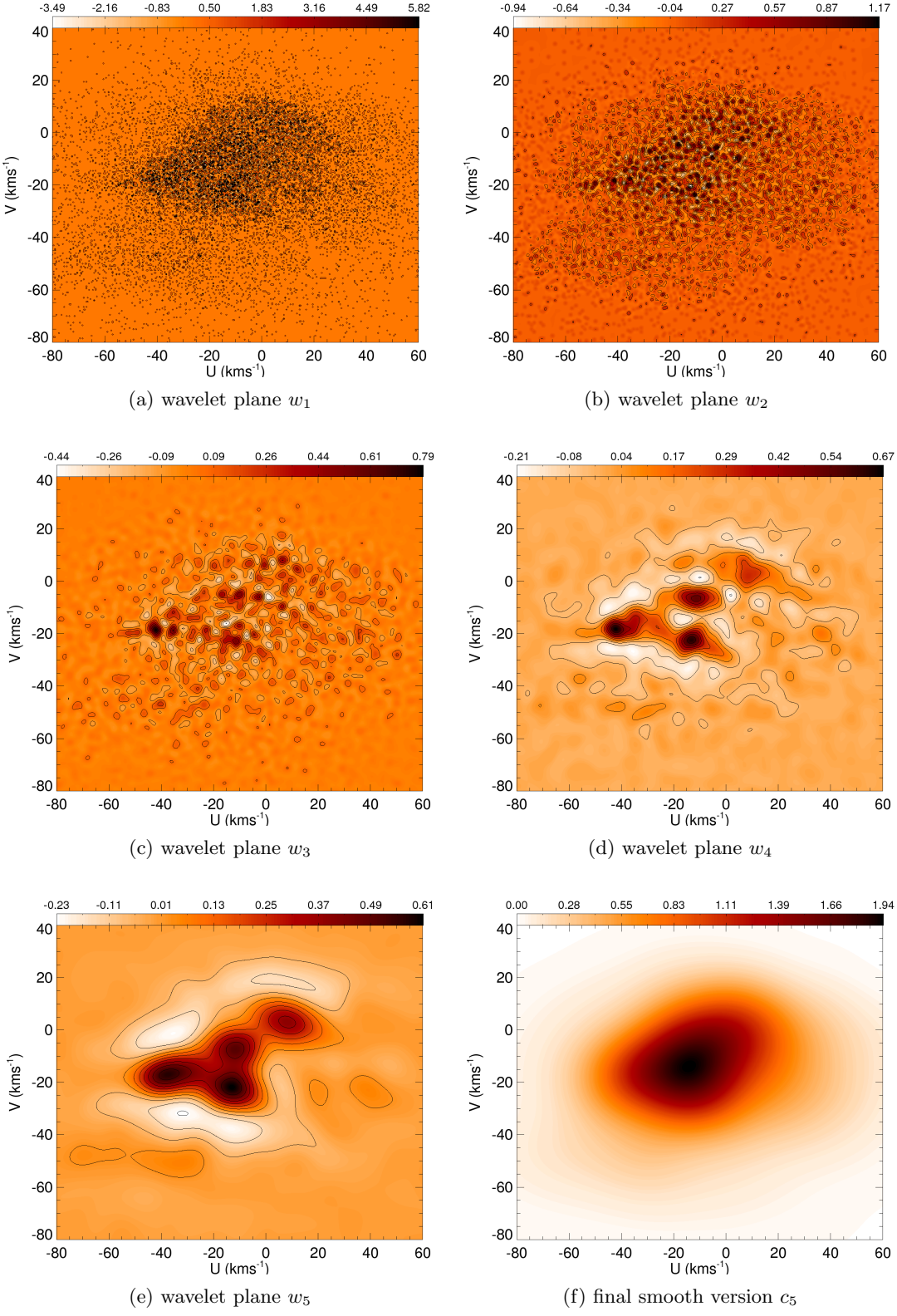

(a) wavelet plane w_1

(b) wavelet plane w_2

(c) wavelet plane w_3

(d) wavelet plane w_4

(e) wavelet plane w_5

(f) final smooth version c_5

Figure 4.3: **Wavelet planes.** WT in the U–V plane: wavelet planes w_i together with the final smooth version c_5.

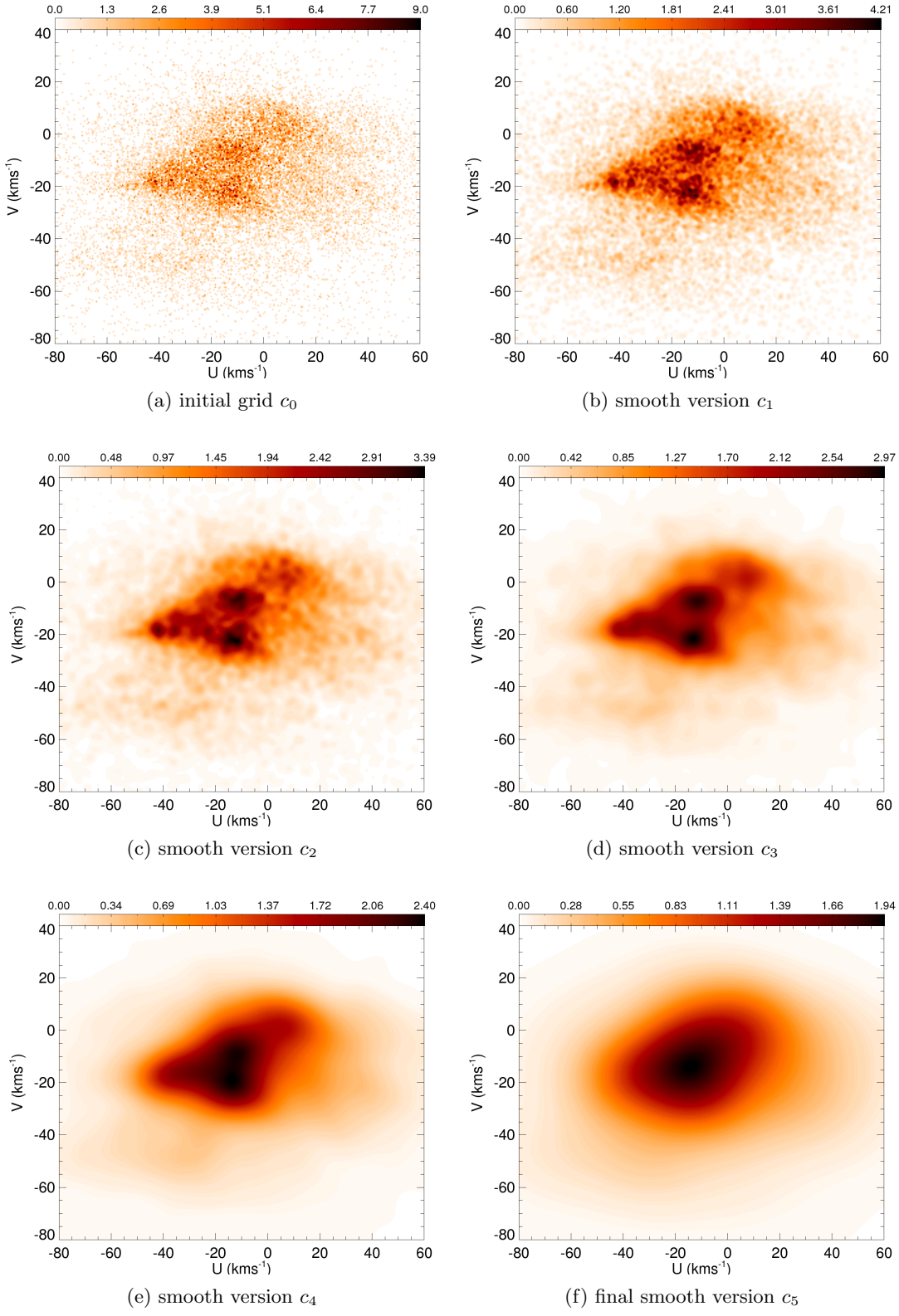

(a) initial grid c_0

(b) smooth version c_1

(c) smooth version c_2

(d) smooth version c_3

(e) smooth version c_4

(f) final smooth version c_5

Figure 4.4: **Subsequent smoothed wavelet planes.** Initial grid c_0 (as in Figure 4.2) and subsequent smooth planes c_i.

4.2 Application of the Wavelet Denoising

The fundamental part of the whole statistical method of this thesis is to ascertain the significance of the wavelet coefficients so as to built a denoised distribution function from the respective denoised planes of the WT. The Poisson noise is concentrated basically in the first scales but the WD must be carried out in a stipulated number of scale as it has been seen in Section 3.3. Figure 4.5 show the denoised scales, where the wavelet coefficients have been weighted according to their significance through the multiresolution Wiener filtering. Comparing this Figure to 4.3 it can be seen that many of the structures, specially the ones at smaller scales, have disappeared as a consequence of the WD.

The final and essential step of the WD is the reconstruction of the denoised data adding the denoised planes at different scales $\widetilde{w_i}$ to the final smooth version. The result can be seen in Figure 4.6 which will be extensively analysed in Chapter 6 as well as the equivalents in other planes with age and metallicity.

As Figure 4.5 shows, the Poisson noise is concentrated basically in the first scales but the WD must be carried out in a stipulated number of scales (Section 3.3). However, in most of the analyses of this study, it is also reasonable to use $J_{plateau}$ which is the minimum number of J for which no change is observed in the reconstructed denoised signal. For instance, Figure 4.7 shows the case with $J = 1$, $J = 2$, $J = 3$ and $J = 4$. Whereas there are evident differences between Figure 4.7a, 4.7b, 4.7c, and 4.7d, there are no clear changes between Figure 4.7d with $J = 4$ and 4.6 with $J = 5$. This means that a $J = 4$ is enough for the example of this chapter and therefore $J_{plateau} = 4$. Actually, in most cases $J_{plateau}$ is equal to or even lower than $\log_2(N) - 1$ or $\log_2(N) - 2$ (the recommended by the authors of the implementation, see Section 3.3). Nevertheless, for some specific cases, especially when dealing with a signal with fewer counts per pixel, we find that $J_{plateau}$ is higher than the practical values proposed. Most probably, in these cases, WD up to $J_{plateau}$ could imply very few data values in the final scales and consequently, too much loss of signal. These cases will be clearly flagged, as the conclusions derived from them would demand the use of larger samples for definitive confirmation. In these situations the J up to which the WD has been carried out will be specified, whereas in all other cases WD has been done up to $J_{plateau}$.

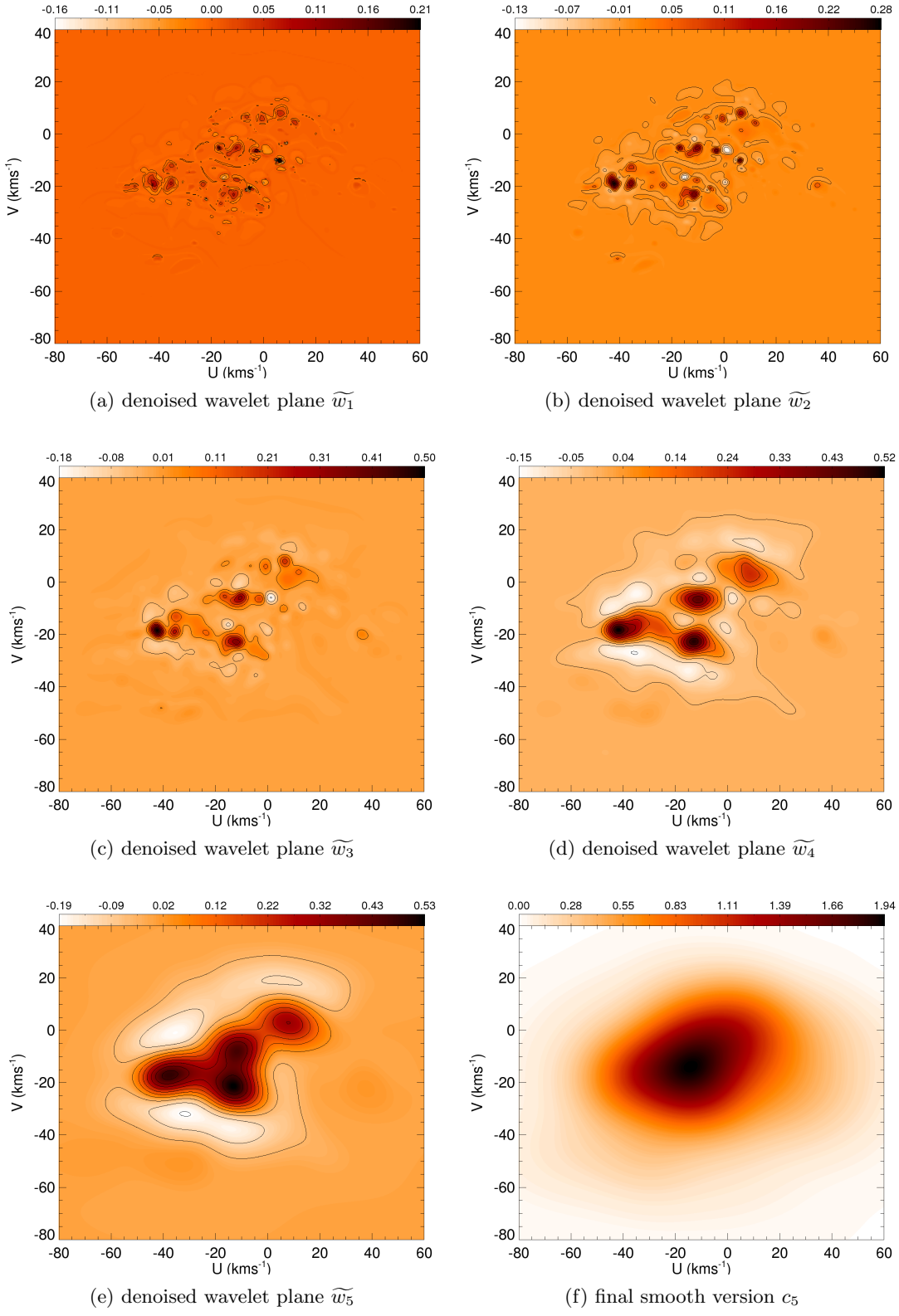

(a) denoised wavelet plane $\widetilde{w_1}$

(b) denoised wavelet plane $\widetilde{w_2}$

(c) denoised wavelet plane $\widetilde{w_3}$

(d) denoised wavelet plane $\widetilde{w_4}$

(e) denoised wavelet plane $\widetilde{w_5}$

(f) final smooth version c_5

Figure 4.5: **Denoised wavelet planes.** WD of the wavelet planes $\widetilde{w_i}$ together with the final smooth version c_5 which does not change.

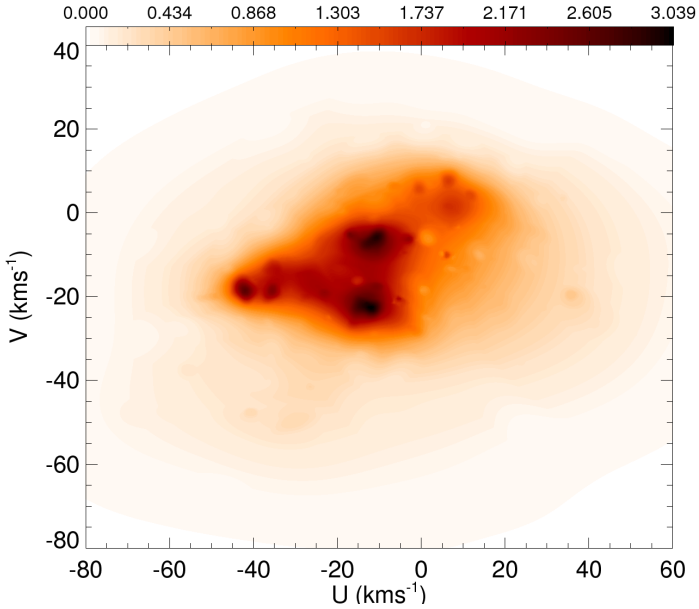

Figure 4.6: **Final denoised plane.** Final result of the WD process $\widetilde{c}$ with $J = 5$.

4.3 Comparison with other statistical methods

Several general advantages of the WD method are described in Section 3.3 but a direct comparison between this and other methods used in this field is particularly interesting. Many statistical techniques have been used up to now to study the velocity distribution in the solar neighbourhood and in particular the structures present in this distribution. This section is focused on the comparison between the WD and the main methods used nowadays: maximum likelihood methods, parametric and non-parametric methods.

Methods such as the *convergent point* still used in relatively recent studies (Chereul et al. 1998) are not considered in detail in this section as they are just specific methods to recover the three velocity components U, V and W for samples with only proper motions, which is not the case of the present thesis. Also the *Maximum Penalized Likelihood estimate* by Dehnen (1998) was used to reconstruct the 3D velocity field from the positions and tangential motions of stars in the Hipparcos catalogue. Poisson noise dominated in such a way that only 2D projections of the whole 3D velocity space could be used. Also the *Spaghetti Method* presented in Aguilar & Hoogerwerf (2001) and references therein has the aim to search for moving groups using only astrometric data.

The method designed by Luri et al. (1996) was used in Famaey et al. (2005) to recover the 3D velocity field from angular positions, proper motions and radial velocities but with low accuracy

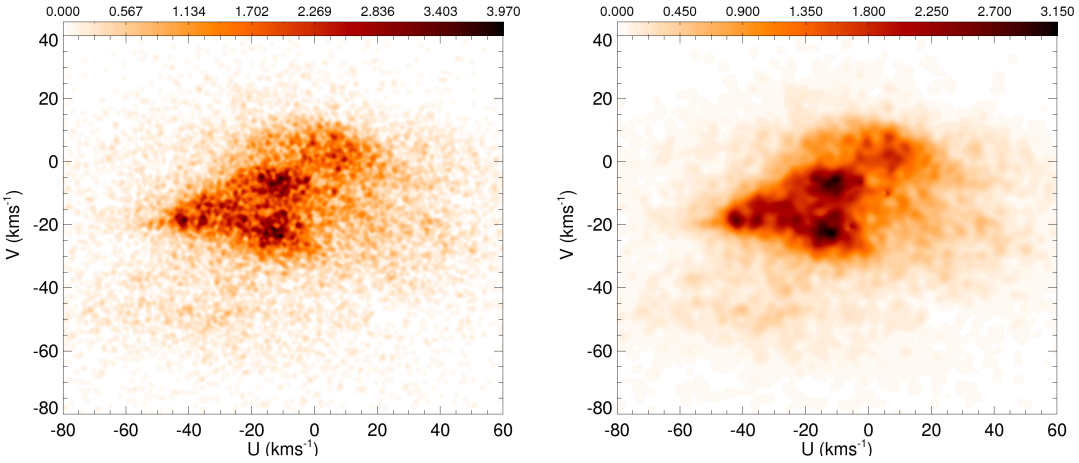

(a) denoised data $\widetilde{c}$ with $J = 1$

(b) denoised data $\widetilde{c}$ with $J = 2$

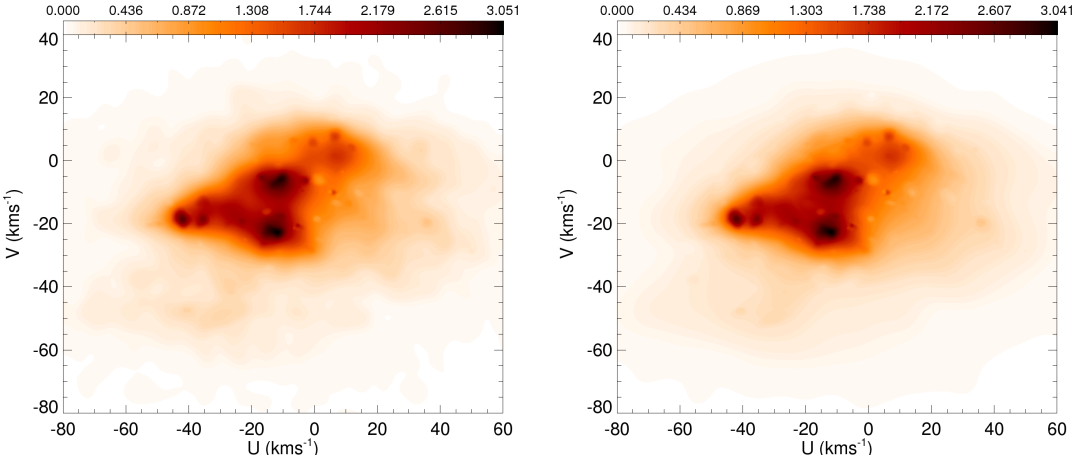

(c) denoised data $\widetilde{c}$ with $J = 3$

(d) denoised data $\widetilde{c}$ with $J = 4$

Figure 4.7: **Final result of the WD process with several J.**

data on parallaxes in some cases. It consists of a maximum likelihood technique, based on Bayesian inference, that constructs a velocity distribution function composed by several groups. Although this procedures takes into account the individual uncertainties of the data, too many assumptions on the characteristics of these groups are assumed such as a Schwarzschild ellipsoid with respect to LSR for the velocities or a Gaussian distribution for the absolute magnitude for each group. The recovered U, V and W are used in the present study (Chapter 5) without taking into account the member assignation. In this sense, this is a very parametric method. Also a new technique has been developed in Bovy et al. (2009) to reconstruct the velocity distribution with the lack of radial velocities through a maximum likelihood estimation. In this method the function is modelled with a mixture of a certain number (left as a free parameter) of Gaussian distributions and taking care of the individual uncertainties. This last advantage contrast with the extreme complexity of the method to find that the number of final groups is not so large (10) and again assumed to have a Gaussian shape. Also the same authors recognised that the amount of information provided by radial velocities is significant and should be used in such studies. In the WD the individual errors on the data are not treated so sophisticatedly but only in the election of the bin size. However, a robust treatment of the Poisson fluctuations is carried out and no assumptions at all on the velocity distribution and the moving groups are assumed.

Among the methods used when the 3D velocities are available or have been obtained through the previous methods, non-parametric methods have the advantage that they do not assume any predefined hypothesis about the velocity distribution or the moving groups themselves. The kernel estimator of the density (Chen et al. 1997) or the wavelet analysis restricted to specific scales are examples of these kind of methods. In both cases, the data in convolved with a function with certain amplitude to obtain a smooth distribution function. The main weakness of these methods is that the amplitude of the functions or the smoothing parameter limit the size of the detected structures. Refinements of these methods which consist of choosing a more proper scale for the wavelet in terms of the observational errors (Figueras et al. 1997) or calculating the optimum value for the amplitude such as in Asiain et al. (1999a) do not improve the previous problem. Neither does the application of the WT at many but fixed scales (Chereul et al. 1998, Skuljan et al. 1999). In this sense, the WD offers an analysis which is not restricted to one specific scale or band-width because all scales are visualised at the same time in the final distribution. On the other hand, the Gaussian smoothing degrades resolution and is shown to introduce Gaussian features into the distribution (Martínez et al. 2005) so the WD is more precise than these other smoothing methods and is more suitable for the detection of structures that may be far from Gaussian.

Non-parametric methods such as the adaptive kernels where the smoothing scale varies locally according to the density are used in other studies Skuljan et al. (1999), Bobylev &

Bajkova (2007). But additional treatment for the noise is required in these methods. The noise treatment is often combined with multiscale techniques, which means that the noise is dealt in the wavelet space. For example Skuljan et al. (1999) used this adaptive kernel to estimate first the probability density function in the U–V plane and afterwards the WT was applied to characterise the structures in several fixed scales and their significance. In order to do this, simulations to create Poisson random copies of the original distribution were carried out and the significance of the wavelet coefficients was assigned according to the number of random realisations where they were positive. Only the coefficients that had 90% of probability of being real were considered. A very similar procedure is used by Zhao et al. (2009). Also local thresholds for the wavelet space were calculated with the support of a set of Poisson noise simulations in (Chereul et al. 1998, 1999). The WD method used in this thesis is more straightforward than these other methods used in this field. It offers smoothing with a unique recipe and it does not require additional simulations for the treatment of Poisson fluctuations. Furthermore, it allows an automatic local filtering as the denoising is carried out at several scales.

4.4 Implementation

To perform the calculations of the WT and WD the MR software[1] developed by CEA (Saclay, France) and the Nice Observatory has been used. It was originally built for astronomical use but they have been employed in other subjects. It consists of a set of C++ executable programs for Linux platform, among others, that implements multiresolution (multiscale) methods for processing and data analysis of 1D signals, 2D images, and 3D data volumes[2]. The package includes also a series of IDL routines to interface the executables to the processing packages, making the use of the executables easier.

Particularly, the MR/1 package (*Multiresolution Analysis Software Environment*) has been used with the following programs:

mr_transform: This program computes several multiresolution transforms of an image. In this case the bspline wavelet transform with the à trous algorithm has been applied specifying the desired number of scales. It returns a cube corresponding to the decomposition of the original image into the wavelet planes and the smooth plane.

mr_filter: This filters an image using several methods for noise modelling. In this case, the multiresolution Wiener filtering is used assuming Poisson noise. The multiresolution transform

[1] http://thames.cs.rhul.ac.uk/∼multires/

[2] As discussed in Page 27, the 3D implementation is not applied in this thesis.

and the number of scales must be chose. Again the bspline wavelet transform is used here with the selected number of scales. It returns the final filtered image.

Additionally we have implemented the computation of the initial grid $c_0(x, y)$, which is previous to the application of the WT and the WD. Also to obtain and visualise the final images of the WT and WD, we have developed specifically for this study several IDL programs based on the routines *contour* and *ColorBar*.

Finally, the CPU time is rather low for the whole process. The complexity of the computation of the initial grid $c_0(x, y)$ is proportional to the number of points (stars) in the sample, which gives a computing time of 4 s for the grid construction process for the example of this chapter (the whole observational sample with 24190 stars). As seen in Sections 3.1 and 3.3, the WT and WD have complexities of $\mathrm{O}(NJ)$ (where N is the total number of pixels in the grid and J is the number of scales[3]). This gives computing times are 1 s and 4 s respectively in a typical grid of 400×400 pixels and $J = 5$ with an Intel(R) Xeon(TM) processor at 3.0GHz, which as explained in Section 3.2, are very affordable computation times.

[3]Note that in the MR software a different notation is used: the parameter n there is here $n = J + 1$.

Part III

MOVING GROUPS IN THE KINEMATICS–AGE–METALLICITY SPACE

Nowadays, two important observational contributions provide new material to complement the Hipparcos and Tycho astrometric data: i) the CORAVEL radial velocity data for a significant number of late-type stars belonging to the Hipparcos catalogue (Nordström et al. 2004 for dwarf stars and Famaey et al. 2005 for giant stars) and ii) the uvby–β survey of FGK dwarf stars, which have allowed the derivation of ages and metallicities (Nordström et al. 2004). Lastly, data on OBA-type stars (Asiain et al. 1999a, Torra et al. 2000) and M dwarfs (Reid et al. 2002, Bochanski et al. 2005) complete an extensive sample of more than 24000 stars ready to be used for the characterisation of moving groups. It is necessary to complement these new data with more powerful statistical tools (Part II) to interpret the data in the space of U–V–age–$[Fe/H]$.

This Part III is the observational part of this thesis and deals with the characterisation of the observed moving groups. In particular, we characterise the observed kinematic structures in the U–V–age***-***$[Fe/H]$ ***space by applying new statistical techniques with the aim of establishing observational constraints that will help to reveal their origin. Chapter 5 of this thesis presents the observational data that we use together with their precisions and possible biases. Chapter 6 characterises in detail the structures in the velocity plane. Then, Chapters 7 and 8 analyse the age and metallicity distributions of these structures, respectively. Finally, the main outcomes of this part are summarised in Chapter 9.***

Chapter 5

Observational sample

5.1 Compilation of data

The observational data is compiled from several recent catalogues and is restricted to samples with precise radial velocities and astrometric data, as these are necessary to compute the U, V and W heliocentric velocity components. Also, in order to study the evolutionary state of the kinematic structures, stellar ages and metallicities are required. For this reason, we aim to cover a wide range of ages as well as spectral types and luminosity classes. Therefore, catalogues where ages are estimated using photometric calibrations as well as catalogues containing parameters closely related to age (H_α equivalent width[1]) are considered. Table 5.1 shows the data available in each catalogue. Altogether our sample contains 24190 stars and the age of over 16000 stars can be used. Table 5.2 shows a summary of the source of each parameter (positions and proper motions, distances, radial velocities, ages and metallicities). The following list shows a detailed description of the sample.

- *OBA-type Stars*: Sample of 4283 main sequence or relatively evolved stars compiled by Asiain et al. (1999a) (2025 A-type stars) and Torra et al. (2000) (2258 O- and B-type stars) with astrometric data from Hipparcos and stellar physical parameters and ages computed from Strömgren photometry. Most of the radial velocities came from the radial velocity survey of Hipparcos early-type stars (Fehrenbach et al. 1987, Grenier et al. 1999) planned to complement the kinematically unbiased CORAVEL database for late-type stars. For the OB stars, when both trigonometric and photometric distances were available, the one with smaller relative error was used. Relative error on photometric distance ranges from

[1] Equivalent width of the H_α emission line can be used in this case as an indicator of the chromospheric activity and, consequently, as age information.

14% to 25%, depending on spectral type and luminosity class. In the compilation of A stars, the Hipparcos distance was adopted when the relative error in the parallax was $\sigma_\pi/\pi < 20\%$ and the photometric distance otherwise.

- *FGK-type Dwarfs*: Sample of 13257 dwarf stars[2] selected from the 16682 stars in the catalogue of the Geneva-Copenhagen survey (Nordström et al. 2004) with kinematic data, ages and metallicities. Proper motions come from Tycho-2 and most of their radial velocities were obtained from CORAVEL. As detailed in Nordström et al. (2004), the Hipparcos parallax was used when $\sigma_\pi/\pi < 13\%$ and otherwise the photometric distance was employed. Ages and $[Fe/H]$ were calculated from uvby-β photometry. The Bayesian estimation method in Jørgensen & Lindegren (2005) was used for age computation[3].

- *M-type Dwarfs*: A set of 863 dwarf stars selected from the spectroscopic surveys in Bochanski et al. (2005) (428 stars) and Reid et al. (2002) (435 stars). The former catalogue gives spectroscopic distances obtained from the TiO_5 band, radial velocities from cross-correlation in the 6000-7400 $\mathring{A}$ range and USNO-B proper motions (Monet 2003). Reid et al. (2002) use mainly proper motions and trigonometric distances from the Hipparcos catalogue and radial velocity data from Gizis et al (2002) and Delfosse et al. (1999). Both surveys give the equivalent width of the H_α line, which is indicative of the magnetic activity in the chromosphere and is directly related to stellar age. Following the criteria in Bochanski et al. (2005), this sample can be split into two subsamples: active stars (182 young stars) and non-active stars (681 older stars) depending on whether the width of the H_α line is $> 1\mathring{A}$ or $\leq 1\mathring{A}$, respectively.

- *KM-type Giants*: A group of 5787 giant stars from the catalogue by Famaey et al. (2005). They belong to the Hipparcos catalogue and have radial velocities given in the CORAVEL database and proper motions taken from Tycho-2. Their distances were computed using the maximum likelihood method developed by Luri et al. (1996) as explained in Section 4.3, which is based on a Bayesian and parametric approach. The assumptions of this method to derive the velocity components should be taken into account in subsequent chapters.

5.2 Analysis of the sample, errors and biases

First of all, Figure 5.1 shows the distance distribution of the stars from the different catalogues that make up our sample. As expected, the volume of sampled space is highly dependent on

[2]This is the number of stars with available U, V and W.

[3]In the original catalogue, ages are rounded up to the nearest 0.1 Gyr but in this study, ages (and upper and lower 1σ confidence limits) rounded up to 0.01 Gyr are used (Jørgensen, private communication).

Table 5.1: **Composition of the sample.** Number of stars with kinematic data, age and metallicity from each catalogue and for the total sample.

	OBA (1, 2)	FGK (3)	M (4, 5)	KM giants (6)	total
$U\ V\ W$	4283	13257	863	5787	**24190**
$U\ V\ W\ age$	3977	11215	863[2]	0	**16055**
$U\ V\ W\ [Fe/H]$	0	13109	0	0	**13109**
$U\ V\ W\ age\ [Fe/H]$	0	11215	0	0	**11215**

References. (1) Asiain et al. (1999a); (2) Torra et al. (2000); (3)Nordström et al. (2004); (4) Reid et al. (2002); (5) Bochanski et al. (2005); (6) Famaey et al. (2005).

Table 5.2: **Sources of the sample data.** Source of the astrometric, photometric and spectroscopic measures for each catalogue. References from Table 5.1

	OBA	FGK	M (4/5)	KM giants
astrometry	Hipparcos	Hipparcos (Tyc-2)	Hipparcos/ USNO-B	Hipparcos (Tyc-2)
rad vel	Hipparcos survey	Coravel	PMSU survey	Coravel
distances	Hipparcos + uvby-β	Hipparcos + uvby-β	Hipparcos/ spectr (TiO_5)	Max. Likelihood
ages	uvby-β	uvby-β	Hα	...
$[Fe/H]$	...	uvby-β	...	...

the spectral type, which will be taken into account in our subsequent analysis. For the M-type stars, the peak at short distances corresponds to the stars by Reid et al. (2002), whereas the extended distribution is that of stars by Bochanski et al. (2005). Distance error distributions and possible biases in the adopted distance are discussed in the publications associated with each catalogue. As mentioned by Skuljan et al. (1999), large distance errors could lead to features in the kinematic U–V plane being artificially radially elongated (relative to the point $(U, V) = (0, 0)$). We have checked that in our sample, distance errors are smaller than 25%, except for 4% of stars, all of them KM giants, which in any case exceed 40%.

On the other hand, no systematic bias in the photometric distances is expected (see e.g. Nordström et al. 2004). For trigonometric distances ($1/\pi$), Brown et al. (1997) showed that a symmetric error law for parallaxes such as a Gaussian results in a non-symmetric or systematic error in distances, which leads to a biased overestimated distance distribution. This relative bias is shown to be $\approx (\sigma_\pi/\pi)^2$ (Arenou & Luri 1999). This expression gives a maximum bias of 2% for stars with trigonometric distances of the FGK subsample –all of them with $\sigma_\pi/\pi \leq 0.13$–, which accounts for about ∼75% of all the trigonometric parallaxes in our sample. Moreover, the bias for the whole sample is estimated to be always less than 6%. The maximum likelihood method used to derive distances for the KM giants corrects this and other systematic trends (see Figure 8 in Famaey et al. 2005). However, as discussed in Section 6.3, other kinds of biases caused by the a priori parametrisation of the kinematic distribution function cannot be ruled out.

With these distances, radial velocities and astrometric data, the heliocentric velocities and their errors have been recalculated following Meillon et al. (1997), with the exception of the M dwarfs for which the necessary data were not available. For the OBA-type stars and KM-type giant stars, most of which have distances $> 100\,\mathrm{pc}$, the velocities have been corrected for Galactic differential rotation with values for Oort's constants of: $A = 14.82\,\mathrm{km\,s^{-1}kpc^{-1}}$ and $B = -12.37\,\mathrm{km\,s^{-1}kpc^{-1}}$ (Feast & Whitelock 1997). The error distribution for each subsample is shown in Figure 5.2 and the mean errors in the velocity components and more information on the accuracy of the parameters are shown in Table 5.3. The larger errors in the OBA-type stars (mainly due to the OB stars) and KM-giants is due to their larger distances. In the case of the M-type stars no errors in the velocity could have been recalculated. But for these stars, their errors are mainly due to errors in radial velocity and this are $1\,\mathrm{km\,s^{-1}}$ for echelle data and $10\,\mathrm{km\,s^{-1}}$ for low-resolution data.

At this point it is of utmost importance to ascertain the possible kinematic biases of our sample due to selection effects. As stated by Binney et al. (1997), high proper motion stars were preferred in pre-Hipparcos radial velocity programmes, which leaded to kinematically severely biased samples. During the last two decades, specific observational programmes for radial ve-

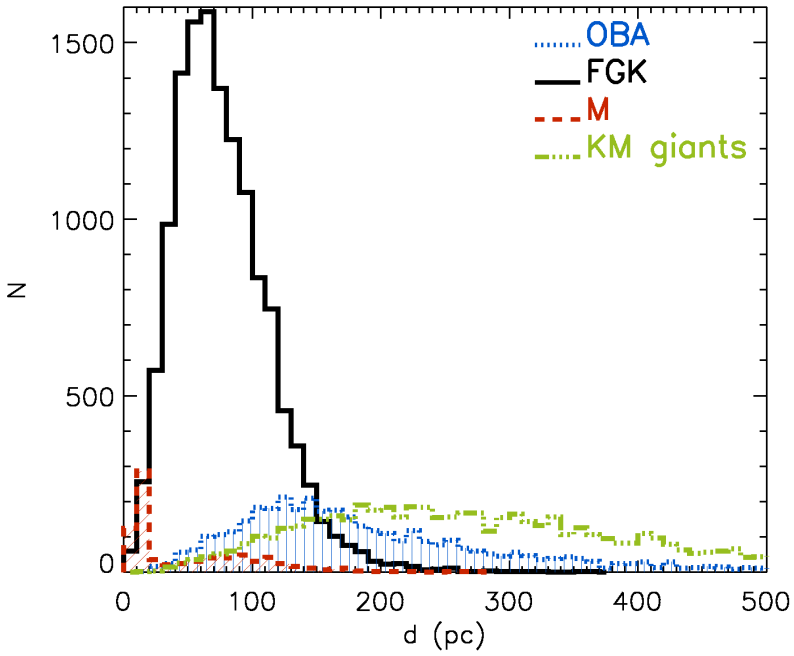

Figure 5.1: **Distances of the sample.** Distance distributions of stars from the catalogues that make up the sample.

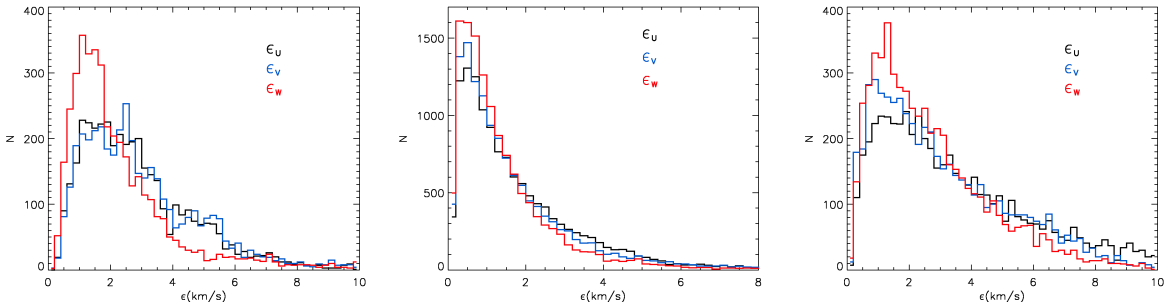

(a) OBA (b) FGK (c) KM giants

Figure 5.2: **Kinematic errors of the sample.** Histogram of heliocentric velocity errors for the different subsamples.

Table 5.3: **Sample accuracy.** Error information for the kinematic data, age and metallicity for each catalogue.

	OBA	FGK	M	KM giants
$\epsilon_{U,V,W} \leq 2\,\mathrm{km\,s^{-1}}$	21%	54%	...	17%
$\bar{\epsilon}_U$, $\bar{\epsilon}_V$, $\bar{\epsilon}_W$ $(\mathrm{km\,s^{-1}})$	4.5, 4.4, 3.9	2.0, 1.9, 1.6	...	4.0, 3.5, 2.8
$\epsilon_{age} \leq 30\%$	32%	50%	...	...

locities were undertaken in parallel with the Hipparcos mission (CORAVEL and Fehrenbach et al. 1987) to complete kinematic data for stars of the Hipparcos survey. Most of the stars in the subsamples of FGK dwarfs and KM giants belong to this survey. Consequently, this bias is expected to be suppressed for 79% of the stars of our whole sample. For the OB stars, Torra et al. (2000) discussed in detail a small kinematic bias in their subsample (see Figure 3 therein). Numerical simulations allowed these authors to demonstrate that it had negligible effects on their kinematic analysis. Regarding the A-type stars, some of the photometric programmes on which the Asiain et al. (1999a) compilation is based favoured stars with known pre-Hipparcos radial velocity data. Although a slight bias is expected for this subsample, it only represents about 8% of the whole sample. Finally, as was evaluated by Reid et al. (2002), their M dwarfs catalogue –a volume limited sample– shows no evidence of any systematic bias (see Figure 4 therein). On the other hand, the early M-type stars from Bochanski et al. (2005) were photometrically selected by colour and magnitude and thus no kinematic bias from the selection process is expected. Thus, all these considerations allow us to assume confidently that no sample selection bias affects our kinematic study in the next chapters.

Regarding the evolutionary state of the stars in the sample, Figure 5.3 shows the age distribution for the OBA- and FGK-type dwarf stars. The precision of this parameter (Table 5.3) deserves special attention. The vast majority of the OBA-type stars are main sequence or moderately evolved stars and, therefore, a reliable estimate for their ages is available from uvby-β photometry (see the error distribution in Figure 1b of Asiain et al. 1999a and Figure 7 of Torra et al. 2000). As stated by Torra et al. (2000), an overestimation in age as large as 30-50% is expected for highly rotating stars, that are a substantial fraction of the OB main-sequence stars. This, however, implies an absolute bias of always less than 50 Myr whose effect in our age-kinematic analysis undertaken in Chapter 7 is almost negligible.

Figure 15 in Nordström et al. (2004) shows the distribution of upper and lower 1σ relative errors in age for the FGK subsample. Large relative errors in age lead to the evolutionary state of late-type stars being largely undetermined, which require to evaluate carefully any result derived from the use of this parameter. Furthermore, certain biases in the age estimation would

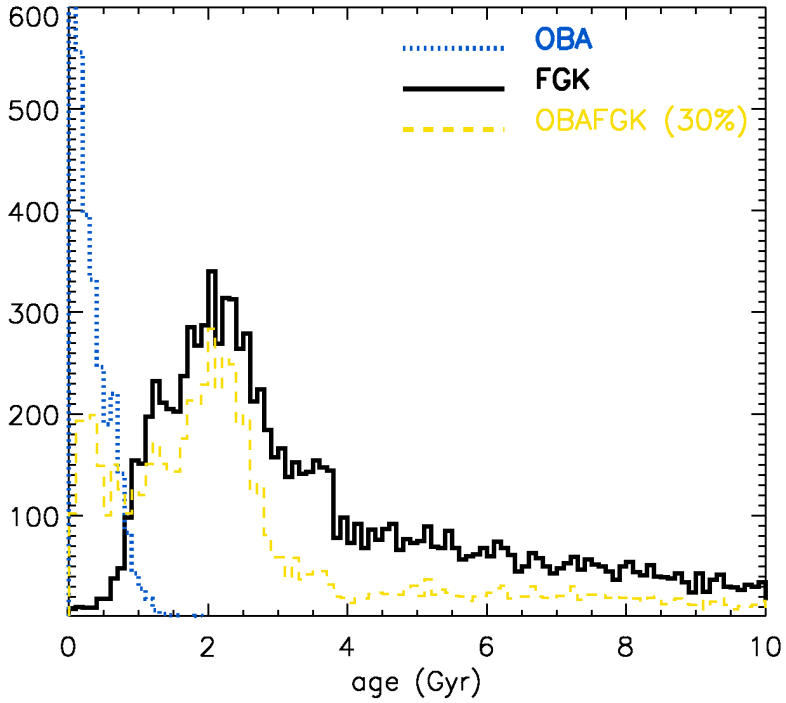

Figure 5.3: **Ages of the sample.** Age distribution for the OBA-type stars (dotted line) and for the FGK-type stars (solid line). The dashed line shows the histogram for stars with relative errors in age of less than 30%.

have non-negligible consequences for our study: dependence on the evolutionary models used or biases that arise in certain regions of the HR diagram[4].

Using improved calibrations, Holmberg et al. (2007) recomputed ages and error estimates for the Nordström et al. (2004) sample. They stated that the differences between old (used here) and new values[5] are insignificant and are much smaller than the estimated individual uncertainties. Furthermore, they find an agreement between the new ages and the independent age determination by Takeda (2007) (see Figure 19 of Holmberg et al. 2007). All these results allow us to be slightly more confident of the age values and their uncertainties. However, a cut-off by error for this parameter allows us to work with the more reliable ages. The distribution of stars with relative errors in their ages[6] of less than 30% is shown in Figure 5.3. This condition is fulfilled by 32% and 50% of stars in the OBA and FGK samples, respectively. It has to be kept in mind that employing this cut-off results in a change in the content of the working sample (e.g. uncertainties in isochrone ages increase when less massive main sequence stars are considered[7]). The most significant feature of this age histogram is the peak around 2 Gyr. This peak results from a combination of selection effects in the sample in Nordström et al. (2004): apparent magnitude, spectral type, etc. However, the lack of stars younger than ~ 1 Gyr –a direct result of the blue cut-off at $b-y=0.205$– is partially corrected in our sample by adding in the OBA sample.

Finally, as shown in Table 5.1, the $[Fe/H]$ metallicity parameter is only available for the FGK-type stars in Nordström et al. (2004) but no explicit errors for this parameter are given. The metallicity calibration by Holmberg et al. (2007) provided new $[Fe/H]$ estimates for this sample. Differences between old and new estimates reach values up to ± 0.2 dex. (see Figure 7 in Holmberg et al. 2007). However, Reid et al. (2007) compared the photometric estimate used in Nordström et al. (2004) with values obtained using echelle (high resolution) spectroscopy and found a dispersion of only ~ 0.1 dex. In addition, as shown by Haywood (2006), explicit biasing of the atmospheric parameters can lead to structures and spurious patterns in the age–metallicity diagrams. Undoubtedly, these considerations should be taken into account in the metallicity study of moving groups (Chapter 8).

[4]For instance, Pont & Eyer (2004) demonstrate that the isochrone dating method is subject to significant biases that arise inevitably in regions of the HR diagram where the effects of age on the atmospheric parameters become small. Haywood (2006) recently studied this in depth and showed how biases, similar to those expected in real samples, greatly influence the physical interpretation of the Galactic age-metallicity distribution.

[5]They were not available when the present work was completed.

[6]Nordström et al. (2004) provides upper and lower limits for error estimates. Here we consider that a star has $\epsilon_{age} \leq 30\%$ if this is true for both limits.

[7]For a discussion of the dependence of the degree of completeness of their sample on the cut-off by error in ages see Nordström et al. (2004).

Chapter 6

Structures in the velocity space

In this chapter, the kinematic plane U–V is analysed with the method described in Part II. In Section 6.1 we compare our results for the velocity plane to the classic moving groups found in other studies. Next in Section 6.2 we deal with the kinematic branches that dominate the observed U–V plane. Finally, Section 6.3 deals with the subsamples of different spectral type and in Section 6.4 we look for possible variations of the kinematic properties of the branches with Galactic position.

We deal only with these two components of the velocity because classic moving groups are less visible in the W distribution due to the more thorough phase-mixing of the movement perpendicular to the Galactic plane[1] (Dehnen 1998, Seabroke & Gilmore 2007). Figure 6.1 shows the velocity distribution in the U–V plane for the whole sample of 24910 stars obtained by means of the WD method. This Figure can be compared to Figure 6.2 where the velocities of the individual stars are plotted as dots. Table 6.1 and Figure 6.3 show the positions of the centres of the classic moving groups according to Dehnen (1998) and Eggen (1971, 1996b)[2]. Connections and continuity can be seen between these classic kinematic structures. As was first pointed out by Skuljan et al. (1999), these connections arrange classic moving groups in several branches whose approximate positions can be shown also in Figure 6.3. These superstructures (the branches), structures (moving groups) and their substructures are characterised in this chapter.

[1]This assumption must be called into question, however, for the other moving groups such as the ones that could be remnants of an accreted satellite in the disc (see Chapter 2).

[2]The list could be far more extensive; only the most significant groups have been chosen. Similar values for their components have been reported by other authors (see e.g. Montes 2001, López-Santiago et al. 2006).

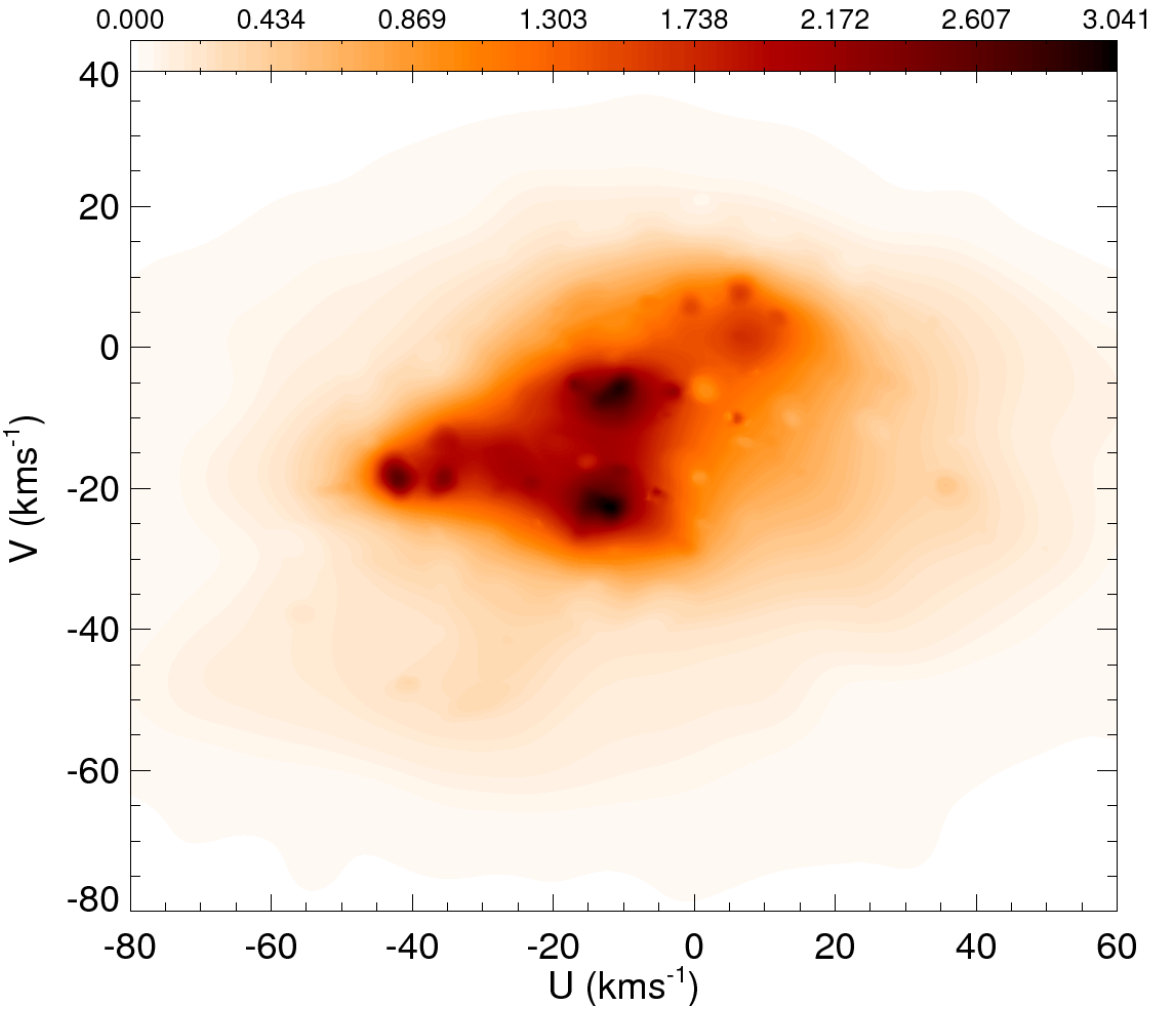

Figure 6.1: **Velocity distribution in the solar neighbourhood.** Density field in the U–V plane for the whole observational sample obtained by WD ($J_{plateau} = 4$).

6.1 Classic moving groups

The established understanding of classic moving groups immediately leads to the following points when analysing Figure 6.3:

- The Sirius, Coma Berenices, Hyades and Pleiades moving groups are clearly identified but they have neither a clearly defined shape nor defined limits. Furthermore, they present substructure.
- The centre of the Sirius moving group is not well-defined, which could explain the discrepancies in its position on the U–V plane found in the literature. This moving group seems to be better described by a branch-like shape with a clear extension.
- Similar arguments can be applied to the Hercules moving group, although it is less prominent in Figure 6.3 due to its low density. The two peaks proposed by Dehnen (1998) (groups 8 and 9 in Table 6.1) are faintly observed but this structure appears to be a continuous elongated feature.
- The Hyades and Pleiades moving groups are clearly grouped together, forming just one branch. The centres established by Eggen and Dehnen for NGC 1901 and IC 2391 (groups 5 and 12 in Table 6.1) seem to be placed slightly above the crest of the branch (less negative V), in a low density region within the distribution.
- Groups such as NGC 1901 (group 5), HR 1614 (group 6) or IC 2391 (group 12) are not observed, possibly due to the small contribution they make compared to the main structures.
- New structures such as that centred at $(35, -20)\,\mathrm{km\,s^{-1}}$, which is weak and does not have a well-defined shape, may all be considered as part of the elongation of the Sirius or Coma Berenices structures, rather than being necessarily linked to the nearest identified groups (11 or 17 in this case).

6.2 Kinematic branches

Skuljan et al. (1999) detected the existence of at least three long, parallel and equidistant branches in the U–V plane: the *Sirius branch*, the *middle branch* (here Coma Berenices branch) and the *Pleiades branch* (here Hyades-Pleiades branch). The increased extent of our sample, in terms of both luminosity and spectral type, allows us to characterise these three branches and also the Hercules branch. In this section the properties of these branches in the whole sample are studied.

Table 6.1: **Velocities of the moving groups by other studies.** Heliocentric velocities of the main moving groups according to (1) Dehnen (1998) and (2) Eggen (1971, 1996b, and references therein).

Moving group	(1)		(2)	
	U ($\mathrm{km\,s^{-1}}$)	V ($\mathrm{km\,s^{-1}}$)	U ($\mathrm{km\,s^{-1}}$)	V ($\mathrm{km\,s^{-1}}$)
1 Pleiades (Stream 0)	−12	−22	−11.6	−20.7
2 Hyades (Stream I)	−40	−20	−40.4	−16.0
3 Sirius (Stream II)	9	3	14.9	1.4
4 Coma Berenices	−10	−5		
5 NGC 1901	−25	−10	−26.4	−10.4
6 HR1614	15	−60	5.8	−59.6
7	20	−20		
8	−40	−50		
9	−25	−50		
10	50	0		
11	50	−25		
12 IC 2391			−20.8	−15.9
13	−70	−10		
14	−70	−50		
15 61 Cygni			−80	−53
16 ζ Herculis			−30	−50
17 Wolf 630			25	−33

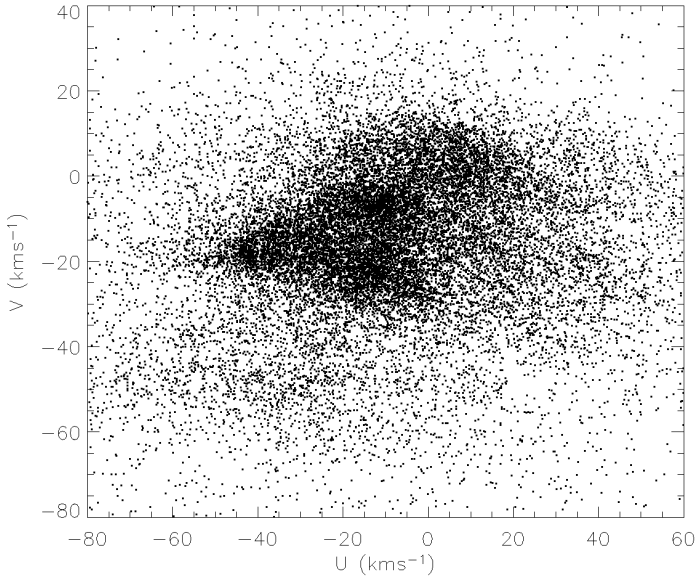

Figure 6.2: **Stellar velocities in the solar neighbourhood.** Stellar velocities in the U–V plane for the whole observational sample.

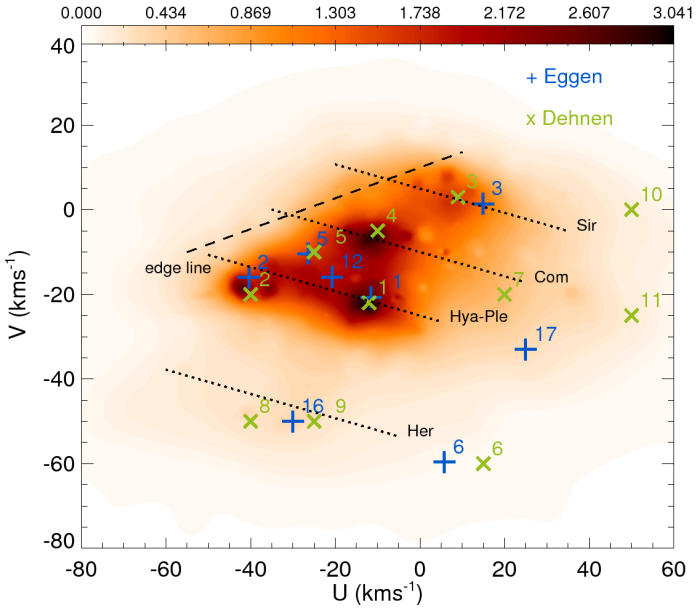

Figure 6.3: **Kinematic branches and moving groups.** As Figure 6.1 but with the superposition of the classic moving groups in Table 6.1, the approximate trace of the branches and the trace of the edge line (see text in Section 6.2).

The branches seem to have a similar and slight curvature. This curvature can be critical to evaluating whether some old moving groups are part of the branches. For example, this is the case of Wolf 630 (group 17 in Table 6.1) located at $(25, -33)\,\mathrm{km\,s^{-1}}$ and one of the oldest groups proposed in Eggen (1971). In addition, this curvature could be a decisive parameter to bear in mind when constraining the models proposed for the origin and evolution of the kinematic branches.

To simplify the study of the branches, a clockwise rotation through an angle β is applied to the original (U, V) components. In the new coordinate system (U_β, V_β) the branches are better aligned with the horizontal axis (except for their slight curvature). Although Skuljan et al. (1999) proposed a turn of 25°, a value of $\beta \sim 16°$ is more suitable for the data we present here, especially for the three main branches. Their approximate positions are delineated as dotted lines with this slope in Figure 6.3.

Figure 6.4 shows the density along the V_β component for the whole sample. The WD is carried out up to different J (3, 4, 5) in order to illustrate the discussion regarding the choice of J in Sections 3.3 and 4.2. The four branches are clearly seen and their approximate positions are marked with vertical lines. We notice that J has become rapidly $J_{plateau}$ and results almost do not change from J to J. Our data confirm the nearly equidistant character of the branches. The first three branches are found to be separated in intervals of approximately 15 $\mathrm{km\,s^{-1}}$. The possible dependence of this interval on spectral type or age is discussed in Section 6.3 and Chapter 7. The separation between the Hyades-Pleiades and the Hercules branch is $\sim 30\,\mathrm{km\,s^{-1}}$.

Skuljan et al. (1999) noticed the existence of a fairly sharp "edge line" at 30° to the U axis and connecting the extremes of the branches at low U and high V (see their Figure 5). This feature can be evaluated by computing the density field in the direction perpendicular to this hypothetical edge line (direction of $U_\perp$ from now on). First, several directions were scanned to look for the sharpest distribution: a lower inclination of about 20° was found here. This edge line is plotted in Figure 6.3 and the perpendicular density distribution along $U_\perp$ is presented in Figure 6.5. Undoubtedly, the asymmetry and the long tail at positive $U_\perp > 0$ observed would support the existence of a sharp edge line. However, we want to stress that:

- The upper part of the edge line is not empty: a considerable number of stars occupy this region of the U–V plane (see Figure 6.2).
- Equivalent importance should be given to other similar edge lines such as the sharp distribution observed in Figures 6.2 and 6.1 near the Hyades-Pleiades branch towards low U and low V, which is manifested in Figure 6.4 with the drop at the left of this branch.
- Each branch presents a different density distribution near the edge line (Figure 6.1). This is also confirmed by examining the density characteristics along each branch, i.e. in the direction of the component U_β, plotted in Figure 6.6. These density distributions are

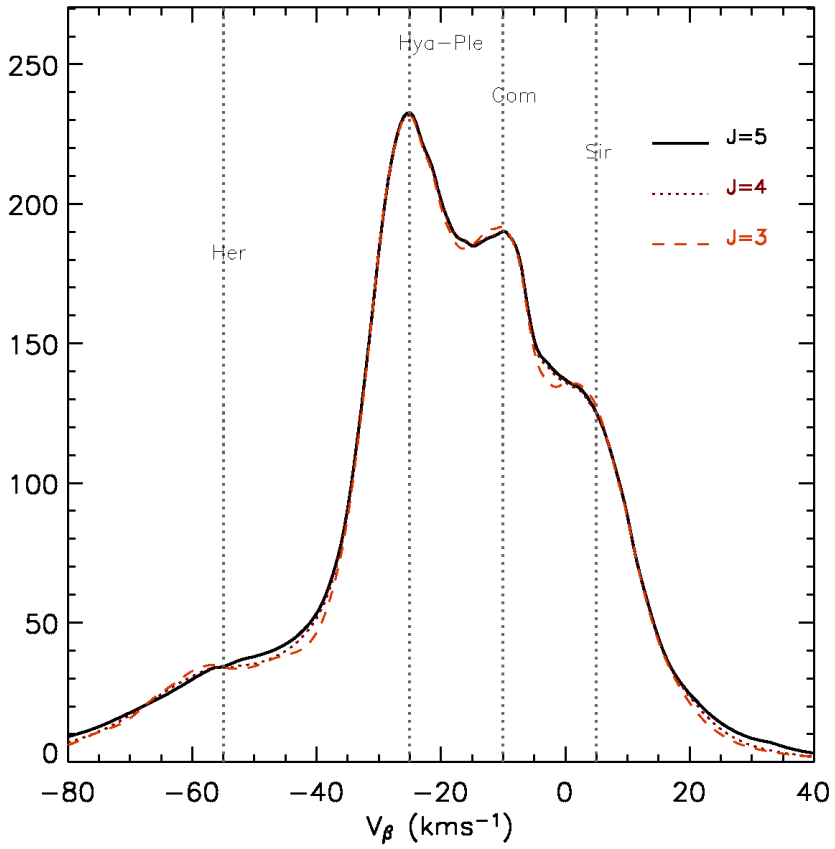

Figure 6.4: **Kinematic distribution perpendicular to the branches.** Density field for the V_β component. The approximate positions of the four branches of Hercules, Hyades-Pleiades, Coma Berenices and Sirius are marked with vertical lines according to the maximums.

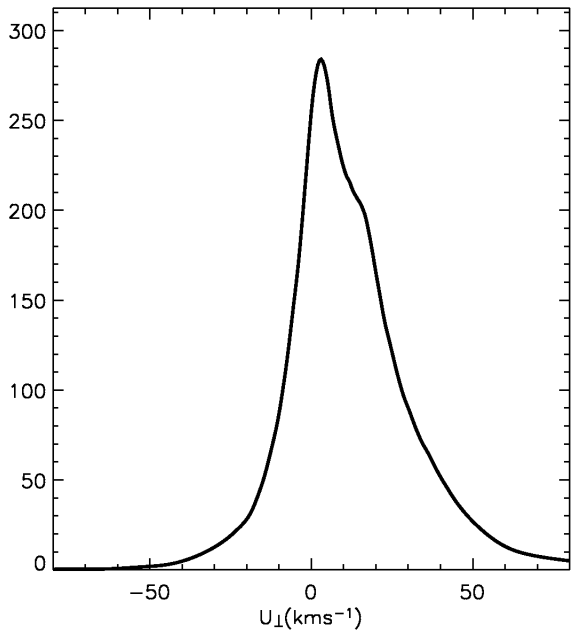

Figure 6.5: **Kinematic edge line.** Density field in the direction perpendicular to the edge line ($U_\perp$) for the whole observational sample ($J_{plateau} = 4$).

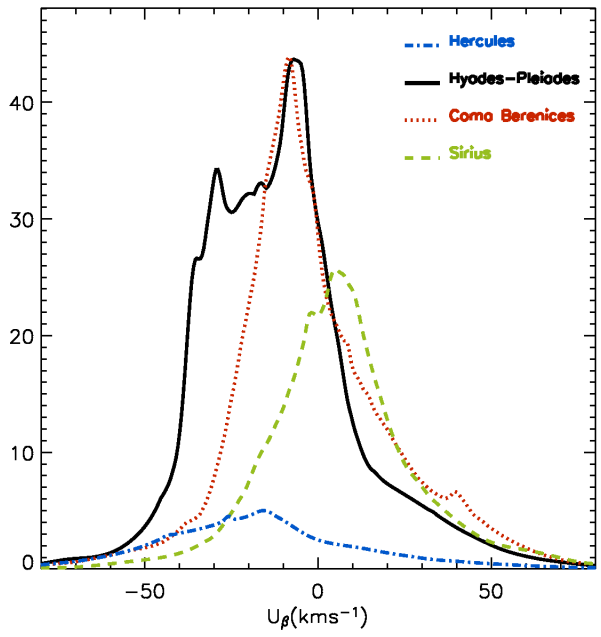

Figure 6.6: **Kinematic distribution along the branches.** Density field for the U_β component for each of the four branches ($J_{plateau} = 4$).

obtained from the whole U_β–V_β distribution considering the central positions in V_β of the branches according to the maximums in Figure 6.4 (-55, -25, -10 and 5 $\mathrm{km\,s^{-1}}$ for the Hercules, Hyades-Pleiades, Coma Berenices and Sirius branches, respectively) and a width of $\pm 4\,\mathrm{km\,s^{-1}}$. It can be seen that the slope of the density drop at negative U_β is different for each branch, being considerably steeper for the Hyades-Pleiades branch in part due to the gathering of stars of the small substructures at the very beginning of the branch. The drop becomes less abrupt from Coma Berenices to Sirius to the Hercules branch. Moreover, the Hyades-Pleiades and Coma Berenices branches show a slightly asymmetric distribution, with a longer tail of stars at positive U_β.

The existence of all these abrupt features in the U–V plane definitely rules out the classic idea of a smooth velocity field distribution and it even questions the scenario where several structures are superimposed on this smooth field.

6.3 Spectral type analysis

Figure 6.7 shows the density field in the U–V plane (left column) and the density for the V_β component (right column) for the subsamples of OBA, FGK, M dwarfs and KM giants. Some of these subsamples have been used for moving group studies by different authors and using different techniques. This is the first time that the same statistical method is applied to all of them. In this sense, a direct comparison among subsamples deserves special attention.

In the right column plots, the WD has been carried out up to different J (3, 4, 5), as in Figure 6.4 for the whole sample, in order to return to the considerations about the choice of J in Section 3.3. The maximum value of J presented in these plots is always higher than or equal to $J_{plateau}$, which is the one for which the result does not change when higher scales are denoised. For the FGK and OBA subsamples, J becomes rapidly $J_{plateau}$ and the signals almost do not change from J to J. Therefore, the significance of the structures and branches present in these distributions is strongly supported. However, for the subsamples of M dwarfs and KM giants the peaks whose existence has been independently proved by the previous robust results here are drastically diluted when denoising up to the $J_{plateau}$. For this and to avoid the loss of signal (Section 3.3), we present and discuss the U–V distributions with $J = 4$ for all subsamples despite this not being $J_{plateau}$ for all of them.

Some of the well-known characteristics according to spectral type are observed in these figures, for example the predominance of the Coma Berenices and Pleiades groups or the absence of the Hyades moving group for the OBA stars. As some of these features depend on age, they will be studied in Chapter 7. More importantly, the three branches of Hyades-Pleiades, Coma

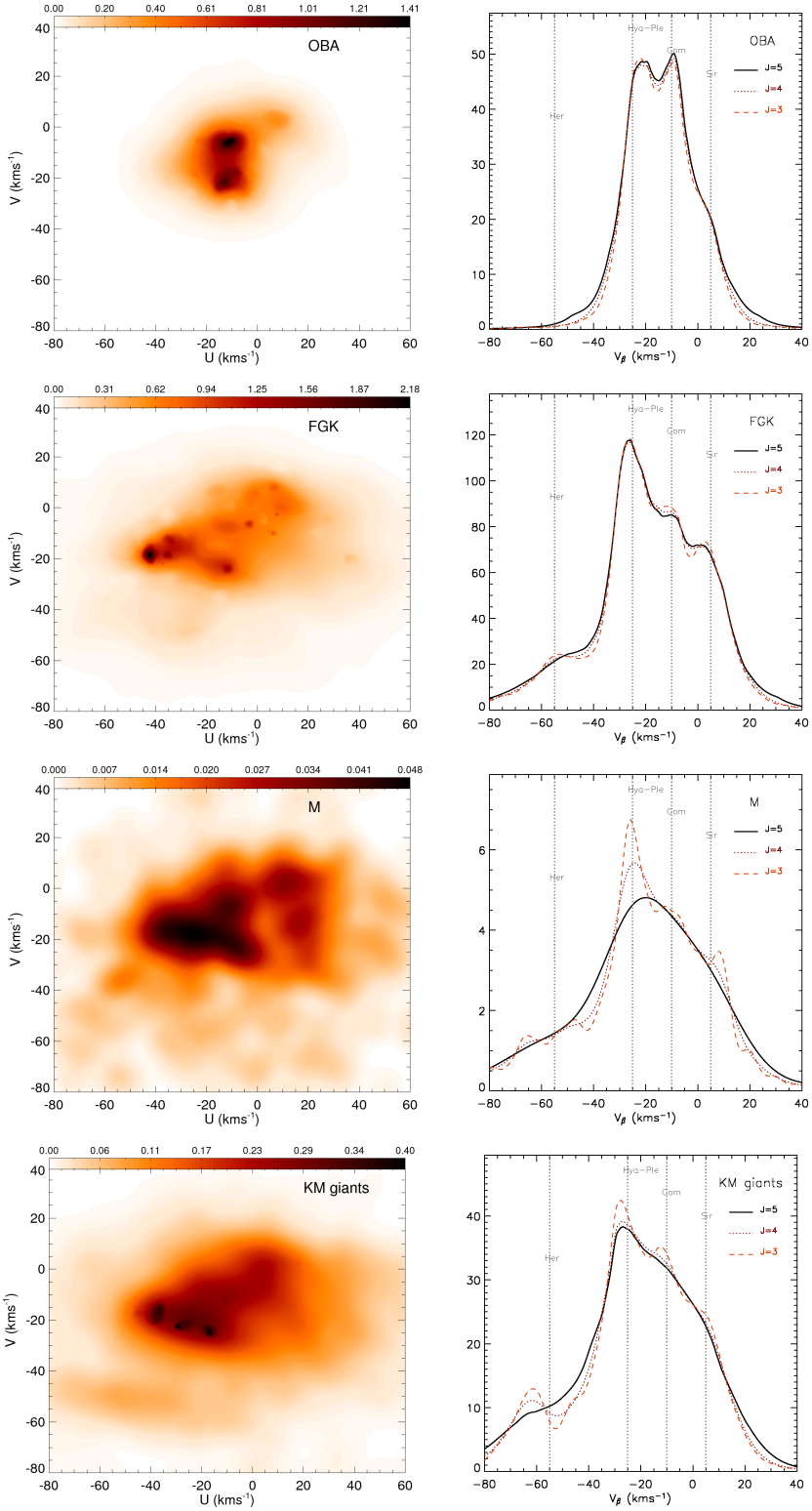

Figure 6.7: **Velocity distributions for spectral types.** Left column: Density field in the U–V plane for the the subsamples of OBA, FGK, M dwarf stars and KM giant stars obtained by WD with $J = 4$. Right column: Density field for the V_β component with different values of J of the WD: 3, 4 and 5.

Berenices and Sirius are detected in all subsamples (Figure 6.7, right). Skuljan et al. (1999), with a different rotation angle β, suggested a separation of $15\,\mathrm{km\,s^{-1}}$ for early-type stars but $20\,\mathrm{km\,s^{-1}}$ for late-type stars. Here, the value of $15\,\mathrm{km\,s^{-1}}$ is more suitable for all subsamples. In all cases, the positions of these three overdensities differ by less than 3-4 $\mathrm{km\,s^{-1}}$ from the values derived for the whole sample (vertical lines).

The comparison between the velocity distributions of the KM giants and the FGK dwarfs deserves special attention since they have very different space volume coverage (see Figure 5.1) and the number of stars in both subsamples is comparable. A similar examination was carried out by Seabroke & Gilmore (2007). We agree with these authors that the kinematic structures are well maintained in both distributions and thus, considering their different spatial extension, moving groups cannot be simple remnants of star clusters. Our method allows us to go further in this comparison. For instance, a clear overdensity appears at $(U, V) \sim (-27, -22)\,\mathrm{km\,s^{-1}}$ in the middle of the Hyades-Pleiades branch for the KM giants sample which is not present for the FGK dwarfs. Most specially, the Hercules branch presents significant differences both in shape and in position of the density maximum. Whereas for the KM giants this branch is seen as a clear elongated structure, for the FGK dwarfs there is a density maximum more localised in the U–V plane. Moreover, Figure 6.7 (right) shows an evident discrepancy between the positions of the Hercules branch located at $V_\beta \sim -62\,\mathrm{km\,s^{-1}}$ for the KM giants but at $V_\beta \sim -55\,\mathrm{km\,s^{-1}}$ for the FGK dwarf stars. Two possible explanations for this discrepancy are: i) errors in distance estimates or biases and ii) real differences due to the different volume coverage or Galactic position. Previous discrepancies in the position of the Hercules group are seen by checking the literature. Fux (2001) found Hercules centred at (U, V)=$(-35, -45)\,\mathrm{km\,s^{-1}}$ using a sample of nearby stars ($d < 100\,\mathrm{pc}$), whereas a value of $(-42, -51)\,\mathrm{km\,s^{-1}}$ was obtained by Famaey et al. (2005) for the KM giants. These values correspond to $V_\beta = -53$ and $-61\,\mathrm{km\,s^{-1}}$, respectively. Also, as mentioned in Section 6.1, Dehnen (1998) detected two peaks in the region of this branch (groups 8 and 9 in Table 6.1) at $V_\beta = -59$ and $-55\,\mathrm{km\,s^{-1}}$. Although density values in the tail of the distribution where Hercules is placed are low, we will pay special attention to this discrepancy.

As mention in Chapter 5, no significant bias is expected for the FGK stars with trigonometric parallaxes (with small relative errors of less than 13%). We have checked that the position of the Hercules branch does not change at all when separately considering the FGK stars with trigonometric parallax or those with photometric distances. Consequently, this establishes the existence of the peak at $V_\beta \sim -55\,\mathrm{km\,s^{-1}}$ for stars nearer than 100-150 pc.

More importantly, we have selected stars from the subsample of KM giants with relative errors in trigonometric parallaxes $\sigma_\pi/\pi < 10\%$. As mentioned, biases in trigonometric distances are negligible for this truncation of the relative error. In Figure 6.8 we compare the density in

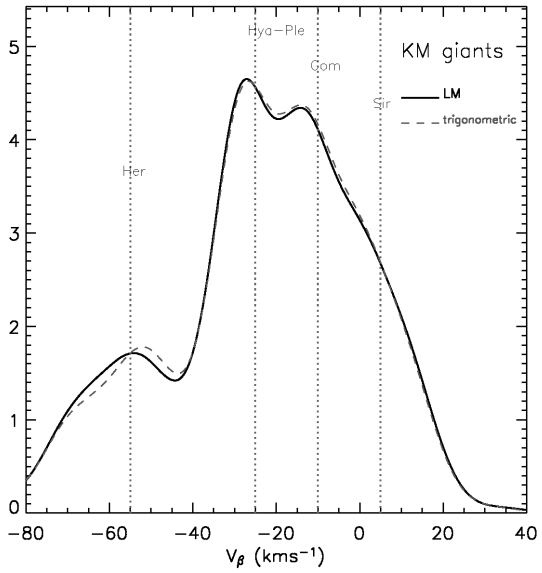

Figure 6.8: **Kinematic distribution of the KM giant stars with trigonometric and LM distances.** Density field for the V_β component for $J = 4$ of the WD for the KM giants with $\sigma_\pi/\pi < 10\%$ (756 stars) using the trigonometric distance (dashed line) and the LM distance (solid line).

the V_β component obtained calculating the velocity using: i) the distance estimates from the method in Luri et al. (1996) –LM distances from now on– (solid line) and ii) the distances from trigonometric parallaxes (dashed line). As expected, both curves are practically identical using LM and trigonometric distances since high-quality information on trigonometric parallaxes was used in the derivation of the LM distances. Remarkably, we observe that the overdensity of the Hercules branch appears at $V_\beta \sim -55\,\mathrm{km\,s^{-1}}$, as for the FGK dwarfs. With this cut in σ_π/π, we are in fact selecting stars with distances $< 150\,\mathrm{pc}$, which proves again the existence of a real kinematic structure at $V_\beta \sim -55\,\mathrm{km\,s^{-1}}$ for the nearer stars. Note that, by contrast, we find that the velocity distributions of the stars located in shells of LM distances further than 100 pc centred in the Sun[3] do present always the peak at $\sim -62\,\mathrm{km\,s^{-1}}$ using the LM distances (Figure 6.9). Therefore, the situation is certainly complex. We conclude that we can not conclusively disentangle the cause of the different position of the Hercules branch for the sample of KM giant stars. It could be either its larger spatial extension or a consequence of the distance determination method.

We want to evaluate whether the subsample of M dwarfs could contribute to solve this

[3]Note that due to its source of radial velocities, this subsample is restricted to the northern equatorial hemisphere (see Famaey et al. 2005) and therefore, stars in these shells are not isotropically distributed around the Sun.

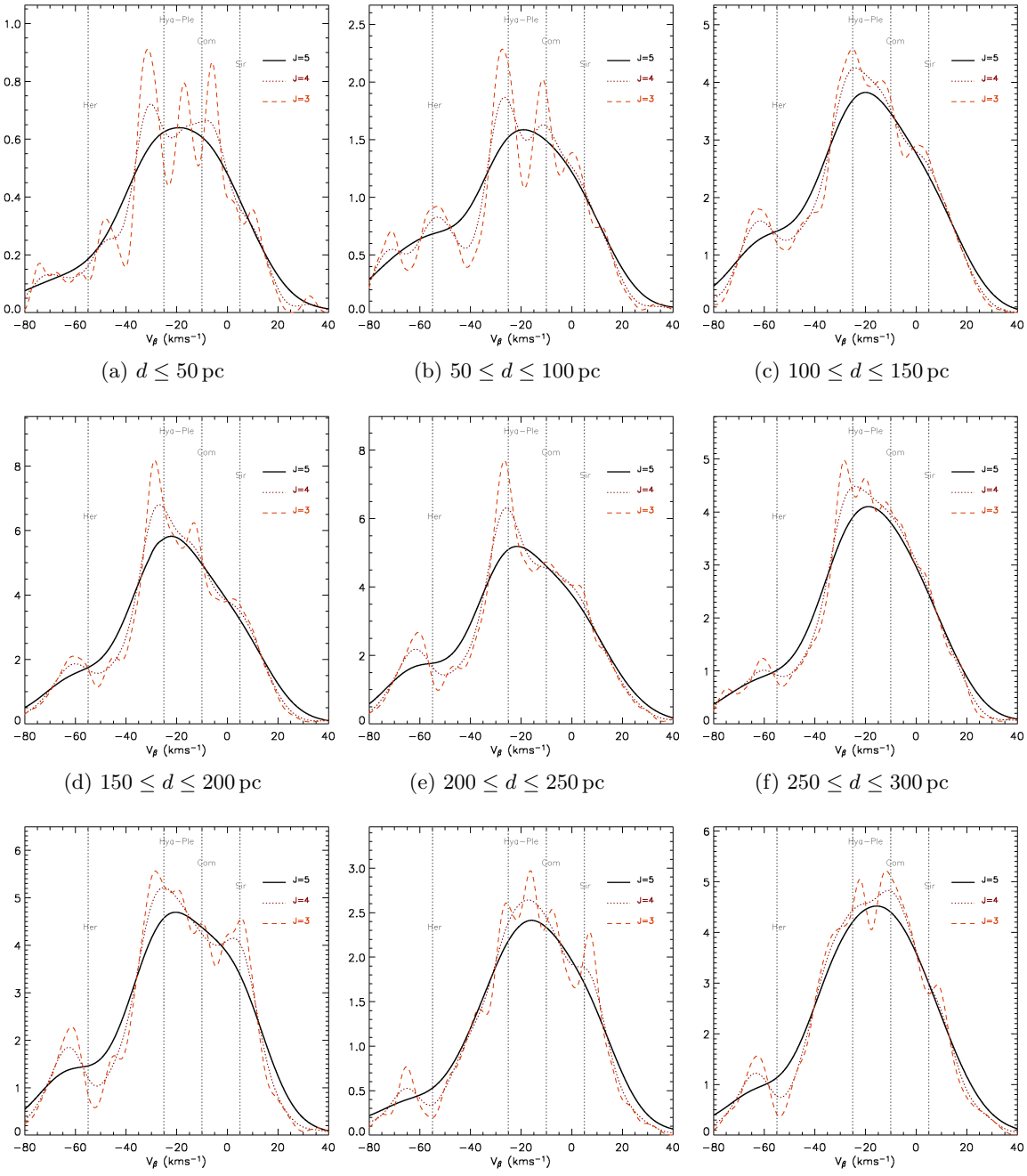

(a) $d \leq 50\,\mathrm{pc}$ (b) $50 \leq d \leq 100\,\mathrm{pc}$ (c) $100 \leq d \leq 150\,\mathrm{pc}$

(d) $150 \leq d \leq 200\,\mathrm{pc}$ (e) $200 \leq d \leq 250\,\mathrm{pc}$ (f) $250 \leq d \leq 300\,\mathrm{pc}$

(g) $300 \leq d \leq 400\,\mathrm{pc}$ (h) $400 \leq d \leq 500\,\mathrm{pc}$ (i) $d \geq 500\,\mathrm{pc}$

Figure 6.9: **Kinematic distribution of the KM giants at different distances.** Density field for the V_β component for $J = 3$, $J = 4$ and $J = 5$ for subsamples of stars located in shells of LM distances.

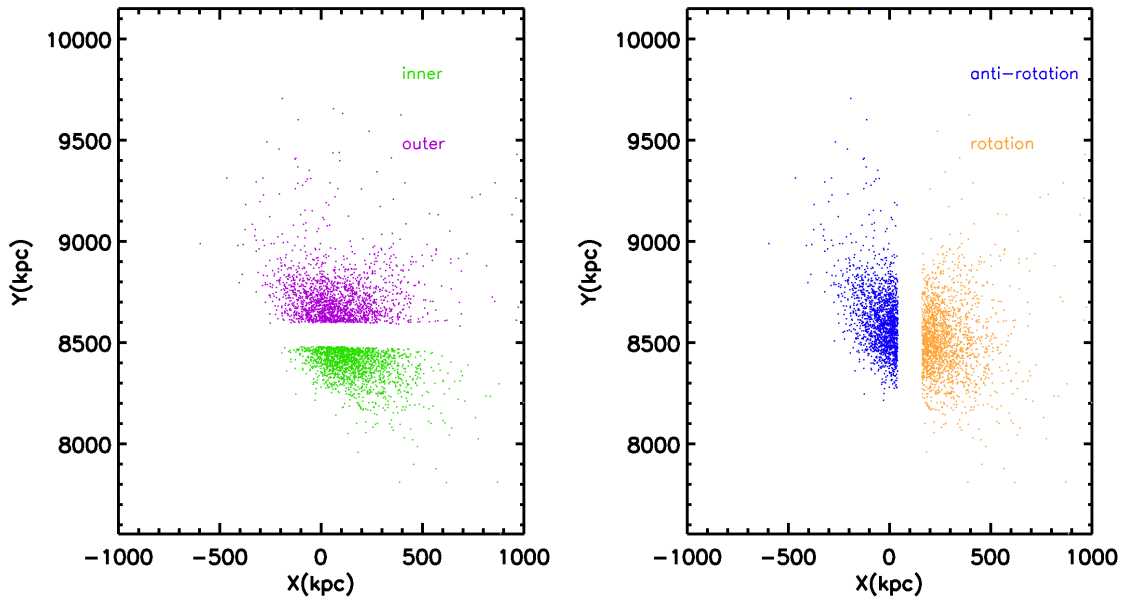

(a) inner and outer subsamples

(b) subsamples towards anti-rotation and rotation

Figure 6.10: **Spatial distribution of the subsamples of KM giants.** Partition of the KM giant subsample in 4 subsamples according their radii and η coordinate.

issue, despite being aware that the low number of stars in this case prevents us from giving any conclusive statement. The V_β distribution for these stars (Figure 6.7) shows two peaks around the Hercules branch at $V_\beta \sim -50\,\mathrm{km\,s^{-1}}$ and $-65\,\mathrm{km\,s^{-1}}$. As this subsample is composed of stars from two different catalogues (see Chapter 5), we ascertain that the stars from Reid et al. (2002) (very nearby stars with $d < 25\,\mathrm{pc}$) show a very broad Hercules branch but centred at $V_\beta \sim -55\,\mathrm{km\,s^{-1}}$, in agreement with the previous results for nearby stars (figures are omitted). However, the stars from Bochanski et al. (2005) (stars from selected areas mostly at $\delta > 0$ and with larger distances up to $\sim 150\,\mathrm{pc}$) contribute to the split of this branch into two peaks. Again, the importance of the mean distance and spatial distribution of the subsample considered is revealed.

6.4 Kinematic structures in different Galactic positions

We look for possible variations of the kinematic properties of the branches with Galactic position. At present, the KM giant subsample is the only one with enough stars and space volume coverage

to undertake this study. We have selected 4 subsamples at different locations and approximately with the same number of stars (1800-2000 stars). Note that the centre of KM giants spatial distribution onto the Galactic plane is placed 100 pc away from the Sun in the direction of Galactic rotation and 40 pc towards the Galactic anti-centre[4]. Stars in the central region are not considered in order to emphasise the properties of the extremes. First, we divide the sample into two subsamples according to their different galactocentric radii, R: $R < R_{\odot} - 20\,\mathrm{pc}$ (inner subsample) and $R \geq R_{\odot} + 100\,\mathrm{pc}$ (outer subsample). Secondly, we build two subsamples with different η (heliocentric Cartesian coordinate towards the direction of the Galactic rotation): with $\eta < 40\,\mathrm{pc}$ (subsample towards anti-rotation with respect to the centre of the sample) and $\eta > 160\,\mathrm{pc}$ (subsample towards rotation). The region occupied by the 4 subsamples are shown in Figure 6.10.

The results are shown in Figures 6.11 and 6.12. The same colour scale is used in all cases for a clearer comparison. From these Figures we conclude that the four branches are present in all regions. Second, the Hyades-Pleiades branch is the dominant structure, except for the region towards Galactic rotation where Coma Berenices has the same density. Furthermore, a significant change of contrast among substructures inside the branches is confirmed and the density maximum along the branches (along the U_{β} component) varies for each region. Note for instance the substructures at $(U, V) \sim (-27, -22)\,\mathrm{km\,s^{-1}}$ and $(U, V) \sim (-20, -10)\,\mathrm{km\,s^{-1}}$ or the Pleiades moving group. Also the shape of the Hercules branch changes between regions and it is more significant for the inner region and through anti-rotation. All these considerations suggest a real effect of Galactic position on the shape of kinematic structures, independently of the possible bias in the LM distances.

Resuming the issue of the discrepancies in the Hercules branch position, we observe that this branch appears at $V_{\beta} \sim -62\,\mathrm{km\,s^{-1}}$ for all these four different galactocentric directions of the KM giants subsample, in strong contrast with the peak at $V_{\beta} \sim -55\,\mathrm{km\,s^{-1}}$ for the central nearby stars of this same subsample. This makes the method for LM distance derivation suggestive of a possible bias entangling kinematics and distances in a complex way. Although the Bayesian parametric LM approach was developed to derive unbiased distances, the a priori adoption of a Schwarzschild ellipsoid for the velocity distribution functions can directly affect the distance estimate of a given kinematic group or branch. Further work along these lines requires the revision of the LM distances and the application of the WD method to larger and spatially more extended surveys (RAVE, Gaia).

[4]Note also that the observational spatial restriction affects the distribution of the subsamples in the direction perpendicular to the Galactic plane.

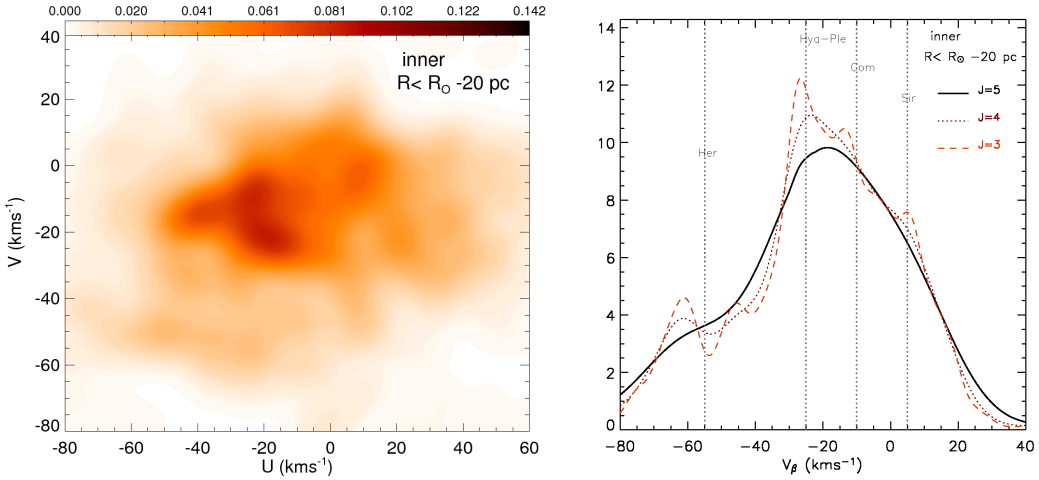

(a) inner subsample $R < R_\odot - 20\,\mathrm{pc}$

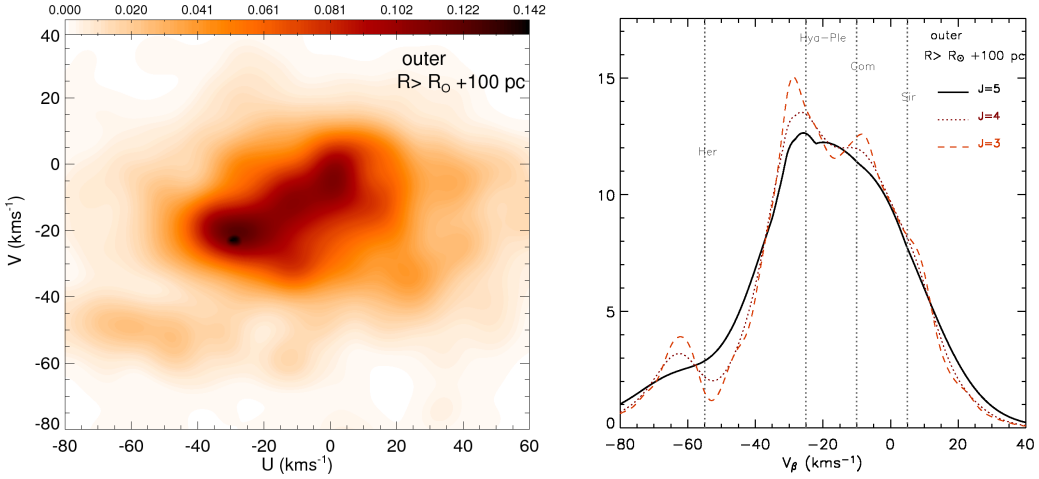

(b) outer subsample $R \geq R_\odot + 100\,\mathrm{pc}$

Figure 6.11: **Velocity distributions at different Galactic radius.** Density field in the U–V plane obtained by WD with $J = 4$ (left) and density field for the V_β component with different values of J (right) of two subsamples of KM giant stars situated at (a): inner galactocentric radii (1812 stars) and (b): outer galactocentric radii (2057 stars).

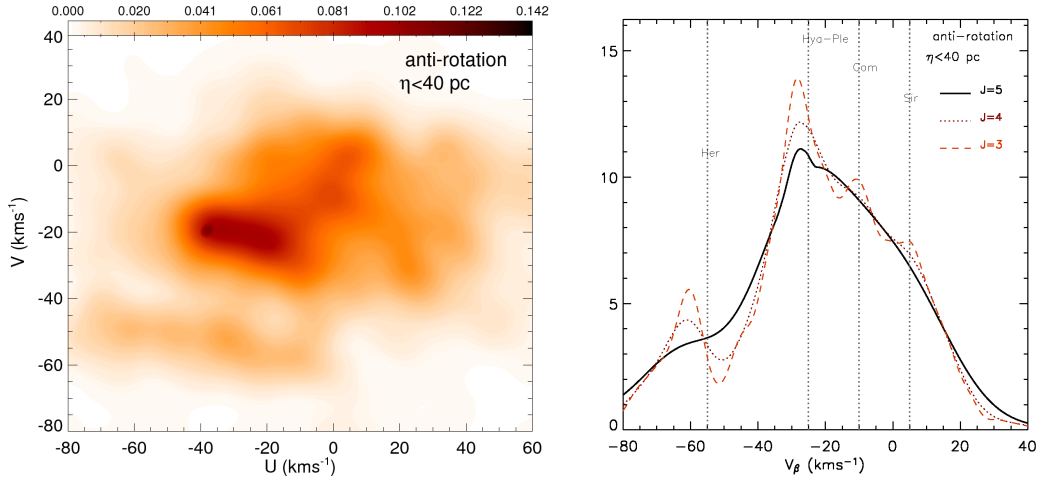

(a) subsample towards anti-rotation $\eta < 40\,\mathrm{pc}$

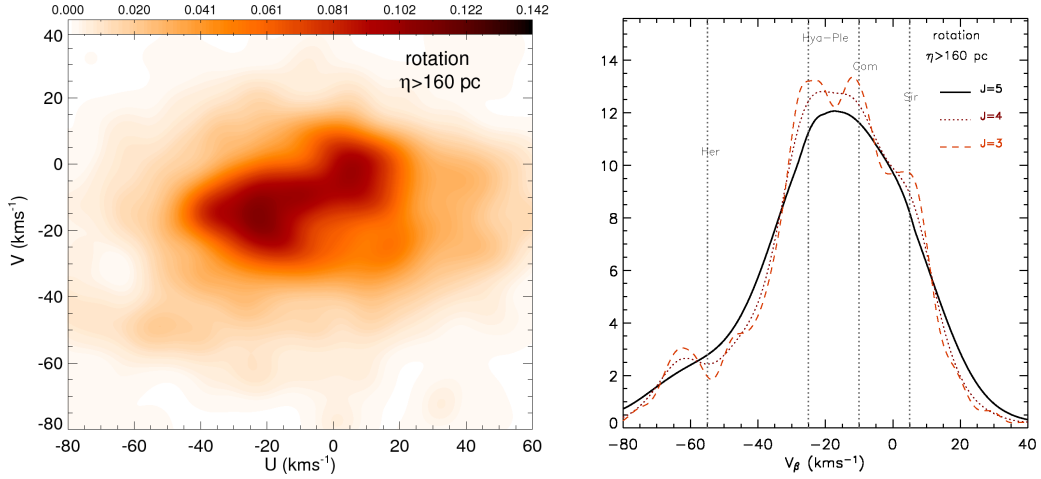

(b) subsample towards rotation $\eta > 160\,\mathrm{pc}$

Figure 6.12: **Velocity distributions at different Galactic azimuths.** Density field in the U–V plane obtained by WD with $J = 4$ (left) and density field for the V_β component with different values of J (right) of two subsamples of KM giant stars situated at (a): azimuths towards anti-rotation $\eta < 40\,\mathrm{pc}$ (1903 stars) and (b): azimuths towards rotation $\eta > 160\,\mathrm{pc}$ (1975 stars).

Chapter 7

Age–kinematics characterisation

Two different approaches are adopted in this chapter. First, the whole sample is divided by age range into statistically significant subsamples to trace the kinematic structures in the U–V plane through age. Secondly, only those stars with the most precise ages –relative errors of less than 30%– are used to study structures and periodicities in U–V–age space and other connections between kinematic structures and the evolutionary state of their members in the context of the branches proposed in Section 6.2. Note that in both analyses the sample of stars used only includes the FGK and OBA dwarfs samples, since individual ages are not available for the other subsamples (see Table 5.1).

7.1 U–V plane dependence on age

Figures 7.1 and 7.2 show the distribution in the U–V plane and the distribution for the V_β component obtained by WD for subsamples with different age ranges. The age bins have been chosen in order to emphasise the changes in these distributions. Important observations derived from these figures are:

- For the youngest stars, only the Pleiades and Coma Berenices kinematic groups appear and the branches are not identified in the U–V plane. For ages between 0.1 and 0.5 Gyr, the Hyades and Sirius structures have begun to appear. The Hyades structure is the most prominent in all the subsamples with age > 0.5 Gyr.
- Certain structures appear and disappear (or at least their contrasts vary considerably in relation to other structures) when subsamples with different age ranges are considered. See, for instance, the Pleiades structure at $(U, V) \sim (-12, -22)\,\mathrm{km\,s^{-1}}$. From top to bottom,

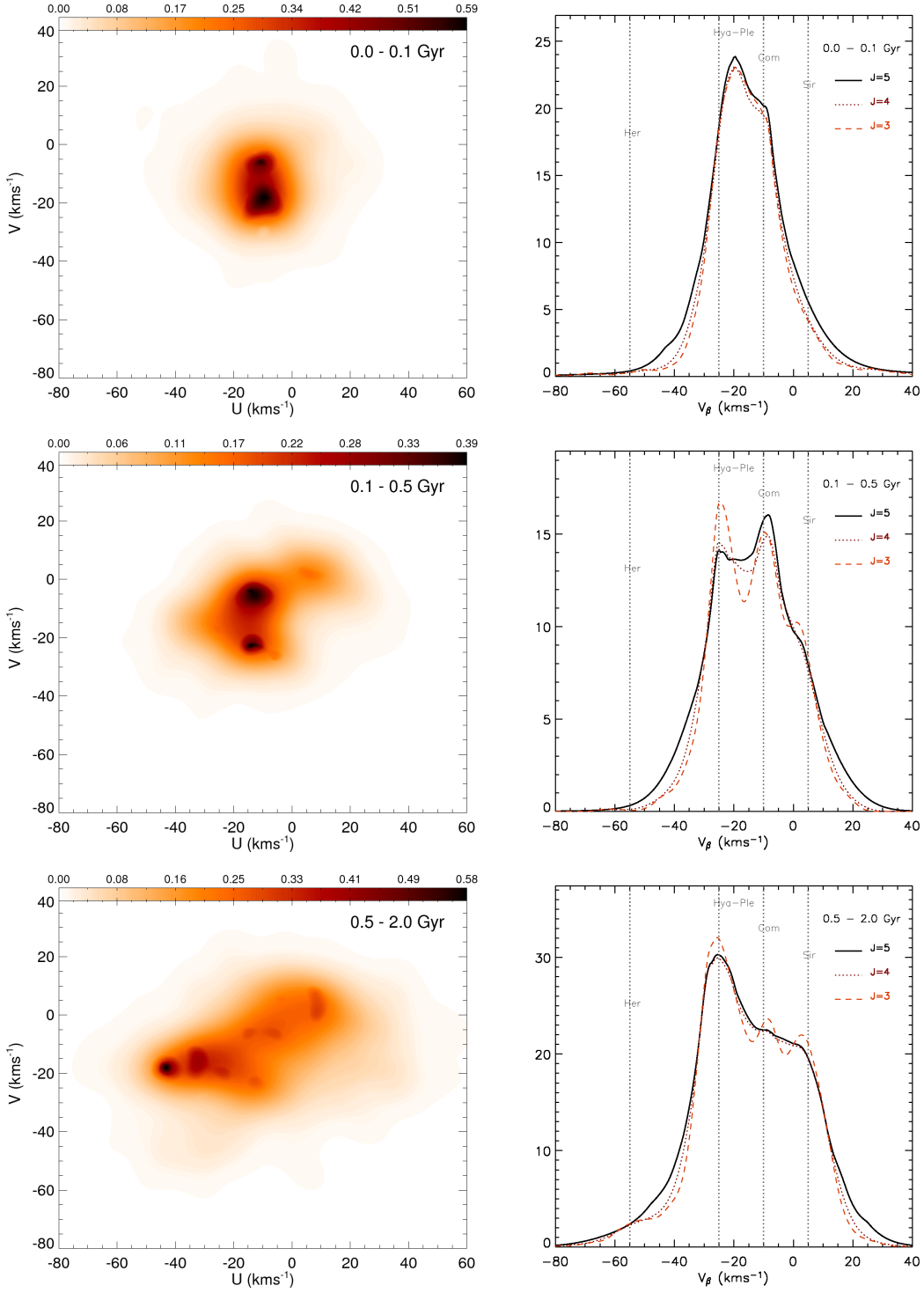

Figure 7.1: **Velocity distributions for different ages (I).** Left column: Density field in the U–V plane obtained by WD with $J = 4$ for subsamples of different ages (in Gyr): 0-0.1 (1792 stars), 0.1-0.5 (1501), 0.5-2.0 (3368). Right column: Density field for the V_β component with different values of J of the WD: 3, 4 and 5.

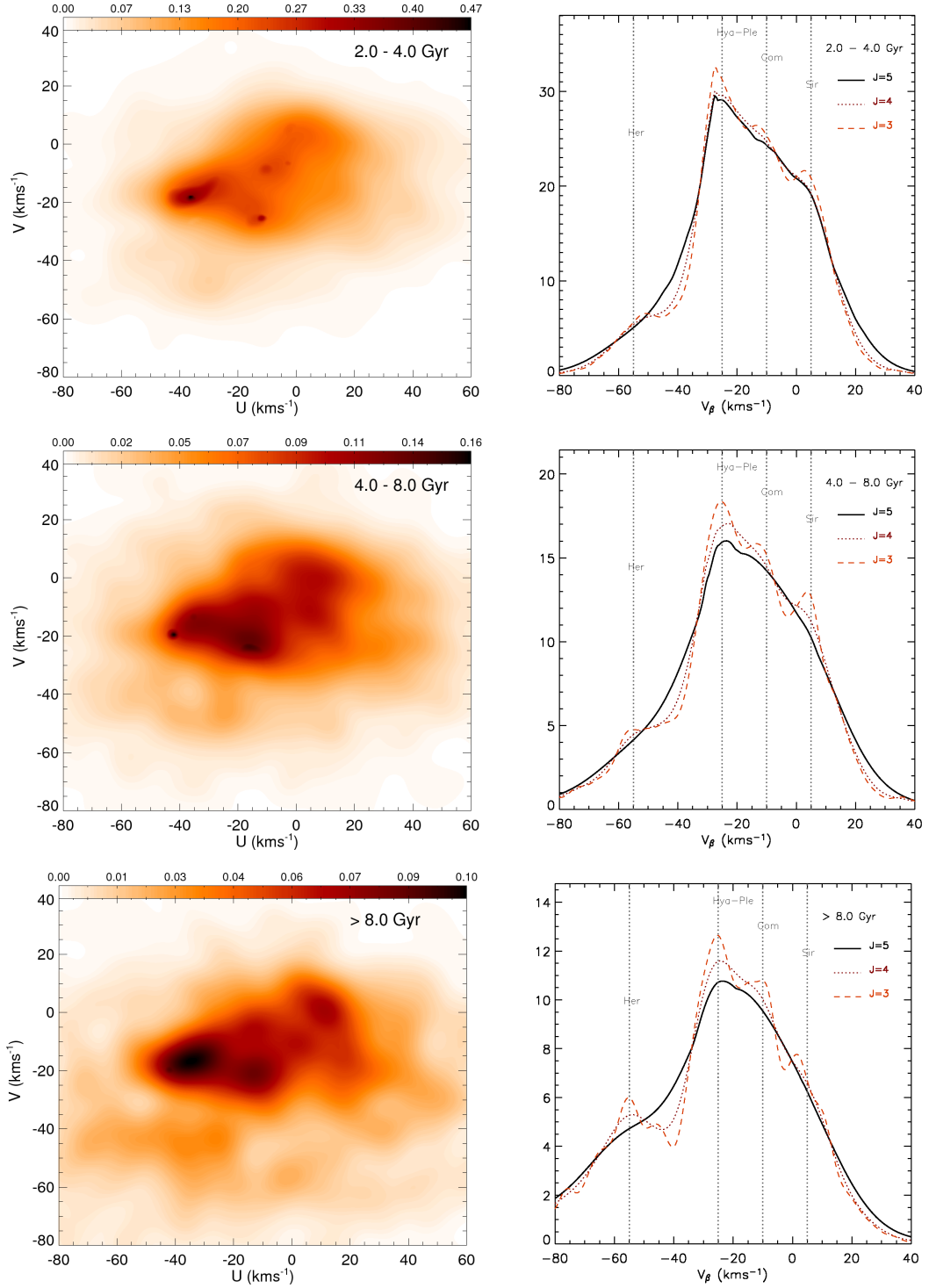

Figure 7.2: **Velocity distributions for different ages (II).** Left column: Density field in the U–V plane obtained by WD with $J = 4$ for subsamples of different ages (in Gyr): 2.0-4.0 (3917), 4.0-8.0 (2561) and >8.0 (2053). Right column: Density field for the V_β component with different values of J of the WD: 3, 4 and 5.

we see how this structure is clearly evident for very young stars but is less significant in the 0.5-2.0 Gyr range, only to reemerge at 4-8 Gyr[1].
- The structure of branches is well traced up to the oldest samples. The minimum age of the stars in each branch is discussed in Section 7.2.
- The separation between branches does not depend on age. The value of $15\,\mathrm{km\,s^{-1}}$ is found to be appropriate except for the youngest stars (<100 Myr) where the Pleiades and Coma Berenices moving groups are closer in V_β.
- The drop of density at the left of the Hyades-Pleiades branch considered in Section 6.2 is noticed in all age ranges. In addition, we observe that the relative density between this branch and the Hercules branch clearly decreases with age.

In Chapter 5 we mention that the Hα equivalent width could be used as information on age for the M dwarfs. We have checked, however, that the number of stars per sample when active and non-active stars are analysed separately is too low to derive significant results from the distributions: too smoothed distributions are obtained by WD with $J_{plateau}$ (Figure 7.3). This study has been postponed until the use of recent new data, i.e. Bochanski et al. (2007).

7.2 Age of the kinematic branches

Figure 7.4 shows the distribution in the V_β–*age* plane for the stars with well-defined ages ($\epsilon_{age} \leq 30\%$, 7016 stars). The age distribution of each branch (Figure 7.5) is computed from the whole distribution, selecting the region of the branches as detailed in Section 6.2 (centres at -55, -25, -10 and 5 $\mathrm{km\,s^{-1}}$ for the Hercules, Hyades-Pleiades, Coma Berenices and Sirius branches respectively with a width of $\pm 4\,\mathrm{km\,s^{-1}}$). Important observations derived from this distributions are:

- An extended age distribution is confirmed for all four branches.
- While the Hyades-Pleiades and Coma Berenices branches have an important fraction of very young stars, Sirius has its first main peak for slightly older stars at $\sim$ 400 Myr. Consequently, the velocity distribution becomes structured by the tree main branches for stars of $\sim$ 400 Myr.
- Dehnen (2000) assigns an age of $>$ 8 Gyr to the Hercules group and Bobylev & Bajkova (2007) claim that it does not show any branch-like shape unless very old ($>$ 8 Gyr) subsamples are studied. Here the kinematic region of the Hercules branch is populated with stars

[1] Asiain et al. (1999b), working only with the sample of B and A main sequence stars, found a significant variation of the Pleiades moving group with age. However, as ages in their sample are $<$ 0.5 Gyr, their interpretations cannot be applied here.

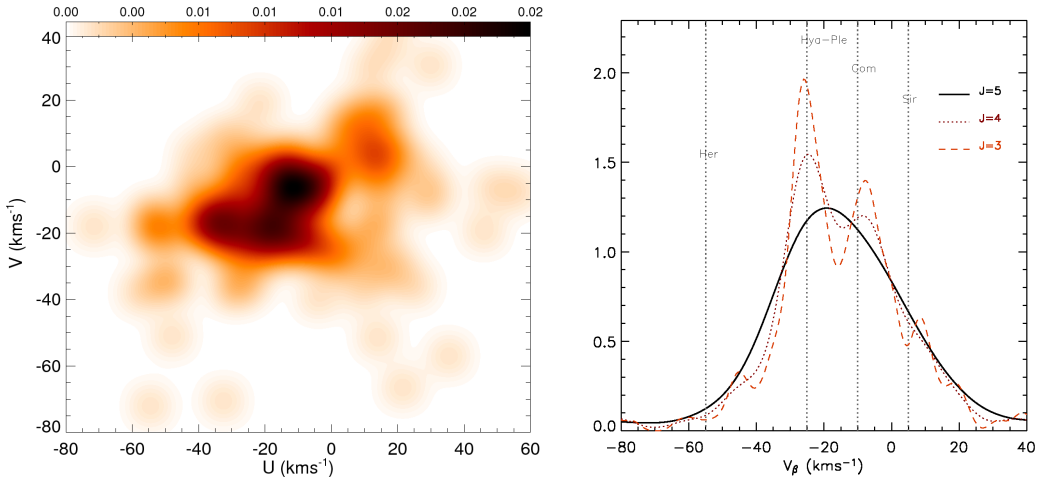

(a) active M-type stars

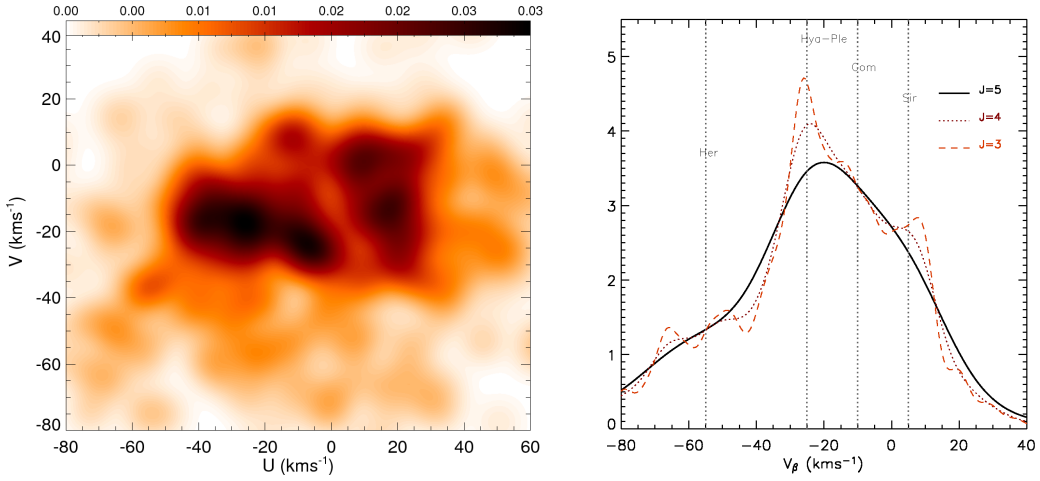

(b) non-active M-type stars

Figure 7.3: **Velocity distribution for different chromospheric activity.** Density field in the U–V plane obtained by WD with $J = 4$ (left) and density field for the V_β component with different values of J (right) for the subsamples of (a): active (182 stars) and (b): non-active (681 stars).

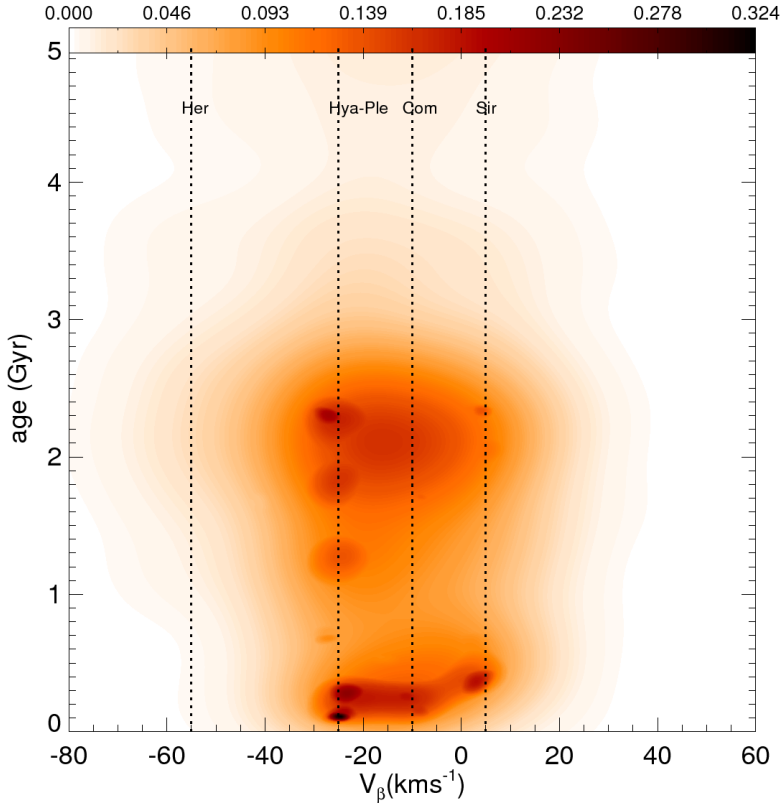

Figure 7.4: **Kinematic-age relation.** Density field in the V_β–*age* plane of the stars with $\epsilon_{age} \leq 30\%$ (7016 stars) obtained by WD.

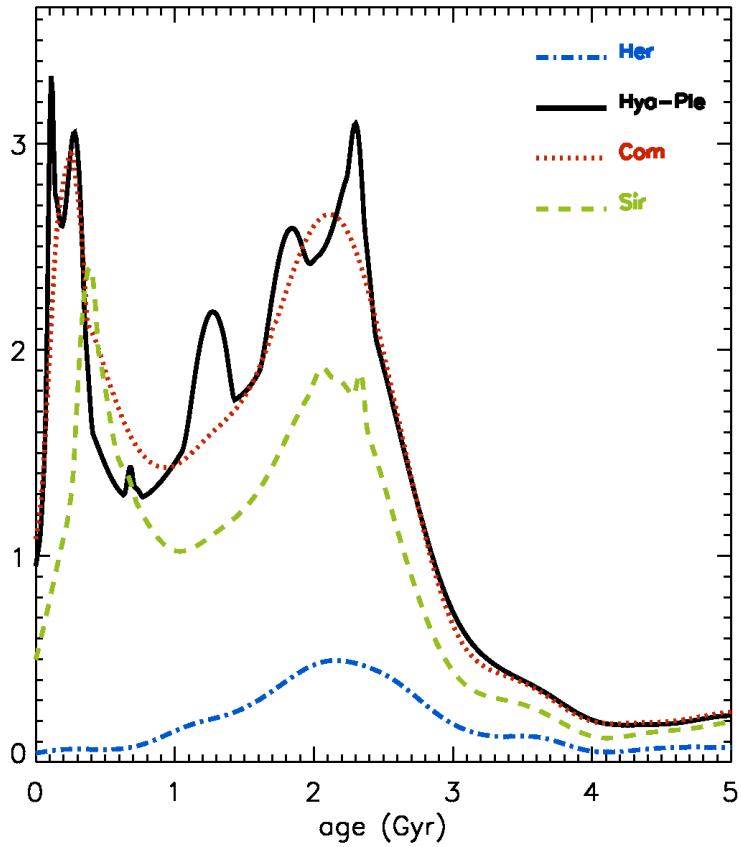

Figure 7.5: **Age distribution of the branches.** Density of stars in each branch as a function of age for stars with $\epsilon_{age} \leq 30\%$ (223, 1195, 1078 and 806 stars in the Hercules, Hyades-Pleiades, Coma Berenices and Sirius branches respectively).

of ages of more than 1 Gyr and its extended branch-like shape is seen in all subsamples with ages > 2 Gyr (Figure 7.2) where it reaches to a quite extended longitude.

- A clumpy distribution is observed inside the Hyades-Pleiades branch, with a periodicity in age of about 500-600 Myr, maintained at least in the 0-2.5 Gyr range. However, this periodicity is marginally significant[2] as the absolute error in age of some stars exceeds the period obtained. We point out that this periodicity should be contrasted in the future with the star formation rate obtained in Hernandez et al. (2000), where an oscillatory component of period ~ 500 Myr is found. For the other branches only an outline of the shape of the whole age distribution is observed.

[2]Notice that the periodicity is statistically significant in the sense of the discussion in Section 3.3 ($J = J_{plateau}$).

Chapter 8

$[Fe/H]$ of the kinematic structures

The study of the $[Fe/H]$ metallicity distribution of the stars along the branches and its relation to kinematics and age is restricted to the FGK dwarfs, which is the only sample for which metallicity data is available (see Table 5.1). In Table 8.1 we present the mean metallicity and dispersion values for each branch with stars selected as discussed in Section 6.2. The values obtained by Helmi et al. (2006), using the same sample but a different definition of the position of the kinematic structures, are included in the table for comparison (Coma Berenices was not included in that analysis). These authors found a common metallicity dispersion of 0.2 dex for all three superclusters. However, we obtain slightly lower mean metallicities for all the branches and a higher metallicity dispersion for the Hercules branch. Haywood (2006) pointed out that systematic biases in the data from Nordström et al. (2004) provoke an artificial increase in the $[Fe/H]$ dispersion at least for ages < 3 Gyr. As the four branches present a wide range of ages (Chapter 7), it will be assumed that this specific bias influences each of the branches similarly.

More importantly, in Figure 8.1 we present the distribution in the $[Fe/H]$–V_{rot} plane. Both the WD method and the rotation of the velocity components by 16° allow us to identify the four conspicuous branches and their rather wide range of metallicity. A general correlation can be seen: a more negative V_{rot} implies a higher mean metallicity[1]. Notice that the correlation is complex due to either the bimodality of the Hyades-Pleiades branch or to the fact that the Hercules branch does not follow the overall pattern of the three main branches.

The bimodality for the Hyades-Pleiades branch shows the peaks at $[Fe/H] \sim -0.05$ and $[Fe/H] \sim -0.15$. The metallicity distribution for the stars along the position that this branch traces in the U–V plane is studied in detail in Figure 8.2. We observe that the $[Fe/H]$ distribution evolves from the Hyades ($U_{rot} \sim -30\,\mathrm{km\,s^{-1}}$) with the peak at $[Fe/H] \sim -0.05$ –in agree-

[1]Notice that this correlation was not as clearly observed in Nordström et al. (2004) (see their Figure 32), despite using the same sample, which demonstrates the capabilities of the WD method and the rotation.

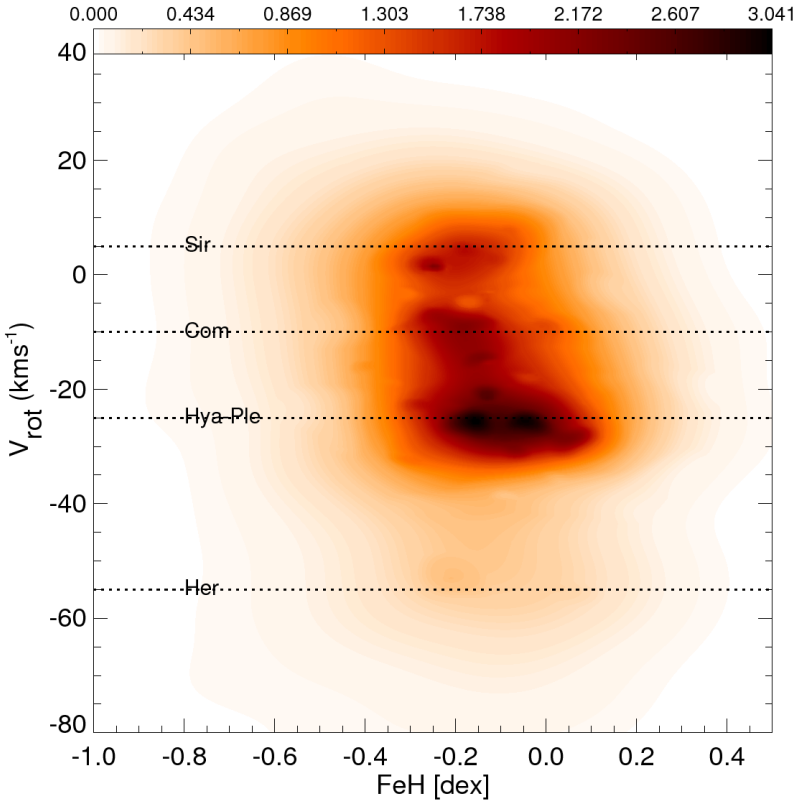

Figure 8.1: **Kinematic-metallicity relation of the branches.** Density field in the V_{rot}–$[Fe/H]$ plane for the sample with available $[Fe/H]$ (13109 stars) obtained by WD.

ment with the results of Famaey et al. (2007)– to the Pleiades, which placed at $U_{rot} \sim -5\,\mathrm{km\,s^{-1}}$ shows a peak at $[Fe/H] \sim -0.15$.

Figure 8.3 shows the distribution of the whole sample in the *age*–$[Fe/H]$ plane. Due to the complexity in the age-metallicity relation (see the exhaustive discussion on the biases in Haywood 2006) any new conclusion is beyond the scope of this thesis. Our analysis is restricted to a comparison between branches. Figure 8.4 shows the distributions in the *age*–$[Fe/H]$ plane for the stars along each of the four branches. To a first approximation these distributions exhibit the same general tendency as the whole sample. The WD treatment allows us to detect other significant features such as the clumps in age for the Hyades-Pleiades branch detected in Chapter 7 which show a decrease in $[Fe/H]$ with increasing age. For the range 1-3 Gyr, where more data is available, although it is preliminary, the slope of the Sirius distribution seems to be slightly more negative than for the other two main branches (from $\sim -0.10 \pm 0.01 dex/$ Gyr for Sirius to $\sim -0.07 \pm 0.01 dex/$ Gyr) for Hyades-Pleiades.

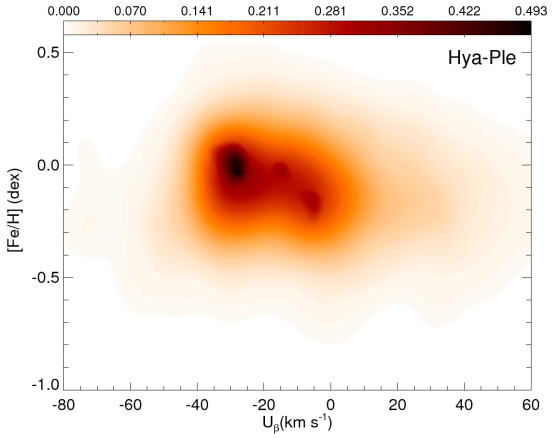

Figure 8.2: **Kinematic-metallicity relation for the Hyades-Pleiades branch.** Density field in the U_{rot}–$[Fe/H]$ plane obtained by WD for the Hyades-Pleiades (2271 stars).

Table 8.1: **Metallicity of the branches.** Mean metallicities and dispersions for the branches considered in the present work and for the superclusters according to (1) Helmi et al. (2006).

	Branches (this work)		Superclusters (1)	
	$\overline{[Fe/H]}$ (dex)	$\sigma_{[Fe/H]}$ (dex)	$\overline{[Fe/H]}$ (dex)	$\sigma_{[Fe/H]}$ (dex)
Hercules	−0.15	0.27	−0.13	0.2
Hyades-Pleiades	−0.11	0.20	−0.08	0.2
Coma Berenices	−0.16	0.22	...	
Sirius	−0.21	0.21	−0.18	0.2

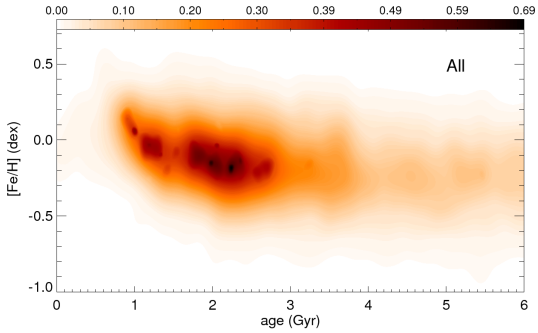

Figure 8.3: **Age-metallicity relation.** Density field in the *age*–$[Fe/H]$ plane for all stars with available metallicities and ages (11215 stars).

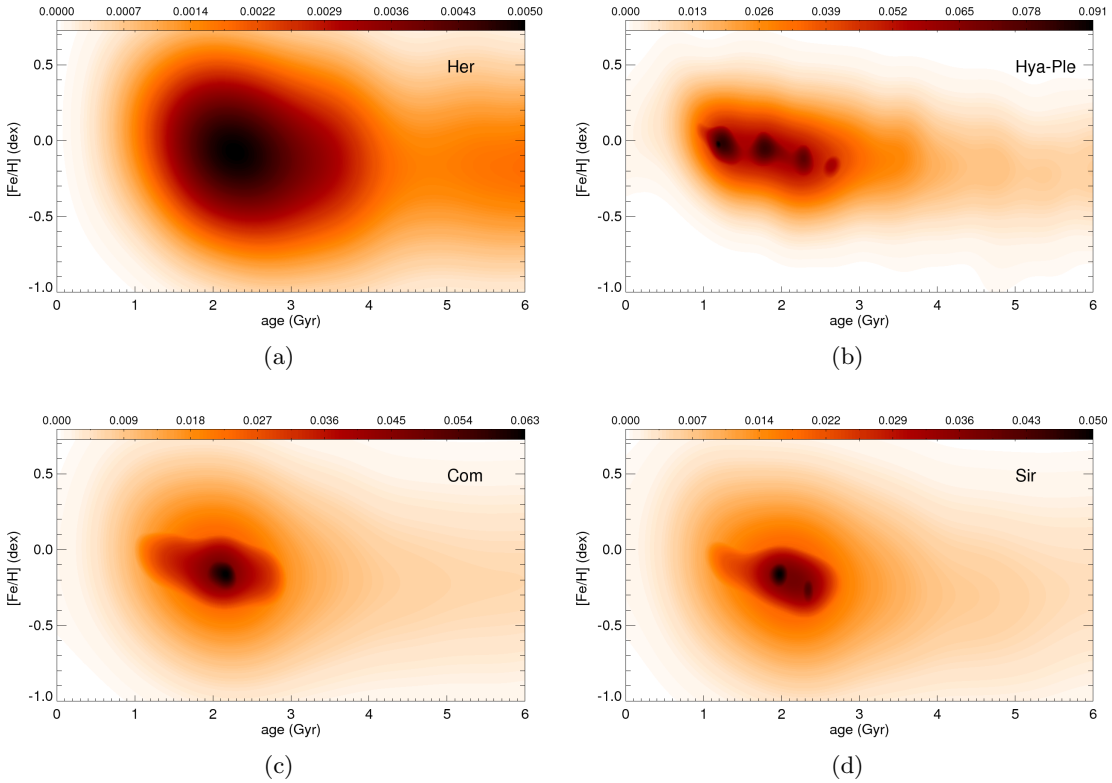

(a) (b) (c) (d)

Figure 8.4: **Age-metallicity relation of the branches.** Density field in the *age*–$[Fe/H]$ plane for the different branches obtained by WD. (a): Hercules(436 stars), (b):Hyades-Pleiades (1973 stars), (c): Coma Berenices (1559 stars), (d): Sirius (1229 stars).

Chapter 9

Summary and conclusions

Moving groups will happen to be a powerful tool for studying the large-scale structure and dynamics of the MW. In this part we have focused our analysis on establishing the observational constraints that will allow us to study the origin of these structures. We have applied multiscale techniques –wavelet denoising– to an extensive compendium of more than 24000 stars in the solar neighbourhood to characterise the observed kinematic structures in U–V–age–$[Fe/H]$ space. Whereas the accuracy in the kinematic data is unprecedented, metallicities and especially ages can lack the desired precision. However, it is the first time that a sample provides us with this exceptional number of stars with these physical parameters. Many of the age determinations have large errors but a cut-off by error allows us to work with the more reliable determinations.

While the advent of Hipparcos astrometric data led to the definitive recognition of a non-smooth distribution function of the solar neighbourhood, our results have corroborated this and gone one step further towards characterising the velocity distribution function. We have found that the branches that connect the classic moving groups in the U–V plane are the dominant structures. We have confirmed the existence of the Sirius, Coma Berenices, Hyades-Pleiades and Hercules branches. The first three branches are spaced at intervals of approximately 15 $\mathrm{km\,s^{-1}}$ with no significant variations with age or spectral type. The Hercules branch is located about 30 $\mathrm{km\,s^{-1}}$ from the Hyades-Pleiades branch. The four branches present a negative slope of $\sim 16^{\circ}$ in the U–V plane, lower than the one found by Skuljan et al. (1999). We identify new structures such as that centred at $(35, -20)\,\mathrm{km\,s^{-1}}$, which may be considered as part of the elongation of the Sirius or Coma Berenices branch.

On the other hand, we have studied the density drops in the U–V plane and the existence of abrupt edge lines have been corroborated. The drops are especially conspicuous at negative U and high V, and between the Hyades-Pleiades and the Hercules branches. Each branch presents a different density distribution in its extremes near these edge lines. For instance, the density

drop is considerably steeper for the Hyades-Pleiades branch in part due to the gathering of stars of the small substructures at one of the extremes. Moreover, the Hyades-Pleiades and Coma Berenices branches show a slightly asymmetric distribution, with a longer tail of stars at positive U. These features definitely rule out the classic idea of a smooth velocity field distribution.

The use of the same statistical method for the samples with different spectral types has allow us an exhaustive comparison between their kinematic planes. The branches are present in all distributions. Some of the well-known characteristics for different spectral type are observed in these distributions. The most important are the predominance of the Coma Berenices and Pleiades groups and the absence of the Hyades moving group for the OBA stars. These features are equivalent to what is observed for the age dependence (stars younger than 100 Myr). Another findings are first the kinematic overdensity in the middle of the Hyades-Pleiades branch for the KM giants sample which is not present for the FGK dwarfs. Second, we observe that the Hercules branch presents significant differences both in shape and in position of the kinematic density maximum. This shift is seen for all velocity distributions of stars from this subsample located further than 100 pc of the Sun. We can not conclusively ascertain whether it is due to the larger spatial extension of the KM giants subsample or whether it is a consequence of the distance determination method that could entangle kinematics and distances in a complex way. Although the subsample of M dwarf also shows this discrepancy in the position of the Hercules branch, we can not be conclusive due to the lack of statistics for this case.

We have also performed a study of the variations of the kinematic structures with Galactic position for the KM giant sample. The four branches are present in all regions studied but a significant change of contrast of the substructures inside the branches have been observed. The Hyades-Pleiades branch is the dominant structure in all the considered regions. The shape of the Hercules branch changes from region to another. It is more conspicuous for inner galactocentric radius, and for a region near the Sun in comparison to a region that is located further in the direction of rotation. All these considerations suggest a real dependence of the kinematic branches on Galactic position.

We have analysed the shape and signification of the kinematic structures in the U–V plane through age. Certain structures inside the branches change their contrasts when subsamples with different age ranges are considered. The clearest case is the Pleiades group that seems less significant in the $0.5 - 2.0$ Gyr range. On the other hand, the structure of branches is well traced up to the oldest samples. The Hercules one is progressively more conspicuous for the oldest cases in comparison to the Hyades-Pleiades branch. Contrary to other findings that claim the Hercules group has an elongated structure for stars with ages > 8 Gyr (Dehnen 1998), here the extended branch-like shape of Hercules is detected in all subsamples with ages > 2 Gyr. The chromospheric activity as age indicator for the M dwarf stars do not allow us to perform a

proper analysis as the number of stars per sample when active and non-active stars are analysed separately is too low.

For the first time, the age and metallicity distributions of the branches has been studied. We confirm an extended age distribution for all the branches. This suggests ruling out those models that propose that these kinematic structures are remnants of disc star clusters. The branches, however, have a different minimum age of their stars. While the Hyades-Pleiades and Coma Berenices branches have an important fraction of very young stars, Sirius has its first main peak for slightly older stars at ~ 400 Myr. We found a periodicity in age of about 500-600 Myr in the Hyades-Pleiades branch. As the absolute error in age of some stars exceeds the obtained period, this finding should be contrasted with more precise accurate. We point out that this periodicity should be contrasted in the future with the star formation rate obtained in Hernandez et al. (2000), where an oscillatory component of period ~ 500 Myr is found. For the other branches only an outline of the shape of the whole age distribution is observed.

A wide range of metallicity is found for each branch, especially for Hercules with a higher metallicity dispersion. The WD have revealed a complex relation between kinematics and metallicity. For the three branches of Hyades-Pleiades, Coma Berenices and Sirius the more negative the V components, the higher the mean metallicity. The Hercules branch does not follow the overall pattern of the three main branches. The metallicity of the Hyades-Pleiades branch shows a two-peak distribution ($[Fe/H] \sim -0.05$ and $[Fe/H] \sim -0.15$) which seem related to the kinematic groups of Hyades (more metallic) and Pleiades. Concerning the age-metallicity relations, differences are observed between branches although they all seem to exhibit the same general tendency as the whole sample. The periodic bumps in the age distribution for the Hyades-Pleiades branch show a decrease in metallicity with increasing age.

All the above observational results and, moreover, the whole set of distributions in the U–V–*age*–$[Fe/H]$ space presented here, are the fundamental elements necessary to check the present and future dynamical models proposed for the formation of kinematic structures. While some of these current models already explain some of the observational results, other observed features remain unexplained. For instance, the simulations of De Simone et al. (2004) produce branches with a slope which fits that measured here. However, features such as the periodic clumps in the age distribution of the Hyades-Pleiades branch demand an in-depth explanation. To make further progress in this field, simulations obtained from orbit integration under a model for the Galactic potential have been undertaken (Parts IV and V). The application of the same statistical technique to both the observed and simulated data will allow a direct comparison between them, conforming a powerful test of the models for the formation of the structures. This comparison may eventually offer a physical interpretation of the formation of the kinematic structures in terms of the MW large-scale dynamics.

Part IV

TEST PARTICLE SIMULATIONS

Part IV is concerned with the methodology of our test particle simulations. We have built a test particle simulation method that considers a great variety of initial conditions and integration times and procedures. These attempt to represent stars born at different times and with different kinematic conditions, like those in the solar neighbourhood. On the other hand, we have taken advantage of the PM04–MW potential model which is a specific model for the MW potential that includes bar and spiral arms (Pichardo et al. 2003b, 2004). This new model is very flexible to be adapted to the observations and it has been tuned to be consistent with several recent observational constraints. It is built directly with a realistic 3D mass distribution from which the gravitational potential and the forces are derived. To our knowledge, the study of the effects of a mass distribution model, and in particular of this new model, on the local velocity distribution has not been considered before. On the other hand, we have also implemented a method to ascertain the regularity of the orbits conforming the kinematic structures created in the test particle simulations. In Part V we apply all this methodology in order to evaluate the role of realistic non-axisymmetric components of the MW, namely the spiral arms and the bar, on the formation of moving groups in the disc.

First, Chapter 10 provides a description of the simulation method and the initial conditions. We present also the method for quantifying the regularity of the orbits. Finally, this chapter examines the advantages and drawbacks of this method as it is compared with other theoretical approaches used in the subject. Chapter 11 describes the essential characteristics of the potential model and also is concerned with contrasting this with other widely used models specially emphasising their force fields.

Chapter 10

Simulation method

10.1 General description of the simulations

In order to study the effect of the non-axisymmetric Galactic structure on the kinematic distribution of the disc and in particular of the solar neighbourhood, numerical integrations of test particle orbits on the Galactic disc have been performed. The method is outlined in Figure 10.1. It consists of integrating the orbits of a set of test particles distributed in a disc with certain initial conditions IC (Figure 10.1a) under a potential model for the MW (Figure 10.1b). The IC are described in Section 10.2. The potential model (PM04–MW potential model) is introduced in Chapter 11. It is three-dimensional and it consists of an axisymmetric part and the non-axisymmetric components (bar and spiral arms). The integration of each particle is initialised at a time value $t = -\tau$ (as a convention) and ended at t= 0, being τ the particle exposure time to the non-axisymmetric potential. After the integration, the final phase space of the disc at $t = 0$ is obtained and studied (Figure 10.1c). In particular, the induced kinematic distribution at the end of the simulation is analysed using the particles inside spheres of radius 500 pc centred at the solar position and at other regions of the disc (Figure 10.1d). Finally these predicted velocity distributions and the observed one (Part III, Figure 6.1) are compared. We use the galactocentric cylindrical coordinates (R,ϕ,z) as well as the Cartesian XY system which are defined in Section 1.4. Initially it will be assumed that the solar position is at $\phi = 0°$, $R = R_\odot \equiv 8.5\,\mathrm{kpc}$ and $z = 0$ ($X = 0$ and $Y = 8.5\,\mathrm{kpc}$). The peculiar velocities U, V, W are also used and defined in Section 1.4. It is worth mentioning that in the previous Part III the notation U, V, W indicated heliocentric velocities, in this part and Part V they indicate peculiar velocities, that is with respect to the RSR as explained in Section 1.4.

The integration of the motion equations is done with the Bulirsch-Stoer algorithm of Press et al. (1992), conserving Jacobi's integral within a relative variation of $|(E_{Ji} - E_{Jf})/E_{Ji}| \approx 10^{-9}$.

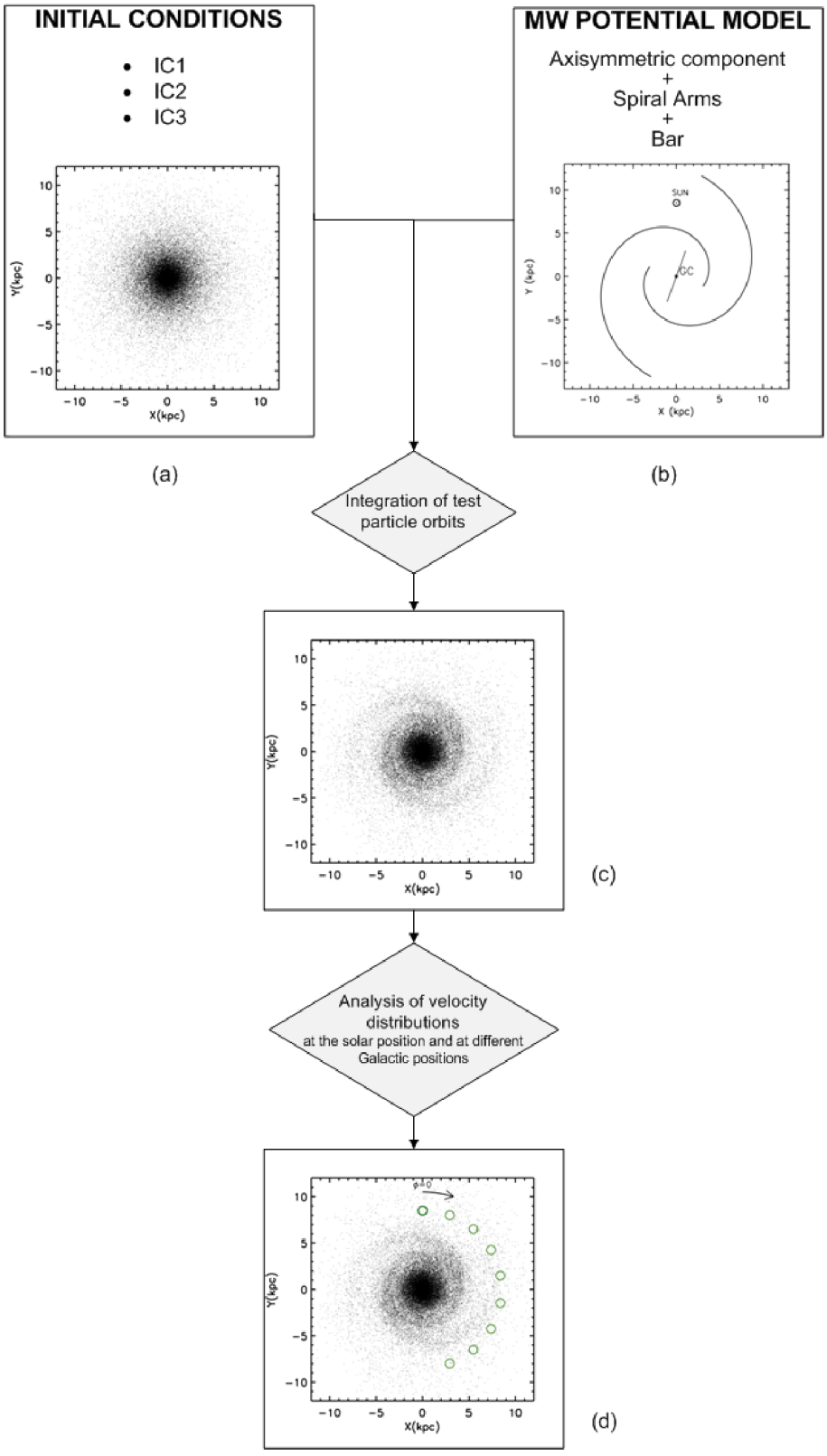

Figure 10.1: **Diagram of the simulation method.**

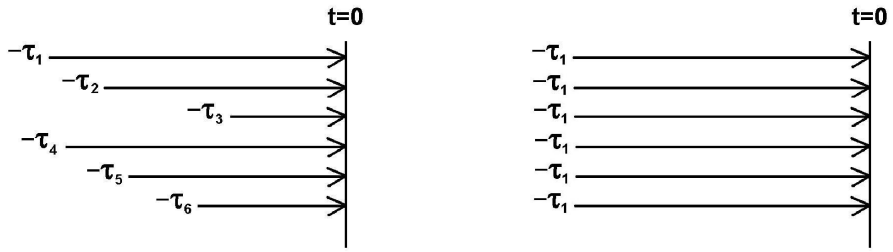

(a) Procedure 1 (b) Procedure 2

Figure 10.2: **Sketch of the different time integration procedures.**

The reference frame used for the calculations is the rotation frame of the spiral arms when only this non-axisymmetric component is considered and the one of the bar otherwise (model with only bar and model with both bar and spiral arms). The number of particles in each simulation is about several million. The symmetries of the Galactic potential ($\Phi(R,\phi)$=$\Phi(R,180^\circ+\phi)$) allows us to double the number of particles in each sphere. In all cases, we check that the number of particles in the final distributions of a particular region (sphere of 500 pc) is large enough (~ 10000) to be statistically robust.

Two different integration procedures are used. The first one (Procedure 1) is schematised in Figure 10.2a. In this procedure, each particle is exposed to the non-axisymmetric components for a time τ chosen at random between two certain values. In particular, τ is chosen between 0 and 2 Gyr as default values. This maximum integration time corresponds approximately to 7 and 15 revolutions of the spiral arms and the bar, respectively (considering for their pattern speeds the general values of $\Omega_{sp} = 20\,\mathrm{km\,s^{-1}kpc^{-1}}$ and $\Omega_b = 45\,\mathrm{km\,s^{-1}kpc^{-1}}$ for the spiral arms and the bar, respectively; see Chapter 11). However, we do not exclude the option of varying these values in Part V. With this procedure, we obtain final velocity distributions resulting of a superposition of particles integrated different times, resembling up to a certain point the real observed distribution with a superpositions of stars of different ages. In Figure 10.2b Procedure 2 is outlined. In this case the integration time is fixed at a certain τ for all particles. The particular default values for τ in this case is $\tau = 400\,\mathrm{Myr}$ corresponding approximately to 1.3 and 3 spiral arm and bar revolutions for the above mentioned pattern speeds. With this procedure and this integration time, we can study the relatively rapid induced effects of the non-axisymmetric components on the local kinematics.

The integration time in our simulations pretends to consider only the last stages in the Galaxy evolution. This late evolution was affected or even dominated by secular dynamical processes. For example Klypin et al. (2009) showed using N-body simulations with different codes that, for certain characteristics of the disc and the halo, bars do not show a tendency to

slow down significantly once they have been form. In general we will avoid longer integration times (larger than 2 Gyr) because they might require to include considerable Galactic evolution like bar weakening or transient arms, as well as the effect of external perturbations to the MW disc, perhaps masking the effect of the current MW structure. Although the effects of a time-varying bar or spirals and the external effects would would be worthy of being studied, it is out of the scope of the thesis. Therefore we focused on the recently induced kinematic structure in the solar neighbourhood. However, in some cases longer integration times will be taken in order to carry out particular exercises.

10.2 The initial conditions

One of the strong points of our method is the variety in initial conditions. We explore three different types of initial conditions: IC1, IC2, and IC3. The stellar disc density is assumed to be axisymmetric. In our PM04–MW potential model the density of the disc corresponds to the Miyamoto-Nagai disc but the in-plane distribution for all IC is approximated to follow an exponential profile:

$$\Sigma(R) \propto e^{-R/R_\Sigma} \tag{10.1}$$

with a given scale length R_Σ, which is taken to be $R_\Sigma = 2.5\,\mathrm{kpc}$ also for all IC (Freudenreich 1998)[1]. The exponential density profile has been observed in the MW and in other galaxies (see e.g. Binney & Tremaine 2008, Freeman 1970) and are commonly considered in the generation of IC (Hernquist 1993). It has also helped us to simplify considerably the generation of IC and specially Equation 10.7 of the asymmetric drift (see below). In Appendix A we have evaluated the effect of having a different initial density profile or scale length on the final kinematic structures created by the bar and the spiral arms, concluding that the results are not significantly sensitive to it. The vertical profile follows a $\mathrm{sech}^2[z/z_s]$ law with a given scale height z_s which depends on the particular IC.

For our density distribution it is not straightforward to derive a consistent DF. Sometimes even if the DF can be obtained it is not unique Binney & Tremaine (2008). In the method that we use to generate the initial discs, the density field is generated exactly and the velocity field is approximated using the collisionless Boltzmann equation to obtain moments of the DF without recovering the complete DF. The default detailed disc scales, kinematic properties, integration procedure and integration times for each IC are summarised next and in Table 10.1.

[1]This scale length is also very similar to the 2.53 kpc adopted in the Besançon Galaxy Model of Robin et al. (2003) for the stars of the thin disc. The value is also similar to the scale length of the thin disc found by Jurić et al (2008) (2.6 kpc) using observations of the SDSS

Table 10.1: **Properties of each type of IC.** Summary of the structural, kinematic and integration times of the different IC of the thesis.

	MOTIVATION	DISC STRUCTURE	VELOCITIES	INTEGRATION TIME
IC1	continuous and uniform birth of stars in a cold disc	$R_\Sigma = 2.5\,\mathrm{kpc}$ $z_\rho = 50\,\mathrm{pc}$	Gaussian distribution constant for all radii $\sigma_U = \sigma_V = 5\,\mathrm{km\,s^{-1}}$ $\sigma_W = 2\,\mathrm{km\,s^{-1}}$	random for each particle [0 Gyr – 2 Gyr] (Procedure 1)
IC2	rapid induced effects on intermediate populations	$R_\Sigma = 2.5\,\mathrm{kpc}$ $z_\rho = 300\,\mathrm{pc}$	moments of the collisionless Boltzmann Eq. σ_U radial exponential profile $\sigma_U(R_\odot) \sim 20\,\mathrm{km\,s^{-1}}$ $\sigma_W \sim 8\,\mathrm{km\,s^{-1}}$	400 Myr (Procedure 2)
IC3	- old populations (between thick and thin disc) - dark disc?	$R_\Sigma = 2.5\,\mathrm{kpc}$ $z_\rho = 500\,\mathrm{pc}$	as IC2 but: $\sigma_U(R_\odot) \sim 40\,\mathrm{km\,s^{-1}}$ $\sigma_W \sim 25\,\mathrm{km\,s^{-1}}$	400 Myr (Procedure 2)

–IC1–

With this IC we aim to simulate the birth of stars in the disc with small velocity dispersion and the effect of having stars with different ages (different integration times) at the final velocity distributions. The disc has a small scale height of $z_\rho = 50\,\mathrm{pc}$ and it is constant through all the disc. This value can be compared with the scale height that is defined by the younger open clusters (Zhu 2009). The initial velocity distribution relative to the RSR is adopted as a Gaussian with low dispersions $\sigma_U = \sigma_V = 5\,\mathrm{km\,s^{-1}}$ and $\sigma_W = 2\,\mathrm{km\,s^{-1}}$ and constant for all radii (see Figures 10.3a and 10.3b). These values are similar to the induced gas velocity dispersions in the plane and in the vertical direction due to Galactic spiral shocks according to Kim (2009) and to the dispersion of the youngest Hipparcos stars (Aumer & Binney 2009). The distributions of the U and V components of a group of particles near the solar radius ($R = R_\odot \pm 0.5\,\mathrm{kpc}$) is shown in Figure 10.4. This type of IC is integrated with Procedure 1 (Section 10.1)[2].

[2] N-body disc simulations assuming a low Q parameter (e.g. Thomasson et al. 1991) show that a configuration with strong spiral arms and low velocity dispersion can be sustained for at least 7 disc revolutions. The conditions of these experiments are similar to our integrations with spiral arms using IC1.

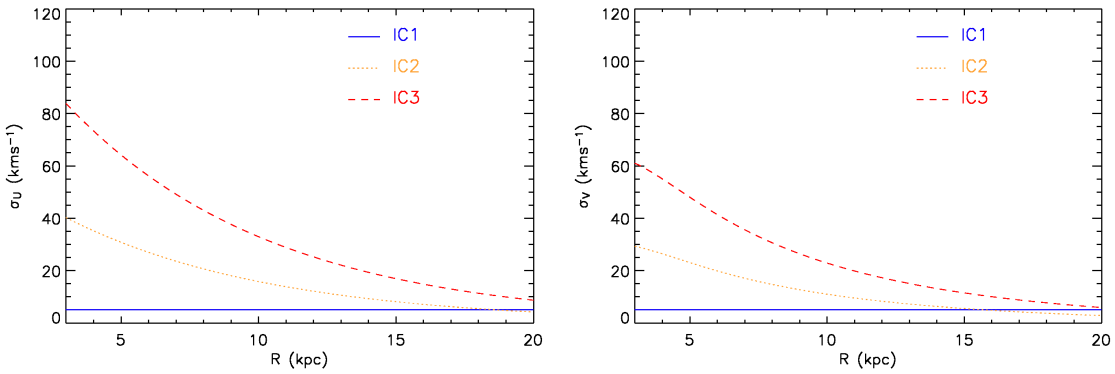

(a) Radial velocity dispersion σ_U (b) Tangential velocity dispersion σ_V

Figure 10.3: **Radial profile of the velocity dispersions.**

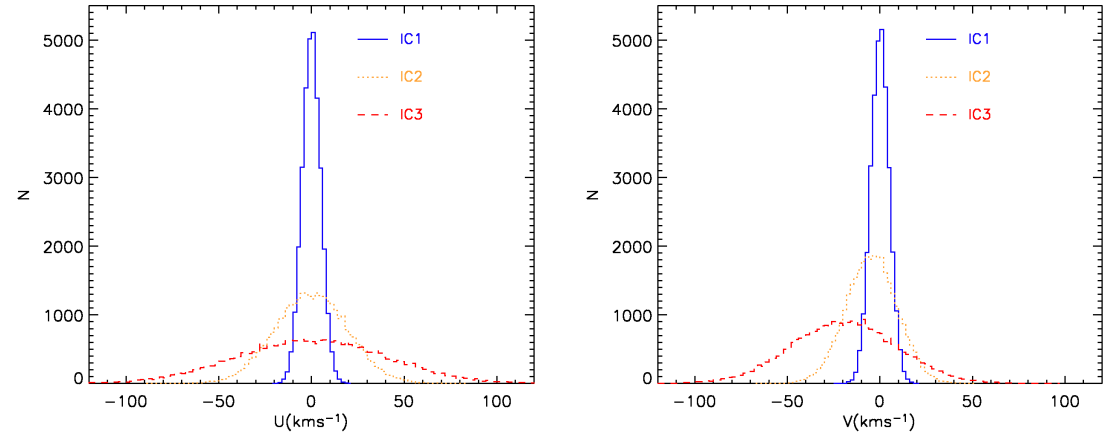

(a) (b)

Figure 10.4: **Initial velocity distributions of the discs.** Initial velocity distributions for each IC for ∼30000 test particles in the solar ring (8-9 kpc) for the components (a) U and (b) V.

–IC2–

In this case the chosen DF confers to the IC2 disc the properties of an intermediate population of the MW thin disc in terms of the age. The integration follows Procedure 2 and therefore, with these IC, we can study the relatively rapid induced effects of the non-axisymmetric component on the local intermediate kinematics. For these IC, the phase space DF of an axisymmetric disc is constructed, as discussed in Hernquist (1993), using the moments of the collisionless Boltzmann equation simplified by the epicyclic approximation and sometimes complemented by observed characteristics of the MW or external disc galaxies.

For the vertical distribution a scale height of $z_\rho = 300\,\mathrm{pc}$ is used. This value is adopted to be constant with R. This was classically taken as an assumption as it was supposedly observed in external galaxies (van der Kruit & Searle 1981). We will adopt this idealisation although more recent studies have shown that this value does vary with R in external galaxies and also in the MW (see studies of the flare in López-Corredoira et al. 2002).

In determining the velocity distribution of this density structure, we use the second order moments σ_U, σ_V, σ_W and the tangential streaming velocity (asymmetric drift). Once the density profile has been established (exponential disc in this case), the lowest order moments of the collisionless Boltzmann equation are determined and the velocity distribution can be approximated by these moments. Isothermal sheets (discs with $\sigma_W \neq f(z)$) have been proved to be a first approximation through an accurate description of disc galaxies (van der Kruit & Searle 1981, Hernquist 1993). For an isothermal sheet and with the constant scale height z_ρ supposition, the Poisson and Lioville equations are solved to give a vertical profile of:

$$\rho(z) = \rho_0 \mathrm{sech}^2 \frac{\mathrm{z}}{\mathrm{z}_\rho} \tag{10.2}$$

where ρ_0 is the spatial density in the plane and:

$$z_\rho = \frac{\sigma_W}{(2\pi G \rho_0)^{1/2}} \tag{10.3}$$

(see e.g. Hernquist 1993). At large distances from the plane, the vertical density falls off close to exponentially. By contrast, close to the plane it is nicely rounded over and the density changes smoothly when crossing from negative to positive z.

With the assumption of constant z_ρ with R, Equation 10.3 gives a radial exponential profile for the vertical velocity dispersion:

$$\sigma_W \propto \Sigma(R)^{1/2} \propto e^{-R/2R_\Sigma}. \tag{10.4}$$

Following Dehnen (1999), we will adopt $\sigma_U^3 \propto \Sigma$, and therefore, the radial velocity dispersion

has an exponential profile[3]:

$$\sigma_U(R) = \sigma_0 e^{-R/3R_\Sigma}. \tag{10.5}$$

The scale length for σ_U is therefore $3R_\Sigma = 7.5\,\mathrm{kpc}$.

The tangential velocity dispersion profile is obtained using the following expression derived from the epicyclic approximation:

$$\frac{\sigma_V^2(R)}{\sigma_U^2(R)} = \frac{\kappa^2}{4\Omega^2} = \frac{-B}{A-B} \tag{10.6}$$

(Equation 4.317 in Binney & Tremaine 2008) where κ is the epicyclic frequency, A and B are the Oort's constants and Ω is the angular frequency (in our case they all can be calculated for the axisymmetric part of the model which is described in Chapter 11).

Also it is relevant one of the first moments of the collisionless Boltzmann equation (or Jeans radial equation) that, under the assumptions that the disc is stationary, axisymmetric and symmetric about its equator, is:

$$\begin{aligned} \sigma_V^2 - \sigma_U^2 - \frac{R}{\Sigma}\frac{\partial \Sigma \sigma_U^2}{\partial R} - R\frac{\partial \sigma_{UW}^2}{\partial z} &= V_c^2 - \overline{V}_\phi{}^2 \\ &= (V_c - \overline{V}_\phi)(V_c + \overline{V}_\phi) \\ &= v_a(2V_c - v_a) \\ &\simeq v_a 2V_c, \end{aligned} \tag{10.7}$$

(Equation 4.227 in Binney & Tremaine 2008[4]) where V_c is the circular speed and $\overline{V}_\phi$ is the mean galactocentric tangential velocity of the population. Note that V_ϕ is different from V which is measured with respect to the RSR. Equation 10.7 gives an expression for the asymmetric drift v_a. Considering that the last term of the left-hand side vanishes under the assumption that the orientation of the velocity ellipsoid remains aligned with the coordinate axes, and using Equations 10.1, 10.5 and 10.6, it can be obtained:

$$v_a = V_c - \overline{V}_\phi = -\overline{V} = \frac{\sigma_U^2}{2V_c}\left(\frac{-B}{A-B} - 1 + R\,(1/R_\Sigma + 2/3R_\Sigma)\right). \tag{10.8}$$

[3] Indeed provided that the ratio σ_U/σ_W is constant with R (uniform anisotropy), the radial velocity dispersion would satisfy $\sigma_U \propto \Sigma(R)^{1/2}$ and the radial velocity dispersion profile would also be $\sigma_U \propto e^{-R/2R_\Sigma}$. Old observations of the MW (Lewis & Freeman 1989) shown that indeed the observed radial velocity dispersion decays exponentially with R with a scale length consistent with the factor $2R_\Sigma$ with R_Σ obtained through independent measures of the density profile. Consequently, the uniform anisotropy was proved to be a good assumption and it could be explained as a result of the velocity dispersion being consequence of secular processes that affect both W and U (van der Kruit & Searle 1982). All these assumptions are somehow controversial and still in the theoretical development for isothermal sheets with constant scale height. Recently, in Binney et al. (2010) it is finally adopted $\sigma_U(R) \propto e^{-R/2.2R_\Sigma}$ for the standard DF that fits density and velocity distributions for stars near the Sun and above the plane.

[4] We have substituted the volume density ν in that study for the in-plane density Σ as for our discs with $\nu \propto f(R)g(z)$ is equivalent.

According to this expression, distinct populations (with distinctive ages or colours) which have different velocity dispersion of the U component, have different mean tangential velocity $\overline{V}_\phi$, being the larger the σ_U, the more rotational lag with respect to the RSR. Again the initial velocity distribution relative to the RSR is adopted as Gaussian with the above dispersions and the value of the asymmetric drift of Equation 10.8.

The local normalisation is chosen $\sigma_U(R_\odot) \sim 20\,\mathrm{km\,s^{-1}}$ and the complete radial profile is shown in Figure 10.3a. With this normalisation, the tangential velocity dispersion at solar radius is $\sigma_V(R_\odot) \sim 14\,\mathrm{km\,s^{-1}}$ according to Equation 10.6 and also in agreement with the previous literature. The complete profile is shown in Figure 10.3b. The asymmetric drift v_a of Equation 10.8 as a function of radius for our axisymmetric part of the model (Chapter 11) is shown in Figure 10.5. At solar radius it is $v_a(R_\odot) = 4.4\,\mathrm{km\,s^{-1}}$. The distributions of the U and V components of a group of particles in the solar radius ($R = R_\odot \pm 0.5\,\mathrm{kpc}$) is shown in Figure 10.4. Finally, the normalisation of the vertical velocity distribution is chosen to be $\sigma_W(R_\odot) = 8\,\mathrm{km\,s^{-1}}$.

Although we do not pretend to model a certain population of the MW, the scale height, the local normalisations of the velocity dispersions or the asymmetric drift of these IC2 would be consistent with the corresponding to a population of $\sim 1\,\mathrm{Gyr}$ of the thin disc in the *age–density–velocity dispersion–scale height* relations of the Besançon Galaxy Model of Robin et al. (2003) (see their Table 2). The scale height is also compatible with the one given by recent observations of the MW thin disc (Jurić et al 2008). Despite the discrepancies about the actual age–velocity dispersion relation in the literature, several studies have found observational evidences for radial velocity dispersions σ_U of $\sim 20\,\mathrm{km\,s^{-1}}$ in populations of $\sim 1\,\mathrm{Gyr}$ in the solar neighbourhood (Holmberg et al. 2007) or only slightly larger (Soubiran et al. 2008). Our chosen vertical velocity dispersion is also similar to the observational study by Holmberg et al. (2007) for a population with this σ_U and ages around 1 Gyr.

–IC3–

They are constructed as in IC2 but with different values for the parameters that confer to these IC the characteristics of an old population of the thin disc or a population between the thin and the thick disc. The integration procedure is Procedure 2 as in IC2. A higher scale height $z_\rho = 500\,\mathrm{pc}$ is used now. Also, we employ higher velocity dispersions with a local normalisation of $\sigma_U(R_\odot) \sim 40\,\mathrm{km\,s^{-1}}$ ($\sigma_0 = 125\,\mathrm{km\,s^{-1}}$). This gives $\sigma_V(R_\odot) \sim 28\,\mathrm{km\,s^{-1}}$ and $v_a(R_\odot) = 19\,\mathrm{km\,s^{-1}}$. The radial profiles are shown in Figures 10.3a and 10.3b. The distributions of the U and V components of a group of particles in the solar radius ($R = R_\odot \pm 0.5\,\mathrm{kpc}$) are shown in Figure 10.4. Finally, we adopt a dispersion of $\sigma_W = 25\,\mathrm{km\,s^{-1}}$ at $R = 8.5\,\mathrm{kpc}$.

For this range of velocity dispersion the discrepancies about the actual age–velocity dispersion

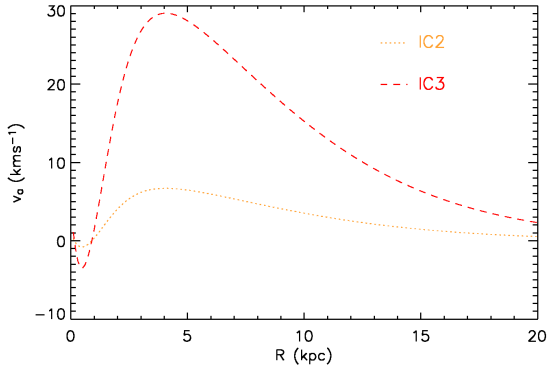

Figure 10.5: **Asymmetric drift as a function of radius.**

relation are more evident in the literature. Some studies have found velocity dispersions of $\sim$ 40 km s^{-1} for populations with ages $\sim$ 6 Gyr (Holmberg et al. 2007) whereas other authors found that this velocity dispersion corresponds to populations approximately $\gtrsim$ 3.5 Gyr (Soubiran et al. 2008). In the Besançon Galaxy Model of Robin et al. (2003) our chosen scale height would correspond to a population with ages $\sim$ 3 Gyr. Our velocity dispersions are similar to the value corresponding to the old population up to $z = 500$ pc of Fuchs et al. (2009).

The (σ_U, σ_V,σ_W) are slightly smaller than the measured for the thick disc. For instance Bensby et al. (2007a) used (67, 38, 35) km s^{-1} or Robin et al. (2003) used larger values (67, 51, 42) km s^{-1}. The values found by Soubiran et al. (2003) were (63, 39, 39) km s^{-1}. Regarding the scale height of the thick disc, values such as 900 pc are found (Jurić et al 2008). The model by Robin et al. (2003) uses 800 pc. On the other hand, recent studies of galaxy formation of MW mass predict that a flattened dark matter structure mirroring the stellar thick disc structural and kinematic properties will form in a Λ-CDM Universe (Bruch et al. 2008, Read et al. 2008). Therefore, these IC3 are also approximately consistent with particles in the thick disc and in the dark disc.

General discussion

As it is not straightforward to obtain and normalise higher moments of the velocity distribution, we have considered the moments of the velocity distribution only up to second order. Higher order moments are indeed very difficult to measure all through the MW disc. On the other hand, the validity of the epicyclic approximation for large velocity dispersions is somehow doubtful. As discussed in Hernquist (1993), these approximations can break down near the centres of the discs, specially due to the derivative of the radial velocity dispersion in Equation 10.7. In

general, the nature of the dispersions in the central part of a disc is not well understood yet, either observationally or theoretically. Whereas some authors includes a softening of the radial velocity dispersion profile near the centre, here we keep the initial dispersion profiles and avoid the central particles in our simulations when necessary. As it will be seen, in the vast majority of cases, the particles that finally reach the solar radius do not come from such inner radius where the approximations are more dangerous. In Appendix A we discussed whether these aspects could suppose a limitation for our study, concluding that only for our hottest disc (IC3) the effects of these approximations are conspicuous in our simulations. In particular for these specific kinematic conditions these approximations favour eccentric orbits in the central region of the disc that tend to reach the solar radius. This will be discussed in the corresponding chapter where these IC are used as tracer of the phase space (Chapter 15).

Other studies in this field used IC derived from a specific phase-space DF but at the cost of using highly simplified potential models very different to the realistic PM04–MW potential model used here. For instance, in Chakrabarty (2007) a warm quasi-exponential disc with a flat rotation curve was used following Evans & Read (1998). This has been constructed adapting power-law discs $\Sigma \propto R^{-(\beta+1)}$ ("doubly cut-out power-law distribution functions") which have been shown to possess simple self-consistent DF that is obtained directly (Evans & Read 1998, Binney & Tremaine 2008). Dehnen (2000) used also an equilibrium disc described by a simple DF that approximately reproduced prescribed surface density and velocity dispersion exponential profile with R. Again the use of the power-law potentials simplified the method. In this case the DF of a warm disc was obtained in Dehnen (1999) by warming up the DF for a completely cold disc (all stars with circular orbits). With our method we do not obtained simple and complete DF but it can be applied to realistic MW models such as the PM04–MW potential model. Currently, some studies are exploring novel methods of IC generation such as made-to-measure (M2M) algorithm consisting of N-body realisations of equilibrium stellar systems (De Lorenzi et al. 2007). We do not exclude the use of these techniques in the future.

The initial conditions IC1, IC2 and IC3 consist of very idealised discs that do not pretend to be strict models of the MW. For instance, we do not have into account observed phenomenas such as the increase of the asymmetric drift and of the velocity dispersions σ_U, σ_V and σ_W with height, the vertex deviation or the tilt of the velocity ellipsoid toward the plane (Fuchs et al. 2009). In general, the vertical distribution of our discs is still very unreliable as it has been obtained supposing an isothermal sheet[5]. We do not have into account the flare of the Galaxy. In the case of IC1 we do not consider a more realistic star formation scenario such as star formation concentrated in the spiral arms, non-uniform star formation with time or large peculiar motions

[5]This aspect will not be critical as the vast majority of our simulations will be carried out in the plane ($z = 0$) as explained in Chapter 12.

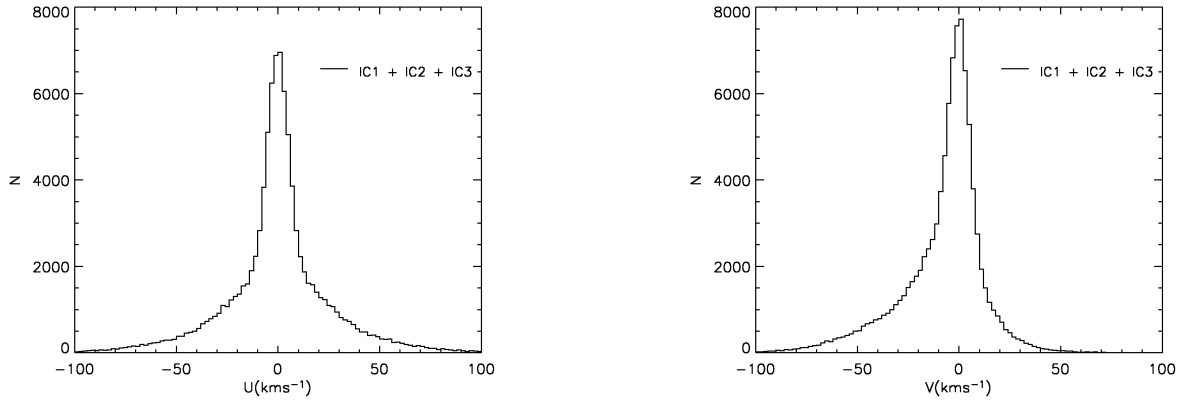

(a) (b)

Figure 10.6: **Kinematic distributions of the discs superposition.** Initial U (a) and V (b) distributions for the naive superposition of the three types of IC (IC1+IC2+IC3) for ∼90000 test particles in the solar ring (8-9 kpc).

of star forming regions (Baba et al. 2009). Nevertheless, these three types discs are provide suitable initial conditions to deal with this thesis aims, allowing us to study the general effects of the spiral arms and the bar in the velocity distribution and the mechanisms that create the moving groups. The real disc of the MW is for sure formed by a much more complex distribution but in a very first approximation it would look like a superposition of several types of IC as the ones proposed in this section (young, intermediate and old populations). To be rigorous, a kind of density percentages to each population should be apply before the superposition. Here, probably unrealistically but as a simple exercise, in Figure 10.6 we show the superposition of IC1, IC2 and IC3 which now, in general terms, is similar to the observed distribution in the solar neighbourhood, except of course the observed substructure (Part III).

To conclude, the choice of appropriate initial conditions is somewhat controversial. Traditionally they are motivated by self-consistency with the present stage of the Galactic disc structure. However, current scenarios of galaxy formation and evolution predict that both external and internal perturbation mechanisms affect the disc kinematics. Moreover, the initial conditions hardly consider the evolution of the MW. Our short integration times try to deal in part with all these issues. Also, using our variety of IC we consider for the first time initial conditions and integration times that attempt to represent stars born at different times and with different kinematic conditions, like those in the solar neighbourhood.

10.3 Quantifying the regularity of the orbits

To support the test particle simulations, a method to quantify the regularity of the orbit corresponding to each point of the U–V plane for a given position of the Galactic disc is used in this thesis. In this section we provide a description of the method which is based on the method used in Quillen & Minchev (2005), applied to a spiral arm model in that case (see Section 10.4). The method is, for the moment, designed to be applied for orbits in the plane.

The orbital regularity corresponding to each (U,V) is computed easily through measuring the dispersions in positions and velocities at the moment that the orbits crosses a given axis of the X'–Y' plane (the reference system that rotates with the non-axisymmetric component[6]). Orbits with small dispersions can be considered more periodic or closed than orbits with large dispersions. Although there are more sophisticated methods to calculate the orbital regularity (e.g. Lyapunov exponents used in Fux 2001, see Section 10.4), this one is easy to implement and has lower execution time. The exact procedure used here is the following:

1. A grid of points in the U–V plane in the range $[-100, 100] \times [-100, 100]\,\mathrm{km\,s^{-1}}$ every $2\,\mathrm{km\,s^{-1}}$ is constructed. This value has been found to be a good compromise between computing time and resolution.

2. For every point of the grid (U,V), the orbit of a test particle with this velocity and located exactly at a given position in the X'–Y' configuration space at $t = 0$ (by default at the solar position with $R = 8.5\,\mathrm{kpc}$ and $\phi = 0°$, but also at other positions) is integrated forward in time from $t = 0$. In contrast to Quillen & Minchev (2005), here the dispersions will be computed in two different arbitrary axis: $X' > 0$ and $Y' > 0$ of the rotating frame of the non-axisymmetric component. The integration stops when at least one of these axes has been crossed 10 times or if the total integration time exceeds 100 Gyr. The same model for the Galactic potential (PM04–MW potential model) and the same method for the integration of the equations of motion as in the test particle simulations (Section 10.1) are used.

3. We compute the dispersions in radius R, in galactocentric radial velocity V_R and in galactocentric tangential velocity V_ϕ (in the reference system that rotates with the non-axisymmetric component) of the phase space points at the moment that the orbit crosses the $X' > 0$ and $Y' > 0$ axes in the clockwise and/or counter-clockwise directions.

[6] Specifically, these reference systems are indicated with X''–Y'' for the spiral arms and X'–Y' for the bar according to the notation of Chapter 11 and shown e.g. in Figures 11.5 and 11.10. Here the general notation X'–Y' is used.

4. We end up with a maximum of 12 values of dispersions for each orbit or point in the U–V grid, depending on whether all the crossings occur for the orbit (Table 10.2).

Table 10.2: The 12 dispersions calculated in this method when the orbits cross the $X' > 0$ and $Y' > 0$ axes.

($X' > 0$, clockwise)	σ_R	σ_{V_R}	σ_{V_ϕ}
($X' > 0$, counter-clockwise)	σ_R	σ_{V_R}	σ_{V_ϕ}
($Y' > 0$, counter-clockwise)	σ_R	σ_{V_R}	σ_{V_ϕ}
($Y' > 0$, clockwise)	σ_R	σ_{V_R}	σ_{V_ϕ}

An example of the distribution of orbital regularity in the U–V plane for the 12 variables of Table 10.2 is shown in Appendix B.1 (Figure B.1). The dark regions show the cases with small dispersions (more periodic). The (U,V) positions marked with a single centred black point correspond to orbits that do not cross that axis enough times. This could be due to several reasons: i) they are "slow" orbits and the integration time has exceed the imposed limit of 100 Gyr without having cross that axis at least 10 times, ii) they are confined orbits in the X'–Y' plane and they do not cross the particular axis chosen, or iii) they are orbits that do not cross the axis in that particular direction (e.g. clockwise), but they do it in the other direction (e.g. counter-clockwise).

5. These 12 values are normalised to unity and subsequently they are quadratically added so as to obtain a single measure of the orbital regularity.

6. The final result is plotted as a colour plot in the U–V plane where again the darker the regions, the more periodic the orbit. Regions in the U–V plane with a single centred black dot correspond to orbits that satisfy i) or ii) conditions above. An example of a final result is shown in Figure B.2. Once this figure is obtained the regular orbital regions in the U–V plane can be identified and the corresponding orbits can be studied.

The aim of using a method to quantify the orbital regularity of the points in the U–V plane are the following. First, it allows as to ascertain if a given structure that has appeared in the test particle simulations corresponds to a group of periodic or quasi-periodic orbits or not. This can be simply done by comparing the positions in the U–V plane of both type of methodologies. As seen in Chapter 2, there is still debate on whether some moving groups correspond to periodic or chaotic orbits of the non-axisymmetric structure. This will help in trying to clarify this.

Second, it allow us to identify the effects of a particular resonance in the U–V plane by studying the shapes of the orbits that have emerged as regular through this method. In other

words, the orbital structure of a given model at a particular region of the disc can be studied and the resonant features identified and characterised in terms of e.g. shape in the U–V plane. Although axisymmetric estimates can be used to determine the position (or positions) of a resonant orbit in the velocity plane as e.g. in Dehnen 2000, these are just approximated calculations as the non-axisymmetric components are not taken into account in them. The exercise is not straightforward when the full model is considered. These approximations creates differences between the predictions and the results of the simulations as it is seen in Part V. We point out that although this method helps us to identify structure in the U–V plane with a certain orbits, it is not our intention to carry out an exhaustive study of the orbital structure of the potential model which is beyond the scope of this thesis.

Third, as the computing time of this method is very affordable, it allows us to scan the parameter space of the potential model more rapidly and study the effects of some interesting parameters on the orbital structure.

On the other hand, this kind of method has sometimes been used in the sense that moving groups are directly ascribed to periodic (or chaotic) orbits of a given potential model (e.g. Quillen & Minchev 2005). According to this procedure, the moving groups could be overdensities of stars around a periodic orbit. However, here this method will be not applied so daringly in this sense. The advantages and disadvantages of this method of studying moving groups are discussed in Section 10.4 where the main simulation methods used in this field are summarised and compared. To conclude, this method has the advantage of being rapid, which allows us to scan the parameter space of the potential model, but has a clear disadvantage: it does not show which structures will be populated and how.

10.4 Comparison with other simulation methods

Differences between the results of this thesis and the results of other works by other authors may arise in part due to the differences between the exact simulation method applied in each case. Apart from this, obviously the specific potential model for the MW and the characteristics of the spiral arms and the bar must have an important role in order to compare this with other studies. Whereas the differences between the potential models are analysed in Section 11.5, in the present section we aim to summarise the simulation methods in other important studies of this field. There are mainly three types of simulation methods used in the literature in the study of moving groups: test particle simulations (with two different integration procedures: backward and forward), N-body simulations and study of periodic orbits.

i) Test particle simulations

Among the test particle simulations, one can find the simulation method of Dehnen (2000) which is called *backward-integrating method* by his author. In this method the phase-space points corresponding to a grid in the U–V plane but at the same position in configuration space $(R_\odot, \phi)$ are integrated backward from t_2 (positive) until $t = 0$. During the integration the bar grows adiabatically from $t = 0$ to t_1 ($t_1 < t_2$) and stays constant from t_1 to t_2. At $t = 0$ a certain DF function of the energy E and the angular momentum L_z is assumed for an axisymmetric equilibrium (in particular one consistent with an old disc population in that study). As the collisionless Boltzmann equation determines that the DF remains constant along stellar trajectories, the DF at t_2 is determined for each orbit or point of the U–V plane.

The main advantages of this method are: i) only the necessary orbits that affects the local velocity distribution are computed, which results in very low execution times and allows an exhaustive scanning of the parameter space, ii) these velocity distributions are not affected by Poisson noise and finally iii) a single simulation must be carried out to study different IC because the DF of these IC only plays its role after the orbit integration. However, this method has been criticised sometimes in the literature. At least two problems with this method have been identified. First, as stated in Fux (2001), it needs long integration times to reduce the effects of the ongoing phase mixing[7] that causes the velocity distribution to change with time and have spurious structures. According to this author, incurved waves appear in some of the regular orbital regions of the U–V plane and also the chaotic regions becomes noisy. He shown that even with integration time equal to 120 bar revolutions the velocity distribution had not still reached a completely stationary state. This technique gives a DF that, according to this author, never smoothes out on sufficiently small scales. Secondly, it was found in Chakrabarty (2004) that no matter how slowly the growth and dissolution of the perturbation were carried out, the resulting velocity distributions were marked with "holes" in them due to those orbits that come too close to the resonance and become chaotic thereby, which might be expected in this kind of simulations.

The forward integration technique is the one used here (Procedure 1 and 2) and in Fux (2001), Chakrabarty (2007). For these two authors, this technique copes with the above mentioned negative effects in the sense that, although the ongoing phase mixing still occurs for the forward integration, it is reduced using averages over time. In that two studies the orbits are recorded in the reference frame rotating with the perturbation (bar or spiral) and the final velocity distribution is the result of averaging it over time in that frame after the perturbation reached

[7] In this context, the phase mixing is defined as the attainment of a stationary state by a system in a regular force field.

full strength. This is presumably consistent with the observed DF, which presents an average over ages and reduces the phase mixing problem[8]. Besides, it is important to note, that to our knowledge, the study of Chakrabarty (2007) is the only one prior to the present thesis that includes bar and spiral arms at the same time in some of its simulations. In these particular case the orbits were recorded in the rotating frame of the bar and the final DF is the average over the times when the bar and the spiral pattern are at the same relative configuration.

By contrast, we do not take averages of the velocity distribution with time. This in an important difference between the forward integration of this thesis and the one in Fux (2001) and Chakrabarty (2007). We consider that the study of the effects of the integration time is necessary as we can not avoid the possibility that the disc is still experiencing the response to the bar or to the spiral arms. Our Procedure 2 (see Figure 10.2b in Section 10.1), allows us to perform this time analysis. As the default integration time for this procedure is 400 Myr , it is initially designed to study the rapid induced effects on the local velocity distribution but it allows us to change the integration time to any desired value. On the other hand, in our simulations using the integration procedure 1 (Figure 10.2a), we can also obtain a final velocity distribution with particles with different ages without loosing the opportunity to consider the effects of time. However, more orbits should be computed, which leads to longer execution times and makes difficult the scanning of the parameter space of the model or the IC. Also, the final velocity distribution does present Poisson noise. Here this drawback is treated using the WD method (Part II).

Nevertheless, the test particle simulations of Dehnen (2000), Fux (2001) and Chakrabarty (2007) differ from the present ones in the following aspect. In those studies the potential of the perturbation is adiabatically added to the axisymmetric potential during a certain number of revolutions of the perturber (spiral arms or bar) and stays stable afterwards. In our method we study the phase space available to the local stellar distribution using the PM04–MW potential model but we do not try to do it completely self-consistently as the other authors. Our initial conditions corresponds to a distribution consistent with a axisymmetric field and our main goal is to find the response of the disc to non-axisymmetric components which are included all time or introduced abruptly. Some experiments were carried out to show that the final periodic orbital structure given the same initial conditions do change significantly with the adiabatic introduction of the non-axisymmetric component (Pichardo et al., private communication). As in our study, we explore the hypothesis that moving groups are related to the orbital structure induced by the bar or the spiral arms this fact will not affect us critically. In fact, even when adding the perturbation adiabatically, still transitory effects due to phase mixing have been

[8]The contribution of each particle to the U–V plane becomes proportional to the time the particle spends within the volume where the distribution is computed (Fux 2001).

shown to occur (e.g. Minchev et al. (2010)), which lead to some authors to take averages with time (Fux 2001, Chakrabarty 2007). Nonetheless, we will explore in some cases the results of simulations where the bar is added progressively to the potential (see Chapter 15).

In later sections we study the effects of the bar and the spiral arms on the velocity distribution. We expect again some transient effects due to the ongoing phase-mixing that disc experiences in response to the bar or to the spiral arms. As explained above, the adiabatic introduction of the perturber do no avoid the appearance of this transient structures. However, this is not a drawback for us as in fact we can not reject the possibility that the observed moving groups are in fact transitory structures due to the bar or the spiral arms. We consider that the study of the effects of different integration time is necessary as we can not avoid the possibility that the disc is still experiencing the response to the bar, to the spiral arms or to any other disturbance that has lead the MW disc to a situation of non-relaxation e.g. a recent passage of an orbiting satellite or other external perturbations.

ii) N-body simulations

Also N-body simulations have been used in order to study the moving groups. In particular, Fux (2001) run a high-resolution simulation developing a bar to study Hercules as due to the effects of the bar OLR. This method has the advantage of being a 3D method, self-consistent and presumably more realistic. The possibility of exploring the time evolution of the U–V plane while the bar evolves consistently is an advantage of this method but in Fux (2001) this capability was not explored and the final distributions were averaged over time in a reference system co-moving with the OLR. Obviously, in these simulations the analysis of the resulting velocity distributions becomes more complex as the formed bar evolves with time and spiral arms can be developed. However, it is has been shown that numerical effects can affect the bar evolution in these simulations (Klypin et al. 2009). On the other hand, the real evolution of the bar is presently not well-known and will depend on which mechanism has given origin to the MW. Of course, this would be also an obstacle for a test particle simulation when trying to model the bar evolution or the recent history of the MW analytically. As main drawbacks of the method, we can find its extensive CPU time if high space, time and velocity resolution are required. Also it is difficult to scan the parameter space because of the time computing but also because of the difficulties in controlling the characteristics of the bar in this type of simulations.

iii) Study of periodic orbits

The method of the study of periodic orbits consist of quantifying the periodicity or regularity of the orbit (or equivalently, quantifying the degree of stochasticity) corresponding to each point in

the U–V plane. This can be done through several methods. Traditionally it is carried out using the Poincaré surface of section but this is for cases at constant value of the Hamiltonian but not at a fixed position in the configuration space which is required in this study. In Fux (2001) the Lyapunov coefficients are used. These characterises the rate of divergence of two trajectories initially close to each other in phase space. There exist several exponents depending on the dimensions of the phase space but all exponents vanish if the orbit is regular, and if the largest coefficient is positive, the orbit is chaotic and the amount of chaos increases with its value.

In Quillen & Minchev (2005) a simpler method is used where the periodicity of each orbit is quantified through the weighting function computed as the sum of the variances in galactocentric radii and in the velocity component U computed using the R and U from each time the orbit crosses a given axis in the rotating frame of the spiral arms. The weighting function estimates the distance in phase space of an orbit from a closed or periodic orbit. The number of orbits is chosen so as to get an stable weighting function. Our method of estimating the orbital regularity (Section 10.3) is based on this study.

Apart from the differences in the method of quantifying the periodicity, the studies of Fux (2001) and Quillen & Minchev (2005) slightly differ in the purpose. In Fux (2001) this method is used as a tool to determine the phase-space extend of the regular orbits trapped around stable periodic orbits and the chaotic orbits and this analysis is complemented by test particle simulations that allow to study how the established orbital structure is actually populated. This approach is similar to ours. As explained in Section 10.3, in this thesis the periodic orbit analysis is used only with the aim of ascertain if a given structure that has appeared in the test particle simulations corresponds to a group of periodic or quasi-periodic orbits or not and to identify the effects of a particular resonance in the U–V plane (more accurate that the axisymmetric approximation, see Section 10.3). By contrast, in Quillen & Minchev (2005) this method is used directly to identify moving groups as they are supposed to be overdensities around periodic orbits. It is assumed that, as stars are born in spiral arms with low velocity dispersion, they are born in orbits that are nearly periodic or closed in the frame rotating with the arms. Therefore, the periodic regions of the U–V plane are orbits where a young star is likely to be born and remain not exactly in that orbit but oscillating at a greater extent about the periodic orbit due to scattering by molecular clouds or transient spiral structure. According to these authors, the theory of adiabatic invariants implies that particles with initially low epicyclic motion settle onto periodic or closed orbits following the slow growth of a perturbation. However, other studies have shown that the usual adiabatic invariants are not applicable in the resonant case (Barbanis 1976). Also in Dehnen (2000) the periodic orbits (in this case calculated using the axisymmetric limit) were used to be identified with moving groups with the assumption that the initially circular orbits will be turned into (nearly) closed, but no longer circular, orbits in the barred

potential when the bar is grown (following the same behaviour as the gas, avoiding encounters). Compared to the integration method, this method is independent of the manner of perturbation growth. Also it has the advantage that it is independent of the initial conditions. However, this advantage becomes a drawback as the process of resonant trapping is still poorly known and this method do not allow to predict which periodic orbit will be populated an to which extent.

Chapter 11

The PM04–MW potential model

For the Galactic potential we use the PM04–MW potential model which is extensively described in Pichardo (2003a), Pichardo et al. (2003b, 2004). It consists of an axisymmetric part and the non-axisymmetric components (prolate bar and self-gravitating spiral arms) which are consistent with several recent observational constraints. The model can be used with only the bar component, only the spiral component or as a spiral-bar model including both non-axisymmetric parts. In Section 11.1 the axisymmetric part of the PM04–MW potential model is summarised and in Sections 11.2 and 11.3 we describe the models for the non-axisymmetric components of the self-gravitating spiral arms and the prolate bar, respectively. We use the spatial and velocity coordinate systems defined in Section 1.4.

The simplicity of the axisymmetric part of the PM04–MW potential model contrasts with the complexity of the construction of the bar and spiral arms components which is carried out as a superposition of small pieces of mass distribution. However, this complexity counterbalances the consequent flexibility to be adapted to observations. The main advantages of the PM04–MW potential model are first this flexibility to fit the observations. Secondly, it is a full 3D model which, instead of taking an ad hoc dependence on the z coordinate for the spiral arms and bar (for example adding a term $\mathrm{sech}^2[z/z_s]$ to the potential), it considers directly a three-dimensional mass distribution from which the gravitational potential and the forces are derived. The self-consistency of the model has been tested through an analysis of the stellar orbital reinforcement of the potential as in Patsis et al. (1991) and is presented in Pichardo (2003a), Pichardo et al. (2003b, 2004).

The non-axisymmetric components of the spiral arms and bar in the PM04–MW potential model have several free parameters that in Pichardo et al. (2003b, 2004) are chosen taking into account the ranges given by recent observations and/or self-consistency reasons. The chosen values for these parameters of the model are shown in Table 11.3 and in Table 11.4 for the spiral

Table 11.1: Adopted observational constraints in the axisymmetric model by Allen & Santillán (1991).

Distance Sun - Galactic centre	$R_\odot = 8.5\,\mathrm{kpc}$	
Local circular velocity	$V_c(R_\odot) = 220\,\mathrm{km\,s^{-1}}$	
Local total mass density	$\rho = 0.15 M_\odot\ pc^{-3}$	
Rotation curve	R (kpc)	V_c ($\mathrm{km\,s^{-1}}$)
	0.43	259.8±10
	1.28	226.2±9.7
	2.55	201.5±9.7
	4.25	213.5±7.5
	6.38	224.0±7.8
	10.63	209.0±15
	15.94	223.0±20
	56.63	206.0±40

Table 11.2: Main constants in the axisymmetric model by Allen & Santillán (1991).

Central mass M_1	$1.4 \times 10^{10} M_\odot$	(1.5 $\%M_T$)
Disc mass M_2	$8.6 \times 10^{10} M_\odot$	(9.5 $\%M_T$)
Halo mass M_3	$8.0 \times 10^{11} M_\odot$	(89 $\%M_T$)
Total mass M_T	$9.0 \times 10^{11} M_\odot$	

arms and the bar respectively and they are thoroughly documented in Pichardo et al. (2003b, 2004). Here we adopt these parameters as *default* values. Nevertheless, as one of our goals is to study the dependence of the properties of the spiral arms and the bar on the kinematics of the disc, in Part V these parameters are changed within their corresponding range and the new used values will be clearly specified and discussed in terms of their consistency with recent observations. The model for these non-axisymmetric components of the PM04–MW potential model are compared with other widely used models in Section 11.5 and elsewhere (Pichardo et al. 2003b, 2004).

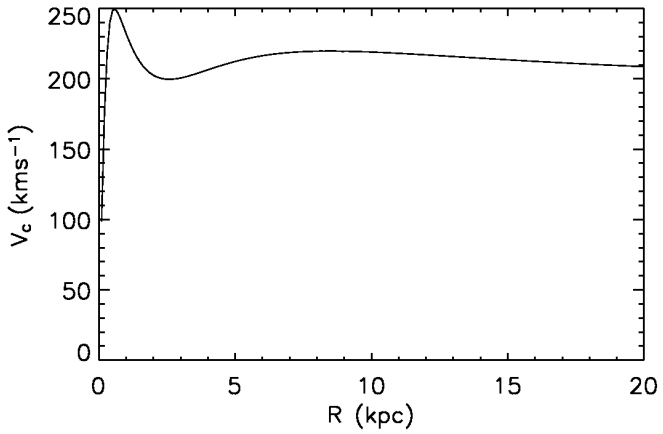

Figure 11.1: **Model rotation curve.** Total rotation curve resulting from the axisymmetric mass model by Allen & Santillán (1991).

11.1 The axisymmetric part

The axisymmetric Galactic model is taken from Allen & Santillán (1991) and it is composed by a bulge, a flattened disc and a massive spherical halo which is assumed to be extended to a radius of 100 kpc. The first two are modelled as Miyamoto-Nagai potentials (Miyamoto & Nagai 1975) and the halo is built as a spherical potential. The main adopted observational constraints of the model are summarised in Table 11.1. In particular, a value of $R_\odot = 8.5\,\mathrm{kpc}$ for the Sun's galactocentric distance and a circular speed of $V_c(R_\odot) = 220\,\mathrm{km\,s^{-1}}$ are adopted. The local circular frequency is therefore $\Omega(R_\odot) = 25.8\,\mathrm{km\,s^{-1}kpc^{-1}}$ and the total mass[1] is $M_T = 9 \times 10^{11} M_\odot$. The particular masses of each component are shown in Table 11.2. The resulting curve of circular velocity of this model is shown in Figure 11.1 and the Oort's constants at the solar position are $A = 12.95\,\mathrm{km\,s^{-1}kpc^{-1}}$ and $B = -12.93\,\mathrm{km\,s^{-1}kpc^{-1}}$. Also the circular and epicyclic frequencies together with the resonance curves are presented in Figure 11.3. Parameters such as $R_\odot$ do not deprive us, however, to consider the Sun in slightly different positions and in fact, our simulations allows us to study the kinematic distributions all over the disc.

[1] Although several recent observational studies have obtained a double mass, there is not a general concordance between the estimated mass of the MW. For a discussion see Baiesi Pillastrini (2009). For instance, Reid et al. (2009) estimated a higher mass similar to that of the Andromeda galaxy and a circular rotation speed of $254 \pm 16\,\mathrm{km\,s^{-1}}$ using parallaxes and proper motions of masers of massive star-forming regions. This would increase the value of the local circular frequency up to $\Omega(R_\odot) = 30\,\mathrm{km\,s^{-1}kpc^{-1}}$. McMillan (2010) reanalysed the same data to find that they do not favour any particular value of $R_\odot$ and $V_c(R_\odot)$. However they constrained the local circular frequency to be in the range $[29.9, 31.6]\,\mathrm{km\,s^{-1}kpc^{-1}}$, which is higher than the value used here.

11.2 The self-gravitating spiral arms

The spiral arm model is a 3D steady model with two arms corresponding to a given mass distribution from which the potential and forces are derived. The main difference between the self-gravitating spiral arms and models obtained through the *tight-winding* approximation (TWA) falls on the construction itself. In the TWA the spiral arms potential is obtained from the self-consistent solution of the Poisson equation for tightly wound spiral and small perturbations. By contrast, the self-gravitating spiral arms allow us to study spiral patterns which are nor tightly wound neither weak perturbations, which could be the case of the MW. A deep discussion about it is offered in Section 11.5 where we directly compare both models.

The model has several free parameters that in Pichardo et al. (2003b) are fixed within a certain range taking into account observations and self-consistency reasons. The default values of the parameters of this model are shown in Table 11.3. The spiral arms trace the locus reported by Drimmel & Spergel (2001) using K-band observations[2]. This locus is taken with the following form:

$$g(R) = -\left(\frac{2}{N\tan i}\right)\ln\left(1+\left(\frac{R}{R_{sp}}\right)^{N}\right), \tag{11.1}$$

where $i = 15.5^\circ$ is the pitch angle, $R_{sp} = 2.6\,\mathrm{kpc}$ is the galactocentric radius of the beginning of the locus and the parameter N is a measure of how sharply the change from a supposed bar-like to spiral-like occurs in the inner regions (Roberts et al. 1979). The limit of $N \to \infty$ produces spiral arms that begin forming an angle of 90° with the line that joins the two starting points of the locus whereas for $N = 0$ this angle would be 180°. Here it is taken the large limit approximated by $N = 100$. Figure 11.2 shows this locus of the spiral arms with respect to the Sun (and also the bar).

This locus results in an orientation such that the angular offset between the Sun and the peak of the spiral at the same radius, ϕ_{0sp}, is 88°. The arms begin in a line that makes 20° with the X axis. This locus is also in agreement with the latest results from Spitzer/GLIMPSE surveys (Benjamin et al. 2005, Churchwell al. 2009). In this two studies only two arms are seen in the IR which are the Scutum-Centaurus arm, or sometimes called Scutum-Crux, and the Perseus arm. This default locus locates the Sun approximately in the middle of the interarm region but, as stated at the beginning of the chapter, this is a flexible parameter as our study extends to kinematic distributions all over the Galactic plane. The Scutum-Centaurus arm is the one near the Sun in the direction to the Galactic centre and the Perseus arm corresponds to the one beyond the Sun in the anti-centre direction. These two massive arms, formed with old stars, would be accompanied by two more arms: Norma and Sagittarius (or Sagittarius-

[2]This corresponds to the second locus of Pichardo et al. (2003b).

Table 11.3: Default parameters for the self-gravitating spiral arms (Pichardo et al. 2003b).

Parameter	Default value
Number of arms	2
Pitch angle i ($^\circ$)	15.5
Orientation of the arms ϕ_{0sp} ($^\circ$)	88
Scale length R_Σ (kpc)	2.5
Beginning of the locus R_{sp} (kpc)	2.6
Beginning of the arms R_i (kpc)	3.3
End of the arms R_f (kpc)	12
Arm width a_0 (kpc)	1
Arm height c_0 (kpc)	0.5
Mass M_{sp} ($M_\odot$)	4.3×10^9 ($5\% M_2$)
New disc mass ($M_\odot$)	8.17×10^{10} ($95\% M_2$)
Pattern speed Ω_{sp} ($\mathrm{km\,s^{-1}kpc^{-1}}$)	20
Revolution period (Myr)	300
Corotation radius (kpc)	10.9
4:1 ILR (kpc)	7.0

Carina). These have less amplitude and are not detected as overdensities in the old stellar disc by Drimmel & Spergel (2001) neither (Benjamin et al. 2005) but are seen in other classic (Georgelin & Georgelin 1976) and recent (Vallée 2008 and references therein) studies from HII regions or CO emission. Hydrodynamic models have shown how it is possible to form arms of compressed gas without increasing the stellar surface density as a response to a 2-armed pattern (Martos et al. 2004), which would explain the existence of the Sagittarius-Carina and Norma arms.

The spiral arms mass distribution is built as a superposition of inhomogeneous oblate spheroids along the above described locus. The separation between the centres of the spheroids along the locus is 0.5 kpc. The overlapping of spheroids allows a smooth distribution along the locus, resulting in a continuous function for the gravitational force. It was checked that no significant change was observed if this separation was decreased thus increasing the smoothness of the spiral mass distribution (Pichardo et al. 2003b). The effective starting distance of the spiral arms, i.e. the beginning of the spheroid superposition, is $R_i = 3.3$ kpc and the arms end at a distance $R_f = 12$ kpc. Regarding the oblate spheroids, they are oriented with the semi-minor axis being perpendicular to the Galactic plane. The semi-major and semi-minor axes of the spheroid, a_0 and c_0, are 1 kpc and 0.5 kpc, respectively, following other studies of the shape and

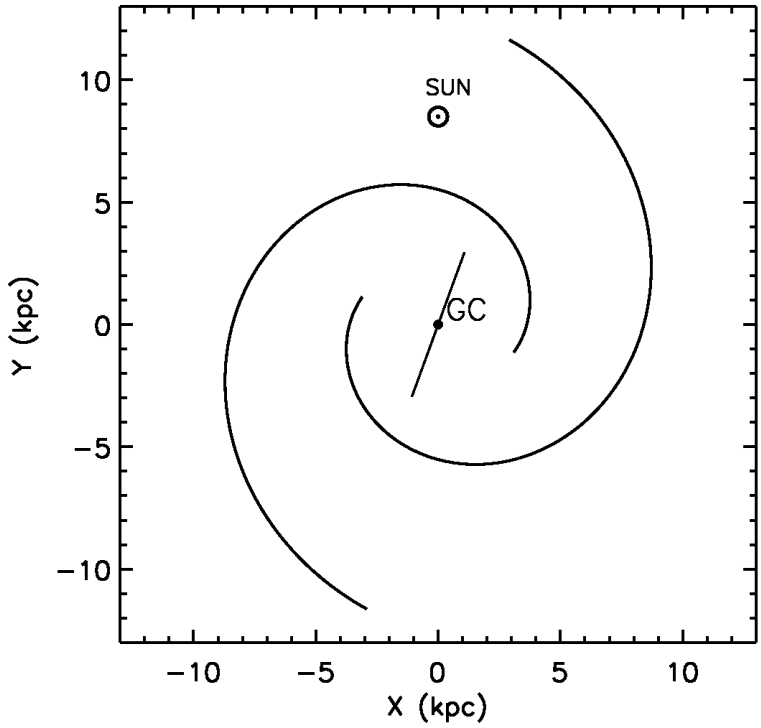

Figure 11.2: **Bar and spiral arms of the MW.** Sketch of the locus and location of the Galactic bar and the spirals arms of the PM04–MW potential model. The solar position according to the default parameters of the PM04–MW potential model is also shown.

size of the arms (Martos & Cox 1998). A linear density law $\rho(a) = p_0 + p_1 a$ in each spheroid is considered, with a being the coordinate along the major semi-axis, and the coefficients p_0, p_1 being functions of the galactocentric distance of the spheroid's centre. Each spheroid has zero density at its boundary. Schmidt (1956) gave the expressions for the potential and force fields for a spheroid with this density law. An exponential fall of the central density of the spheroids along the arms, equal to that of the disc, is taken and therefore the function $p_0(R)$ is:

$$p_0(R) = p_{01} e^{-\left(\frac{R-R_i}{R_\Sigma}\right)}, \tag{11.2}$$

where $R_\Sigma = 2.5\,\mathrm{kpc}$ (e.g. Freudenreich 1998, Robin et al. 2003) and p_{01} is such that the desired total mass for the arms M_{sp} is achieved. The ratio of the this total mass in the spiral arms to the mass of the disc in the axisymmetric part by Allen & Santillán (1991), which is $\mathrm{M}_D = 8.6 \times 10^{10}\ \mathrm{M}_\odot$, is taken to be $M_{sp}/M_D = 0.05$ in our default case. This correspond to a high value between the limits of consistency of the model (Pichardo 2003a) and actually, smaller values for this parameter will be explored in Part V. When the spiral arms are added to the model, the mass of the spiral is subtracted from the disc, which guarantees that the total mass of the model do not change and neither does the mean circular velocity. The force field produce by this mass distribution model is studied in Section 11.5.

With the default pattern speed of $20\,\mathrm{km\,s^{-1}kpc^{-1}}$, the solar radius is close to the 4:1 ILR of the spiral arms. This can be seen in Figure 11.3 where the horizontal line corresponding to this value for Ω_{sp} crosses the curve of $\Omega - 1/4\kappa$ near the Sun radius. The 4:1 ILR resonance is therefore the nearest resonance according to this model. The position of this resonance for $\Omega_{sp} = 20\,\mathrm{km\,s^{-1}kpc^{-1}}$ is $R = 7.0\,\mathrm{kpc}$. A variation of Ω_{sp} will change the resonance position. However, it is important to note that the scheme of Figure 11.3 is a simplification of the study of the resonances as the resonance curves are calculated using only the axisymmetric part of the PM04–MW potential model. Nevertheless, the method can be used to estimate guiding values for the positions of the resonances.

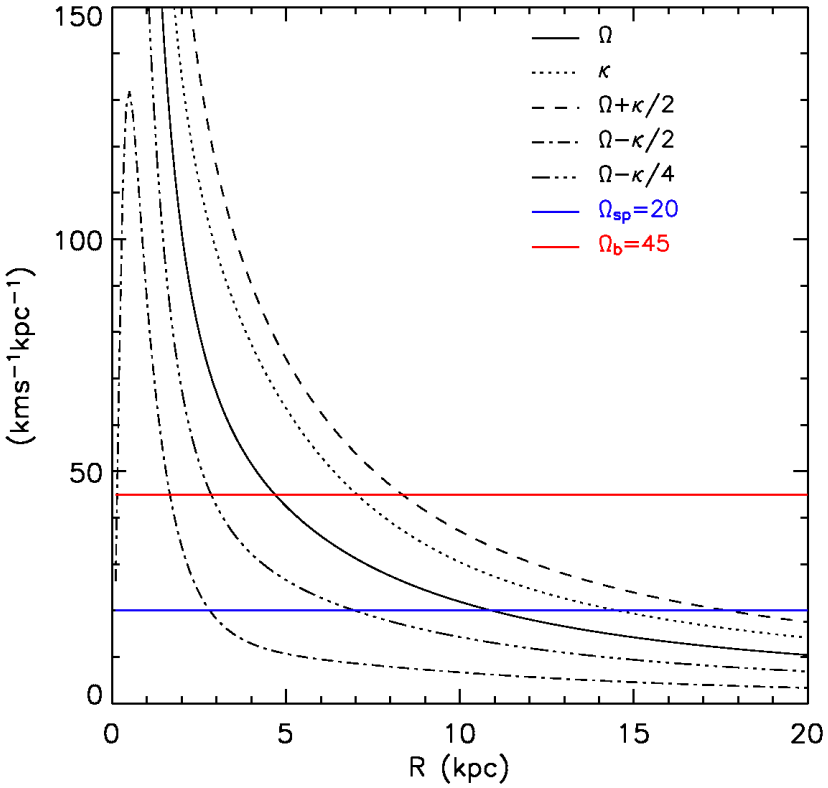

Figure 11.3: **Locations of the bar and spiral arms resonances.** Resonance curves in the Allen & Santillán (1991) axisymmetric model. The horizontal lines are the default values of pattern speed of the bar and the spiral arms rigid rotation.

11.3 The prolate bar

This bar model is extensively described in Pichardo et al. (2004) and its main parameters are presented in Table 11.4. It consists of a prolate mass inhomogeneous distribution[3] that resembles Model S of Freudenreich (1998) from COBE/DIRBE data which has a density of the form:

$$\rho_b(R_s) = \rho_0 \begin{cases} sech^2(R_s) & R_s \leq R_{end_S} \\ sech^2(R_s) e^{-\left(\frac{(R_s - R_{end_S})^2}{h^2_{end_S}}\right)} & R_s \geq R_{end_S} \end{cases}, \tag{11.3}$$

with R_S given by

$$R_S = \left\{ \left[\left(\frac{|x|}{a_x}\right)^{C_\perp} + \left(\frac{|y|}{a_y}\right)^{C_\perp} \right]^{C_\parallel / C_\perp} + \left(\frac{|z|}{a_z}\right)^{C_\parallel} \right\}^{1/C_\parallel}. \tag{11.4}$$

Figure 11.4 shows a scheme of the stratification of the bar in different concentric prolate shells of similar density. The scale lengths of the bar (a_x, a_y and a_z) and the exponents ($C_\perp$ and $C_\parallel$) were fitted to the infrared observations. The effective boundary of the bar on the direction of its major semi-axis, or in other words its length, is $a_b = 3.13\,\text{kpc}$. This is the length where the superposition of prolate shells ends. The constant R_{end_S} is defined as a_b/a_x. For $R_s \geq R_{end_S}$ the density has an additional Gaussian factor with scale length of $h_{end} = 0.46\,\text{kpc}$ to produce a steep but smooth fall in the outer region. The parameter h_{end_S} is the scale length of this Gaussian factor scaled to a_x, i.e. $h_{end_S} = h_{end}/a_x$.

Also following the COBE/DIRBE data, the default orientation of the bar respect to the Sun is chosen $\phi_{0b} = 20°$ as it can be seen in Figure 11.2. Very similar parameters for the orientation and shape of the bar were found with a more recent analysis of the COBE/DIRBE data together with the apparent magnitude distributions of clump giant stars in certain bulge fields (Bissantz & Gerhard 2002).

The mass of the bar is probably the parameter which involves more uncertainty. However, several estimations have given a total central mass (bar + bulge) of about 1×10^{10} $M_\odot$ (e.g. Dwek et al. 1995 from photometric observations with the Hubble Space Telescope). Although greater masses are also found in the literature[4], here a total central mass of 1.4×10^{10} $M_\odot$ has been adopted as default value. In particular, the bar includes the 70% of this central mass

[3] In Pichardo et al. (2004) three different bar models are presented: a triaxial bar, a prolate bar and a boxy bar. The choice of the prolate mass distribution answers to the fact that, although the boxy distribution would match better the observations, the prolate shape is a good approximation to the COBE/DIRBE data and, it is a simpler model that gives lower computation times.

[4] For instance Zhao et al. 1996 reported a value up to 2.2×10^{10} $M_\odot$ using observations of microlenses and models restricted by COBE/DIRBE.

Table 11.4: Default parameters for the bar (Pichardo et al. 2004).

Parameter	Default value
Length a_b (kpc)	3.13
Axis ratio	10:3.12
Scale lengths a_x, a_y, a_z (kpc)	1.7, 0.54, 0.54,
Stratification parameters $C_\perp$, $C_\parallel$	2, 2
Angle respect to the Sun ϕ_{0b} ($^\circ$)	20
Mass M_b ($M_\odot$)	9.8×10^9 ($70\% M_1$)
New bulge mass ($M_\odot$)	4.2×10^9 ($30\% M_1$)
Pattern speed Ω_b ($\mathrm{km\,s^{-1}kpc^{-1}}$)	45
Revolution period (Myr)	136
Corotation radius (kpc)	4.7
OLR (kpc)	8.3

(9.8×10^9 $M_\odot$) whereas the bulge covers the remaining 30% (4.2×10^9 $M_\odot$). Therefore, when the bar is added to the model, the bulge mass is decreased with respect to its original value so as to guarantee that the total central mass of the model do not change and neither does the mean circular velocity (the maximum variation of the circular velocity is less than 0.5% at $R = 8.5\,\mathrm{kpc}$). The force field produce by the prolate bar is studied in Section 11.5.

A bar pattern speed of 45 $\mathrm{km\,s^{-1}kpc^{-1}}$ is the chosen as default value. This is in the lowest part of the range $[40, 60]\,\mathrm{km\,s^{-1}kpc^{-1}}$ favoured by other studies (see a revision of the different values obtained for this parameter in Gerhard 2002). With this pattern speed, the solar radius is close to the bar 2:1 OLR. As it can be observed in Figure 11.3, the horizontal line corresponding to this value for Ω_b crosses the curve of $\Omega + 1/2\kappa$ near the Sun radius. The 2:1 OLR resonance is therefore the nearest resonance according to this model. The position of this resonance for $\Omega_b = 45\,\mathrm{km\,s^{-1}kpc^{-1}}$ is $R = 8.3\,\mathrm{kpc}$. Again it is worth noticing that this a simplified method to calculate the resonance positions (see discussion in Section 11.2). In Part V we explore the results obtained also with different pattern speeds.

It must be stressed that the recent new finding of a long bar using near-infrared colour-magnitude diagrams and star counts (Hammersley et al. 2000) and data from the Spitzer/GLIMPSE (Benjamin et al. 2005) have not been considered yet in the PM04–MW potential model given the recentness of its discovery and the lack of observational constraints about for example its mass or its pattern speed. This bar is called the long bar while the bar of the PM04–MW potential model is usually called triaxial bulge, COBE/DIRBE bar or bulgey-bar (Churchwell al. 2009). The long bar has a half-length of around 4 kpc according to Hammersley et al. (2000)

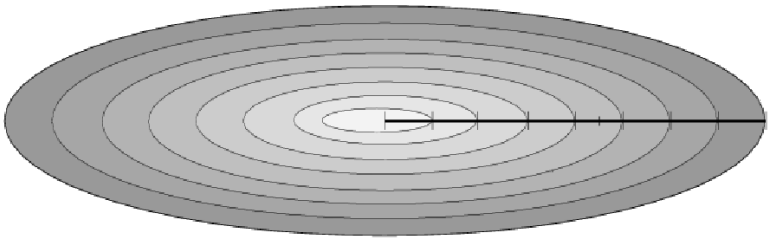

Figure 11.4: **Construction of the prolate bar.** Scheme of the stratification of the bar in different concentric prolate shells of similar density (Figure from Pichardo 2003a).

or even 4.4 kpc according to Benjamin et al. (2005) and it is oriented with an angle of $\phi_{0b} \sim 40°$ (Hammersley et al. 2000, Benjamin et al. 2005). The long bar seems to be less massive. It has a third as many bright stars as the triaxial bulge and considering roughly that the populations of the triaxial bulge and the long bar were similar this would result in a less massive bar (López-Corredoira et al. 2007). Without having an specific component for this long bar in our PM04–MW potential model, we will venture in some cases to analyse its effects on the local velocity distribution considering the described prolate model but with a relative orientation of $\phi_{0b} = 40°$. It will be interesting also to study the combined effects of both bars but this is postponed for a future study.

11.4 The spiral-bar model

The PM04–MW potential model that includes both the bar and the spiral arm components is also used in Part V (Section 16). We will refer to it as spiral-bar PM04–MW potential model. This model adds the spiral arms just as described in Section 11.2 and the bar of Section 11.3 which are relatively oriented as in Figure 11.2. This spiral-bar PM04–MW potential model, with different pattern speeds for the bar and the spirals, is supported by recent observations from external galaxies in Patsis et al. (2009). They reported that the best match between observations and models for the galaxy NGC 3359 is found when different pattern speed for the bar ($39\,\mathrm{km\,s^{-1}kpc^{-1}}$) and for the spiral arms ($15\,\mathrm{km\,s^{-1}kpc^{-1}}$) is considered. Also Bissantz et al. (2003) found that a model with separate pattern speeds for the bar and the spirals explains better the observed ^{12}CO (l,v) diagram in the MW. In particular, they favoured $\Omega_b = 60\,\mathrm{km\,s^{-1}kpc^{-1}}$ and $\Omega_{sp} = 20\,\mathrm{km\,s^{-1}kpc^{-1}}$, which are values studied and discussed in Part V.

11.5 Comparison with other MW potential models

It is interesting to compare the PM04–MW potential model with other MW potentials used in this field. Our comparison is restricted to models that are usually applied to the particular study of moving groups. Therefore, models for the Galactic bar such as the derived from the density of Ferrers (1877) are not considered here. In particular, we explore the basic differences between models, emphasising the differences in the derived force fields.

In order to quantify the strength of non-axisymmetric models some useful parameters can be defined following other studies. Although this formalism has been classically applied to bars, some observational studies have used it recently to measure the strength of spiral arms as well (Block et al. 2004). First, it will be useful the Fourier decomposition of the potential of the bar and the spiral arms. The decomposition of the potential in the $m = 0$, $m = 2$, $m = 4$ and $m = 6$ modes is for the spiral arms:

$$\Phi_{sp}(R, \phi) = \Phi_{sp0}(R) + \sum_m \Phi_{spm}(R) \cos(m\phi) \tag{11.5}$$

and for the bar:

$$\Phi_b(R, \phi) = \Phi_{b0}(R) + \sum_m \Phi_{bm}(R) \cos(m\phi). \tag{11.6}$$

This decomposition allows us to evaluate the relative contribution of the different modes. On the other hand we will compute the forces of the $m = 2$ component relative to the total axisymmetric radial force that is worked out as the $m = 0$ total component of the model. Following Athanassoula et al. (1983), we explore first the parameter q_r which is the $m = 2$ radial component of the Fourier decomposition of the bar force scaled to the radial force of the axisymmetric background. It is computed through:

$$q_r(R) = \Phi_2'(R)/\Phi_0'(R) \tag{11.7}$$

where primes denote derivatives with respect to R. Note that now Φ refers to the whole potential of the model: non-axisymmetric component + axisymmetric part by Allen & Santillán (1991). As it will be seen, the mass models for the non-axisymmetric components that we use have contributions to the total axisymmetric radial force. We can also study the parameter q_t which is the tangential force of the $m = 2$ component of the Fourier decomposition scaled to the radial force of the axisymmetric background. This parameter is calculated as:

$$q_t(R) = 2|\Phi_2(R)/R\Phi_0'(R)| \tag{11.8}$$

following again Athanassoula et al. (1983). Similarly, the parameter $Q_T(R)$ is used in Buta (2001) and is the ratio of the maximum tangential force due to the bar or the spiral arms to the

mean radial axisymmetric force as a function of radius:

$$Q_T(R) = F_\phi^{max} / < F_{R0}(R) > . \tag{11.9}$$

Again the mean radial force represents the whole axisymmetric background due to the bulge, disc, and spiral arms and/or bar. Q_T is larger than q_t as it can include tangential forces due to modes $m \geq 2$. In particular the maximum of $Q_T(R)$, which is the maximum of the tangential-to-radial force ratio, gives a single and quantitative measure of the torque or strength of the bar and the spiral arms. In Block et al. (2004) this maximum is called Q_s for the spiral arms and Q_b for the bar.

Whereas the maximum values for q_r, q_t and Q_T can give general measures of how weak or strong is a non-axisymmetric component, these maximums often occur for small R. As we are interested in the effects of the non-axisymmetric components at outer radius, it is interesting to compared the general profiles of radial and tangential forces and also their values at solar radius or at radius near resonances.

The spiral arms

The more widely used model for the spiral arms is the one derived from the *tight-winding* approximation (TWA[5], see e.g. Binney & Tremaine 2008) for small pitch angles. In the spiral density wave theory (Lin 1971) the spiral structure of galaxies was modelled as a periodic perturbation term to the axisymmetric potential in the disc. The model gives a potential in the Galactic plane of the form:

$$\Phi_{sp}(R, \phi; t) = A \cos[m\big(\Omega_{sp} t - \phi\big) + g(R)], \tag{11.10}$$

where A is the amplitude of the spiral pattern, R and ϕ are the galactocentric cylindrical coordinates, m is the number of arms and the function $g(R)$ defines the shape of the spiral. A can be a function of radius R and time and is $\propto \frac{|\tan\ i|}{m}$. Usually a logarithmic shape such as $g(R) = -\frac{m}{\tan\ i}\ \ln \frac{R}{R_\odot} + \phi_0$ is assumed, where ϕ_0 is a constant to fix the orientation of the arms.

The main difference between the self-gravitating spiral arms and the TWA falls on the construction itself. Whereas in the approximation of the TWA the spiral arms are a small perturbative term of the potential, the self-gravitating spiral arms correspond to an independent mass distribution. More precisely, in the TWA the spiral arms potential is obtained solving the Poisson equation for a plane wave in a razor-thin disc (Binney & Tremaine 2008). The solution is self-consistent but it has several restrictions. First, it is restricted to tightly wound spiral

[5]Sometimes it is called WKB approximation after the Wentzel-Kramers-Brillouin approximation of quantum mechanics.

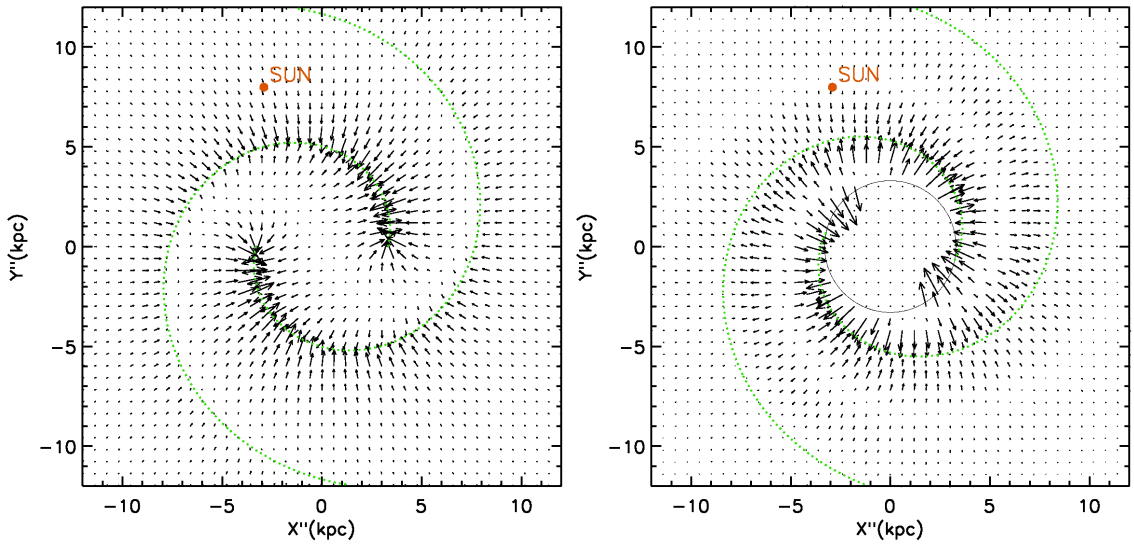

(a) Self-gravitating spiral arms

(b) TWA spiral arms

Figure 11.5: **Force field of different spiral arm models.** Detailed force fields as vector plots for the different models of spiral arms. Note that these figures correspond to a new reference system $X''Y''$ such that the spiral arms begin at the horizontal axis X''. The circle in (b) at $R = 3.3\,\mathrm{kpc}$ indicates that, despite the appearance, the effective start of the TWA arms is the same than in (a) as no arrow begins at a shorter distance.

arms (i.e. small pitch angle) with $|kR| = m/\tan i >> 1$, where k is the radial wave-number. As stated in Binney & Tremaine (2008) this situation is satisfied in most galaxies (with i between 11° and 15°) but not with a very comfortable margin. Specially for the MW, with a default pitch angle of $i = 15.°5$ this assumption is at least doubtfully satisfied. Second, the solution for the TWA requires the spiral arms to be a small perturbation, i.e. it is a perturbative solution for small density contrasts. This produces a cancellation of the contribution from the distant parts of the pattern to the local force. In this sense, the self-gravitating spiral arms allow us to study spiral patterns which are nor tightly wound neither weak perturbations, which could be the case of the MW. By contrast, it is not a self-consistent solution in the sense of potential and induced density. However, as explained in Section 11.2 the self-consistency of the model has been tested through an analysis of the stellar orbital reinforcement of the potential as in Patsis et al. (1991), which is presented in Pichardo et al. (2003b).

It is worth comparing the exact force fields of these two models. For our comparison, we will adopt for the TWA arms the same locus, i.e. the same $g(R)$ function, as in the self-gravitating spiral arms (Equation 11.1). Following Contopoulos & Grosbol (1986), an amplitude with an

exponential decay with radius of the form

$$A(R) = -A_{sp} R e^{-\epsilon_s R} \tag{11.11}$$

is used with $\epsilon_s = 1/R_\Sigma$ which gives the same scale length as for the self-gravitating spiral arms (Table 11.3). A value of $A_{sp} = 850[\,\mathrm{km\,s^{-1}}]^2\,\mathrm{kpc}^{-1}$ for the amplitude normalisation is chosen so as to reproduce approximately the force amplitude range of the self-gravitating arms when the default values are used ($M_{sp} = 0.05 M_d$). Besides, the force of the TWA is set to 0 if the radius is smaller than 3.3 kpc which is the effective beginning of the self-gravitating arms (see Table 11.3). Figure 11.5 represents both force fields in a vector plot. Note that the panels in this Figures correspond to a new coordinate system $X''Y''$ oriented such that the spiral arms begin at the horizontal axis[6] X''.

For given azimuths ϕ and radius R, the radial and tangential forces (in this case scaled to the axisymmetric radial force) are compared in Figures 11.6 and 11.7. The solid line corresponds to the self-gravitating arms whereas the dotted line shows the model of the TWA. In general, the self-gravitating spiral arms present more abrupt features and different positions for the minima and maxima of the force for both the radial force and the tangential force. The contribution to the force from the entire spiral pattern in the self-gravitating spiral arms model, in contrast to the TWA in which the force is determined by local properties of the arms, produces important differences regarding the force profiles. For instance, it causes the radius at which the radial force changes from negative to positive values to be closer to the spiral locus than for the TWA model. For example, if we look at the bottom-left panel of Figure 11.6a corresponding to $\phi = 120^\circ$ we see that the radius of the locus is 7.2 kpc: this coincides by definition with the potential minimum in the TWA and it is the point where the force changes from positive to negative. The radius at which the force changes from negative to positive (interarm region) is 4.7 kpc for the TWA but 6.4 kpc for the self-gravitating arms which is closer to the locus. Also the maxima of the radial force are achieved at larger R for the self-gravitating spiral arms. In addition, the attraction of the whole spiral pattern shifts the radial force to negative values at larger radius. See for example the variation of the radial force with R in any of the panels of Figure 11.6a or the variation of the radial force as one moves to panels corresponding to larger radius in Figure 11.6b.

Pichardo et al. (2003b) also compared the potential and force fields produced by the present 3D-spiral mass distribution with a TWA but showing examples using different parameters from the ones that are used here. Their conclusions are however extensible to our study. They conclude that the observed differences between models are due to the effect of the self-gravitation of

[6] Although it would seem that the beginning of the TWA arms is set to smaller R in Figure 11.5b than in Figure 11.5a, the circle at $R = 3.3$ kpc in this plot shows that the no arrow begins at a shorter R.

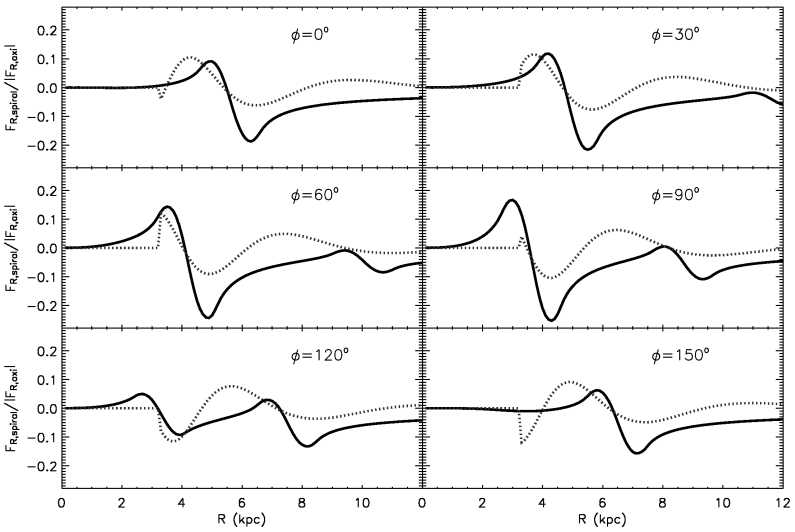

(a) As a function of radius for fixed azimuths

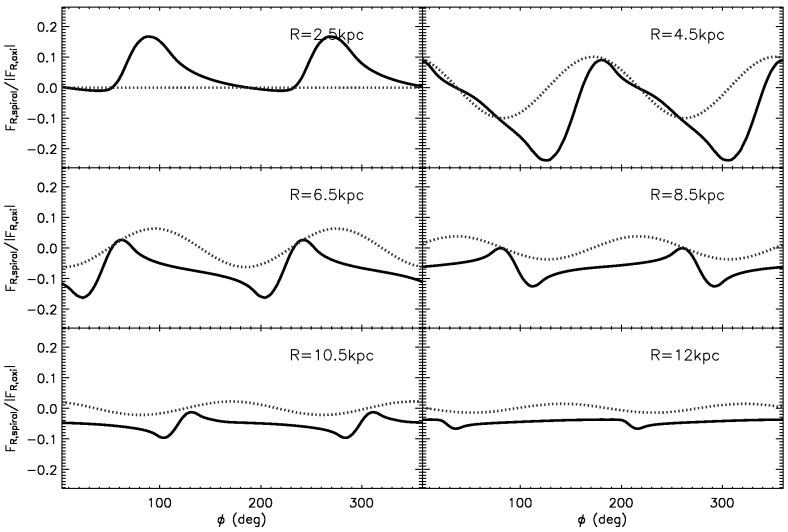

(b) As a function of azimuth for fixed radii

Figure 11.6: **Spiral arms radial force.** Radial force scaled to the radial axisymmetric force. The solid line corresponds to the self-gravitating arms whereas the dotted line shows the model of the TWA.

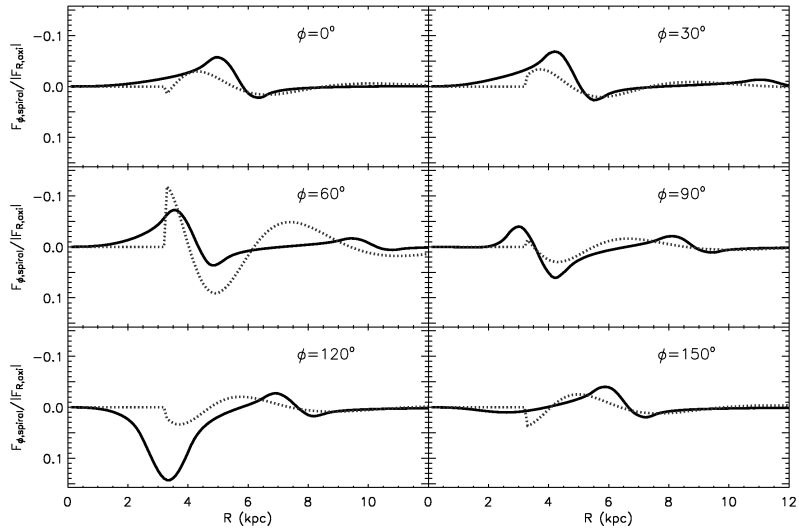

(a) As a function of radius for fixed azimuths

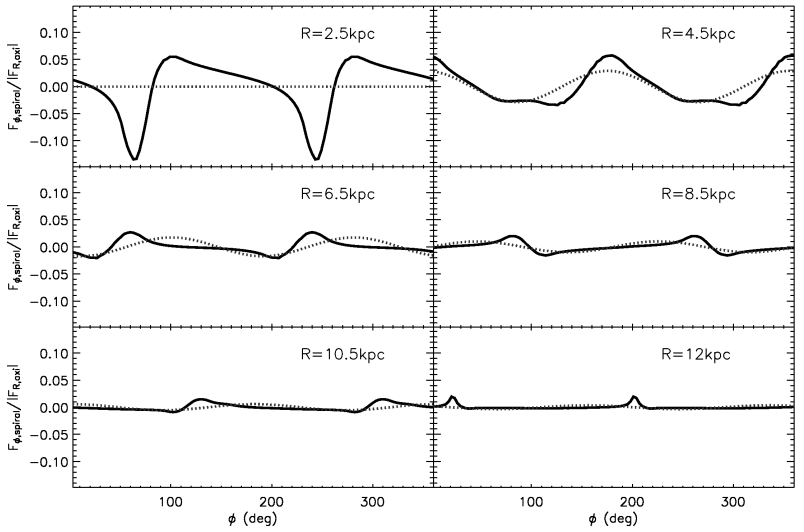

(b) As a function of azimuth for fixed radii

Figure 11.7: **Spiral arm tangential force.** Tangential force scaled to the radial axisymmetric force. The solid line corresponds to the self-gravitating arms whereas the dotted line shows the model of the TWA.

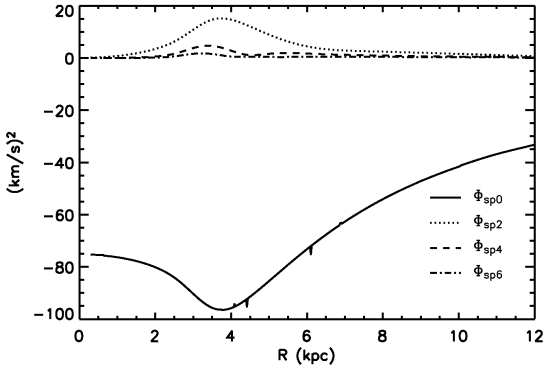

Figure 11.8: **Fourier decomposition of the spiral arms potential.** Modes of the Fourier decomposition of the potential of the self-gravitating spiral arms.

the mass of the spiral arms, important in the middle and outer Galactic regions. The self-gravity of the spiral pattern (i.e. contributions to the potential from the entire pattern), which is not accounted for in a potential like that of the TWA (which acts more like a local approximation), cause the local spiral potential to adopt shapes that are not correctly fit by the simple perturbing term that has been traditionally used. As proved in Franco et al. (2002), this difference have far-reaching consequences on the gaseous dynamical behaviour in a potential of this type and consequently, differences in the stellar response may be expected too. The study of the effects of this new model on the local stellar velocity distribution which is addressed here have not been considered before.

From this study we see that the quotient between the radial force of the self-gravitating spiral arms and the background peaks at 0.24. This corresponds to the minimum reached for $R \sim 4\,\mathrm{kpc}$ and $\phi \sim 90^\circ$ (see middle right panel of Figure 11.6a). At the solar position the radial force produced by the arms scaled to the radial axisymmetric force is 0.06. However, in order to be compared with observational values of the spiral strength, this must be done in terms of the parameters described at the beginning of the section. The Fourier decomposition (Equation 11.5) of the self-gravitating spiral arms potential is shown in Figure 11.8. Obviously, in the decomposition of a TWA model for the spiral arms only an $m = 2$ component would show up whereas the self-gravitating spiral arms have a large $m = 0$ component that contributes to the axisymmetric part of the global potential. It also has a non-vanished $m = 4$ and $m = 6$ terms. Figure 11.9a shows the parameter q_r for this model (Equation 11.7). From this we see that the $m = 2$ radial force of self-gravitating spiral arms with respect to the total axisymmetric radial force is 13%. When comparing this Figure with the radial forces of Figure 11.6 we see that the peaks of that Figure were enhanced only due to the contribution of the $m = 0$ component of the

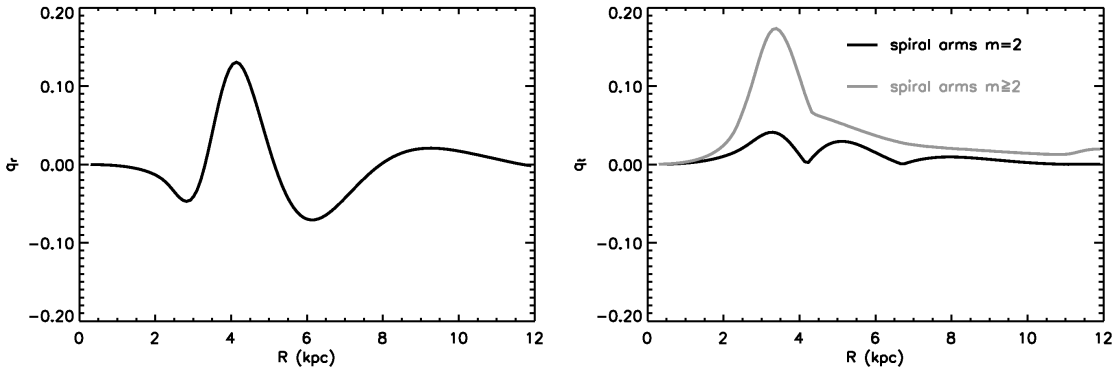

(a) q_r (b) q_t

Figure 11.9: **Spiral arms strength.** Quantification of the spiral arms strength through the parameter q_r and q_t. The grey curve in (b) corresponds to the parameter Q_T.

force that we were attributing to the spiral arms instead of to the axisymmetric background. Around $R_\odot$ the parameter q_r takes a value of 0.02. According to Patsis et al. (1991), strong spirals are those in which the force produced by the spiral perturbation is greater than 6% of the background force. Galaxies with a percentage up to 16% were found. However, an specific potential model for the axisymmetric background and for the spirals were used in that study to estimate values and, therefore, we believe that it is not straightforward to consider our default self-gravitating spiral arms as strong.

The parameter q_t (Equation 11.8) is shown in Figure 11.9b. The grey curve in Figure 11.9b is directly the parameter Q_T (Equation 11.9) and is equivalent to q_t but includes all the modes with $m \geq 2$. In this case weird shapes are obtained for this parameters as in the case of observed external spiral galaxies (see Figure 6 of Block et al. 2004). The maximum value for q_t is 0.041 whereas Q_s (maximum Q_T) is 0.18. In Block et al. (2004) the spiral strengths Q_s range from 0 to 0.46. It is again risky to compare the obtained Q_s for our model with the observations. There are only 15 galaxies in the sample of galaxies for which that observational study was carried out and also the observational method entails a delicate separation between spiral and bars which is direct in our potential model. Nevertheless, this preliminary study points to the conclusion that the self-gravitating spirals of the PM04–MW potential model are in the middle of the range that is found for external galaxies.

Among the specific studies that use a potential model for the spiral arms that are also devoted to study moving groups we find for example, Chakrabarty (2007) who used a model following the TWA with 4 equivalent arms. This number of arms, which seems in disagreement with the

latest observations (Benjamin et al. 2005), makes it difficult to compare directly her results with the present ones. Moreover, in that case spiral arms at the weaker end of the observational range (with a fractional amplitude of less than 4% of the background disc density) were used whereas in the present study relatively moderate spirals are obtained when the default value of the mass is used. As stated in Section 11.2, smaller values for this parameter will be explored in Part V.

On the other hand, the locus of the TWA spiral arm in Quillen & Minchev (2005) is based on Drimmel & Spergel (2001) as the self-gravitating arms. However, the location of the Sun is nearer the Perseus spiral arm in their favoured model. In terms of the parameter ϕ_{0sp}, which is defined as the angular offset between the Sun and the peak of the spiral at the same radius, their best match with observations is obtained using $\phi_{0sp} = 15^\circ$ (parameter γ in that study, see their Figure 5). By contrast, the present model has $\phi_{0sp} = 88^\circ$. In other words, the orientation of the arms in that study is equivalent to locate the Sun at $\phi = 73^\circ$ in our coordinate system keeping fixed the orientation of the arms (see Figure 1.1). However, the indetermination of the exact position of the arms and in the general distance scale of the Galaxy, makes it difficult to fix the exact orientation of the spiral arms. This characteristic of the spiral arms, despite having a first guiding default value, will be kept variable in our study as well as other uncertain parameters. Besides, the range of pattern speed in Quillen & Minchev (2005) was $\sim 15{-}17\,\mathrm{km\,s^{-1}kpc^{-1}}$. Here we will use a range that reaches larger values ($15 - 25\,\mathrm{km\,s^{-1}kpc^{-1}}$) and the default pattern speed is $\sim 20\,\mathrm{km\,s^{-1}kpc^{-1}}$. Regarding the strength of the spiral, Quillen & Minchev (2005) quantifies it in terms of density, fitting it to the values offered by Drimmel & Spergel (2001). This latter study pointed out that the density contrast of the spiral arms of the MW appears to be smaller than that of found in other galaxies. Therefore, the strength of the spiral in Quillen & Minchev (2005) could be considered as relatively weak. However, in Drimmel & Spergel (2001) it is suggested that their obtained weak spiral arms may result from several underestimations of their method. The confirmation of these underestimations would imply the existence of more massive arms in the MW.

The bar

A comparison between this model for the bar and the ones used in the other studies of this field deserves also special attention. The usually used model is the one in Dehnen (2000) which consist of an elaborated version of a potential dominated by the quadrupole ($m = 2$ component of the Fourier decomposition of the potential):

$$\Phi_b = A_b \cos\left(2[\phi - \Omega_b t]\right) \times \begin{cases} -(R_b/R)^3 & \text{if } R \geq R_b, \\ (R/R_b)^3 - 2 & \text{if } R \leq R_b \end{cases} \tag{11.12}$$

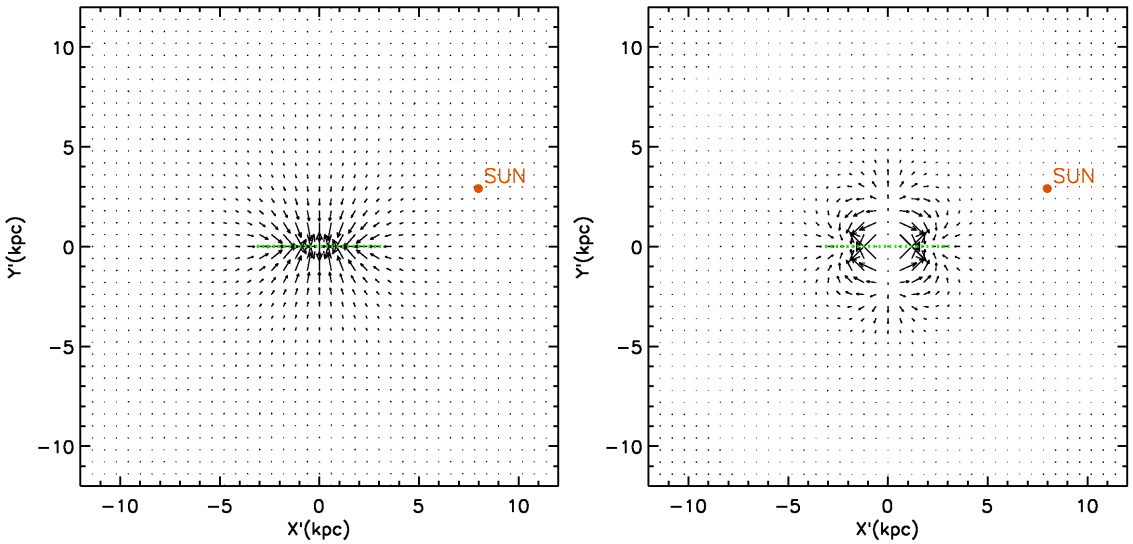

(a) Prolate bar (default parameters of Table 11.4)

(b) Quadrupole bar with $\alpha = 0.01$

Figure 11.10: **Force field of different bar models.** Detailed force fields as vector plots for the different models. Note that in this plots the $X'Y'$ reference system has been oriented so as to place the major semi-axis of the bar along the X' axis.

where R_b and A_b are the size and the amplitude of the bar, respectively. The strength of the bar is quantified by the parameter $\alpha = 3\frac{A_b}{v_0^2}\left(\frac{R_b}{R_\odot}\right)^3$ which is the ratio of the radial forces due to the bar and the axisymmetric background at the Sun galactocentric radius on the bar's semi-major axis, being v_0 the circular velocity at $R_\odot$.

To compare the different bar models it is useful to study their force fields. These are presented in Figure 11.10 as the absolute force field in a vector plot. The amplitude of the quadrupole bar has been chosen so as to produce $\alpha = 0.01$ (as in Dehnen 2000) at the present default solar radius $R_\odot = 8.5\,\mathrm{kpc}$. Note that these panels have a new reference system $X'Y'$ where the long semi-axis of the bar is on the X' axis. The evident differences between these panels are next explained in terms of the decomposition of the forces in the monopole and quadrupole components.

In order to compare the quadrupole potential and the prolate bar, Figure 11.11a is a cut of the previous Figure 11.10. It corresponds to the bar's radial force as a function of radius along the direction of the major axis of bar for the prolate and the quadrupole bar with $\alpha = 0.01$. The radial force has been scaled to the same axisymmetric radial force to facilitate the comparison. In particular, we use the model by Allen & Santillán (1991) of the PM04–MW potential model. Note that for the prolate bar we have reduced the mass of the bulge of the axisymmetric part

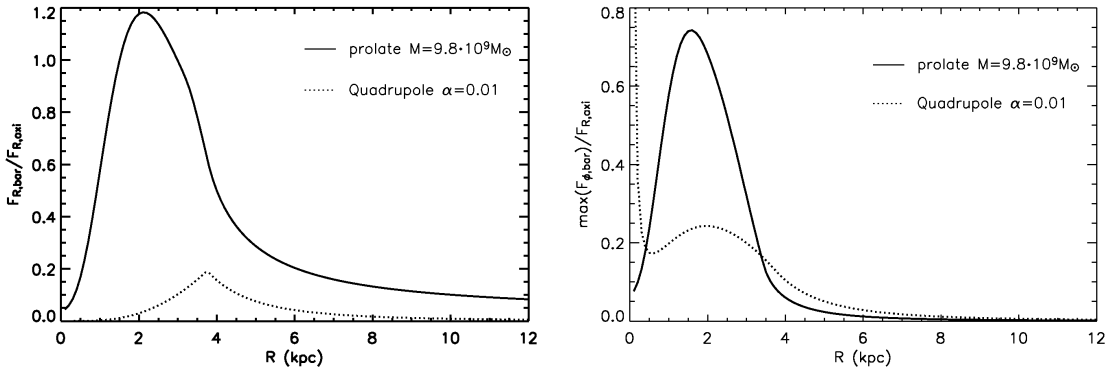

(a) (b)

Figure 11.11: **Radial force of the bar.** Comparison of (a) the bar's radial force along the major axis of the bar and (b) the bar's maximum tangential force for the different models.

in order to maintain the total central mass (see Section 11.3). On the other hand, Figure 11.11b compares the tangential force of the bar for different bar models. This is done using the maximum bar's tangential force along all azimuths for a given radius. The values are also scaled to the radial axisymmetric force of the model by Allen & Santillán (1991). From these two panels of Figure 11.11, it might appear that the prolate bar seems to be by far the strongest one. However, to perform a fair comparison we must do it in terms of the Fourier decomposition of the forces. The prolate bar contributes substantially to the monopole component of the potential as its introduction has involved an additional mass component to the global model. The not null radial force curve for the prolate model at very large R in Figure 11.11a is an indicative of this fact. By contrast, the quadrupole bar entails an total integrated mass of 0.

The Fourier decomposition of the potential in the $m = 0$, $m = 2$, $m = 4$ and $m = 6$ modes according to Equation 11.6 allows us to prove the important contribution to other modes apart from the $m = 2$ in the prolate model. This decomposition is shown in Figure 11.12a for the prolate bar and in Figure 11.12b the quadrupole bar with $\alpha = 0.01$. Obviously, in the decomposition of the quadrupole only an $m = 2$ component shows up whereas the prolate bar has a large $m = 0$ component that contributes to the axisymmetric part of the global potential. It also has a non-vanished $m = 4$ and $m = 6$ terms.

Our last exercises allow us to compare the $m = 2$ force component of the different bar models scaled to the total axisymmetric radial force from the $m = 0$ component. The parameter q_r calculated as in Equation 11.7 is shown in Figure 11.13a. Note that for the model with the quadrupole bar the $m = 0$ component comes exclusively from the axisymmetric force of the

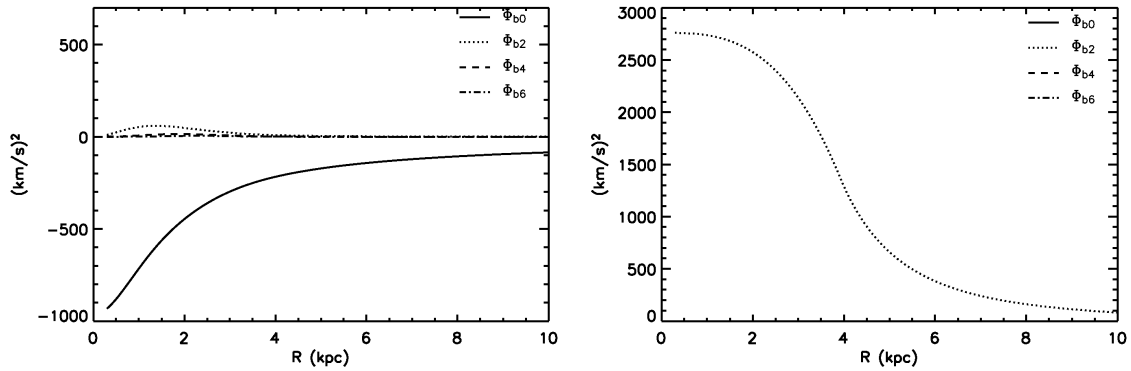

(a) Prolate bar

(b) Quadrupole bar with $\alpha = 0.01$

Figure 11.12: **Fourier decomposition of the bar potentials.** Comparison of the modes of the Fourier decomposition of the potential of the different models. The grey curve in (b) corresponds to the parameter Q_T.

Allen & Santillán (1991) model. By contrast, the prolate bar also contributes in the $m = 0$ potential, i.e. in the denominator of Equation 11.7. This Figure demonstrates that the peak of the radial force of the prolate bar is slightly lower than for the quadrupole bar. The maximum $m = 2$ component of the radial force with respect to the total axisymmetric radial force is of 19% for the quadrupole bar and 14% for the prolate bar. Besides, the curves are completely different in terms of the shape. Note the non-differentiable cusp of the quadrupole model at the inner parts of the disc which is totally solved for the prolate bar. It is worth mentioning that the radius of this peak for the quadrupole model depends on the pattern speed of the bar (here set to the default value) through the relation between corotation radius and bar length. Also note the negative values of q_r for the prolate bar at inner radii. This negative contribution is counterbalanced by the other terms of the multi-pole expansion as no negative values appear in the global case (Figure 11.11a). However, at large distances around $R_\odot$ the parameter q_r takes lower values for the prolate bar than for the quadrupole model. In particular, in terms of the α parameter of Dehnen (2000) (ratio of the radial forces due to the bar and the axisymmetric background at the Sun Galactocentric radius) it is 0.005 for the prolate bar and it has been set to 0.01 for the quadrupole bar.

We can also study the parameter q_t. For the two models, these are shown in Figure 11.13b. Again we see that at larger radius the prolate bar produces lower force than the quadrupole bar. This plot also shows that the prolate bar has only slightly higher q_t at the inner regions. The maximum value for the prolate bar is 0.3 and for the quadrupole bar it is 0.24. The grey curve in Figure 11.13b is the parameter Q_T (Equation 11.9) which is equivalent to q_t but includes

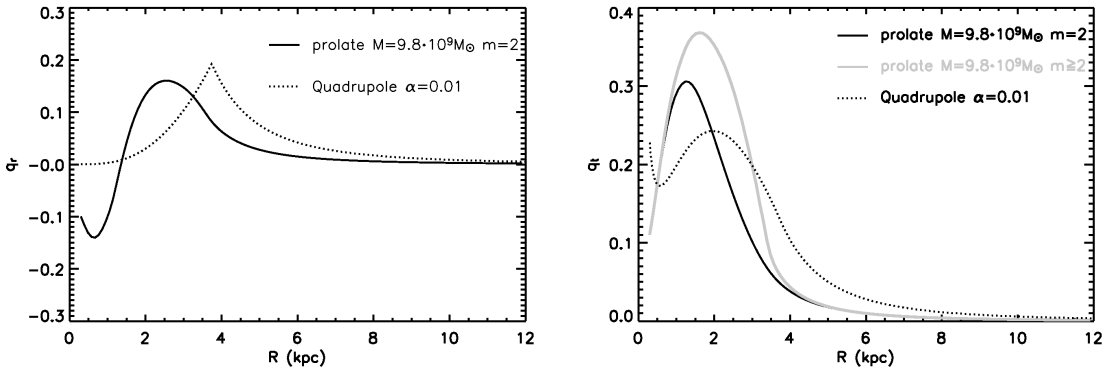

(a) q_r (b) q_t

Figure 11.13: **Bar strength.** Comparison of (a) the bar's parameter q_r and (b) the bar's parameter q_t for the different models.

all the modes with $m \geq 2$. In particular the maximum of these curve Q_b gives a single and quantitative measure of the torque or strength of the bar according to Buta (2001). This value is 0.38 for the prolate bar and 0.24 (equal to q_t) for the quadrupole bar. These values of Q_b for the two models are in perfect agreement with the range of values found by Block et al. (2004) with a sample of external galaxies which is from 0 to 0.75.

To quantify how weak or strong is the bar of our study, their maximum values for q_r and q_t (or similarly Q_b) and also the value of α can be compared with the ones of the literature. In particular, the quadrupole bar of Equation 11.12 is used in Dehnen (2000), Fux (2001) and Minchev et al. (2010). The bar of Chakrabarty (2007) is a pure quadrupole term. Differently to the previous analysis in this section, those studies were carried out with a different axisymmetric potential. In general, power-law potential were used. Recalculating the values of q_r and q_t using the corresponding axisymmetric potentials, we found the values of Table 11.5. The bar in Minchev et al. (2010) is equal to that of Dehnen (2000) and Chakrabarty (2007) uses a quadrupole bar quantified to be between the Dehnen (2000) and Fux (2000). The strength in the inner parts of the disc can be quantified by the maximums of the parameters q_r and q_t. We conclude that at small radius the prolate bar is comparable to the bar in Fux (2001). However, in the outer parts of the disc the prolate bar is substantially weaker than the other quadrupole bars. In particular, the range used by Dehnen (2000) for the strength parameter α is $[0.007, 0.013]$ (the standard value is taken as 0.01). Fux (2001) used the same model but with a stronger bar with α in the range $[0.011, 0.022]$. By contrast, the prolate bar used in this study has $\alpha = 0.005$. In the fourth row of Table 11.5 we show the parameters for the quadrupole bar with the axisymmetric part of Allen & Santillán (1991) that is used in this thesis in some of the

Table 11.5: Parameters q_r, q_t and α for the bar of the present study and for the standard models of other studies in the field.

	q_r max	q_t max	α
Prolate bar (axisymmetric part of Allen & Santillán 1991)	0.140	0.30	0.005
Quadrupole bar Dehnen (2000) (axisymmetric power-law potential)	0.085	0.11	0.010
Quadrupole bar Fux (2001) (axisymmetric power-law potential)	0.190	0.25	0.022
Quadrupole bar of this thesis (axisymmetric part of Allen & Santillán 1991)	0.190	0.24	0.010
Massive prolate bar (axisymmetric part of Allen & Santillán 1991)	0.190	0.36	0.007

simulations devoted to compared the prolate and quadrupole bars. This model has been fixed to have the same parameter α as in Dehnen (2000). However the forces at the inner parts of the disc resembles our default prolate bar. Also a more massive prolate bar ($M_b = 1.4 \times 10^{10} \mathrm{M}_\odot$) will be used in the simulations. Its corresponding strength parameters are shown in the last row of Table 11.5.

To conclude with this analysis, the prolate bar is comparable to the quadrupole model in terms of its quadrupole term in the multi-pole expansion but is a more sophisticated and realistic model which includes also other terms. Although the maximum values of the forces of both models are similar, the shapes of the forces at inner radius are significantly different. Specially the prolate bar describes better the regions near or in the bar itself whereas the quadrupole bar is an approximations for outer regions. We have also seen that the prolate bar of the PM04–MW potential model has a very low strength at the outer parts compared with other quadrupole models used in the literature. Any attempt of make these models more similar fails. Trying to have similar bars in the inner regions will cause the outer regions to differ substantially and vice versa due to the different shapes of the bar potential and of the axisymmetric part.

Part V

MOVING GROUPS AS IMPRINTS OF THE MILKY WAY STRUCTURE

This part reports the results of the test particle simulations of the methodology developed in Part IV. Our method allows us to evaluate the role of realistic non-axisymmetric components of the MW, namely the spiral arms and the bar, on the formation of moving groups in the disc. In particular we obtain the induced kinematic distribution not only of the solar neighbourhood but in other positions of the disc. We explore the parameter space of the PM04–MW potential model using different simulations in order to evaluate the effects of each particular characteristic of the spiral arms or the bar on the velocity distributions. We also explore the results on disc with different initial conditions and compare our results with studies by other authors obtained through other methods. The final velocity distributions are treated also with the WD multiscale technique as the observational sample in order to be statistically analysed and compared with observations and with the results of other studies.

Chapter 12 deals with some preliminaries regarding the presentation of the results, by giving more specific details about the simulations and methodology. Chapter 13 examines the effects of the spiral arms while Chapter 14 does the same with the bar. Next the effects produced on a hotter population (IC3) are shown separately in Chapter 15 as they deserve special considerations. Finally, Chapter 16 presents the results of the spiral-bar PM04–MW potential model (the model that includes bar and spiral arms). At the end of the main chapters in this part, we summarise and discuss the results. In all cases, the simulations are presented beginning with the default values of the PM04–MW potential model and with the default parameters of the IC described in Part IV. After this, variations of these parameters will be studied and the corresponding resultant Figures are mostly shown in Appendix B.

Chapter 12

Preliminaries

The complexity of the problem lead us to simplify the methodology as follows. First, we need to study the effects of each non-axisymmetric component separately before considering the more complex problem of the spiral-bar model including both components. Therefore, separate results are presented for the PM04–MW potential model including only spiral arms (Chapter 13), the PM04–MW potential model including only the bar (Chapter 14) and the spiral-bar model (Chapter 16). Secondly, for the moment our main aim is to study the effect of these non-axisymmetric Galactic components on the kinematic distribution of regions located in the plane ($z = 0$) or near the plane. We will assume that the vertical motion is decoupled with the in-plane movement, which is reasonably true for nearly circular orbits and that do not take larger heights above the plane (see e.g. Binney & Tremaine 2008). For these orbits the timescales of the vertical motion is short compare to in-plane motion and the vertical frequency do not change significantly along the orbit. The validity of these assumption for our hottest IC (IC3) will be discussed in Chapter 15. For this reason, as a first natural step, our analysis is for the moment restricted to simulations for $z = 0$ and the 3D study is postponed to future work. This allows us also to reduce significantly the computing time of the simulations.

We use the galactocentric cylindrical coordinates (radius R and azimuth ϕ) detailed in Section 1.4. In general, figures with 9 panels will be offered for each simulation corresponding to the circular regions of 500 pc located at $R = 8.5$ kpc, on the Galactic plane and at $\phi = 0°, 20°, 40°, 60°, 80°, 100°, 120°, 140°, 160°$ (circles in Figure 12.1. The Sun is located at $\phi = 0°$ and $R = R_{\odot} = 8.5$ kpc but as this is uncertain, it will be worth studying other regions on the plane. Note that if we want to relate the azimuthal angle ϕ of a certain region with the corresponding phase with the bar or the spiral is:

$$\phi_{0sp} = 88° - \phi \tag{12.1}$$

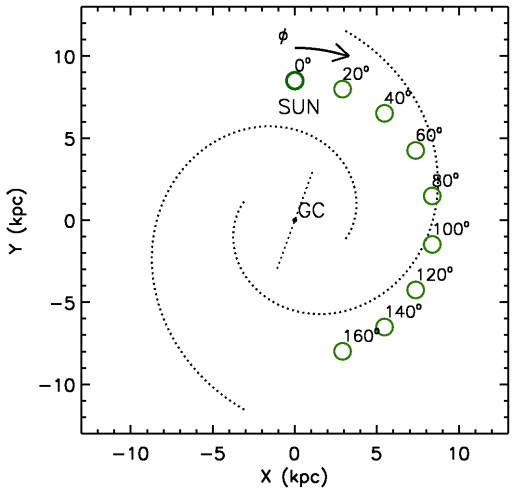

Figure 12.1: Diagram of the regions where the velocity distributions are analysed superimposed to a sketch of the MW disc.

$$\phi_{0b} = 20^\circ - \phi \tag{12.2}$$

More important, the results must be compared to the observed velocity distributions which at this moment is available with enough accuracy only for the solar neighbourhood (Figure 6.1 of Part III). An additional limitation appears in this comparison due to the uncertainty in the velocity of the Sun with respect to the LSR. Although the commonly used values for $(U_\odot,\ V_\odot,\ W_\odot)$ are around $(10, 5, 7)\,\mathrm{km\,s^{-1}}$ (Dehnen & Binney 1998), several new studies suggest that these values should be modified to $(11, 12, 7)\,\mathrm{km\,s^{-1}}$ (Binney et al. 2010, Schoenrich et al. 2009). In Figure 6.1 the heliocentric velocities are presented, that is not corrected for the solar motion. The simulations show peculiar velocities and a certain value for the solar motion should be assumed in order to compare exact positions in the U–V plane. The indetermination in the solar motion and specially in the $V_\odot$ component, means a limitation for the comparison.

The denoising method WD described in Part II as been applied to the results of the simulations as with observations in Part III. This helps us to treat the Poisson noise of the results. Also contour lines have been added in some cases to highlight the structures. The simulations have been run mainly at KanBalam (HP CP 4000 cluster with distributed memory and 1368 processors with AMD Opteron 2.6 GHz core) at the DGSCA/UNAM and at Sol (CATON cluster with 72 cpus Intel Xeon 2,73Ghz core) at the DAM/UB.

Chapter 13

Imprints of the spiral arms

In this chapter the kinematic structure developed by the self-gravitating spiral arms of the PM04–MW potential model is presented. First in Section 13.1 the results of these simulations with the default parameters of Tables 11.2 (for the axisymmetric component) and 11.3 (for the spiral arms) are presented for IC1 (default values of Table 10.1). Afterwards, the effect of the variation of some default parameters is shown. Finally, the model with only spiral arms is applied to IC2 (default values of Table 10.1). The results for IC3 are postponed for Chapter 15 as the hottest disc deserve special considerations. In Section 13.2 we study the regularity of the orbits on the U–V plane for the self-gravitating spiral arms. At the end, Section 13.3 shows a summary and a discussion of the results of this chapter.

13.1 New insights on the influence of the spiral arms

IC1– Figure 13.1 shows the U–V plane for the regions of Figure 12.1 at different azimuths ϕ and at $R = 8.5\,\mathrm{kpc}$, assuming the IC1. We find that the self-gravitating spiral arms produce interesting effects on the velocity distribution in these positions. In general, the model produces a central group (low epicyclic energies) that in some cases presents several structures inside and a branch at low angular momentum (with $V \sim -40\,\mathrm{km\,s^{-1}}$) separated from a central structures.

Regarding the central structures, the richest case is achieved at $\phi \sim 100°$ where three slightly tilted branches appear, resembling some of the observed central kinematic branches. Figure 13.2 compares the branches for the observations of the solar neighbourhood and the simulations at this position. The component V_β is the projection of the U and V velocities to an axis perpendicular

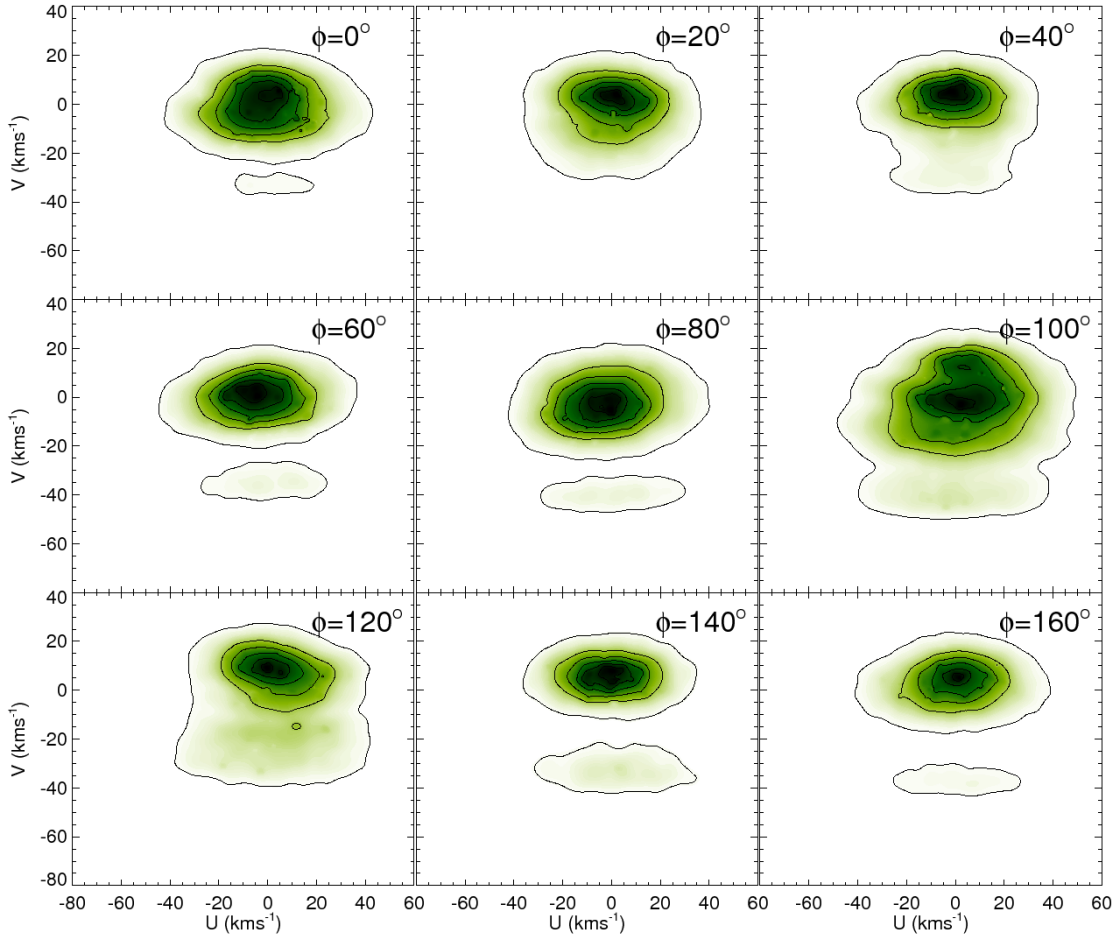

Figure 13.1: **Kinematic effects of the spiral arms on a cold disc.** U–V velocity distributions after WD at $R = 8.5\,\mathrm{kpc}$ and at different azimuths ϕ for the simulations with the PM04–MW potential model using only spiral arms and IC1.

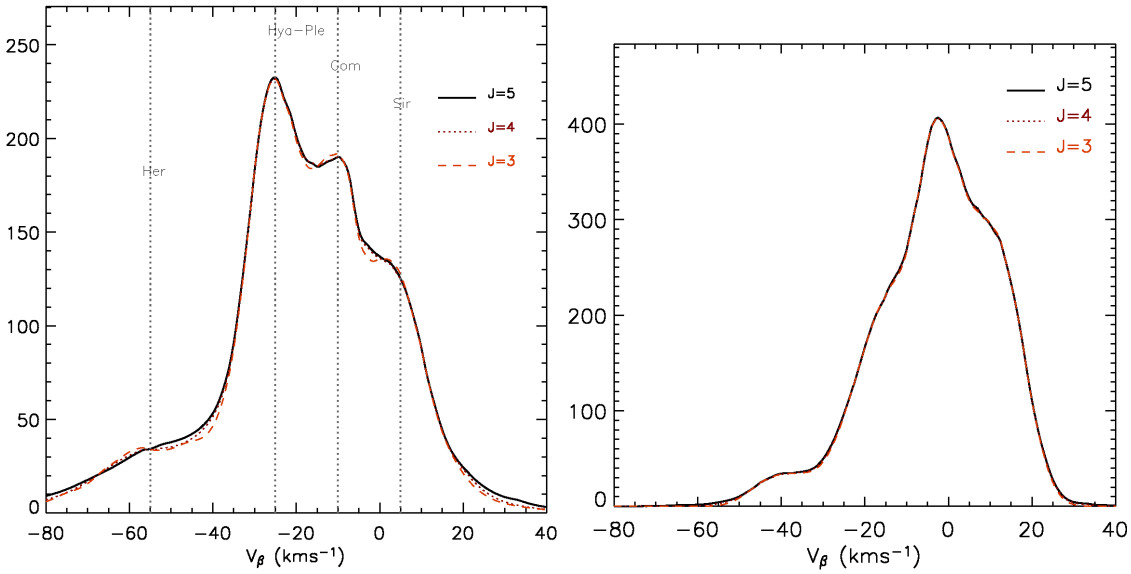

(a) Observations (heliocentric)

(b) Simulations (RSR)

Figure 13.2: **Observational kinematic branches and branches induced by the spiral arms.**Comparison between the branches of the observational sample and the branches generated by the simulations with the PM04–MW potential model using only spiral arms and IC1 at $\phi = 100°$ and $R = 8.5\,\mathrm{kpc}$. The branches are shown in the V_β component (clockwise rotation of $\beta = 16°$ of the U–V plane) after WD for several scales.

to the branches (clockwise rotation of $\beta = 16°$). Please note that due to the fact that Figure 13.2a shows the heliocentric velocities whereas Figure 13.2b shows the velocities with respect to the RSR, the V_β axis are not directly comparable. The fact that the spiral arms are able to produce these similar branches is encouraging. This position corresponds to an azimuth very close to the arm (see Figure 12.1), which in principle is not a plausible position of the Sun with respect the K-band spiral arms. However, the uncertainty about the real positions of the arms of the MW is large and complex due to the existence of the additional gaseous arms (see Section 11.2) that deprive us from rejecting the possibility that the Sun is near an spiral arm. The first panel of Figure 13.1 ($\phi = 0°$) shows the U–V plane for the supposed solar position according to the default PM04–MW potential model. At this position the central part of the distribution seems to be split into two groups or branches.

In addition, the model reproduces for a wide range of ϕ a branch at low angular momentum with $V \sim -40\,\mathrm{km\,s^{-1}}$ which is consistent with the V velocity of the observed Hercules structure. Up to now this structure has been believed to be exclusively due to bar resonances (see Chapter 2). To our knowledge, this is the first time that an unbarred model has produced a similar structure. Although the shape of the structure at $V = -40\,\mathrm{km\,s^{-1}}$ is not exactly equal to the

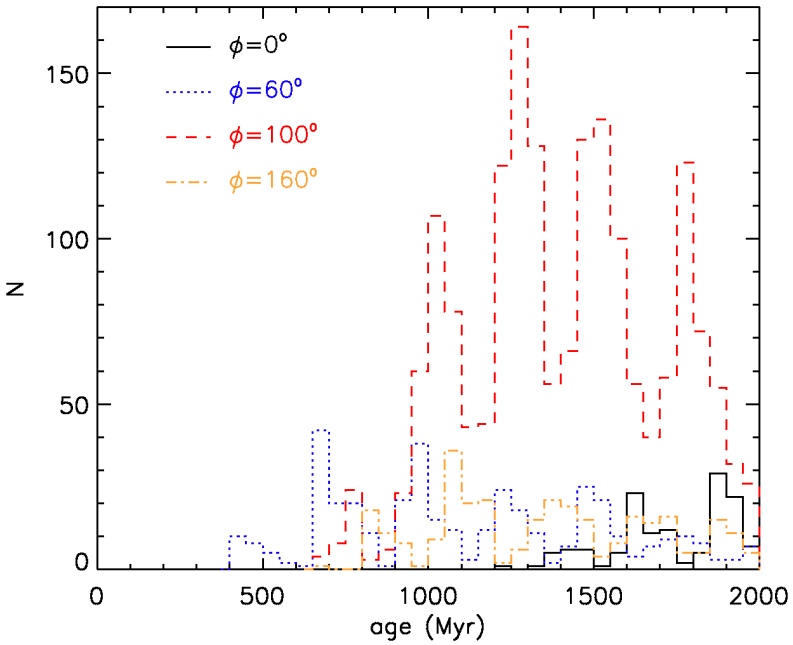

Figure 13.3: **Age distribution of a simulated kinematic structure.** Age (or integration time) distribution of the particles belonging the supposed Hercules structure at different galactic regions ϕ.

Hercules branch, especially regarding its inclination in the U–V plane and regarding its average radial motion $\overline{U} < 0$ (Figure 6.1), our simulations show that the spiral arms by themselves crowd the velocity space at these negative V. At $\phi = 0°$, which would correspond to the solar neighbourhood according to the PM04–MW potential model, despite being fainter than in other azimuths, the analogous to the Hercules moving group also appears. Given the uncertainty on the exact position of the arms, it is interesting to consider also small variations respect to the configuration of Drimmel & Spergel (2001). Consequently, velocity distributions such as the one for $\phi = 160°$, corresponding also to inter-arm regions, with a more prominent Hercules structure should be highlighted.

It is very significant that we find that the Hercules structure may be produced by the spiral arms and not only by bar resonances as traditionally believed. Dehnen (2000) concluded that the Hercules branch is unlikely to have been produced by resonant scattering processes due to spiral arms. His main argument was that spiral arms do not act on stars with epicycles greater than the interarm separation. However, in our case the interarm separation in the locus of our default model is in the range $5.5 - 7\,\mathrm{kpc}$ whereas the particles in the structure created in

our simulations (at $U \sim [-30, 30]$ and $V \sim [-45, -35]$) have a radial excursion amplitude[1] of about 3 kpc. This is sufficient to produce the Hercules structure and still in agreement with the argument by Dehnen (2000).

The fact that the test particles in the simulations with IC1 have different integration times (Procedure 1) allows us to study the ages (age$=-\tau$) of the particles in each velocity distribution or in particular structures in the U–V plane. It is very interesting for instance, to look at the ages of the particles belonging to the structure equivalent to the Hercules moving group. We see that this kinematic group have a distribution of integration times different for each region at different ϕ. Figure 13.3 shows the age histograms of the regions $\phi = 0°$, $\phi = 60°$,$\phi = 100°$ and $\phi = 160°$ for this particular structure. The minimum age of the distribution for these 4 regions are respectively: 1200 Myr, 420 Myr, 660 Myr and 650 Myr. In next Section 13.2, it will be seen that this can be explained in terms of the orbits of these particles and the gap near age$= 0$ in Figure 13.3 is due to the fact that particles need a certain minimum time to reach the orbital condition that corresponds to this structure.

Other characteristics of the particles forming this kinematic structure at $V \sim -40\,\mathrm{km\,s^{-1}}$ are the following. First, they all come from inner radii compared with the rest of particles that have ended up in this region. The grey particles in Figures 13.4a and 13.4b are the particles of the supposed Hercules kinematic structure of the regions at $\phi = 0°$ (inter-arm region) and $\phi = 100°$ (arm region) respectively. The initial radius of all the particles in these regions are shown in the histograms of Figures 13.4c and 13.4d, where the grey dashed lines correspond to the particles of the supposed Hercules. These particles are distributed at inner radii compared to all particles that end up in the final region at 0° and 100°. Secondly, if the final distribution in the X-Y plane of the particles is studied, we see that the particles of the structure at $V \sim -40\,\mathrm{km\,s^{-1}}$ are located in the inner parts of the region considered. This can be seen in Figures 13.4e and 13.4f for $\phi = 0°$ and $\phi = 100°$ respectively where again the grey points correspond to the particles in the supposed Hercules. Note that for $\phi = 100°$ the GC is located at the left side of the panel approximately in straight line whereas for $\phi = 0°$, it is located just below the panel (see Figure 12.1). Note also that for $\phi = 100°$ the particles are more extended all through the whole final region of 500 pc, reaching a larger fraction of the region. It is expected that considering regions near $\phi = 0°$ but at slightly different radius or azimuths, we would obtain different spatial extensions of the particles of this kinematic structure. This is be very useful in order to compare with observations. For instance, our preliminary results of Section 6.4 shown that the Hercules structure was weaker for a region located at $X > 160$ pc. For the moment, the spatial study of the observed moving groups is limited by the extension and precision of the current observational

[1] This value is obtained theoretically by calculating the epicyclic amplitude from the epicycle approximation (e.g. Asiain et al. 1999b) or directly from the orbits obtained in the simulation (see Section 13.2).

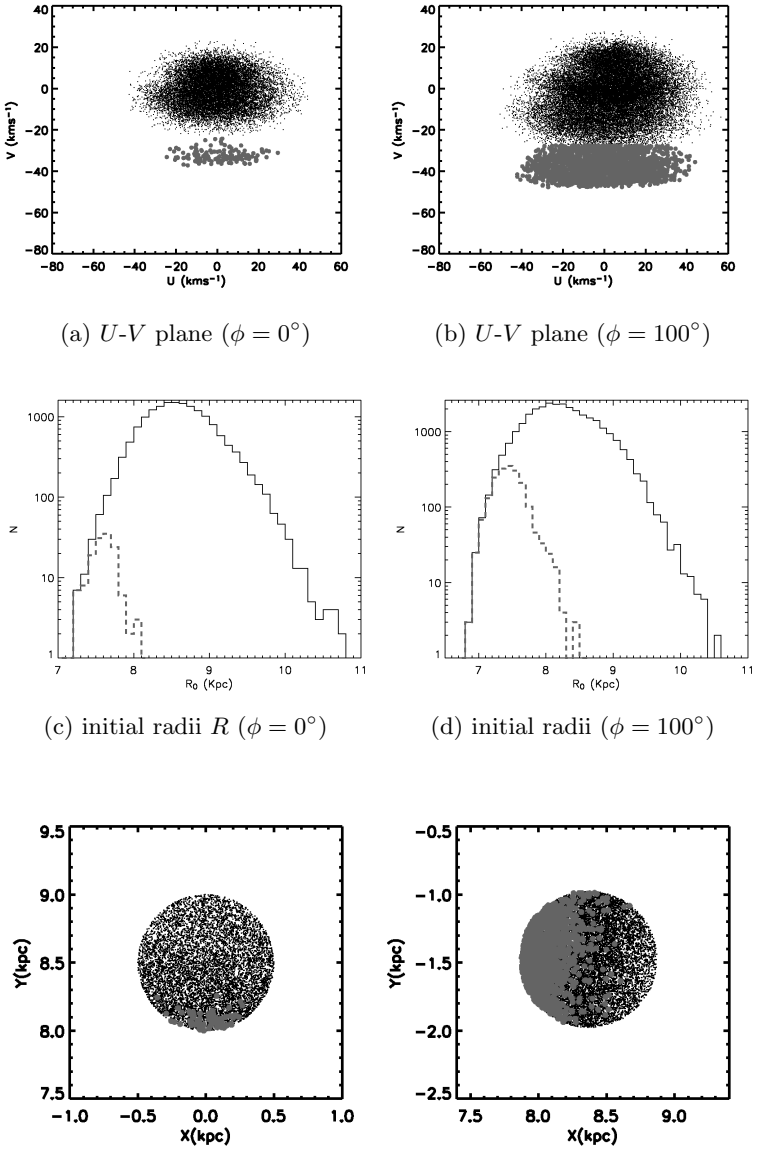

(a) U-V plane ($\phi = 0°$)

(b) U-V plane ($\phi = 100°$)

(c) initial radii R ($\phi = 0°$)

(d) initial radii ($\phi = 100°$)

(e) final X-Y plane ($\phi = 0°$)

(f) final X-Y plane ($\phi = 100°$)

Figure 13.4: **Spatial characteristics of a simulated kinematic structure.** Characteristics of the particles in the regions at $\phi = 0°$ (left column) and at $\phi = 100°$ (right column). The particles in the kinematic structure equivalent to Hercules are indicated with grey circles and grey dashed lines in the histograms and the rest of the particles are indicated with black dots and black solid lines.

samples and this deprives us to draw a definitive conclusion about the spatial extension of the observed Hercules moving group. However, the future characterisation of the spatial distribution of the stars in each moving group would suppose useful additional constrains in this study.

Varying the default parameters– Next we present the results of the simulations when the default values for some relevant parameters (pattern speed, pitch angle and mass) of the PM04–MW potential model are changed.

- **Pattern speed:** Changing the pattern speed Ω_{sp} of the spiral arms corresponds to bringing the resonances nearer or closer the solar radius and therefore we expect an important change in the velocity structures. With the default model $\Omega_{sp} = 20\,\mathrm{km\,s^{-1}kpc^{-1}}$, the ILR 4:1 is the nearest one as detailed in Section 11.2 and is located at radius $R = 7.0\,\mathrm{kpc}$. In Figure 13.5, the positions of the 4:1 ILR for several pattern speeds of the spiral arms are shown as vertical lines. This positions are obtained with the crossing of the horizontal lines corresponding to each Ω_{sp} with the $\Omega - \kappa/4$ curve. The vertical black line shows the radius of the default Sun, where the simulations are analysed. We have repeated the simulation for the values of Figure 13.5: $\Omega_{sp} = 15\,\mathrm{km\,s^{-1}kpc^{-1}}$, $\Omega_{sp} = 18\,\mathrm{km\,s^{-1}kpc^{-1}}$, $\Omega_{sp} = 22\,\mathrm{km\,s^{-1}kpc^{-1}}$ and $\Omega_{sp} = 25\,\mathrm{km\,s^{-1}kpc^{-1}}$ moving the ILR 4:1 to 9.5 kpc, 7.8 kpc, 6.2 kpc and 5.4 kpc. The results are shown in Appendix B in Figures B.5, B.6, B.7 and B.8 respectively. In the last two cases of higher pattern speed, the resonances are far from the Sun and only few significant structures are seen specially near the arm ($\phi \sim 100°$). However, for the first two cases corresponding to regions placed nearer the resonance different and abundant substructure appears. Specifically, these two cases correspond to being at 1 kpc out of the ILR 4:1 ($\Omega_{sp} = 18\,\mathrm{km\,s^{-1}kpc^{-1}}$) and being $\sim 1\,\mathrm{kpc}$ inside the ILR 4:1 ($\Omega_{sp} = 15\,\mathrm{km\,s^{-1}kpc^{-1}}$). For instance, it is interesting that for $\Omega_{sp} = 18\,\mathrm{km\,s^{-1}kpc^{-1}}$ the upper part of the distribution on the U–V plane is shifted to $U > 0$ as the observed Sirius moving group for $\phi = 0°$ and $\phi = 100°$. For $\Omega_{sp} = 15\,\mathrm{km\,s^{-1}kpc^{-1}}$ this also happens at $\phi = 20°$, $\phi = 40°$, $\phi = 100°$ and $\phi = 120°$.

- **Pitch angle:** Regarding the influence of the pitch angle i, a change from $i = 15.5°$ to $i = 12.0°$ (still between the limits of the observed values) causes the results of Figure B.9. The decreasing of the pitch angle results in a near position of the arms with respect to $\phi = 0°$ (see Figure 13.6). The phase difference is exactly of 53° at solar radius (the new orientation of the arms is $\phi_{0sp} = 35°$ whereas the default is $\phi_{0sp} = 88°$). Therefore the results for $i = 12.0°$ are very similar to Figure 13.1 for the default model except that it seems to be rotated $\sim 60°$ ($\phi = 0°$ for this case is approximately equal to $\phi = 60°$ for the default case in Figure 13.1). Apart from this difference, a slight weakening of the group

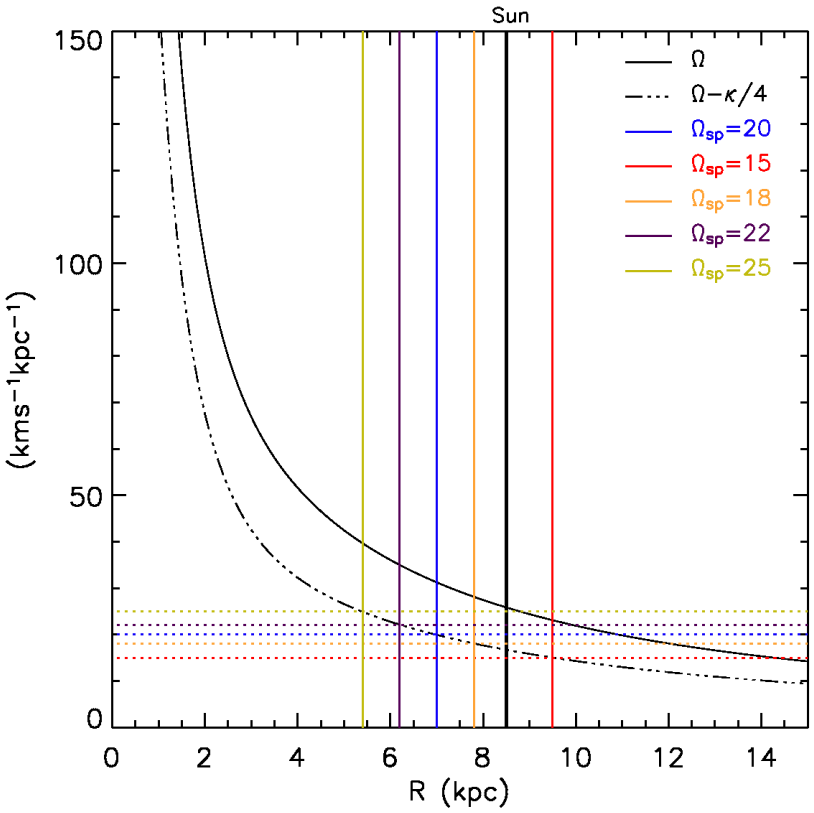

Figure 13.5: **Location of the spiral arm resonances.** Resonance curves in the Allen & Santillán (1991) axisymmetric model for corotation (Ω) and 4:1 ILR ($\Omega - \kappa/4$). The horizontal blue line corresponds to the default value of pattern speed of the spiral arms. The other coloured lines corresponds to several variations for this parameter. The vertical lines coloured following the same pattern indicates the position of the 4:1 ILR for each pattern speed. The default position of the Sun is shown with a black vertical line.

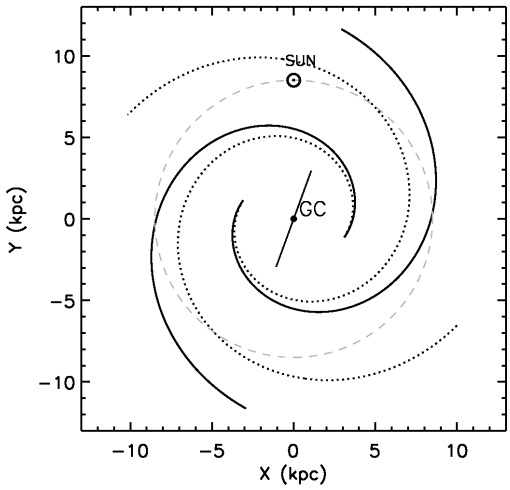

Figure 13.6: **Two different locus of the spiral arms.** Comparison between models with pitch angle $i = 15.5°$ (solid line) and $i = 12°$ (dotted line).

at low angular momentum (Hercules) but no other significant differences in the velocity distributions are observed.

- **Mass:** It is also worth mentioning that if the mass M_{sp} of the spiral arms is decreased from $M_{sp} = 0.05M_D$ to $M_{sp} = 0.03M_D$, only several but minor differences are observed (Figure B.10). First, the group at low angular momentum is still present although it is less extended in the U–V plane compared to the central structures. That is however, also similar to the observed U–V plane where the Hercules structure has significantly less contrast than the central regions. Second, the central branches of the velocity distribution at $\phi = 100°$ have also become less strong but are still visible. In the other regions, the central part is also very similar to the default case. It is worth noticing that the default mass of the self-gravitating spiral arms correspond to a high value between the limits of consistency of the model (Pichardo 2003a) and higher compared to other studies in this field as explained in Sections 11.2 and 11.5. In this sense, considering $M_{sp} = 0.03M_D$ is still a proper value for the model that produces also interesting results.

- **Integration time:** If the maximum integration time τ for IC1 is increased to 3000 Myr (Figure B.11), no significant increase in the crowding of Hercules and neither changes in the central structure are observed. This means that an stationary state has been reached although with these IC we have in our final velocity distributions particles with very low integration times.

Comparison with the TWA– Unfortunately, the detailed comparison of our results with other mentioned studies using the TWA (Section 11.5) is not straightforward. First, they used a model with different spiral arm characteristics such as the locus, the pattern speed and in some cases, even a four-armed model (Chakrabarty 2007), while ours includes two arms. These differences between the models have been analysed in Section 11.5. Finally, they used a different simulation strategy: Quillen & Minchev (2005) assigned the moving groups to periodic orbits of the spiral potential and in Chakrabarty (2007) the final result of each simulation was an average over time in the reference frame of the spiral arms as explained in Section 10.4. With the different method and model, Quillen & Minchev (2005) reproduced the Hyades-Pleiades and Coma Berenices branches as ascribed to periodic orbits related to the spiral arm 4:1 ILR, but not the Hercules structure (see Section 13.2). A more recent study (Chakrabarty 2007) argues that a model with only weak spiral arms does not reproduce the observed local velocity distribution as efficiently as a model with the combined effect of a bar and spiral arms. In the spiral-only models more but less strong kinematic structures were generated. However a particular description of these structures was not offered in that study.

Here we aim to study the effects of the TWA in the more similar conditions as our previous simulations with the self-gravitating spiral arms as possible. This means that we should use the same IC1, the same axisymmetric background and the same method. Also we have used the same pitch angle, locus and pattern speed as in the default model for the self-gravitating spiral arms and an approximately equivalent amplitude of the force range ($A_{sp} = 850(\,\mathrm{km\,s^{-1}})^2\,\mathrm{kpc}^{-1}$, see Section 11.5). Nevertheless, we have seen in Section 11.5 that this two models have very significant differences in their force field shape. Figure B.12 shows these equivalent results to Figure 13.1 but for the TWA. We see now that the velocity distributions in this case are very poor in terms of structures. An homogeneous central small group appears for all ϕ. If the amplitude of the TWA arms is doubled to $A_{sp} = 1500(kms)^2\,\mathrm{kpc}^{-1}$ (Figure B.13), surprisingly the structure at $V \sim -40\,\mathrm{km\,s^{-1}}$ appears again but only for the range $\phi = 80° - 100°$. By contrast, we have seen that the self-gravitating spiral arms create rich structures even if the mass is decreased. Therefore, we can conclude that the self-gravitating spiral arms produce ample substructure compared to the TWA arms. This should be due to the differences in the force field shape discussed in Section 11.5 (Figure 11.6 and Figure 11.7).

IC2– Also interesting is the case of IC2 (Figure 13.7) where the rapid induced effects of the spiral arms is shown. With an integration time of 400 Myr, the spiral arms with the default parameters have rotated only for 1.2 revolutions. In this case, a clear bimodality appears at several ϕ but mainly for $\phi = 120°$ and the adjacent ones. In particular for $\phi = 100°$ the two groups has positions and inclinations on the U–V plane that resemble the branches of Hyades-

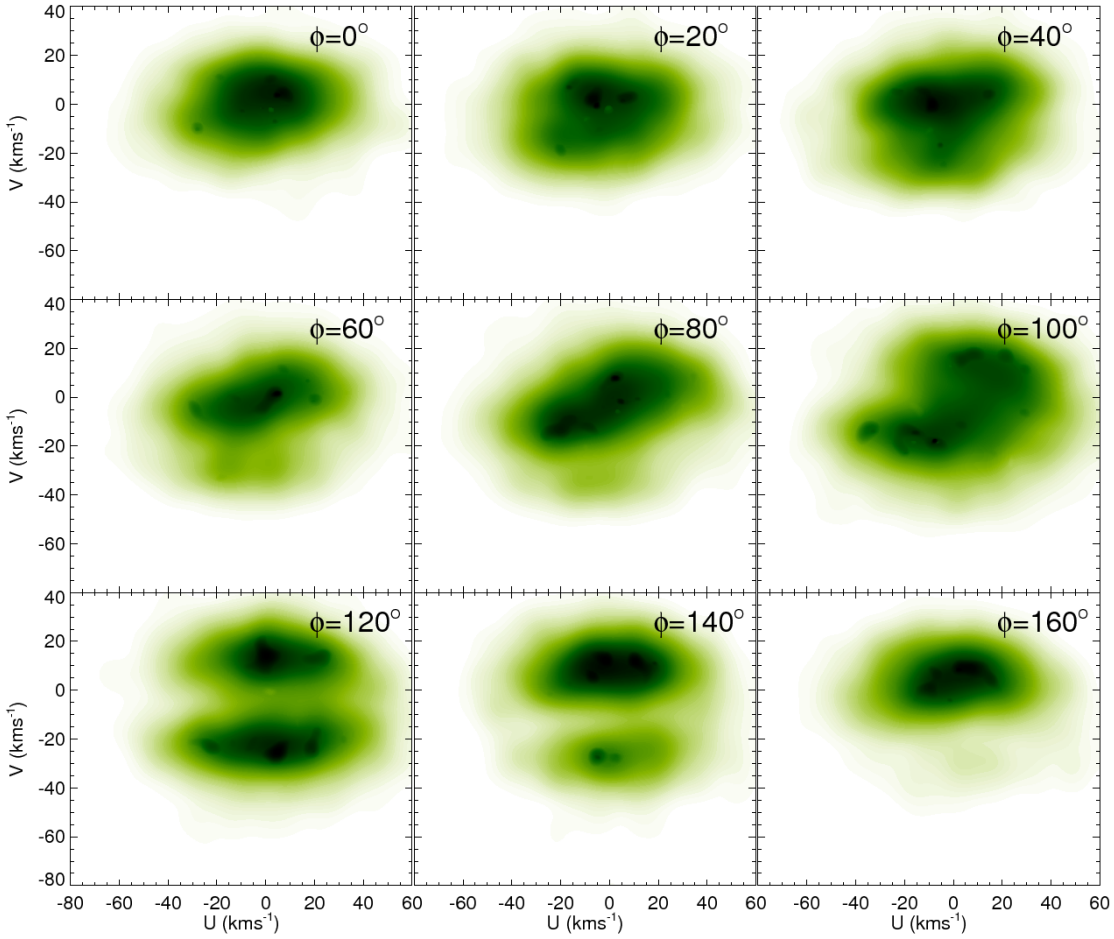

Figure 13.7: **Kinematic effects of the spiral arms on the intermediate disc.** U–V velocity distributions after WD at $R = 8.5\,\mathrm{kpc}$ and at different azimuths ϕ for the simulations with the PM04–MW potential model using only spiral arms and IC2.

Pleiades and Sirius. Also for $\phi = 60°$ and $\phi = 80°$, a structure similar to the one discussed for IC1 ($V \sim -40\,\mathrm{km\,s^{-1}}$) is observed at smaller $|U|$. Although there are particles that reach $V \sim -40\,\mathrm{km\,s^{-1}}$ (e.g. at $\phi = 120°$), they do not appear as a clear structure separated from the central region as in Figure 13.1. This is probably due to the lower integration time of IC2 compared with IC1 because, as previously seen, the integration time of the particles in that structure was at least 420 Myr (Figure 13.3). It can be checked that if the integration time for IC2 is increased to 1000 Myr (3 spiral arm revolutions), the panels change and the structure equivalent to Hercules emerges (Figure B.14) but no at all ϕ. The integration time of IC2 is short for the spiral arms (only 1.2 revolutions) to produce stable distributions and in this case we are therefore studying a velocity distribution that is still experiencing the response of the spiral arms (see Chapter 10). This situation demonstrate that recent spiral arms produce transient but strong and interesting kinematic structures.

13.2 Relation to regular orbits of the spiral arms

In this section the method of quantifying the regularity of the orbits corresponding to each region of the U–V plane is applied. The method and the aims of using it are detailed in Section 10.3. Basically we intend to ascertain if a given structure that has appeared in the test particle simulations corresponds to a group of periodic or quasi-periodic orbits or not and to identify the effects of a particular resonance in the U–V plane. The corresponding result for the default model of spiral arms (Table 11.3) at $\phi = 0°$ and $R = 8.5\,\mathrm{kpc}$ is shown in 13.8. In this Figure some of the main periodic regions are indicated with a coloured circle and a character. The corresponding orbits are shown in Figure 13.9 with the same colours. The analysis of these two Figures leads to the following conclusions.

First, the locations of the resonances are clearly marked as arches opened to the $V < 0$ direction as discussed for instance in Fux (2001). The more negative or smaller the V, the smaller the guiding radius or centre[2] of the orbit and therefore the inner the resonance associated. This Figure helps us to illustrate the discussion about the axisymmetric estimates of the resonances begun in Section 10.3. As shown in Dehnen (2000) for a case applied to the bar of the MW these kind of estimates predicts that the local velocities of orbits that are in resonance (in that case the OLR) satisfy a parabola whose maximal V occurs at $U = 0$. Nevertheless, we see in this Figure (and equivalently for the simulations with the bar of Section 14.2 and in Dehnen 2000) that some features corresponding to the resonances are asymmetric in U. This demonstrate that calculations of the location of the resonances in the U–V plane using only the axisymmetric potential as a simplification are not very accurate.

[2]The radius around which the orbit oscillates according to epicyclic theory.

Second, the region of $V \sim -40\,\mathrm{km\,s^{-1}}$ equivalent to the Hercules stream that appears in most of the previous simulations of Section 13.1 is here discovered to be a dark region in this map or, equivalently, a quasi-periodic region in the U–V plane. This region is marked with points (b) and (c). These two points and all the surrounding points follow a square orbit related to the 4:1 ILR of the arms finishing 4 radial oscillations during one angular revolution (Figure 13.9b and 13.9c). This type of orbits support the arms near two of its four vertexes. The radius of the orbits oscillates between $\sim 6\,\mathrm{kpc}$ and $8.5\,\mathrm{kpc}$, which is well-around $\sim 7\,\mathrm{kpc}$ where the 4:1 ILR is located according to the simplified method of Figure 13.5. For the orientation of these orbits, we conclude that the particles following this orbit are exactly at the vertex of the square when they cross the $\phi = 0°$ and $R = 8.5$ position. Also, the structure at $V \sim -40\,\mathrm{km\,s^{-1}}$, which was specially prominent for $\phi = 100°$ in the test particle simulations, coincides with the position of the other vertex. However, as these orbits are not exactly periodic orbits but oscillate around the closed square, the vertexes of the orbit also oscillates around the disc and eventually covers all azimuths at solar radius. That is the reason why this structure appears for all azimuths but have different minimum time of exposure to the spiral arms (or age) at different azimuths (Section 13.1).

Figure 13.9a is similar to the mentioned squared orbit (Figure 13.9b) but has loops in its vertexes. It may be also related to 4:1 ILR. By contrast, Figure 13.9p corresponds to an effect of the 4:1 OLR of the spiral as it is an orbit that finishes exactly 4 radial periods for a complete azimuthal oscillation but around a larger guiding radius than the one associated with the 4:1 ILR ($R_{4:1OLR} \sim 14.3\,\mathrm{kpc}$). The effects of the 5:1 ILR resonance can be seen in Figure 13.9d. The 6:1 ILR has its imprints in orbits such as Figures 13.9e, 13.9g and 13.9i, the 7:1 ILR in Figures 13.9f and 13.9h and continuing similarly depending on the number of radial oscillations for one angular revolution (Figures 13.9j, 13.9k, 13.9l and 13.9m).

The strong black stripe at $V \sim 50\,\mathrm{km\,s^{-1}}$ and covering a large range of U correspond to orbits such as Figure 13.9n. These are orbits around one of the equilibrium points of the spiral arms potential located at corotation radius ($R_{cr} = 10.9\,\mathrm{kpc}$). In the frame of reference rotating with the spiral structure (X''–Y'') there are 4 equilibrium points at corotation distance. L_4 and L_5 are stable and located at the effective potential maxima whereas L_1 and L_2 are saddle points of the effective potential, therefore, unstable. For the PM04–MW potential model with only spiral arms the curves of equipotential and the equilibrium points of the model in the X''–Y'' reference system are shown in Figure 13.10. As studied in Barbanis (1976), the resonant orbits at corotation can be divided in 3 types according to their shape which depends on the particular value of the Hamiltonian and the initial position. In our case in the centre of the stripe we find an elongated ring orbit around the L_4 (or L_5) stable equilibrium point such as Figure 13.9n (a-type orbits in Barbanis 1976). The rest of the stripe surrounding this centred point corresponds

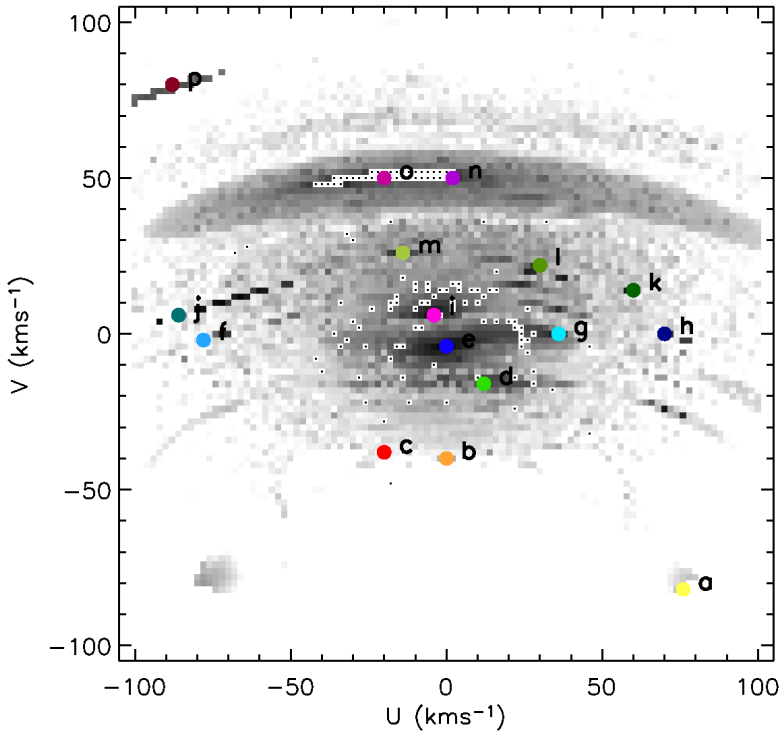

Figure 13.8: **Orbital regularity of the self-gravitating spiral arms.** U–V plane coloured according to the periodicity of the corresponding orbits for the default model of spiral arms at $\phi = 0°$ and $R = 8.5\,\mathrm{kpc}$. The darker the region is, the more periodic or closed the corresponding orbit is. The points corresponding to orbits in Figure 13.9 are marked with coloured circles.

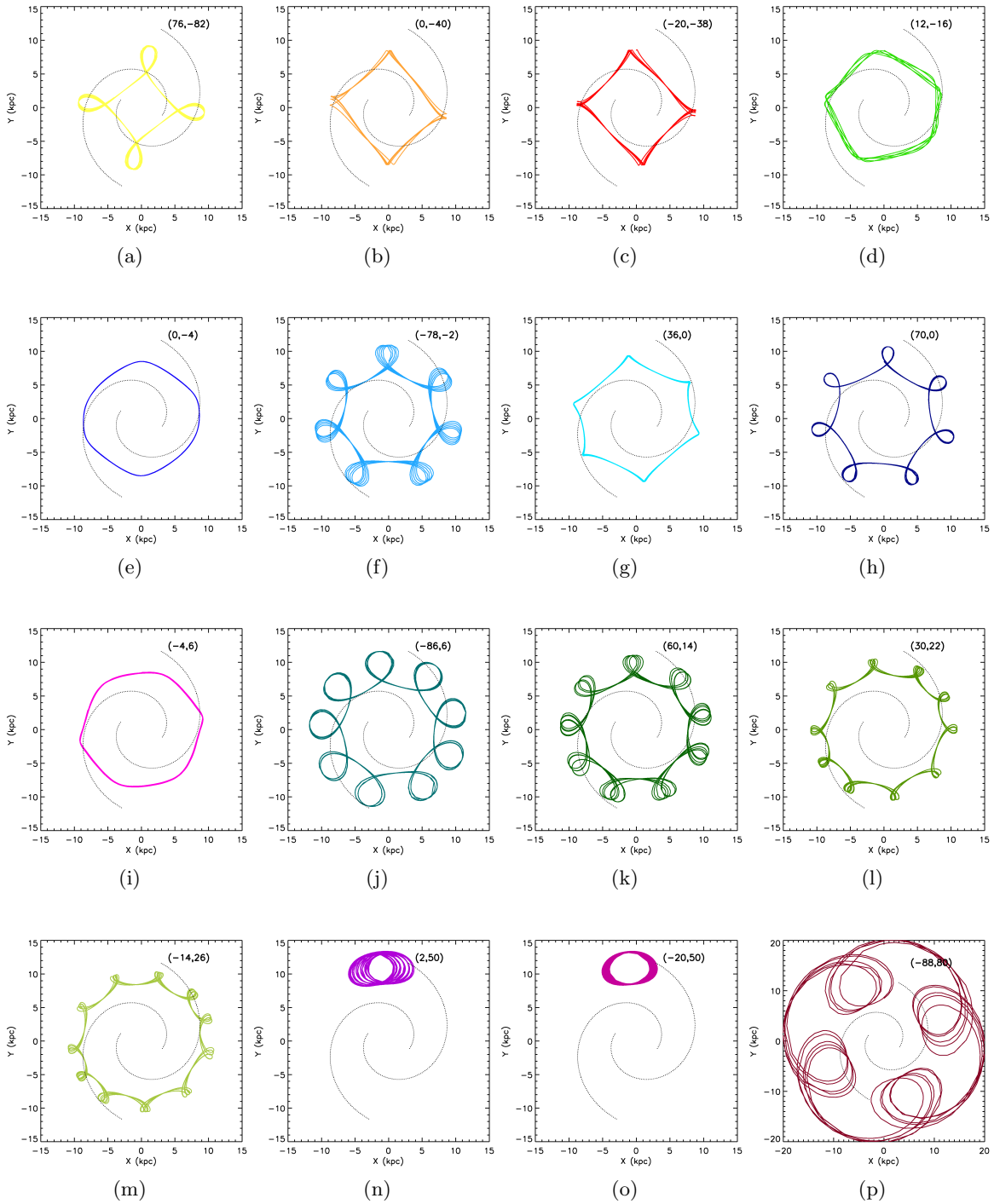

Figure 13.9: **Spiral arm-induced regular orbits.** Orbits of the U–V points indicated in Figure 13.8 with the same colour and character. The velocity (U, V) is indicated in the top-right part of each panel.

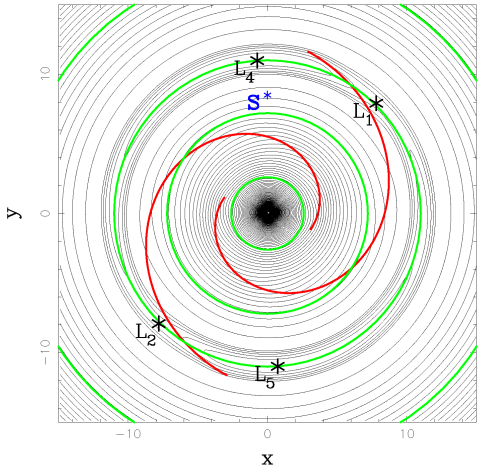

Figure 13.10: Equipotential curves (black lines) and the equilibrium points of effective potential of the PM04–MW potential model with only spiral arms. The positions of the resonances for the default value of the pattern speed of the arms are shown (green lines). From inside out these are the 2:1 ILR, the 4:1 ILR, the corotation resonance and the 2:1 OLR. The Sun corresponds to the blue symbol. Plot courtesy of M. Romero-Gomez.

to *asymmetric banana orbits* (c-type orbits in Barbanis 1976) following an oval curve around the stable L_4 and unstable L_2 points (or L_5 and L_1) such as in Figure 13.9o. This particular orbit and all the white region inside these stripe is formed by similar orbits oriented in a way that do not cross the axes (X'' and Y'') where the periodicity is calculated (through the dispersions). In our test particle simulations (Section 13.1), all these orbits, however, are unpopulated by the chosen initial conditions. Besides, no observed moving group (Figure 6.1) appears to be in a so large positive V. The b-types of orbits in Barbanis (1976) (*banana orbits* librating around L_4 orL_5) have not been localised in this Figure.

In the comparison between the map of periodic orbits in the U–V plane (Figure 13.8) and the test particle simulations (Figure 13.1 for $\phi = 0$ and $R = 8.5\,\mathrm{kpc}$) we find the following similarities. First, as mentioned above, the square orbit at $V \sim -40\,\mathrm{km\,s^{-1}}$ due to the 4:1 ILR has its corresponding kinematic structure in the test particle simulations made from a set of points oscillating around this square orbit. On the other hand, it is not trivial to associate other periodic orbits with the structures that are crowded in our test particles. For instance, in the U–V plane at $\phi = 0$ and $R = 8.5\,\mathrm{kpc}$ of our test particle simulations the central region is occupied continuously by particles and there is not a clear separation between the three regions of points (d), (e) and (g), and (i) such as in the regularity map. Only the central region of the

distribution in Figure 13.1 for $\phi = 0$ and $R = 8.5\,\mathrm{kpc}$ is elongated to negative and positive V similarly as the central structure of Figure 13.8 passing through points (e) and (g). The orbit (g) is related to the 6:1 ILR whereas (e) is a rounded orbit which seems to have influence of the 6:1 ILR and/or the 4:1 ILR.

As discussed in Chapter 12, because of the uncertainty in the solar motion we must be very careful when comparing the black regions in Figure 13.8 with the velocities of observed moving groups of Table 6.1 and Figure 6.1. They can differ up to $11\,\mathrm{km\,s^{-1}}$ in U and $12\,\mathrm{km\,s^{-1}}$ in V. However, special attention would deserve orbits such as (d), (e), (g) and (i) that correspond to periodic orbits at the central region of the U–V plane: (12,-16), (0,-4), (36,0) and (-4,6) $\mathrm{km\,s^{-1}}$ respectively. Although it is too venturous to compared the exact values of the U and V of these orbits with the kinematic groups that are seen in the observations, we can conclude that the spiral arms are able to carve the orbital structure corresponding to the central velocity distribution following similar shapes to the branches in the observed U–V plane. Other resonant orbits at the outer parts of U–V plane such as that of points (f) or (j) produce very thin features which can hardly be associated with groups in the test particle simulations or to observed moving groups.

The periodic orbits of this model are expected to change with position and also with model parameters. In the rest of the panels in Figure 13.11, the results for the default case is shown in panel 13.11a and small variations from the default model are shown in the rest of the panels. Our preliminary important conclusions are listed next.

- **Pattern speed:** When decreasing the pattern speed of the spiral arms to $\Omega_{sp} = 18\,\mathrm{km\,s^{-1}kpc^{-1}}$ (Figure 13.11b), the 4:1 ILR are brought closer from $R = 7.0\,\mathrm{kpc}$ to $7.8\,\mathrm{kpc}$ (see Figure 13.5). The resonant orbits are closer in radius to $R = 8.5\,\mathrm{kpc}$ and consequently, they have larger (less negative) V compared to Figure 13.11a. For example, the 4:1 ILR that we find at (0,-40) $\mathrm{km\,s^{-1}}$ is now positions such as (0,-6) $\mathrm{km\,s^{-1}}$ or (44,-24) $\mathrm{km\,s^{-1}}$. With this pattern speed, the 4:1 ILR could be associated with the Hyades-Pleiades structure which has smaller $|V|$. In Quillen & Minchev (2005) similar pattern speeds were explored (see Section 11.5) which also located the effects of the 4:1 ILR in the position of this observed kinematic structure. However, the differences in the shapes of the structures in our panels may be due to the differences in the underlying model of spiral arms. New periodic orbits corresponding to inner new resonances are now able to reach the solar position. For instance, the orbits at smallest V ($\sim -36\,\mathrm{km\,s^{-1}}$) of this plot seem to be related with the 7:2 ILR.

  The contrary is expected for $\Omega_{sp} = 22\,\mathrm{km\,s^{-1}kpc^{-1}}$ (Figure 13.11c). The 4:1 OLR corresponds for instance to the periodic orbit at $\sim$(-80,70) $\mathrm{km\,s^{-1}}$ instead of at (-80,80) $\mathrm{km\,s^{-1}}$.

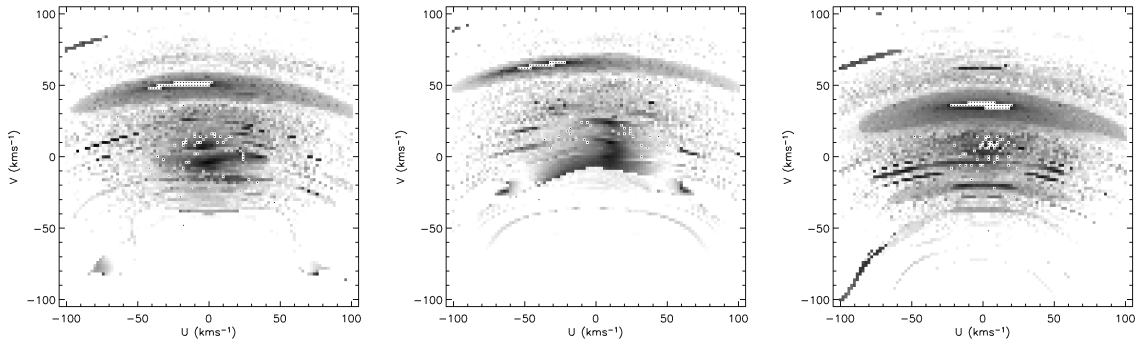

(a) Default (b) $\Omega_{sp} = 18\,\mathrm{km\,s^{-1}kpc^{-1}}$ (c) $\Omega_{sp} = 22\,\mathrm{km\,s^{-1}kpc^{-1}}$

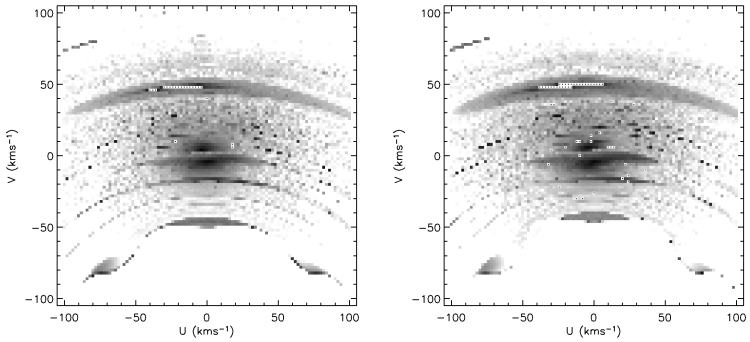

(d) $M_{sp} = 0.0175 M_d$ (e) $M_{sp} = 0.03 M_d$

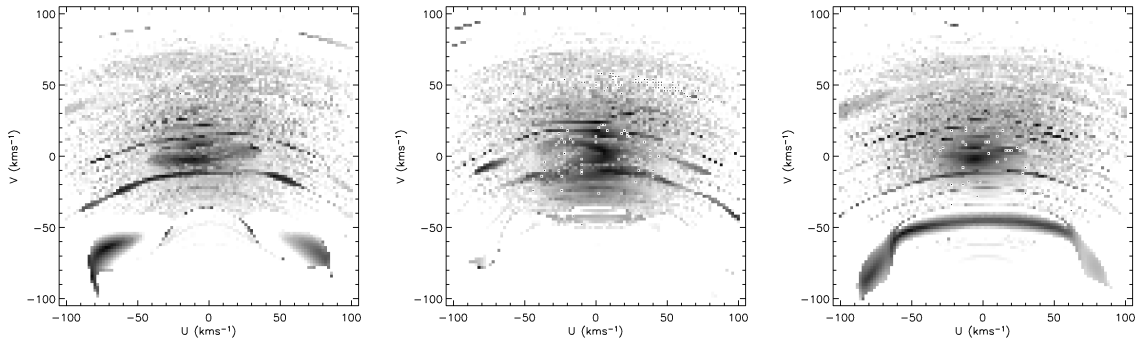

(f) $\phi = 60^\circ$ ($\phi_{0sp} = 28^\circ$) (g) $\phi = 100^\circ$ ($\phi_{0sp} = -12^\circ$) (h) $i = 12^\circ$

Figure 13.11: **Orbital regularity of the self-gravitating spiral arms with different properties.** U–V plane coloured as the periodicity of the corresponding orbits for several variations of the parameters of the default model of the spiral arms.

Now some orbits correspond to outer resonances not previously seen so clearly such as the 8:1 OLR at ∼(0,62) $\mathrm{km\,s^{-1}}$. The 6:1 ILR is now at $(0, -20)\,\mathrm{km\,s^{-1}}$ and the clear group at ∼(0,-38) $\mathrm{km\,s^{-1}}$ is not the 4:1 ILR (as in Figure 13.11b) but the 5:1 ILR. The effects of the 4:1 ILR are barely seen here.

- **Mass:** No significant differences are seen when the mass is decreased to $M_{sp} = 0.0175 M_D$ and $M_{sp} = 0.03 M_D$ (Figures 13.11d and 13.11e). The positions of the resonances do not change significantly as a result of the mass change as they depend mainly on the pattern speed. Only minor changes are expected due to the fact that when varying the mass, despite conserving the total mass of the model because the spiral mass is subtracted to the disc, minor and local variation in the resonant curves are expected. However, the shape of the resonant regions can slightly change. In fact, more clear periodic structures and arches are seen in these two cases probably due to the higher regularity of the orbits for lower strengths of the spiral arms. The structure at $V \sim -40\,\mathrm{km\,s^{-1}}$ is maintained when the mass is decreased but is now located at slight more negative V ($\sim -50\,\mathrm{km\,s^{-1}}$) due to the above mentioned minor changes expected. It appears even more relevant than before. We have seen in Section 13.1 that in our test particle simulations for $M_{sp} = 0.03 M_D$ (Figure B.10) the group at these negative V had became very weak for $\phi = 0°$. But we see now that the resonant structure at negative V ($V \sim -40\,\mathrm{km\,s^{-1}}$) exists for masses of the spiral arms lower than the default case but becomes less populated in our test particle simulations.

- **Orientation of the arms:** Figures 13.11g and 13.11f are obtained with the default model but at different azimuths: 100° ($\phi_{0sp} = -12°$) and 60° ($\phi_{0sp} = 28°$) respectively. The position of the resonances do not change for these cases. However, the periodic orbits crosses these ϕ in different parts of the orbit (for example nearer the apocentre or pericentre) and therefore the periodic regions can be observed in different positions of the U–V plane. The structure at $V \sim -40\,\mathrm{km\,s^{-1}}$ appears enhanced in Figure 13.11g and at lower V compared to Figure 13.11a as it happen with the test particle simulations at $\phi = 100°$. Also very clear and strong central regular regions appears for this region near the arms.

- **Pitch angle:** Figure 13.11h shows the same as Figure 13.11a but with a pitch angle of 12°. In this case a clear arched stripe at $V \sim -46\,\mathrm{km\,s^{-1}}$ corresponding to the squared orbit of the 4:1 ILR. However this was not populated in our test particle simulations (Figure B.9). This panel is very similar to panel (g) because, as discussed in Section 13.1, a model with this new pitch angle produce an orientation of the arms of $\phi_{0sp} = 35°$ similar to the orientation of (g).

All in all, the orbital regular structure is very sensitive to the pattern speed or to the orientation of the spiral arms. For instance, we have seen that only slightly smaller pattern speeds ($18\,\mathrm{km\,s^{-1}kpc^{-1}}$) can shift the kinematic structures in the U–V plane as largely as about $20\,\mathrm{km\,s^{-1}}$. Also, for changes in pattern speed not only the resonant regions are shifted to upper or lower region of the U–V plane but they change their shapes and their mutual separation.

13.3 Summary and discussion

To our knowledge the effects of self-gravitating spiral arms on the velocity distribution have not been studied before. Here we report that these spiral arms produce significant strong imprints on the velocity plane. This contrasts with the findings of other authors who used the TWA. They claim that the spiral arms create abundant but weak kinematic structures. Comparison with other authors is not straightforward because of differences in the model used (TWA), the characteristics of the spiral arms (pattern speed, number of arms or locus) and simulation strategy followed. Here we have studied the TWA model in the same conditions as our experiments with the self-gravitating spiral arms: same initial conditions and simulation method, same axisymmetric background, same pattern speed and locus, and similar force amplitude range. We conclude that the self-gravitating spiral arms produce ample substructure compared to the TWA arms. This can be attributed to the differences between the force-field shape of a TWA model and the force-field shape derived from a mass distribution. The differences in the velocity fields could help to stablish whether the arms of the MW follow the TWA and are, therefore, weak and tightly wound, or whether they are strong self-gravitating arms.

When the self-gravitating arms act on a cold disc for a long time (~ 10 spiral arm revolutions), they create a centred group in the velocity distributions (low epicyclic energies) at solar radius that usually contains several structures. In particular, near the locus of the arms three slightly tilted branches appear, resembling some of the observed central kinematic branches. In addition, the spiral arms by themselves can crowd the velocity space at $V \sim -40\,\mathrm{km\,s^{-1}}$. For a wide range of azimuths the model reproduces a branch at low angular momentum at that V which is consistent with the V velocity of the observed Hercules structure, although it is not inclined in the U–V plane and does not have negative average radial motion. It is significant that we find that the Hercules structure may be populated by the spiral arms and not only by bar resonances, as traditionally believed. As spiral arms act mainly on stars whose epicycles are small or similar to the interarm separation, the current plausible interarm separation of the spiral arms indicates that stars of the Hercules kinematic structure are influenced by the spiral arms.

Our simulations indicate that the velocity distributions induced by the self-gravitating arms do not change significantly with slight variations of mass or pitch angle. In contrast, higher

pattern speeds that brought the 4:1 ILR further, do not induce strong kinematic groups. Smaller pattern speeds that locate the Sun near this resonance create different and strong kinematic structures. In particular for these cases and for several relative orientations of the arms with respect to the solar position, the upper part of the distribution on the U–V plane is shifted to $U > 0$, as for the observed Sirius moving group.

When the spiral arms affect a hotter disc for short times ($\sim$ 1 spiral arms revolution), strong kinematic imprints are also seen. A clear split into two groups appears at several azimuths, especially near the arms. We see that if they act on this disc for longer times ($\sim$ 3 revolutions) the kinematic structures change, and therefore with this integration time the velocity distributions are still responding to the effects of the spiral arms. This demonstrates that recent spiral arms produce transient but strong kinematic structures.

The strong imprints that the self-gravitating spiral arms induce on the velocity distributions at solar radius and the sensitivity of our results to the properties of the arms indicate that kinematics could be one of the constraints on the current observational ambiguities surrounding the spiral arms (e.g. pattern speed, orientation, strength), whether they are long-lived or whether short-lived non-axisymmetric components.

Our preliminary investigations about the characteristics of the particles that belong to a particular kinematic group suggest interesting consequences for this study. First, these particles can have distinctive final spatial distributions when they are compared to all particles in the region or to the particles of a similar kinematic structure in other disc regions. Although the spatial study of the observed moving groups is limited by the extension and precision of the current observational samples, we expect a future improvement in the characterisation of the spatial distribution of the stars in each moving group and in the velocity distributions in other disc regions. Second, the particles of a kinematic group can also have distinctive initial spatial distribution and distinctive time of exposure to the spiral arms. For the moment our initial conditions are idealised. When our method is complemented with chemical models of galaxy evolution which refine the relation between age, chemical abundances and migration, these distributions can be used as tracers of the chemistry or the age of these particles, and they may eventually be able to be compared with the distinctive metallicities and ages of the observed moving groups. The inclusion of all these additional elements in the comparison between observed and simulated moving groups may provide useful additional constraints. Although we have only studied the test particle properties of a particular simulated structure as an example with the spiral arms model, this analysis can be extended to any other kinematic group in our simulations.

Regarding our analysis of orbit regularity, we have derived some interesting conclusions. We identify several resonant orbits that cross the solar neighbourhood. First, the kinematic

structure at $V \sim -40\,\mathrm{km\,s^{-1}}$ coincident with the velocity of Hercules is found to be a region of orbits oscillating a around a square orbit due to the 4:1 ILR. Second, the central part of the U–V plane is filled with strong regions of regularity which are mainly related to the 6:1 ILR. Although it is not trivial to associate these central regular orbital regions with the structures that are crowded in our test particles or with the observed moving groups, we conclude that the spiral arms can carve the orbital structure corresponding to the central velocity distribution following similar shapes to the branches in the observed U–V plane. For other strong signals of orbital regularity on the U–V plane, we have not found their counterparts in the test particle simulations nor in the observed U–V plane. There are also other resonant orbits in the outer parts of U–V plane that produce thin features in the U–V plane which can hardly be associated with observed moving groups. The regular orbital structure is mainly sensitive to the pattern speed and to the orientation of the spiral arms, which is encouraging in order to use this method in support to the test particle simulations to constrain the characteristics of the spiral arms.

Chapter 14

Imprints of the bar

In this chapter the kinematic structure developed by the the prolate bar of the PM04–MW potential model with is presented. First in Section 14.1the results of these simulations with the default parameters of Tables 11.2 (for the axisymmetric component) and 11.4 (for the bar) are presented for IC1 and IC2 (default values of Table 10.1). Afterwards, the effect of the variation of some default parameters is shown and discussed. The case of out hottest IC3 is analysed only in a central parts of the U–V plane as the lower parts are studied in Chapter 15. In Section 14.2 we study the regularity of the orbits on the U–V plane for the prolate bar. At the end, Section 14.3 shows a summary and a discussion of the results of this chapter.

14.1 The bimodality induced by the bar

The effects of the bar on the local velocity distribution have been exhaustively studied by other authors (Dehnen 2000, Fux 2001). All these studies agreed in the fact that the bar creates a bimodality, that is two groups, in the U–V plane for some parameters of the bar. The velocity of one of these two groups coincides with the observed Hercules moving group, whereas the other one is approximately centred on the U–V plane (here called the central mode). These authors have claimed that the bimodality is related to the effects of the bar 2:1 OLR on the orbits, although the studies do not agree in the exact mechanisms that take part in it. In Section 14.2 a discussion about this in terms of periodic and chaotic orbits is offered. However, all these studies are carried out using a quadrupole bar. We want to explore the kinematic structure developed by the the prolate bar that has not been considered prior this thesis.

IC1– Figure 14.1 shows the U–V plane for several Galactic azimuths ϕ at $R = 8.5\,\mathrm{kpc}$ and assuming low velocity dispersions (IC1). We find that this model hardly produces substructure. For $\phi = 100°$ a kind of bimodality or two small groups can be observed but this bar inclination ($\phi_{0b} = 100°$) is very unrealistic. Unlike the spiral arms, currently the relative orientation bar-Sun is relatively tightly constrained. Among the panels of Figure 14.1, realistic velocity distributions are the ones around $\phi = 0°$ (corresponding to a bar orientation of $\phi_{0b} = 20°$) and also around 160° (with a bar orientation of $\phi_{0b} = 40°$ which would correspond to the case of the long bar, see Section 11.3). For this likely positions ϕ, we observe only a group in the central position of the U–V plane but that is distorted towards positive U. Although for the default value $\Omega_b = 45\,\mathrm{km\,s^{-1}kpc^{-1}}$, the resonance is very near to the solar radius ($R_{OLR} = 0.98R_\odot = 8.3\,\mathrm{kpc}$) the low velocity orbits of IC1 seem to be barely affected by the resonance except for the mentioned distortion towards positive U. We conclude that orbits from IC1 which have guiding centres around a very narrow range of radius around the solar radius and very low epicyclic amplitudes fall on a region of short influence.

IC2– In agreement with previous studies with the quadrupole bar (e.g. Dehnen 2000), we find that the prolate bar can trigger a bimodality in the velocity distribution at solar radius for its default parameters. For example, a kinematic group at $V \leq 0$ and $U \leq 0$ appears at $\phi = 160°$ and surroundings ($140°, 160°, 0°$, and $20°$) if the bar is used with IC2 (Figure 14.2). These positions correspond to a bar inclination ϕ_{0b} of approximately $[0, 60]°$ which are realistic values according to the recent observations of the Galactic bar with $\phi_{0b} \sim 20°$ and the long bar with $\phi_{0b} \sim 40°$ (see discussion above and Section 11.3). As this structure was not formed for IC1, we confirm that the bimodality is obtained only when hotter initial conditions are used. The increase of the initial velocity dispersion allows more inner particles to reach the solar radius and populate this structure. However, it is worth mentioning that in the study of Dehnen (2000) the initial conditions were hotter ($\sigma_U(R_\odot \sim 0.2V_c)$ than IC2 ($\sigma_U(R_\odot \sim 0.09V_c)$. Also Chakrabarty (2007) found that the bar could also induce a bimodality for cold discs with $\sigma_U \sim 10\,\mathrm{km\,s^{-1}}$ (between our IC1 and IC2).

As discussed in the beginning of the chapter, the group at low angular momentum have been usually associated with the Hercules moving group. However, the mean branch velocity V in our simulations is slightly smaller ($V \sim -20\,\mathrm{km\,s^{-1}}$) than the mean velocity of the observed Hercules structure ($V \sim -40\,\mathrm{km\,s^{-1}}$). Therefore, even accepting a large mean velocity for the Sun $V_\odot = 12\,\mathrm{km\,s^{-1}}$ as discussed in Chapter 12, our bimodality would be still inconsistent with the Hercules kinematic group. Alternatively, this simulated structure could be associated with Hyades-Pleiades in our case. For other ϕ the structure at negative V shifts to the central regions of U axis (e.g. $\phi = 100°$). The central mode in this simulation is distorted towards positive U, as

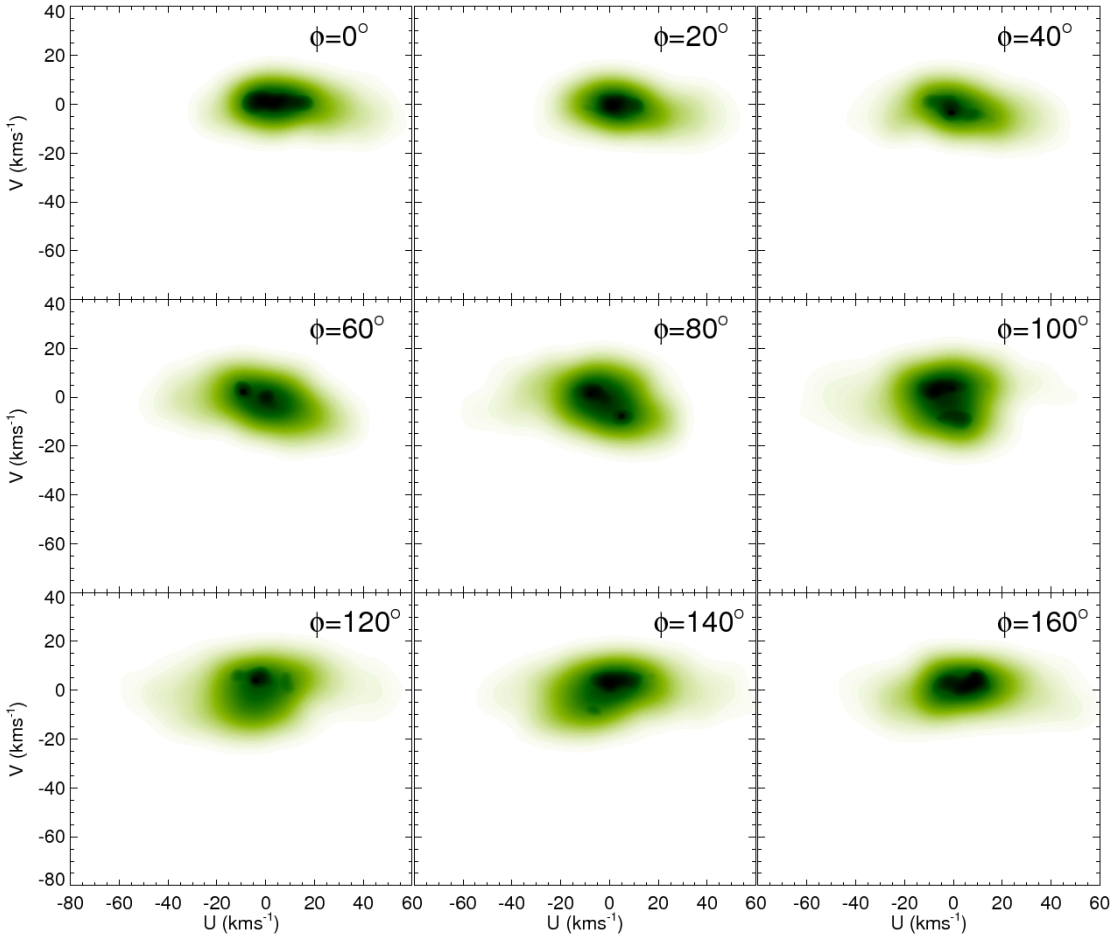

Figure 14.1: **Kinematic effects of the bar on a cold disc.** U–V velocity distributions after WD at $R = 8.5\,\mathrm{kpc}$ and at different azimuths ϕ for the simulations with the PM04–MW potential model using only bar and IC1.

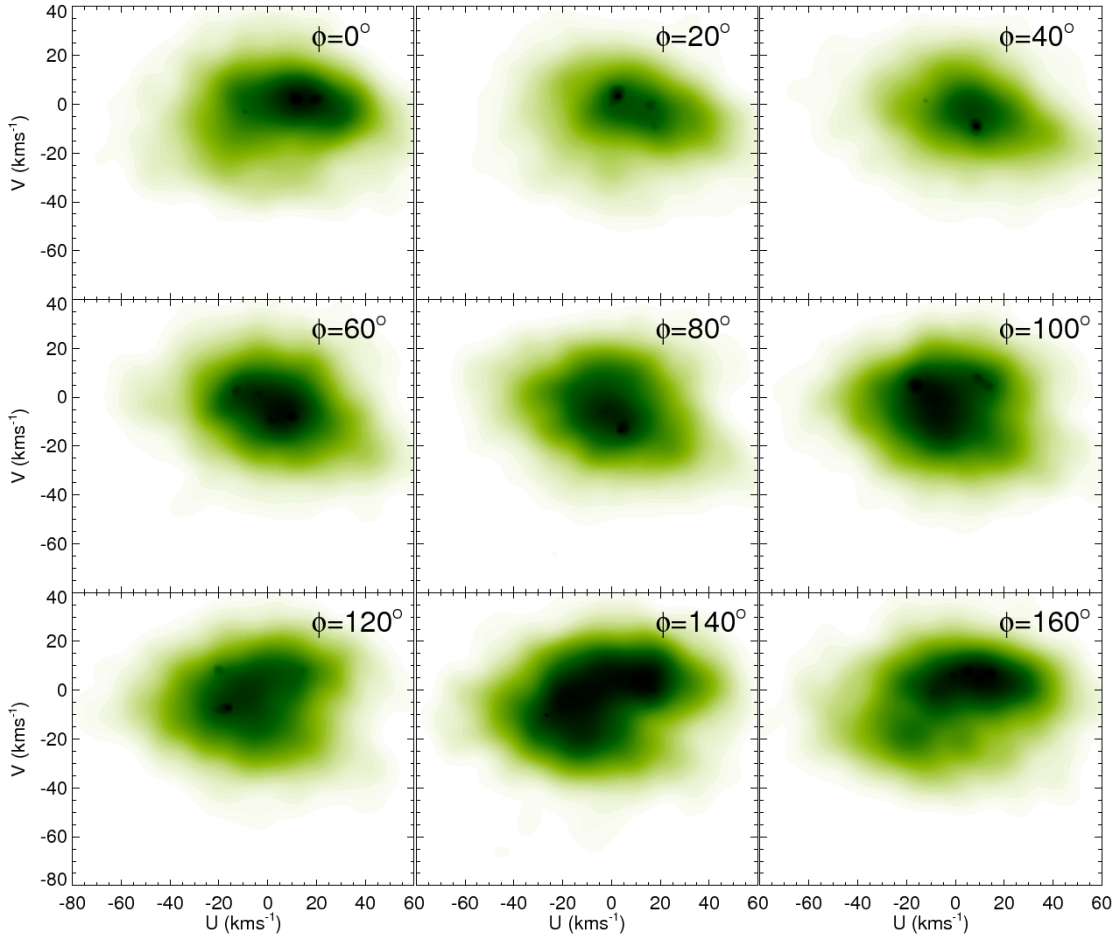

Figure 14.2: **Kinematic effects of the bar on an intermediate disc.** U–V velocity distributions after WD at $R = 8.5\,\mathrm{kpc}$ and at different azimuths ϕ for the simulations with the PM04–MW potential model using only bar and IC2.

observed for IC1, and reaches velocities up to $U \sim 60\,\mathrm{km\,s^{-1}}$. The relative fraction of particles in this position in the U–V plane exceeds the observed relative fraction in the observational sample (Figure 6.1).

Varying the default parameters– Next we present the results of the simulations when the default values for some relevant parameters (pattern speed, mass, initial conditions) of the PM04–MW potential model are changed.

- **Pattern speed:** A small change in pattern speed from $\Omega_b = 45\,\mathrm{km\,s^{-1}kpc^{-1}}$ to $\Omega_b = 48\,\mathrm{km\,s^{-1}kpc^{-1}}$ produces a shift in the OLR from 8.3 kpc to 7.8 kpc (see Figure 14.3). The test particle simulation for this new pattern speed (Figure B.15) indicates that in this case the group of low angular momentum is less populated than in the default case at least for $\phi = 0°$ and $\phi = 160°$. The distortions of the central mode is still clearly observed.

  The situation reverses when a bar pattern speed of $\Omega_b = 60\,\mathrm{km\,s^{-1}kpc^{-1}}$ under IC2 (Figure B.16). Now the OLR resonance is located at even inner radius $R_{OLR} = 0.74R_{\odot} = 6.3\,\mathrm{kpc}$ (Figure 14.3). In this case, also a bimodality is induced in the U–V plane. Now the group at low angular momentum is clearly separated from the central mode and is located at more negative V ($\sim -60\,\mathrm{km\,s^{-1}}$). However, this branch is at an incorrect position in U ($U \geq 0$) for the realistic positions ($\phi = 0°$ or $\phi = 160°$) to be consistent with the Hercules group.

- **Radius:** If the pattern speed is kept to $\Omega_b = 60\,\mathrm{km\,s^{-1}kpc^{-1}}$ but we study the velocity distribution of a region located at different radius but $\phi = 0°$, the results of Figure B.17 are obtained. For very inner radius $R = 6.5\,\mathrm{kpc}$ we are studying velocity distributions nearer the OLR which is now at $R_{OLR} = 6.3\,\mathrm{kpc}$ ($R_{OLR}/R \sim 0.97$). Only in this case a structure appears at $U \leq 0$ and it has more negative V ($\sim -30\,\mathrm{km\,s^{-1}}$). This value is still not negative enough to be consistent with Hercules but is better than for $\Omega_{sp} = 45\,\mathrm{km\,s^{-1}kpc^{-1}}$. We conclude that only by bringing the resonances nearer (changing Ω_b or looking at smaller radius), an Hercules structure at $U < 0$ is obtained. On the other hand, the distortion of the central mode at $R = 6.5\,\mathrm{kpc}$ reaches values that are higher than $60\,\mathrm{km\,s^{-1}}$, which seems even more unrealistic than for $\Omega_{sp} = 45\,\mathrm{km\,s^{-1}kpc^{-1}}$ and $R = 8.5\,\mathrm{kpc}$. This case of $\Omega_b = 60\,\mathrm{km\,s^{-1}kpc^{-1}}$ and $R = 6.5\,\mathrm{kpc}$ is apparently equivalent to considering $\Omega_{sp} = 45\,\mathrm{km\,s^{-1}kpc^{-1}}$ and the solar radius at 8.5 kpc ($R_{OLR}/R \sim 0.98$). The only difference between these two cases than can explain the more negative V for the supposed Hercules structure in the case of $\Omega_b = 60\,\mathrm{km\,s^{-1}kpc^{-1}}$ and $R = 6.5\,\mathrm{kpc}$ is the slightly higher initial dispersion of the particles of IC2 at this inner radius ($\sigma_U \sim 25.2\,\mathrm{km\,s^{-1}}$ in front of $20\,\mathrm{km\,s^{-1}}$ at 8.5 kpc). This higher dispersion would allow more

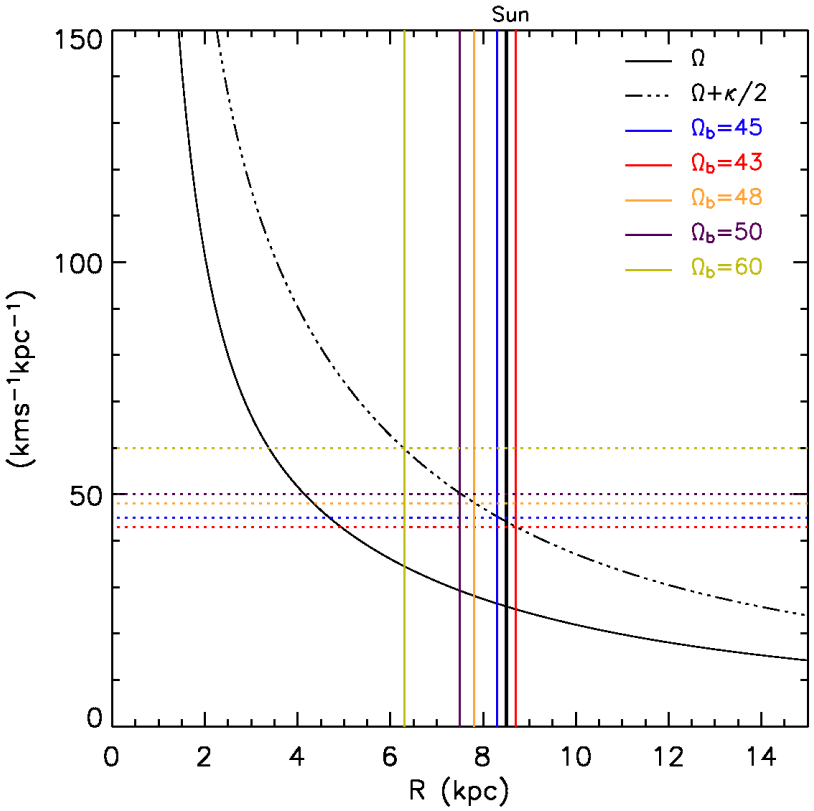

Figure 14.3: **Location of the bar resonances.** Resonance curves in the Allen & Santillán (1991) axisymmetric model for corotation (Ω) and 2:1 OLR ($\Omega + \kappa/2$). The horizontal blue line corresponds to the default value of pattern speed of the bar. The other coloured lines corresponds to several variations for this parameter. The vertical lines coloured following the same pattern indicates the position of the 2:1 OLR for each pattern speed. The default position of the Sun is shown with a black vertical line.

inner particles to reach the solar radius and populate this structure. It also would explain the higher distortion of the central mode.

- **Mass:** Now we increase the mass of the bar from 9.8×10^9 (default) to $M_b = 1.4\times10^{10}\mathrm{M}_\odot$. If this more massive bar is used for IC2 (Figure B.18), the hypothetical Hercules branch appears far more clearly and differentiated from the central mode but is still at V not negative enough to be consistent with Hercules. Again the central model is shifted to very high and U. This more massive bar has now the strength parameters of Table 11.5. In particular, the parameter α is 0.007, which is higher than for the default bar. This indicates this more massive bar has higher values of the radial force at radius where the resonances are located (in particular the OLR). The fact that the resonant feature are more clear in this simulations could answer to this.

- **Integration time:** In Figure B.19 we show the simulations for IC2 with a longer integration time. Whereas the default value was 400 Myr, now the particles are integrated for 1 Gyr. Similarly to what found in Dehnen (2000), longer integration times seem to produce to stronger resonant feature in the U–V plane. The distortion of the central mode is greater than in Figure 14.2, that is reaches higher U. Regarding the low angular momentum group of the bimodality, it appears clearer and sharpen. For instance see the clearer valley between the two groups of the bimodality for $\phi \sim 100°$. Also the group at low angular momentum at $\phi = 0°$ and $\phi = 160°$ is more extended.

- **Initial velocity dispersion:** If we consider hotter initial conditions without modifying the parameters of the bar's potential, slightly different results are obtained. We will use IC3 but studied only in the same range as in IC1 and IC2. The lower parts are studied in Chapter 15 as they deserve special analysis. Figure 14.4 shows this simulation. As it can be seen, now the supposed Hercules branch appears at $V \sim -40\,\mathrm{km\,s^{-1}}$ at $\phi = 0°$ more in agreement with the observed structure. With this simulation we conform the influence of the initial velocity dispersion that allows more particles to reach the solar radius and populate this structure as we have seen for the analysis of the variation with R. For instance, the work by Dehnen (2000) obtained good results for initial local radial velocity dispersion of $0.2V_c \sim 44\,\mathrm{km\,s^{-1}}$ similar to our IC3 for which σ_U is $40\,\mathrm{km\,s^{-1}}$(for our IC2 it is $\sigma_U = 20\,\mathrm{km\,s^{-1}}$). As it will be seen in Section 14.2, the separation between the two groups of the bimodality depends on the resonant structure of the potential and this is not modified if the initial disc is hotter. The higher initial velocity dispersion of the IC simply populates the supposed Hercules structure at more negative V. This is in agreement with the studies in Fux (2001).

  For the realistic positions $\phi = 0°$ and $\phi =\sim 160°$ (consistent with the Galactic bar and

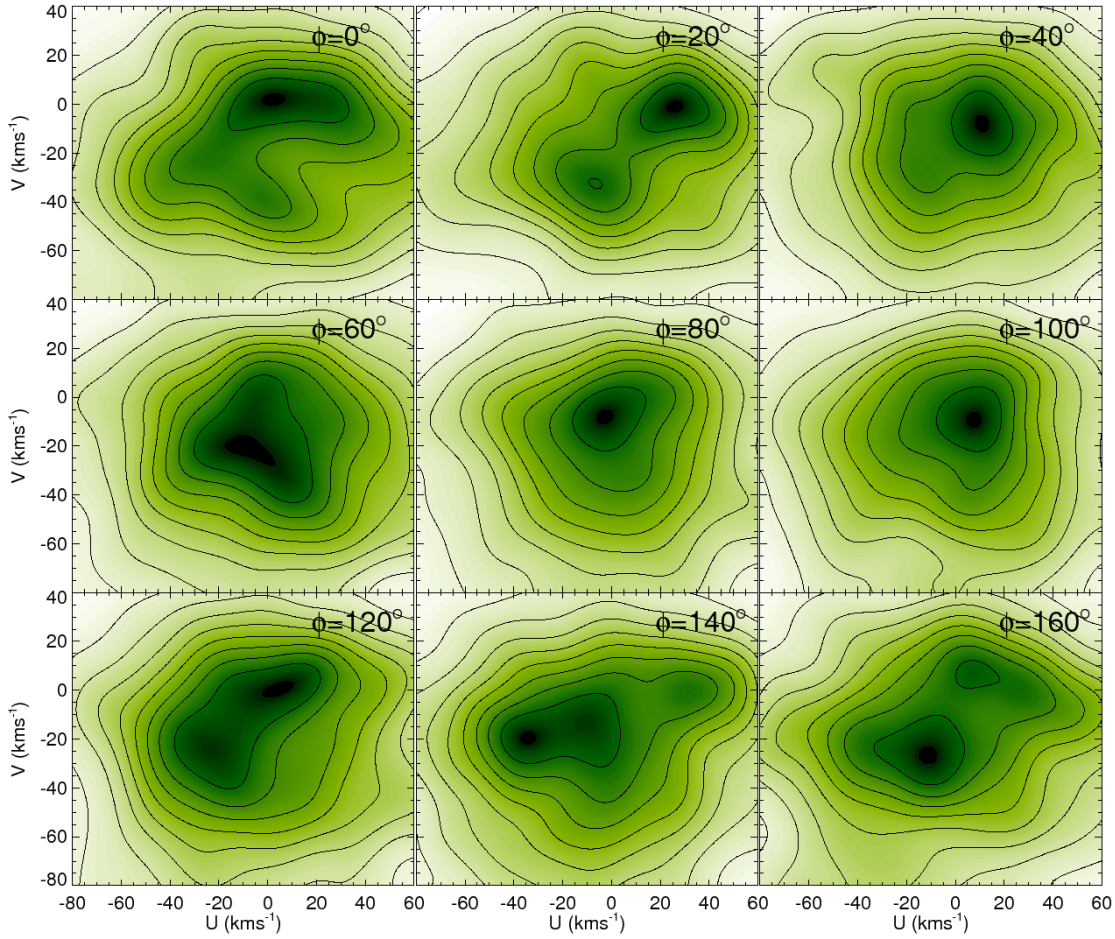

Figure 14.4: **Kinematic effects of the bar on a hot disc.** U–V velocity distributions after WD at $R = 8.5\,\mathrm{kpc}$ and at different azimuths ϕ for the simulations with the PM04–MW potential model using only the bar and IC3.

the long bar), the structure of Hercules is clearly observed and has a negative slope in the U–V plane similar to that observed (Chapter 6). At opposite positions $\phi \sim 100°$, the vast majority of particles with negative V are in the positive U range.

Comparison with the quadrupole bar– It has been repeated the default simulation for the quadrupole bar described in Section 11.5. As we have concluded in that section, the forces of this bar are not very different in terms of their maximum values in the inner regions but the profiles of these forces with radius show very different shapes. Also the radial force at solar radius has doubled with respect the prolate bar and therefore it is also higher at the R_{OLR}. Figure B.20) shows the results of this simulation. The more evident difference is that the equivalent to the Hercules structure appears more separated from the central group but it still has not negative enough V. Also the difference between the mean U of the two groups of the bimodality has become larger. The shift of the central mode to high U is also present and in this case very strong. The results of this simulation are very similar to that of the simulation of the prolate bar with higher mass that we have discussed in a previous paragraph (Figure B.18). This would be due to the similarities in the parameters α and maximum q_r of the massive prolate bar model and quadrupole model. The fact that the bimodality is clear for these two bars can be due to the stronger force of the quadrupole bar at the R_{OLR} as discussed above.

It is worth noticing that in the literature the values obtained for the best pattern speed of the bar with different methods are directly compared without having into account differences in the local circular frequency, solar radius or rotation curve. In Dehnen (2000), the best match with observation is obtained for $\Omega_b \sim 1.85\Omega_0$ that with his assumed local circular frequency ($28.5\,\mathrm{km\,s^{-1}kpc^{-1}}$) it gave him a good fit for a pattern speed of $\Omega_b \sim 53\,\mathrm{km\,s^{-1}kpc^{-1}}$. In our model with a local circular frequency of $25.8\,\mathrm{km\,s^{-1}kpc^{-1}}$ this would give $\Omega_b \sim 48\,\mathrm{km\,s^{-1}kpc^{-1}}$. In other words, the results for Dehnen (2000) with $\Omega_b \sim 53\,\mathrm{km\,s^{-1}kpc^{-1}}$ should be equivalent to our results using $\Omega_b \sim 48\,\mathrm{km\,s^{-1}kpc^{-1}}$. The results for this value are shown in Figure B.15. The fact that in these simulations the supposed Hercules structure is less populated than in Dehnen (2000) maybe due to the different initial conditions and/or the strength of the bar as we have previously seen and discussed. In Chakrabarty (2007) a value of $\Omega_b \sim 57\,\mathrm{km\,s^{-1}kpc^{-1}}$ (with a local circular frequency of $27.5\,\mathrm{km\,s^{-1}kpc^{-1}}$) gave her the best value in terms of a goodness of fit parameter for the models with only bar[1]. This value would correspond to $\Omega_b \sim 54\,\mathrm{km\,s^{-1}kpc^{-1}}$ in our simulations. A comparison between the values for the best pattern speed of the bar according to several studies based on the effects of the resonances are shown in the second column of Table 14.1. In the third column, the approximate equivalent result for the conditions of our simulations is shown. Also an example of pattern speed obtained through an completely

[1]Her simulations with bar+spiral arms are discussed in Chapter 16

Table 14.1: Results for the Ω_b and ϕ_{0b} obtained by other studies and equivalent Ω_b in the PM04–MW potential model. The error in brackets in the last row indicates the possible systematic error reported by the authors.

	Ω_b ($\mathrm{km\,s^{-1}kpc^{-1}}$)		ϕ_{0b} (°)
	Obtained	Equivalent in the PM04–MW potential model	Obtained
Dehnen (2000)	$\Omega_b = 1.85 \pm 0.15\Omega = 53 \pm 4$	48 ± 4	10-70
Chakrabarty (2007)	$\Omega_b = 57 \pm 3$	54 ± 3	0-30
Debattista et al. (2002)	$\Omega_b = 59 \pm 5(\pm 10)$	$55 \pm 5(\pm 10)$	-

different method (Tremaine & Weinberg method , Tremaine & Weinberg 1984) is shown in the last row of Table 14.1. Their value is higher than the ones obtained through the fitting of observed moving groups but all values are consistent if we take into account the errors reported by these studies. Finally, the fourth columns of Table 14.1 shows the values for bar inclination ϕ_{0b} according to several studies. Regarding this parameter our results are similar to the values for which the bimodality is formed in these other studies.

14.2 Relation to regular orbits of the bar

In this section the method of quantifying the regularity of the orbits corresponding to each region of the U–V plane is applied. This method and its goals are detailed in Section 10.3. Basically we intend firstly to ascertain if a given structure that has appeared in the test particle simulations corresponds to a group of periodic or quasi-periodic orbits or not, and secondly to study the variation of the orbital structure of the prolate bar with the parameter variation with special emphasis to the location of the Hercules branch. The debate about the periodicity or chaoticity of the stars in the moving groups is specially interesting for the simulations of the bar as the Hercules structure has been associated with both cases (Dehnen 2000, Fux 2001). Although this do not pretend to be an exhaustive study of the periodic orbits of the model, it has the aim of comparing with some of the results obtained by other studies. The analysis of the existent periodic orbits of the bar potential has been performed for instance in Contopoulos & Grosbol (1989), Dehnen (2000) and Fux (2001). Here we will focus on the study of the orbits that crosses a particular region of the disc that could be considered as the solar neighbourhood.

The periodicity map on the U–V plane for the default model of the prolate bar (Table 11.4)

at $\phi = 0°$ and $R = 8.5\,\mathrm{kpc}$ is shown in 14.5. In this Figure some of the main periodic regions are indicated with a coloured circle and a character. The corresponding orbits are shown in Figure 14.6 with the same colours. The analysis of these two Figures leads to the following conclusions.

Figure 14.6a and 14.6c show interesting orbits corresponding to the 4:1 and 3:1 OLR. More complex but noticeable resonant orbits are the ones that stand for the 7:2 (Figure 14.6b), the 4:2 OLR (Figure 14.6d) and the 3:2 OLR (Figure 14.6j). Also an orbit close to the so-called 1:1 *asym* orbit is present (Figure 14.6k). An orbit that is called asymmetric in a barred potential is an asymmetric orbit with respect to the short axis of the bar according to the usual notation (Dehnen 2000, Fux 2001). However, these resonance at high V is not specially populated in the test particle simulations of Section 14.1.

As other authors have claimed, the bimodality is related to effects of the 2:1 OLR on the orbits. According to Dehnen (2000) for $\phi_{0b} \sim 25°$ and $R_{OLR}/R_\odot \sim 0.9$ the bimodality is caused by the separation that produces a group of unstable chaotic orbits called $x_1 * (2)$ just in the position of the valley that appears between the central mode and the supposed Hercules structure. With our method, we find that the valley is perfectly seen in Figure 14.5 as a white thin arched line at $V \sim -12\,\mathrm{km\,s^{-1}}$ at negative U which goes towards more negative V for positive U. For its colour we know that this region or line on the U–V plane corresponds to a region of non-regular orbits.

There is controversy regarding the orbits of the particles of the supposed Hercules itself (the low angular momentum group of the bimodality). According to Kalnajs (1991), the bimodality is caused by the crossing of $x_1(1)$ and $x_1(2)$ orbits in a given position relative to the bar. The antialigned orbits $x_1(2)$ would form the group at low angular momentum although he identified this group with the Hyades stream instead of Hercules. In Fux (2001) it consist of chaotic orbits which have been forced to avoid the regular region of orbits called $x_1(2)$ at the other side of the U–V plane ($U > 0$) which are orbits antialigned with the bar. By contrast, according to Dehnen (2000) the orbits of Hercules are simply orbits scattered by the OLR. In Chakrabarty (2007), the orbits forming the structure that would support the Hercules stream consist of a great variety of orbits apart from antialigned or the chaotic orbits. According to this author, the variety of orbits depend on the initial velocity dispersions of the disc. For a cold disc, only aligned and antialigned orbits appear similar to Kalnajs (1991). When the disc is hotter and the bar is stronger, also chaotic orbits appear but only at more negative U ($U \leq 70\,\mathrm{km\,s^{-1}}$). On the other hand, according to Dehnen (2000) for $\phi_{0b} \sim 25°$ and $R_{OLR}/R_\odot \sim 0.9$ in the central mode there are two periodic orbits of the family $x_1(1)$ which is a family of orbits that are aligned with the bar and originated out of the OLR. One is almost a circular orbits and therefore centred at $(U, V) \sim (0, 0)$ and the other is the one that causes a distortion of the central mode to positive U and negative V. Depending of the radius and the orientation of the bar, this orbital structure

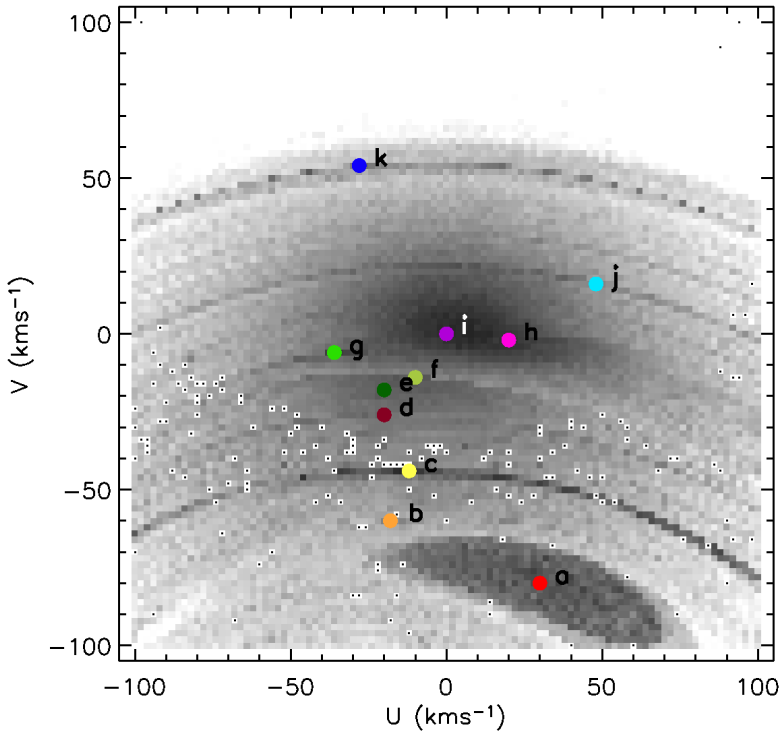

Figure 14.5: **Orbital regularity of the prolate bar.** U–V plane coloured according to the periodicity of the corresponding orbits for the default model of bar at $\phi = 0°$ and $R = 8.5\,\mathrm{kpc}$. The darker the region is, the more periodic or closed the corresponding orbit is. The points corresponding to orbits in Figure 14.6 are marked with coloured circles.

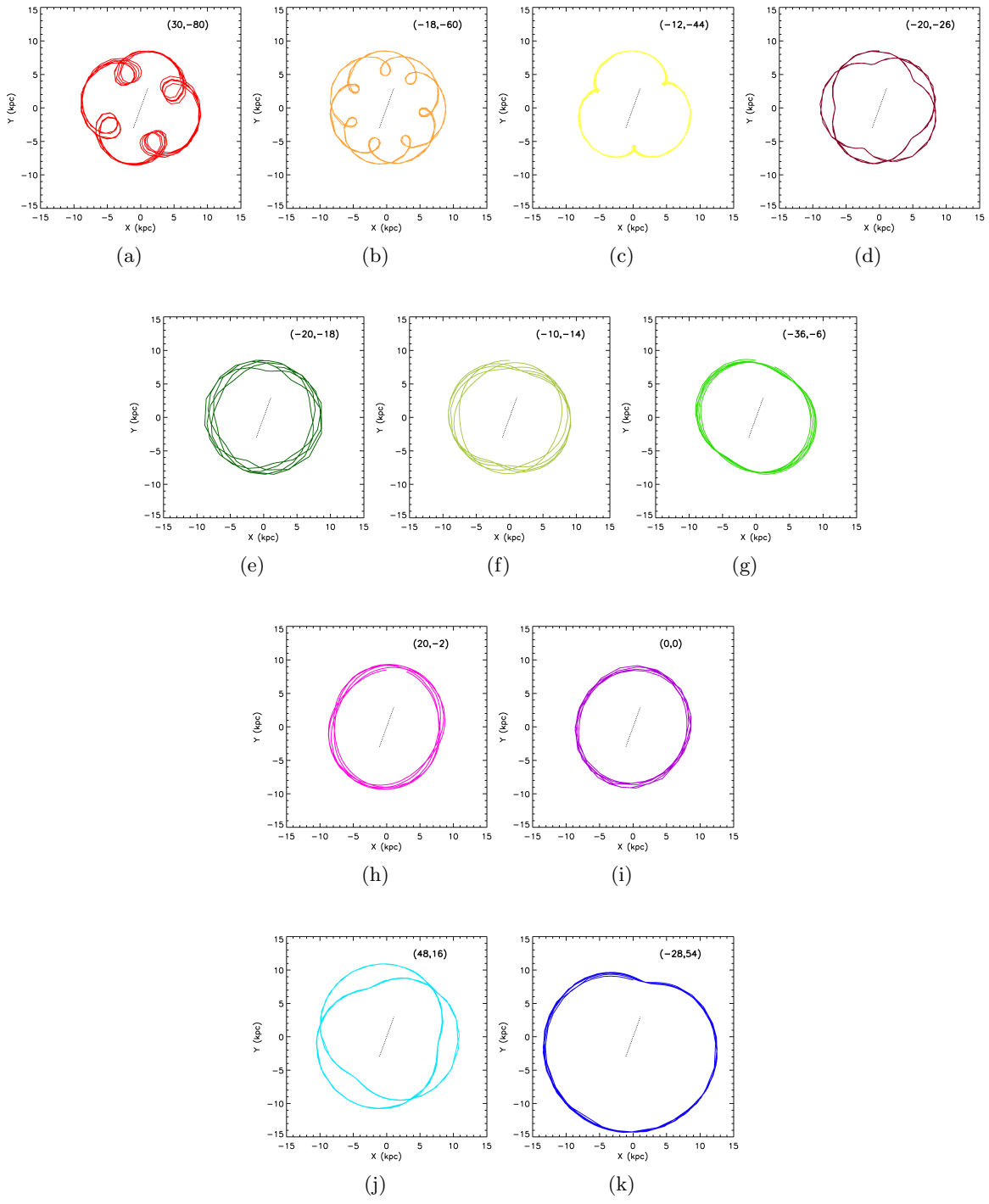

Figure 14.6: **Bar-induced regular orbits.** Orbits of the U–V points indicated in Figure 14.5.

changes. Some of these periodic orbits do not cross the studied region and other new closed orbits such as the antialigned $x_1(2)$ can show up, as in out simulations.

Here the bimodality will be exemplified with the orbits from Figure from 14.6e to 14.6i. The periodic orbits of the central mode are identified also in our simulations. They are those of Figure 14.6h and Figure 14.6i which are quite elliptic orbits aligned with the bar. In particular Figure 14.6h is the orbit that creates the above mentioned distortion of the central mode. In our test particle simulations this distortion was also appreciated as mentioned in Section 14.1 for the simulations with IC1, IC2 and IC3 at $\phi = 0$ and at other positions.

In the region that would correspond to the Hercules moving group just below the valley or the white line in 14.5 we find the orbit of Figure 14.6f which despite not presenting clear periodicity, it is an orbit more or less antialigned with the bar. At more negative V and still in the region of the group at low angular momentum, we find orbits such as Figure 14.6e, which do not seem to be specially periodic. It is unclear if the orbit of Figure 14.6d due to other resonances as explained above (4:2 OLR), would be part of this group. Here, orbits close to the antialigned $x_1(2)$ orbital family are surprisingly found also just above the valley of unstable orbits (Figure 14.6g).

In Figures 14.7 and 14.8 some results of the application of this method with other parameters of the bar potential are presented and compared with the default model. From now on we refer to the position of the valley as the largest V (lowest $|V|$) reached for the curvature of the valley.

- **Orientation of the bar:** For instance if ϕ is changed, the valley moves from negative to central U (Figure 14.7c and even to positive U 14.7b). This explains why the vast majority of particles at $V < 0$ move from $U < 0$ to $U \sim 0$ and to $U > 0$ for $\phi = 60°$ ($\phi_{0b} = -40°$) and $\phi = 100°$ ($\phi_{0b} = -80°$) in our test particle simulations (Figures 14.2 and 14.4). Other structures in this panels have also moved to different regions of the U–V plane (e.g. the one due to the 4:1 OLR).

- **Mass:** We now explore the changes with bar mass. We see that the valley has moved from $V \sim -12\,\mathrm{km\,s^{-1}}$ (default case) to $V \sim -10\,\mathrm{km\,s^{-1}}$ when the mass is decreased (Figure 14.7d) and to $V \sim -14\,\mathrm{km\,s^{-1}}$ when it is increased (Figure 14.7e). Although we have not modified the pattern speed of the bar for these two simulations the resonant structure has changed to a small degree. The reason is the fact that varying the mass of the bar, despite conserving the total mass of the model (the bar mass is subtracted to the bulge), can produce minor and local variations in the rotation curve (different shape and normalisation). Consequently the model has slightly different resonant orbital structure. With these figures we ascertain the dependence of the valley of the bimodality on the curve of circular speed pointed out e.g. in Dehnen (2000).

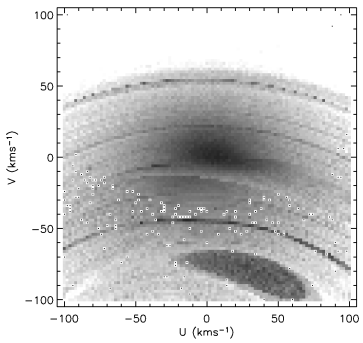

(a) Default

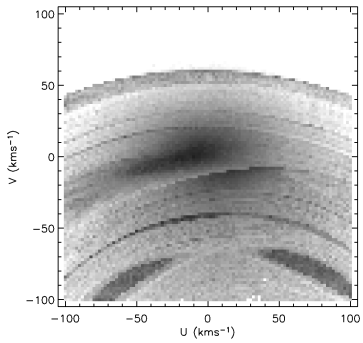

(b) $\phi = 60°$ ($\phi_{0b} = -40°$)

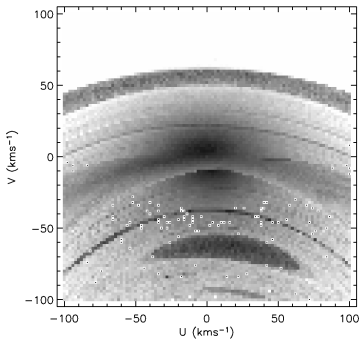

(c) $\phi = 100°$ ($\phi_{0b} = -80°$)

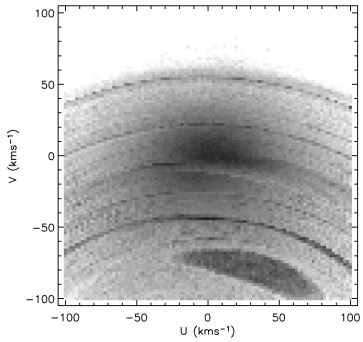

(d) $M_b = 7.0 \cdot 10^9 \mathrm{M}_\odot$

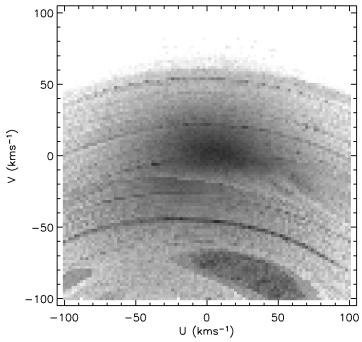

(e) $M_b = 14 \cdot 10^9 \mathrm{M}_\odot$

Figure 14.7: **Orbital regularity of the prolate bar with different properties (I).** U–V plane coloured as the periodicity of the corresponding orbits for several variations of the parameters of the default model of the bar.

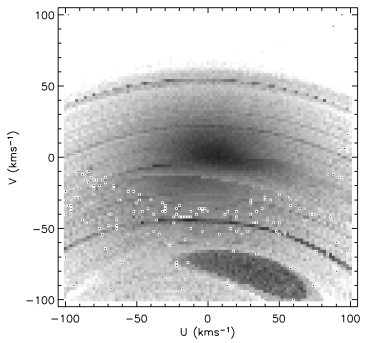

(a) Default

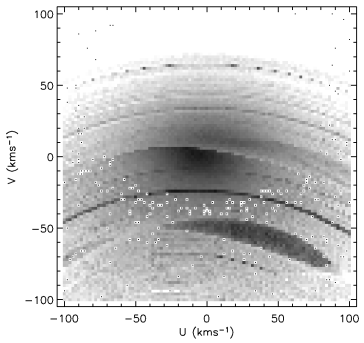

(b) $\Omega_b = 43\,\mathrm{km\,s^{-1}kpc^{-1}}$

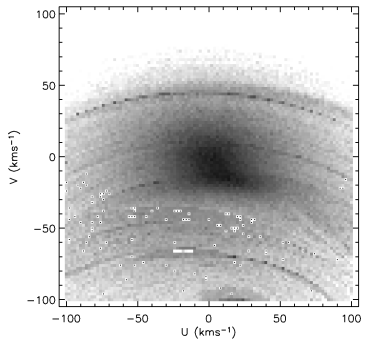

(c) $\Omega_b = 48\,\mathrm{km\,s^{-1}kpc^{-1}}$

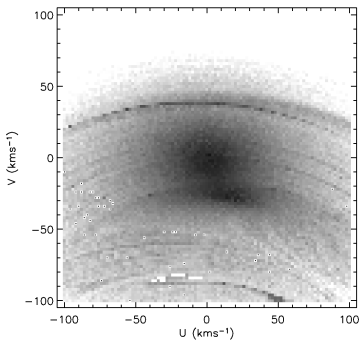

(d) $\Omega_b = 50\,\mathrm{km\,s^{-1}kpc^{-1}}$

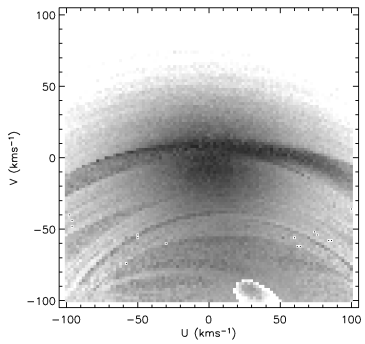

(e) $\Omega_b = 60\,\mathrm{km\,s^{-1}kpc^{-1}}$

Figure 14.8: **Orbital regularity of the prolate bar with different properties (II).** U–V plane coloured as the periodicity of the corresponding orbits for several variations of the parameters of the default model of the bar. The darker the point is, the more closed the corresponding orbit is.

- **Pattern speed:** When the pattern speed is changed, the orbital structure changes (more or less equivalently to a change in the solar radius) and the resonant orbits appear at different position in the U–V plane. For a value of $\Omega_b = 43\,\mathrm{km\,s^{-1}kpc^{-1}}$ (Figure 14.8b) the valley that separates the central mode and the Hercules branch is located at $V \sim +8\,\mathrm{km\,s^{-1}}$. For $\Omega_b = 48\,\mathrm{km\,s^{-1}kpc^{-1}}$ (Figure 14.8c) the valley moves to $V \sim -34\,\mathrm{km\,s^{-1}}$ and therefore the particles below the valley have V more consistent with the observed Hercules group as the valley is at $V \sim -35\,\mathrm{km\,s^{-1}}$ for the observed sample. This observed value is determined from Figure 6.1 (without taking into account the solar motion $V_\odot$). Larger pattern speed such as $\Omega_b = 50\,\mathrm{km\,s^{-1}kpc^{-1}}$ produces a more diffused gap at approximately $V \sim -52\,\mathrm{km\,s^{-1}}$ which is too negative. For $\Omega_b = 60\,\mathrm{km\,s^{-1}kpc^{-1}}$, the valley locates at $V \sim -60\,\mathrm{km\,s^{-1}}$ and has moved to the right side of the U–V plane consistently with B.16. Apart from the valley, the other orbits have also changed with pattern speed.

Now we will try to estimate the pattern speed of the bar that would produce a valley around the position where it is really observed if the bimodality is assigned to the Hercules moving group. From Figure 6.1, we determine that the heliocentric velocity of the observed valley is approximately $V \sim -35\,\mathrm{km\,s^{-1}}$. Assuming the classic estimates for the solar motion $V_\odot = 5\,\mathrm{km\,s^{-1}}$ (see Chapter 12), the peculiar motion of the observed valley is $V = -35 + 5\,\mathrm{km\,s^{-1}} = -30\,\mathrm{km\,s^{-1}}$. This value is still subject to the uncertainty in the solar motion which gives sometimes values as large as $11\,\mathrm{km\,s^{-1}}$ (see Chapter 12). For this reason we will take an assume an extreme error of $10\,\mathrm{km\,s^{-1}}$ in the position of the observed valley: $V = -30 \pm 10\,\mathrm{km\,s^{-1}}$. For our simulations, a plot of the velocity V of the mentioned valley (again taken as the largest V or lowest $|V|$ reached for the curvature of the valley) versus the pattern speed of the bar Ω_b shows approximately a linear relation [2] (Figure 14.9). The points of Figure 14.9 are directly

[2] Equation 10 and 9 of Dehnen (2000) can be combined to give that the the V component of the valley that separates the central mode and the supposed Hercules structure is (in our notation):

$$V \approx a\widetilde{V} - (b + c\beta)V_0 \tag{14.1}$$

being β a parametrisation of the shape of the rotation curve $V_c = V_0(R/R_\odot)^\beta$ and $\widetilde{V}$ defined as:

$$V + \frac{U^2}{2V_0} \cong V_0 \frac{1+\beta}{1-\beta}\left[1 - \frac{\Omega_b/\Omega_0}{1+\sqrt{(1+\beta)/2}}\right] \equiv \widetilde{V}, \tag{14.2}$$

which is the relation that the orbits that are in OLR satisfy approximately. For the same rotation curve (shape β and normalisation V_0), the velocity V of the valley is proportional to Ω_b. These equations however are obtained neglecting the effect of the bar, that is only considering the axisymmetric part in the potential, and estimating the orbits that would be exactly resonant. According to Equation 14.2 these set of orbits would have a parabolic shape in the U–V plane centred in the U component. A simple glance at the panels of Figure 14.7 indicates that despite the approximate parabolic shape of the resonances, the parabolas are not centred in the U direction. However, these equations give us a first estimate.

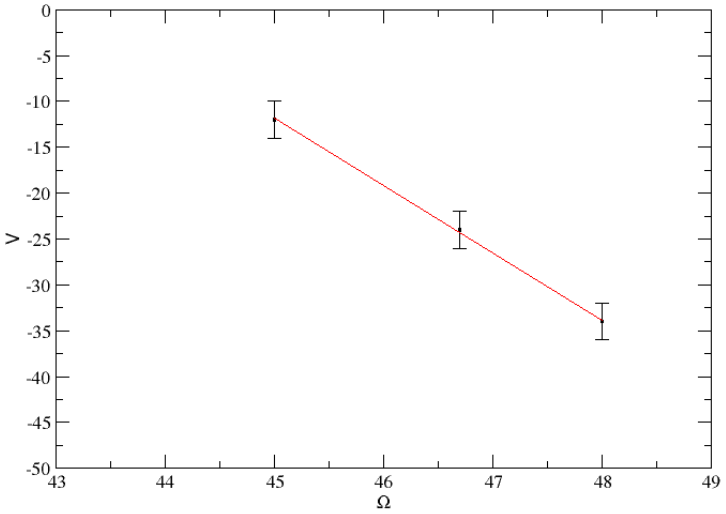

Figure 14.9: **Fit to the Hercules moving group.** Linear regression of the velocity of the valley between the central mode and the supposed Hercules branch versus the pattern speed Ω_b.

read from Figure 14.8b, 14.8a, 14.8c and other additional similar simulation for $\Omega_b = 46.7$ with the valley located at $24\,\mathrm{km\,s^{-1}}$. We have consider only the simulations that approaches more the observed value of the valley. The vertical error bars correspond to the pixel size in Figure 14.8. The linear regression gives:

$$V(\,\mathrm{km\,s^{-1}}) = 317.5(\pm 8.3) - 7.320(\pm 0.18)\ \Omega_b(\,\mathrm{km\,s^{-1}kpc^{-1}}) \tag{14.3}$$

Equation 14.2 gives a pattern speed of $\Omega_b = 47.5 \pm 1.6\,\mathrm{km\,s^{-1}kpc^{-1}}$ to obtain the valley at $V \sim -30\,\mathrm{km\,s^{-1}}$. The largest contribution to the uncertainty in Ω_b comes from the uncertainty in V. It is worth mentioning that all these calculations are carried out for $\phi = 0°$ (which corresponds to a bar's inclination of 20°), which may not be necessarily true. The result of this simulation for $\Omega_b = 47.5\,\mathrm{km\,s^{-1}kpc^{-1}}$ is shown in Figure 14.10.

Having fitted the position of the observed valley between the central mode and the supposed Hercules structure for our model of the prolate bar, it is important to look for other similarities between the observational U–V plane (Figure 6.1) and other structures associated with the bar's resonances. In Figure 14.10 we have also plotted the branches of Part III and the groups of Dehnen (2000) (Table 6.1) corrected for the classic solar motion ($U_\odot = 10\,\mathrm{km\,s^{-1}}$ and $V_\odot = 5\,\mathrm{km\,s^{-1}}$).

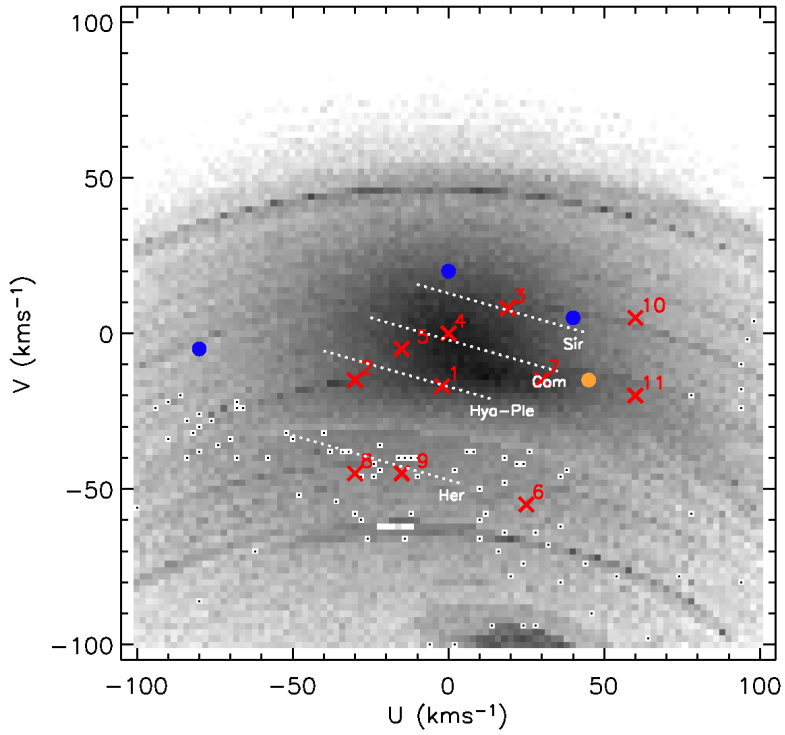

Figure 14.10: **Orbital regularity of the prolate bar with a pattern speed of** $47.5\,\mathrm{km\,s^{-1}kpc^{-1}}$ **.**U–V plane coloured according to the periodicity of the corresponding orbits for the prolate bar with $\Omega_b = 47.5\,\mathrm{km\,s^{-1}kpc^{-1}}$ at $\phi = 0°$ and $R = 8.5\,\mathrm{kpc}$. The white dotted lines show the position of the observational branches (Chapter 6 and the red crosses are the groups found by Dehnen (2000)). These observed features have been all corrected for the classic solar motion ($U_\odot = 10\,\mathrm{km\,s^{-1}}$ and $V_\odot = 5\,\mathrm{km\,s^{-1}}$).

For instance, in Dehnen (2000) the effects of the 1:1 sym resonance in the U–V plane were related to an the observed small wave that he called *ripple* at $(U, V) = (-80, -5)$ and at $(U, V) = (40, 5)$ and to the excess of stars at $|U| < 20\,\mathrm{km\,s^{-1}}$ and $V > 20\,\mathrm{km\,s^{-1}}$. These feature are indicated with blue circles in Figure 14.10. However, the arch-shaped structure caused by the effects of the 1:1 resonance (point (k) in Figure 14.5) goes through $V \sim 46\,\mathrm{km\,s^{-1}}$ at $U = 0\,\mathrm{km\,s^{-1}}$ in Figure 14.10 and therefore is considerably above these observed features in the U–V plane. Moreover, in our case this region of the U–V plane is related to the 1:1 asym orbit which is unstable according to Dehnen (2000) or Fux (2001). By contrast, these observed ripples as well as group 10 (red cross) and the elongation of the Sirius branch seem to coincide more with the arch due to the 3:2 OLR although this is a very thin features in the U–V plane which is difficult to be associated with this observed moving group.

Also the ripple and the new group found in Part III at $(U, V) = (35, -20)$ (orange circle),

the groups 7 and 11 and the elongation of the Coma Berenices branch could be related here to the distortion of the central mode due to the $x_1(1)$ orbits. Dehnen (2000) related this effect to the extension of the connection between Hyades and Pleiades but pointed out that at this low epicyclic energy, the orbits will be additionally distorted by the spiral arms and other deviations of the local smooth field and therefore, he is less conclusive about this issue. This discussion will be resumed in Chapter 16 where the effects of the spiral-bar PM04–MW potential model are studied. Here the Hyades group coincides with the position of the $x_1(2)$ orbits. In agreement with Dehnen (2000) it is important to point out that these groups should be studied in more detail as effects such as these ones, should be taken into account in order to constrain the bar's characteristics and to reduce systematic errors (for example due to the uncertainty of the movement of the LSR).

On the other hand, another intriguing and prominent structure is the one around point (a) corresponding to the 4:1 resonance (Figure 14.6a). This strong kinematic structure with $V \sim 90\,\mathrm{km\,s^{-1}}$ could be tentatively associated with observed structures at low angular momentum such as the Arcturus moving group. These groups have been usually associated with remnants of accreted satellites. The possibility that they can also be due to resonances of the bar is specially encouraging and Chapter 15 is devoted to study and discuss this subject.

14.3 Summary and discussion

We have studied a bar potential model derived from an observationally constrained density distribution and whose effects on the velocity distribution has never been studied before. We find that this prolate bar model create significant and strong imprints on the velocity plane as in the case of the self-gravitating spiral arms. By contrast to the spiral arms whose orientation with respect to the Sun is very uncertain, in this case the bar inclination is relatively well constrained by other independent studies. For this reason, we have focused on the results for a bar orientation of around 20° corresponding to the Galactic bar (or triaxial bulge) and around 40° similar to the recently discovered long bar of the MW.

When the prolate bar with those realistic inclination acts on a cold disc during long times ($\sim$ 15 bar revolutions), it hardly produces kinematic substructures except for a unique central group that is distorted towards positive U. However, when the bar acts on a slightly hotter disc during short times (e.g. only 3 bar revolutions), the prolate bar can produce clear kinematic structures. In particular the prolate bar triggers a bimodality, i.e. two groups, in the velocity distribution at solar radius if the bar has certain characteristics, specially concerning its pattern speed. One of the groups has negative V. The other one is approximately centred on the U–V plane (here called the central mode). For the bar orientations which are consistent with

independent bar restrictions, the group at negative V have mean negative radial motion U. Additionally, in most of these simulations the central mode of the bimodality is distorted towards positive U. This causes a relative density of particles in this region higher than that in the observed velocity field.

These resonant features are far more clear and sharpen when the prolate bar is stronger ($M_b = 1.4 \times 10^{10}\mathrm{M}_\odot$) and if the integration time is longer ($\sim$ 10 bar revolutions) but these parameters do not change the position of the line that discriminates the groups of the bimodality. What probably produce stronger resonant imprints on the U–V plane is the higher strength of the massive bar at radius where the resonances are located (in particular the OLR).

The group at negative V of the bimodality has usually been associated with the Hercules branch (Dehnen 2000, Fux 2000). Depending on the pattern speed of the bar, this simulated group at negative V shifts to upper or lower positions on the U–V plane. We find that for some pattern speeds this group could be better related to Hyades-Pleiades instead of Hercules as it is usually assigned.

We find that only a disc with intermediate velocity dispersions is necessary to create the bimodality in contrast to other studies that used a hotter disc (Dehnen 2000). However, higher velocity dispersions contribute to populate the structure towards more negative V, showing that higher initial velocity dispersion allow more particles to reach the solar radius and crowd that region of the U–V plane. The line that separates the two groups, however, do not change since it depends on the resonant structure of the potential but not on the initial disc. This exemplifies the differences between the existing resonant or orbital structure of a potential model and how the groups are actually crowded given a certain initial disc.

Here we have also studied the effects of the quadrupole bar in the same conditions that our experiments with the prolate bar: same initial conditions and simulation method, same axisymmetric background and same pattern speed. We have found that, if the force of the quadrupole bar at solar radius is comparable to our massive prolate bar, only minor differences between the effects of both models are observed at solar radius: the bimodality created by the quadrupole seems to be stronger as when the more massive prolate bar is studied. Therefore we attribute this to the strength of these two bar models at the R_{OLR} as discussed above. From this comparison we conclude that in contrast to the case of the spiral arms where important differences were found between models, it seems more difficult to discriminate between bar models. At the outer parts of the disc, the force curves and amplitude ranges of the two models can be similar. However, in later chapters we work with hotter initial conditions and therefore, we consider orbits that have large radial excursions that can even enter the bar itself where the quadrupole bar model is probably not a good approximation. The prolate model is a more realistic model which includes also other multi-pole terms and therefore describes better

the regions near or in the bar itself. The possible differences between models in this case are discussed in Chapter 15.

We have seen with our method of quantifying the regularity of the kinematic regions on the U–V plane, that what separates the two groups of the bimodality is a thin line in the kinematic plane made of irregular orbits probably related to the 2:1 OLR. This line or valley that separates the two groups is inclined in the U–V plane producing an Hercules group that is slightly tilted as in the observations.The distortion of the central mode seems to be created by quite elliptic orbits aligned with the bar and also a similar group of orbits appears centred in the central mode. These orbits seems to be the stable $x_1(1)$ related to the 2:1 OLR of the bar. Below the valley, we find different types of orbits. For instance, there are orbits more or less antialigned with the bar (probably related to the $x_1(2)$ orbits), orbits that do not show any especial periodicity or orbits finishing 4 radial oscillations in 2 azimuthal periods (related to the 4:2 OLR). Orbits close to the antialigned $x_1(2)$ orbital family are surprisingly found also just above the valley of irregular orbits.

If we assume a bar's inclination of 20° and the bimodality as the cause of the Hercules moving group, our best fit for the pattern speed of the bar is $\Omega_b = 47.5 \pm 1.6\,\mathrm{km\,s^{-1}kpc^{-1}}$ where the largest contribution to the uncertainty comes from the uncertainty in the solar motion and in the velocity V of the observed Hercules moving group considered (for discrepancies in the kinematic position of Hercules see Section 6.3). It is worth noticing that in the literature the values obtained for the best pattern speed of the bar with different methods are directly compared without having into account differences in the local circular frequency, solar radius or rotation curve. However, all values are consistent if we consider the uncertainties in each case.

For our fit, other strong features such the distortion of the central mode due to the $x_1(1)$ orbits could be identified to the new group found in Part III at $(U, V) = (35, -20)$ (orange circle) and, in general, the elongation of the Coma Berenices branch. Besides, the Hyades group coincides with the position of the $x_1(2)$ orbits above the line of irregular orbits. There are also other resonant orbits at the outer parts of U–V plane such as the one related to the 1:1 sym resonance or the arch of the 3:2 OLR but they produce very thin features in the U–V plane which can hardly be associated with observed moving groups. Besides, they do not have their counterparts in the test particle simulations nor in the observed U–V plane.

The position of the Hercules structure is therefore an important constraint to the characteristics of the bar of the MW. However, there is a degeneracy in the parameter space, as the pattern speed of the bar, the orientation of the bar or the rotation curve contribute to the definition of the position of this structure on the U–V plane. On the other hand, we found among all our simulations several alternative interpretations of each moving group. For this reason, it is very difficult to establish conclusively the best fit for the pattern speed.

From our analysis of orbit regularity we confirm that the orbital structure created by the bar is very sensitive to the bar inclination, to the pattern speed, and to the underlying circular velocity curve from which the resonant curves are derived. On the contrary, the valley of the bimodality do not change with parameters such as the strength of the bar. However the strength of the bar, the exposure time to the bar or disc velocity dispersion influences in the way that the structures are populated. This is, as in the case of the spiral arms, very encouraging in order to use this method to constrain the bar characteristics.

Chapter 15

Imprints on models with hotter kinematics

In this chapter we study the kinematic structure developed when our hottest initial disc IC3 (see default values of Table 10.1) are used. First in Section 15.1 we present the results of our simulations when only the axisymmetric part of the PM04–MW potential model is used. Secondly, in Sections 15.2 and Section 15.3 we study specifically the effects of the bar and the spiral arms on hot discs. Section 15.4 deals with the study of the regularity of the orbits on the low angular momentum region of the U–V plane for the prolate bar. Finally, Section 15.5 shows a summary and a discussion of the results of this chapter.

15.1 Transient arches

In Section 10.2 and in Appendix A, we have seen that the IC3 favours eccentric orbits in the central region of the disc that tend to reach the solar radius. With the initial non-homogeneous coverage of the phase space biased to these highly eccentric orbits, a process of radial migration and phase-mixing is triggered becoming apparent in the formation of transient structures in the U–V plane until the complete phase mixing and relaxation are achieved. For these reason, these IC are used as a representation of a disc which is initially non-relaxed. As we know from current scenarios of galaxy formation and evolution that it is plausible that both external and internal perturbation mechanisms perturb the galaxy, we also want to consider this possibility for the MW. This methodology of using unevenly distributed in phase space initial conditions as a proxy for studying an unrelaxed population was first used in Minchev et al. (2009).

In this case the study becomes more complex as the effects of the bar and/or the spiral arms are superposed to the transient effects due to the mentioned phase-mixing. As we do not take averages with time, the transient kinematic structures are susceptible to be mixed up with the kinematic structures created by the bar and the spiral arms that we want to study. Therefore, it is mandatory to study them in the presence of only an axisymmetric potential. This is carried out in the present section. In Section 15.2 we study in detail the effects of the bar and the spiral arms on this non-relaxed disc whereas in Section 15.3 we use several approaches to study the effects of the bar on relaxed IC.

We show now the final velocity distribution of the simulations with the axisymmetric part of the PM04–MW potential model applied to hot initial conditions (IC3). The panels of Figure 15.1 are obtained when the integration is carried out for the default time of these IC (400 Myr). In this panels arch-shaped structures appear specially at lower V. The positions of the arches on the U–V plane are equal for all ϕ as expected for axisymmetric systems. These arches are, however, asymmetric in U and they change with time. Figure 15.2 shows the evolution with time of the arches. From Figure 15.2a to 15.2d we can see how the arches change in snapshots every 100 Myr. For large integration times, the arches successively disappear leading to the smooth and symmetric in U distribution of Figure 15.2g after $2000 - 5000$ Myr.

As we do not expect kinematic structures for an axisymmetric model and we have seen that the arches that appear with IC3 (Figures 15.1 and 15.2) are a transitory effect, we can definitely attribute the existence of these transient features in the U–V plane to the ongoing phase mixing. Similar arches were obtained and discussed in past studies such as Fux (2001). In that case the author was using the backward integration technique (see Section 10.4) applied to a potential were a bar is slowly developed. He found that incurved waves appear in the valley of the bimodality (see Chapter 14) with a spacing between the maxima decreasing with time relating them to a typical signature of ongoing phase mixing in a regular region of phase space. In other regions of the U–V plane similar arches appeared but on a shorter timescale and the orientation of the wave fronts changed from nearly-horizontal to nearly-vertical.

Also recently and simultaneously to the development of this thesis, Minchev et al. (2009) reported that they found that the velocity distribution exhibited waves travelling in the direction of positive V and these waves becoming closer as the system relaxes when using a non-relaxed model (a population unevenly distributed in phase space). In that study a high velocity dispersion of $\sigma_U = 50\,\mathrm{km\,s^{-1}}$ was used and they discussed the possibility that the MW disc is in a non-relaxed situation due to e.g. a recent merger and that these arches were similar to some observed kinematic groups at low angular momentum. Using a semi-analytical model, Minchev et al. (2009) were able to explain their arches and the decreasing separation with time. It is however noteworthy that according to this model, the arches appear to be symmetric with re-

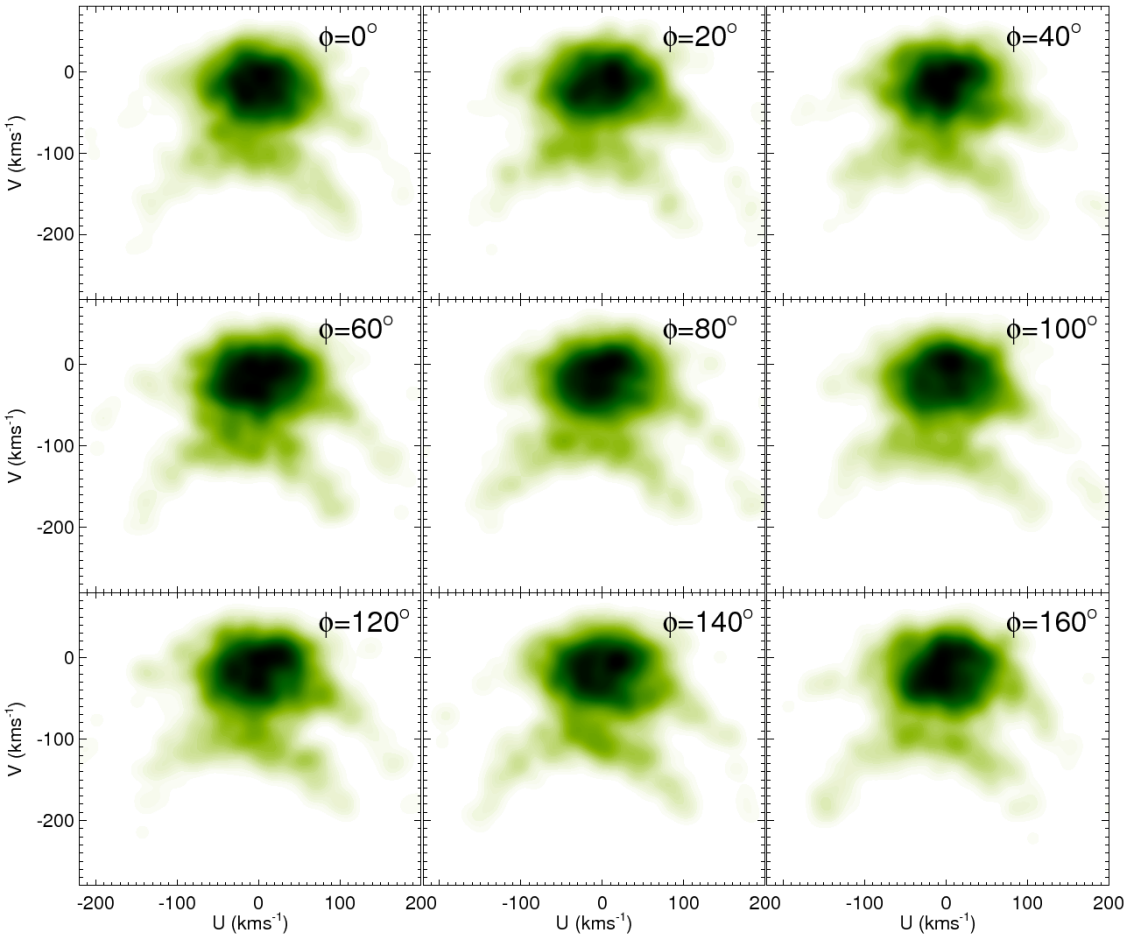

Figure 15.1: **Transient kinematic arches in the axisymmetric potential.** U–V velocity distributions after WD at $R = 8.5\,\mathrm{kpc}$ and at different azimuths ϕ for the simulations with the PM04–MW potential model with only the axisymmetric part and IC3.

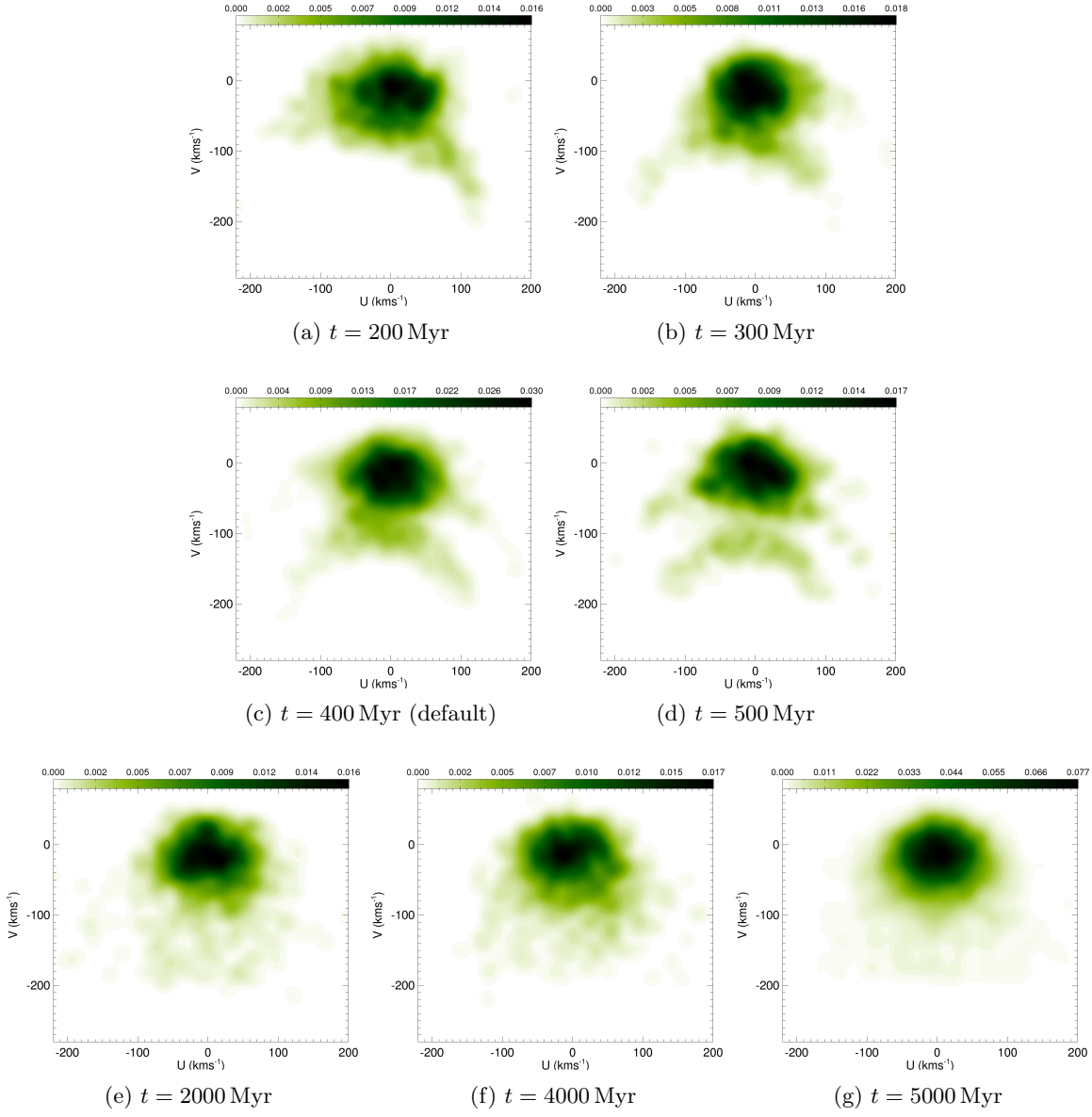

(a) $t = 200\,\mathrm{Myr}$ (b) $t = 300\,\mathrm{Myr}$

(c) $t = 400\,\mathrm{Myr}$ (default) (d) $t = 500\,\mathrm{Myr}$

(e) $t = 2000\,\mathrm{Myr}$ (f) $t = 4000\,\mathrm{Myr}$ (g) $t = 5000\,\mathrm{Myr}$

Figure 15.2: **Time evolution of the kinematic arches.** U–V velocity distributions after WD at $R = 8.5\,\mathrm{kpc}$ and $\phi = 0°$ for the simulations with the PM04–MW potential model with only the axisymmetric part and IC3 for different integration times.

spect to the U axis whereas in their test particle simulations (see their Figure 1) we identify an asymmetry for the some of the arches with lower integration times that it is not mentioned in that study. Similar asymmetry is observed in the arches of our simulations.

In next section we study the effects of the bar and the spiral arms on the velocity distribution of this non-relaxed disc. We expect again some transient effects in the case of IC3 due to the ongoing phase-mixing. However, we consider this as a plausible situation for the MW as it is possible that the disc is still experiencing the response to certain perturbation such as a recent passage of an orbiting satellite.

15.2 Transient groups influenced by non-axisymmetric components

The discs with hot kinematic allow us to discuss the influence of the non-axisymmetric components at the region of low angular momentum of the U–V plane. The observed groups with low angular momentum have been sometimes associated with remnants of past accretion events of satellite galaxies (e.g. Arcturus as discussed in Navarro et al. 2004). The possibility that these groups can be influenced and indeed caused by the resonances of the bar is a very new and promising subject of study. In this section and in Section 15.3 we provide some new preliminary clues to this so poorly understood issue.

In this section we study the effects of the bar and the spiral arms on IC3. As we have discussed in Section 10.2 and in Appendix A, the use of IC3 is representative of a non-relaxed disc that favours eccentric orbits in the central region of the disc which tend to reach the solar radius. This is a plausible possibility for the disc of the MW if it has suffer a certain perturbation. Therefore, assuming this possibility, we want to examine how the arches seen in the velocity distribution due to the readjustment of the disc (Section 15.1) are influenced by the effects of the bar or the spiral arms.

We study first what happens to the velocity distribution if we use IC3 and the PM04–MW potential model with only spiral arms. The results are shown in Figure 15.3. It is expected that the transitory features or arches in the U–V plane still appear: the disc is experiencing phase-mixing. The fact that a non-axisymmetric component has been include in this simulation can actually intensify the process. Effectively, we still see the arches in the velocity distribution in Figure 15.3. In fact they appear to be the same arches than in the axisymmetric case (Figure 15.1) with the same integration time and again they are equal for all ϕ. With this we conclude that the spiral arms with the default parameters have not a noticeable influence on the structures of low angular momentum. This can be explained by the fact that at V so negative

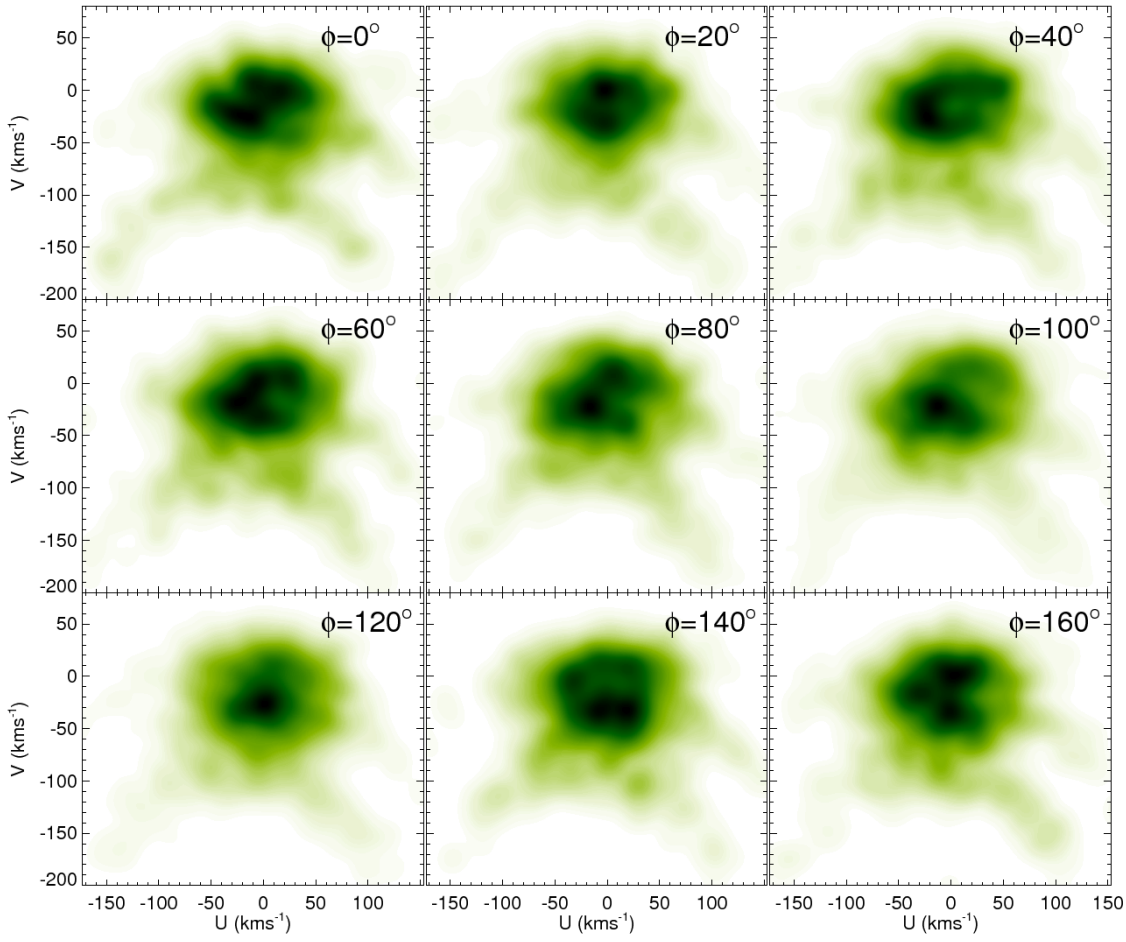

Figure 15.3: **Effects of the spiral arms on the transient arches.** U–V velocity distributions after WD at $R = 8.5\,\mathrm{kpc}$ and at different azimuths ϕ for the simulations with the PM04–MW potential model using only spiral arms and IC3.

(large epicyclic frequencies) the spiral arms hardly affect the orbits (see discussion in Chapter 13).

The results become more interesting when we apply to IC3 the PM04–MW potential model with the bar component with the default values (Figure 15.4). Again arch-shaped structures appear at lower V. But what is encouraging is that in these simulations these kinematic arches have changed. The arches are no longer equal to the ones in the axisymmetric case (Figure 15.1) and now depend on ϕ. For instance, the arch at $V \sim -100\,\mathrm{km\,s^{-1}}$ is shifted to the left for $\phi = 0^\circ$ compared with $\phi = 80^\circ$ where it appears more or less centred in U. Also, differences are observed if we use either $\Omega_b = 45\,\mathrm{km\,s^{-1}kpc^{-1}}$ (Figure 15.4) or $\Omega_b = 60\,\mathrm{km\,s^{-1}kpc^{-1}}$ (Figure B.21). For example the arch developed at $V \sim -100\,\mathrm{km\,s^{-1}}$ for the lower bar pattern speed at $\phi = 0^\circ$ is not seen now when $\Omega_b = 60\,\mathrm{km\,s^{-1}kpc^{-1}}$. Furthermore, the velocity distributions at other ϕ are quite different for these two pattern speeds. All these are evidence that the bar's resonances influence significantly the orbits with inner guiding centres which at solar radius achieve so negative V.

The arch developed at $V \sim -100\,\mathrm{km\,s^{-1}}$ for the lower bar pattern speed has a V components closer to the Arcturus observed structures[1]. For the positions $\phi = 0^\circ$ and $\phi = 160^\circ$ (corresponding to realistic bar orientations ϕ_{0b} of 20° and 40° respectively) the arches, despite being extended through a wide range of U, have mean negative U. That is exactly what was determined in the observational study of (Williams et al. 2009): the Arcturus stars are observed to preferred negative U. This result should be considered for the moment only as evidence of sensitivity to the model but not necessarily as favouring a particular Ω_b value. To conclude, these simulations show the important role of the bar in the development of the local kinematic structure suggesting that both kinematic initial conditions and Galactic structure contribute to create the kinematic groups.

Minchev et al. (2009) was the first to suggest that Arcturus and other groups at low angular momentum could have an origin related to non-relaxed initial conditions. In that study, four observed moving groups at low angular momentum were used to fit the time since the perturbing event that caused the transient arches in the U–V plane: the new group at $V \sim -160\,\mathrm{km\,s^{-1}}$ that was found by Klement et al. (2008), the Arcturus group at $V \sim -100\,\mathrm{km\,s^{-1}}$, the group of Arifyanto & Fuchs (2006) at $V \sim -80\,\mathrm{km\,s^{-1}}$ and HR1614 at $V \sim -60\,\mathrm{km\,s^{-1}}$. However, they used only an axisymmetric model and did not take into account that some of these groups have a mean U component different from 0 (Arcturus according to Williams et al. 2009) or that some other groups have low chemical and age scattering and seem to be remnants of a dispersed star

[1]Notice that the observed Arcturus structure do not appear in Figure 6.1 (it is actually out of the range of the Figure) as this structure is not prominent in our observational sample used in Part III. See Figure 2 of Williams et al. (2009) for a U–V plane containing the Arcturus structure and built using sample from Schuster et al. (2006).

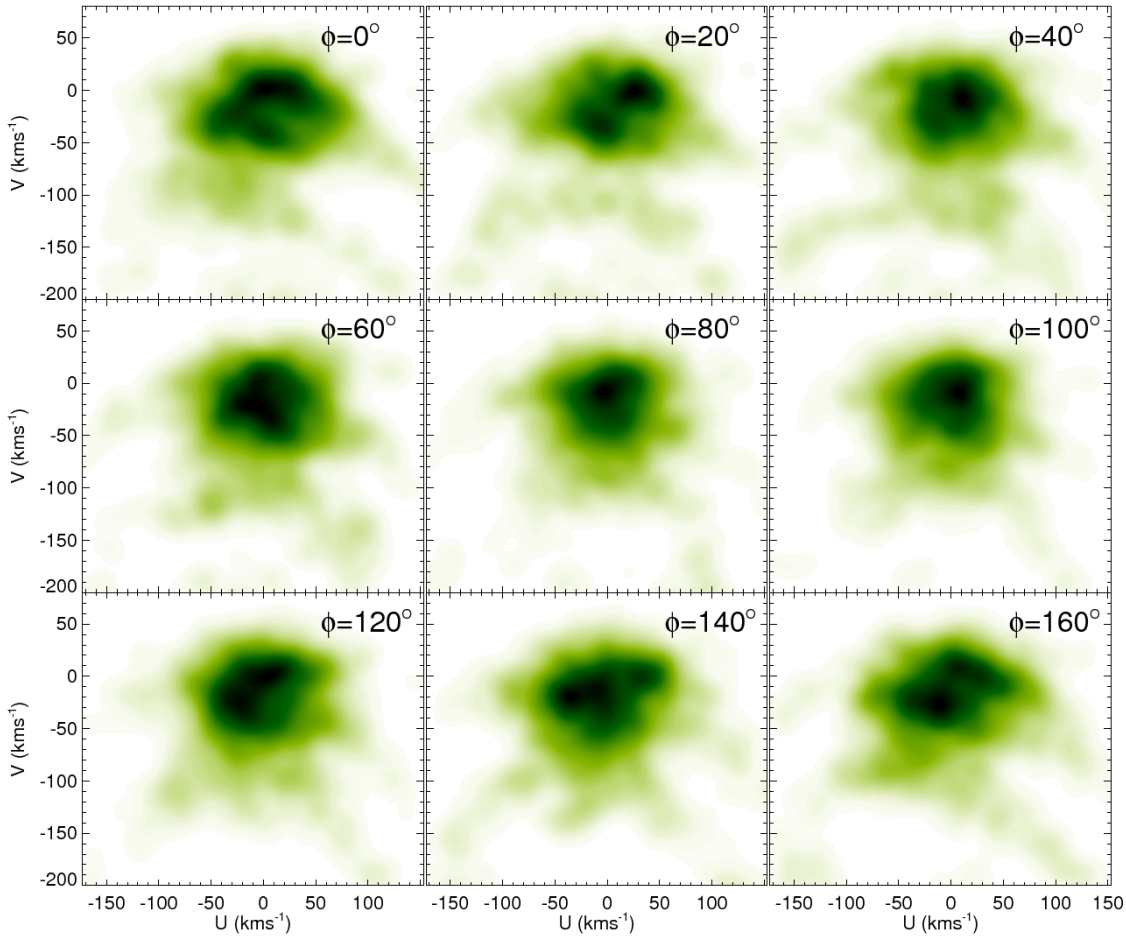

Figure 15.4: **Effects of the bar on the transient arches.** U–V velocity distributions after WD at $R = 8.5\,\mathrm{kpc}$ and at different azimuths ϕ for the simulations with the PM04–MW potential model using only bar and IC3.

forming event (HR1614 according Feltzing & Holmberg 2000 and De Silva et al. 2007).

15.3 Non-transient structures at low angular momentum

The simulations of Section 15.2 have shown us that both the conditions of the disc and the influence of the bar can create and shape the kinematic structures at low angular momentum. We now want to study specifically the long-lasting effects of the bar at the region of low angular momentum of the U–V plane. We use several approaches with the aim of avoiding the transient structures.

Longer integration times. First, we extend the integration time of Figure 15.4 in order to stabilise the possible transient kinematic features. As we have seen in Section 15.1 (Figure 15.2) the arches have disappeared with integration times of 5000 Myr. Therefore, we choose this integration time for the new simulation. As discussed in Chapter 10, such a longer time would require to include many phenomena of Galactic evolution. As it is warned also in that chapter this simulation should be taken as a particular experiment that do not try to mimic the evolution of the MW. We just aim to isolate the effects of the bar resonances avoiding transient features on the U–V plane. The simulation with the prolate bar with IC3 and integration time of 5000 Gyr is shown in Figure 15.5. In the central parts of these distributions, the structure at $V \sim -30\,\mathrm{km\,s^{-1}}$ in most panels is the group of low angular momentum of the bimodality which is usually associated with the observed Hercules group. This structure has been discussed in Chapter 14 and here it follows the same behaviour. For example, at $\phi = 0°$ this group appears to be shifted towards negative U and that is why it can be associated with the Hercules structure. Particularising for the groups at lower angular momentum we see some weak substructures below the bimodality. An arch can be glimpsed between $V \sim -50\,\mathrm{km\,s^{-1}}$ and $V \sim -100\,\mathrm{km\,s^{-1}}$ at almost all ϕ. The fact that this structure changes the U component depending on ϕ (for instance is shifted to positive U for $\phi = 100°$ but is shifted towards negative U for $\phi = 140°$) may indicate that it is caused by the influence of the bar. However, the weakness of this structure deprive us to formulate a definitive conclusion about it.

Massive bar. We know from Section 14.1 that a more massive bar can produce stronger resonant features. We now explore the effects of a stronger bar. We will use the quadrupole bar described in Section 11.5 that has comparable strength at inner radius ($R < 2\,\mathrm{kpc}$) but it is stronger for approximately $R > 2\,\mathrm{kpc}$. We apply the quadrupole bar to IC3 with an integration time of $t = 5000\,\mathrm{Myr}$ in order to avoid transient features in the U–V plane. The results for this simulation are shown in Figure 15.6. Again arched structures appear and in

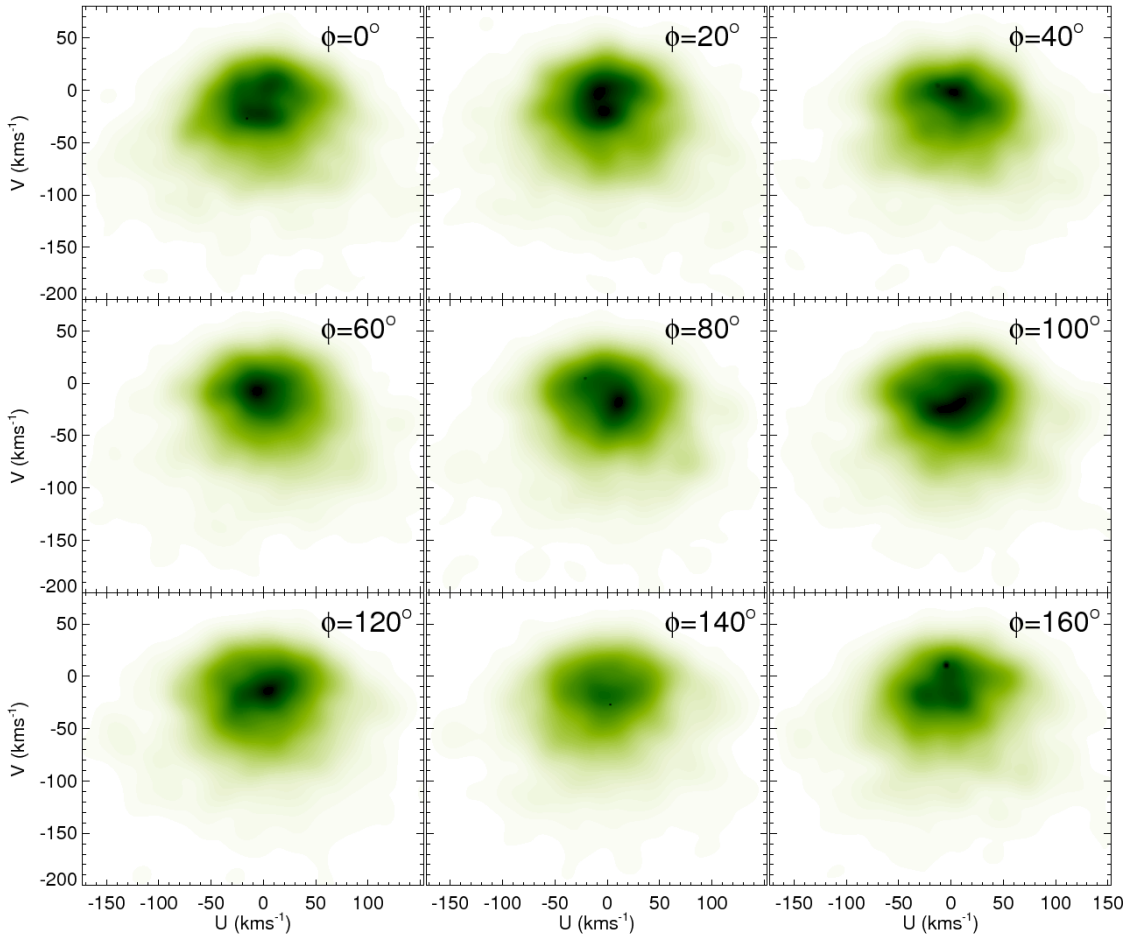

Figure 15.5: **Kinematic effects of the bar on a hot disc.** U–V velocity distributions after WD at $R = 8.5\,\mathrm{kpc}$ and at different azimuths ϕ for the simulations with the PM04–MW potential model using only bar and IC3 with integration time of 5000 Gyr.

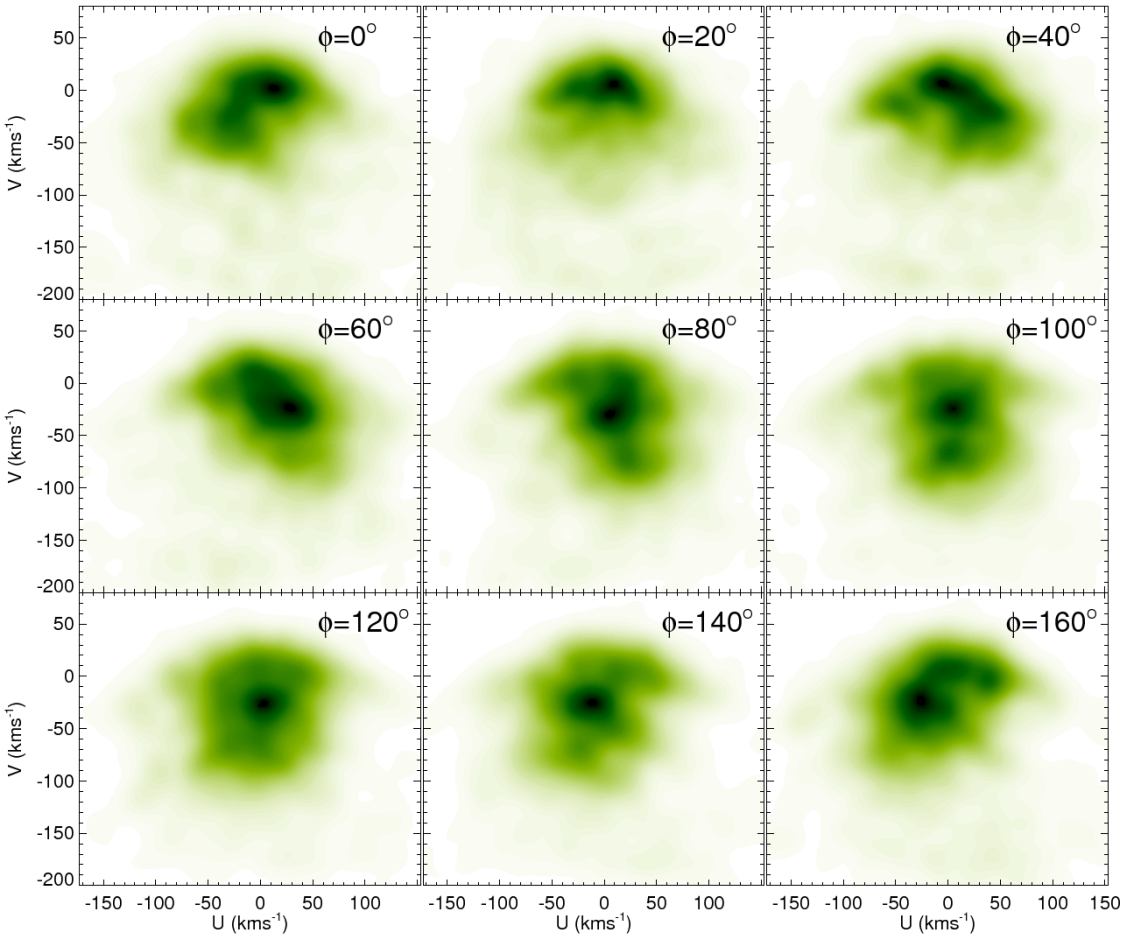

Figure 15.6: **Kinematic effects of a stronger bar on a hot disc.** U–V velocity distributions after WD at $R = 8.5\,\mathrm{kpc}$ and at different azimuths ϕ for the simulations with the quadrupole bar model and IC3 with integration time of 5000 Myr.

particular, the presence of at least three very clear arches can be noticed conspicuously from $\phi = 60°$ to $\phi = 160°$. We have performed a simulation corresponding to an integration time of 5500 Myr (Figure B.22) where exactly the same structures show up. With this we check that these structures are not-transient kinematic groups, or at least, they are stable groups at these long time scales.

In particular the velocity distribution at $\phi = 160°$ is the one that corresponds to a bar orientation of $\phi_{0b} = 40°$. This orientation is consistent with the orientation of the recently discovered long bar of the MW (see Section 11.3). At this position the structure is located at $V \sim -70\,\mathrm{km\,s^{-1}}$. Its mean U is $\sim -50\,\mathrm{km\,s^{-1}}$. We check that with the pattern speed of $\Omega_b = 47.5\,\mathrm{km\,s^{-1}kpc^{-1}}$ which has been derived in Section 14.2 to fit the position of the Hercules moving group, all the structures of the panel shift towards more negative V (Figure B.23). In particular the arch at $V \sim -70\,\mathrm{km\,s^{-1}}$ achieve $V \sim -100\,\mathrm{km\,s^{-1}}$ and would be consistent with the V of the observed Arcturus moving group and also with its mean negative U. The central kinematic arch at this ϕ is compatible with the Hercules structure. At $\phi = 0°$, which corresponds to a bar orientation of $\phi_{0b} = 20°$ as the Galactic bar, this central kinematic structure similar to the Hercules groups is also very conspicuous.

According to these simulations we see that the bar create also kinematic groups at low angular momentum. However, we must be careful in interpreting these results. First, particles with $V \sim -100\,\mathrm{km\,s^{-1}}$ in this potential have radial excursions that arrive to very inner regions that can even enter through the bar itself for which the quadrupole potential is not a very accurate model (see Section 11.5). Therefore, this requires a confirmation using the massive prolate bar which, as it is a potential model derived from an observationally constrained density distribution, gives a better description at the inner regions. We expect that this arch would also appear as we have recognised some weak structures following the same behaviour for the default prolate bar. Secondly, it is worth mentioning that our simulations have consider the Galactic bar and the long bar separately. Simulations including both bars with their corresponding orientations have not been carried out yet. If the two bars rotate at different pattern speeds the results can vary significantly (see discussions in Chapter 16 where we combine two non-axisymmetric components –bar and spiral arms– rotating at different speeds). By contrast, we expect that if the bars rotate at similar pattern speed we will have an approximate combination of the previous panels at $\phi = 0°$ and $\phi = 160°$. Besides, the relative strength of these two bar would play an important role on the final induced effects. In any case, this conclusion is awaiting for a confirmation with a simulation including both bars at the same time.

Progressive introduction of the bar. A more elaborated exercise consist of the following. First we built a new set of IC with the following process. We run a simulation using IC3 and

integrating for 5000 Myr in the PM04–MW potential model with only the axisymmetric part in order to get a relaxed distribution as in Figure 15.2g where the arches had disappeared. The final result of the simulation is taken as IC for new simulations. These new IC will be named IC4. In particular, we design a simulation whose novelty with respect to the previous simulations is that the bar grows progressively during the initial times of the integration and stays stable after this period. Several N-body experiments have concluded that the bar growth and evolution depends on its mechanism of formation and on several parameters (e.g. Athanassoula 2003). We indeed do not know which has been the case of the MW. We do not pretend to model the real MW bar formation but we only intend to add it slowly to the potential in order to avoid an abrupt or response of the disc. We have chosen arbitrarily the growth following Equation 4 by Dehnen (2000) which is flexible and can be easily fit to a a slower of faster growth. For the moment we only explore the values used in that study. In our case is the mass of the bar instead of the amplitude of the potential which changes as a function of time[2]. The integration is carried out as usually from t_i (negative, see Section 10.1) to $t_f = 0$ and the bar grows progressively from t_i to t_1 according to this expression:

$$M_b = M_{bf}\left(\frac{3}{16}\xi^5 - \frac{5}{8}\xi^3 + \frac{15}{16}\xi + \frac{1}{2}\right), \quad \xi \equiv 2\frac{(t-t_i)}{t_1 - t_i} - 1. \tag{15.1}$$

In this equation M_{bf} is simply the mass of the default model (Table 11.4). The period of the growing of the bar is $T_g = t_1 - t_i$ and this is usually taken as a certain number of periods of the bar rotation. Preliminary, we will take 2 bar revolutions. Afterwards, the bar stays stable up to t_f.

A first example of this simulation is shown in Figure 15.7. For this case, $t_i = -400$ Myr. The vertical arches at $V \sim -100\,\mathrm{km\,s^{-1}}$ which are very similar to the vertical arches obtained by Fux (2001) show that with only 400 Myr of integration the velocity field has not achieved a stationary state. As the bar is growing during his first two revolutions with a period of 136 Myr, in this simulation the bar has been fully grown for only one more revolution. The region of Hercules is however well populated and consistent with all the results of Chapter 14. If the integration is carried out for a longer time of $t_i = -1000$ Myr we obtained the results of Figure 15.8. Now the bar has accomplished 5 revolutions from the moment it was fully grown. The vertical arches have disappeared. Again three weak arches are seen at some ϕ and are specially visible at 40°, 80°, 120° or 140°.

As these kinematic structures at low angular momentum appear to be very weak in most cases, we study the component V_β is the projection of the U and V velocities to an axis perpendicular to the structures (clockwise rotation of $\beta = 16°$). We use this rotation β as it is

[2]Contrary to the case of the quadrupole model, in this model there is a global increase of the total mass. In future simulations a progressive transfer of mass from the bulge/disc to the bar will be implemented.

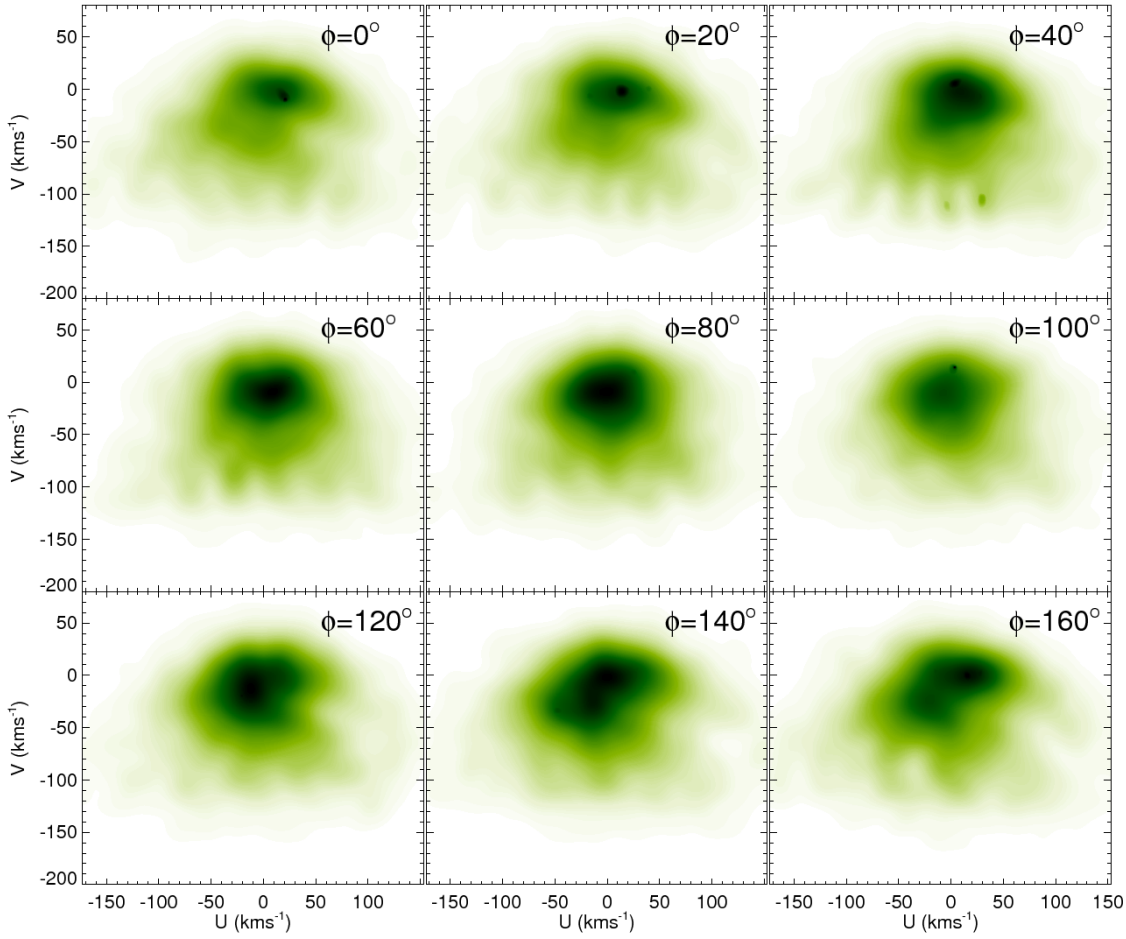

Figure 15.7: **Kinematic effects of the recently introduced bar on a hot disc.** U–V velocity distributions after WD at $R = 8.5\,\mathrm{kpc}$ and at different azimuths ϕ for the simulations with the PM04–MW potential model using only bar but introduced progressively in time with IC4 and integration time $t = 400\,\mathrm{Myr}$.

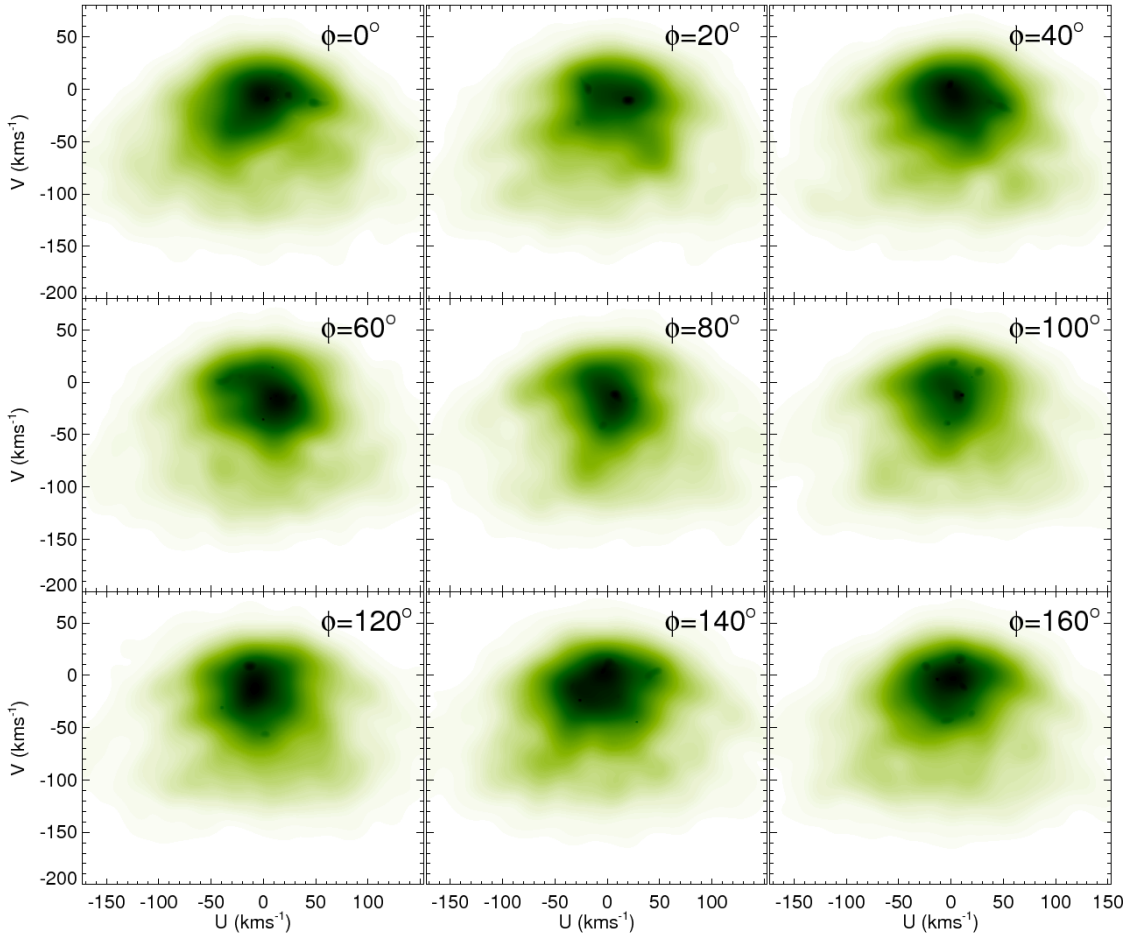

Figure 15.8: **Kinematic effects of the progressively introduced bar on a hot disc.** U–V velocity distributions after WD at $R = 8.5\,\mathrm{kpc}$ and at different azimuths ϕ for the simulations with the PM04–MW potential model using only bar but introduced progressively in time with IC4 and integration time $t = 1000\,\mathrm{Myr}$.

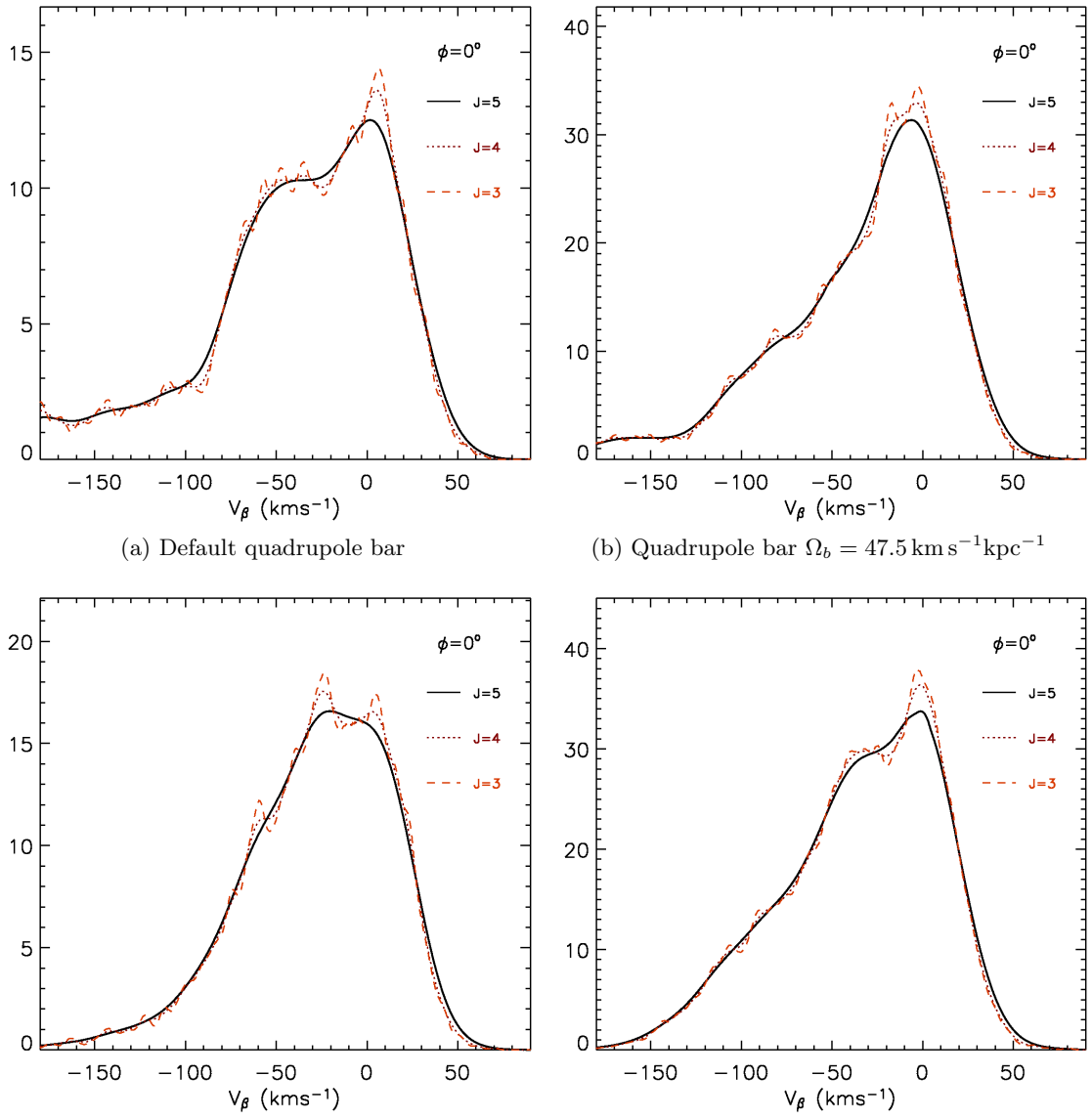

(a) Default quadrupole bar

(b) Quadrupole bar $\Omega_b = 47.5\,\mathrm{km\,s^{-1}kpc^{-1}}$

(c) Default prolate bar

(d) Progressive introduction of the prolate bar

Figure 15.9: **Bar-induced branches at low angular momentum.** Comparison between the kinematic branches at low angular momentum generated by different simulations at $\phi = 0°$ ($\phi_{0b} = 20°$) and $R = 8.5\,\mathrm{kpc}$. The branches are shown in the V_β component (clockwise rotation of $\beta = 16°$ of the U–V plane) after WD for several scales.

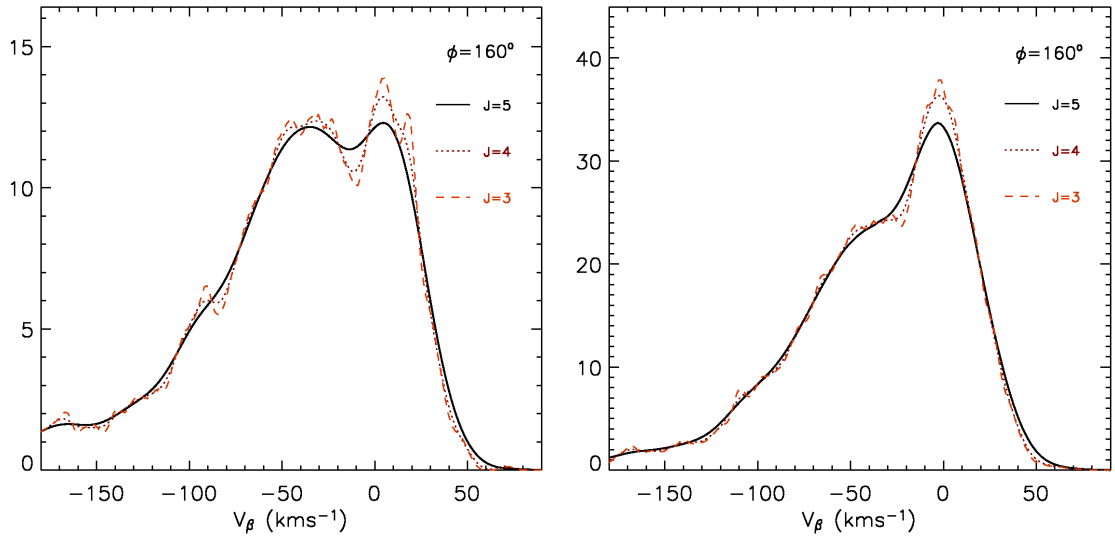

(a) Default quadrupole bar

(b) Quadrupole bar $\Omega_b = 47.5\,\mathrm{km\,s^{-1}kpc^{-1}}$

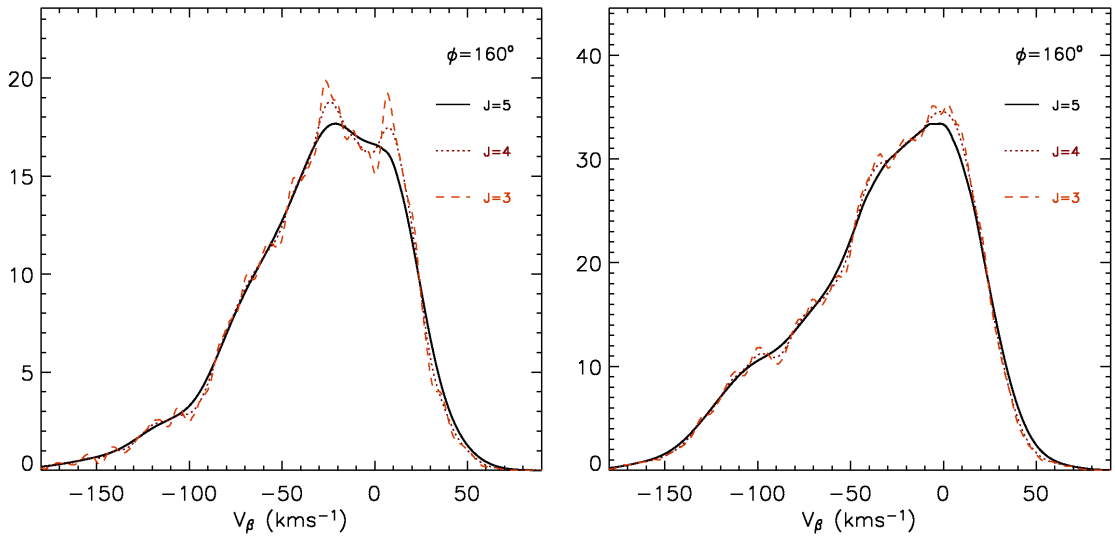

(c) Default prolate bar

(d) Progressive introduction of the prolate bar

Figure 15.10: **Bar-induced branches at low angular momentum with a bar orientation of 40°.** Comparison between the kinematic branches at low angular momentum generated by different simulations at $\phi = 160°$ ($\phi_{0b} = 40°$) and $R = 8.5\,\mathrm{kpc}$. The branches are shown in the V_β component (clockwise rotation of $\beta = 16°$ of the U–V plane) after WD for several scales.

the one that fits the observed branches in Part III and seems approximately the same for the branches created in these simulations for $\phi = 0°$ and $\phi = 160°$ that we assume that are the more plausible ones given independent determination of the bar inclination. At positions such as $\phi = 100°$ different or even null β would be more correct. The results are shown in Figures 15.9 and 15.10 for $\phi = 0°$ and $\phi = 160°$, respectively. In these panels we can notice several clear kinematic structure at low angular momentum ($V_\beta < -50\,\mathrm{km\,s^{-1}}$). For the quadrupole bar and $\phi = 160°$ 3 clear arches were observed in Figure 15.6 which again are seen in Figure 15.10a at $V_\beta = 5\,\mathrm{km\,s^{-1}}$, $V_\beta = -30\,\mathrm{km\,s^{-1}}$ and at $V_\beta = -90\,\mathrm{km\,s^{-1}}$. Even a fourth but weak structure is observed at $V_\beta = -70\,\mathrm{km\,s^{-1}}$. We confirm that with a higher pattern speed (Figure 15.9b) all these arches are shifted towards more negative V_β. Although for $\phi = 0°$ the arches were difficult to notice in Figure 15.6 now we see that weak but several kinematic structures appear. Also for the case of the prolate bar, despite being a less strong bar, we can confirm with these panels the existence of kinematic structure at low angular momentum. See for instance the peaks at $V_\beta = 0\,\mathrm{km\,s^{-1}}$, $V_\beta = -30\,\mathrm{km\,s^{-1}}$ and the two more around $V_\beta = -100\,\mathrm{km\,s^{-1}}$ for $\phi = 0°$ (Figure 15.9d) and the peaks at $V_\beta = 0\,\mathrm{km\,s^{-1}}$, $V_\beta = -40\,\mathrm{km\,s^{-1}}$, $V_\beta = -75\,\mathrm{km\,s^{-1}}$ and $V_\beta = -100\,\mathrm{km\,s^{-1}}$ for $\phi = 160°$ (Figure 15.9d).

It is very tentative to associate these structures with observed moving groups such as Arcturus. However, we must emphasise that the positions of the previous peaks are very sensitive to the parameters of the model which are still very uncertain. On the other hand, these simulated structures at low angular momentum are still very weak to be conclusive. Although the observed groups at this region of the U–V plane are also weak, we require stronger kinematic features in our simulations to confirm these results. Using a more strong bar, higher velocity dispersions or higher density of test particles in the inner regions allowing more particles to populate these groups would help in this.

To study in depth the possible influence of the bar's resonances on the arches Section 15.4 deals with the periodic orbits of the bar located at the low angular momentum part of the U–V plane, repeating the study of Section 14.2 but extending the grid to $V = -300\,\mathrm{km\,s^{-1}}$.

15.4 Regular orbits of the bar at low angular momentum

This section is an extension of Section 14.2 where we will look at the periodicity of the orbits corresponding to the region of low angular momentum of the U–V plane. The procedure is the same as in Section 14.2 but now the region of study is extended to $V = -300\,\mathrm{km\,s^{-1}}$. This method will help us to study the orbital structure of the bar at low angular momentum that can be identify with groups such as Arcturus.

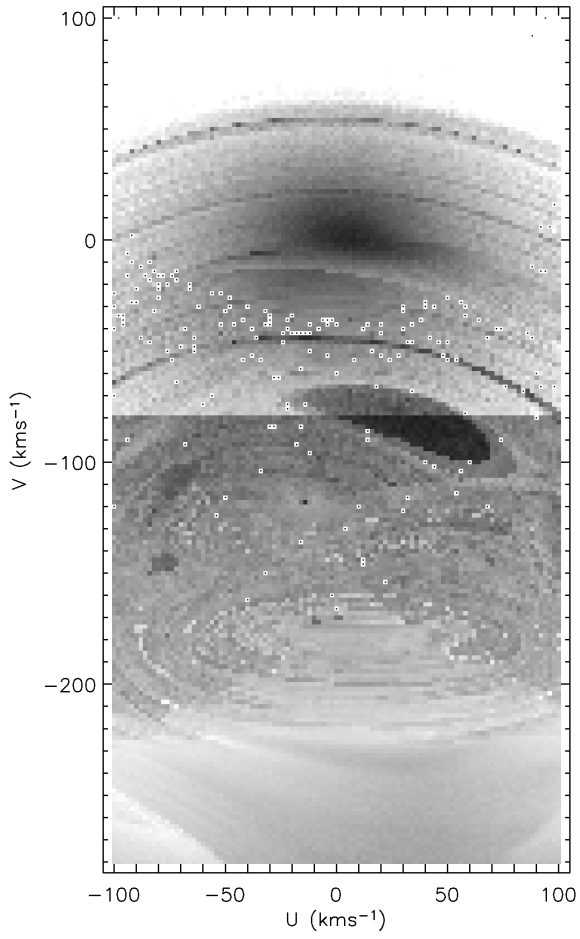

Figure 15.11: **Orbital regularity of the prolate bar model at low angular momentum.** U–V plane at low angular momentum coloured as the periodicity of the corresponding orbits for the default model of bar at $\phi = 0°$ and $R = 8.5\,\mathrm{kpc}$. The darker the region is, the more periodic or closed the corresponding orbit is.

The result for the default model of the prolate bar (Table 11.4) at $\phi = 0°$ and $R = 8.5\,\mathrm{kpc}$ is shown in 15.11. The new region at negative V has been placed below the previously obtained Figure to show the continuity of the structures. The colour scale of the region has been enhanced to make easier the analysis. It can be seen that this region of the U–V plane is far more complex. The more conspicuous structure is the big and oval dark region of regular orbits that spreads out in the range $U \sim [-10, 80]\,\mathrm{km\,s^{-1}}$ and $V \sim [-100, -70]\,\mathrm{km\,s^{-1}}$. As we saw in Section 14.2 this region is formed by orbits related to the 4:1 OLR of the bar. As it is clearly shifted through positive U it can not be related directly to the Arcturus group.

As we have seen in Chapter 14, we have found a new value for Ω_b that shows more consistency in creating the observed Hercules structure. Now we study in detail the region of low angular momentum of the U–V plane using $\Omega_b = 47.5\,\mathrm{km\,s^{-1}kpc^{-1}}$. The result for $\phi = 0°$ and $R = 8.5\,\mathrm{kpc}$ is shown in Figure 15.12. Here the main periodic regions are indicated with a coloured circle and a character. The corresponding orbits are shown in Figure 15.13 with the same colours. The main difference between this an Figure 15.11 is that now all structures have shifted towards more negative V as expected for having moved further the resonances from this position. We find nearly resonant regions on the U–V plane corresponding to the 5:1 and 6:1 resonance at more negative V and the corresponding orbits are shown in Figures 15.13c-15.13f. On the other hand, we check that the orbits forming the big oval region that now extends in the ranges $U \sim [0, 60]\,\mathrm{km\,s^{-1}}$ and $V \sim [-120, -90]\,\mathrm{km\,s^{-1}}$ are orbits related to the 4:1 OLR (point (b) and orbit of Figure 15.13b). Point (a) has the same V component but a negative U and is also a regular 4:1 orbit (Figure 15.13a). The fact that this point and its surroundings are not so highlighted as the region of point (b) shows a weakness of this method for quantifying the regularity of the orbits. With this method the dispersions of the orbit are calculated when the orbit crosses two axes that are in the direction of the bar semi-major and semi-minor axis (see Section 10.3). Particularly for these orbits, we can see how the loops are oriented precisely in these two directions for orbit (a) and by contrast, the loops appear 45° rotated for orbit (b). This produces higher regularity for orbit (b) whereas both orbits are absolutely equivalent in terms of regularity. Periodic orbits of the bar are symmetric with at least one of the axes of the bar (Fux 2001). Therefore, a geometry exercise indicates that there would be no similar problem with other orbits apart from the 4:1 orbits, 8:1 orbits, and in general $4{\times}n$:1 orbits with $n \geq 1$. A change in the axes of the method would fix this drawback.

As in our test particle simulations we have detected kinematic structures at low angular momentum also for a bar orientation of $\phi_{0b} = 40°$ (Section 15.3) we now want to explore if it is due to a resonance of the bar. The map of regularity of the orbits for $\phi = 160°$ and $R = 8.5\,\mathrm{kpc}$ for the default prolate bar is shown in Figure 15.14a. Now the oval dark region of regular orbits have been split into two groups at negative and positive U, respectively. For $\Omega_b = 47.5\,\mathrm{km\,s^{-1}kpc^{-1}}$,

which is the pattern speed that would be favourite to fit the Hercules structure, we obtain Figure 15.14b. From Figure we see that at $V \sim -100\,\mathrm{km\,s^{-1}}$ two conspicuous structures appear. The first is the oval dark region at $U \sim -90\,\mathrm{km\,s^{-1}}$ that now only appears at negative U. The orbit followed by point (b) is shown in Figure 15.15b. Although its negative U is more consistent with the Arcturus groups, this structure seems too shifted to the left compared to the observed structure that is more extended along the U axis. The second feature is indicated with the point (a) and corresponds to the 5:1 sym orbit of Figure 15.15a. Also the 3:1 resonance that produce a region of regularity around $V \sim -65\,\mathrm{km\,s^{-1}}$ as discussed in Section 14.2, could take part in the shaping of some structures at low angular momentum. However, all these regions of regular orbits are difficult to associate with any structure of our test particle simulations due to the weakness of the latter.

To our knowledge, it was the study of Fux (2001) who first pointed out the coincidence of the position of the Arcturus kinematic group with some periodic orbits of the bar. According to his method of quantifying the periodicity of the orbits on the U–V plane, he found for a bar orientation of ϕ_{0b} and $R/R_{OLR} = 1.1-1.2$ (equivalent to $\Omega_b \sim 51\,\mathrm{km\,s^{-1}kpc^{-1}}$ in the PM04–MW potential model) that the stable eccentric orbits $x_1(2)$ and 5/1 asym had a velocity $V/V_c \sim -0.6$ ($V \sim 132\,\mathrm{km\,s^{-1}}$ for the PM04–MW potential model) and $U/V_c \sim -0.1$ ($U \sim -22\,\mathrm{km\,s^{-1}}$ for the PM04–MW potential model). This was not among his main conclusion and it was not discussed in terms of phase space crowding in his section of test particle orbits. Alternatively Williams et al. (2009) recently discussed a possible disc-dynamical origin of Arcturus based on stellar population evidence, and postulated the bar 6:1 OLR as the triggering mechanism from an extrapolation of the 2:1 being the cause of the Hercules group. By contrast, from these panels we see that, assuming a pattern speed that links the Hercules structure to the 2:1 OLR, the region at $V \sim -100\,\mathrm{km\,s^{-1}}$ seems to be influenced by the resonances 4:1 and/or 5:1. Also the 3:1 resonance seem to produce a region or regularity around $V \sim -65\,\mathrm{km\,s^{-1}}$ which could take part in the shaping of some structures at low angular momentum.

Another derived consequence of this orbital study is the fact the the orbits of the structures belonging to this region of low angular momentum of the U–V plane have large radial excursions that arrive to very inner regions ($R \sim 3\,\mathrm{kpc}$) that can even enter through the bar itself (see e.g. Figure 15.15). This indicates that a model with an accurate description of the potential in the region near the bar is necessary in this study. The prolate bar of the PM04–MW potential model fulfils this requirement but it is doubtful if pure quadrupole bars give proper descriptions for inner radius.

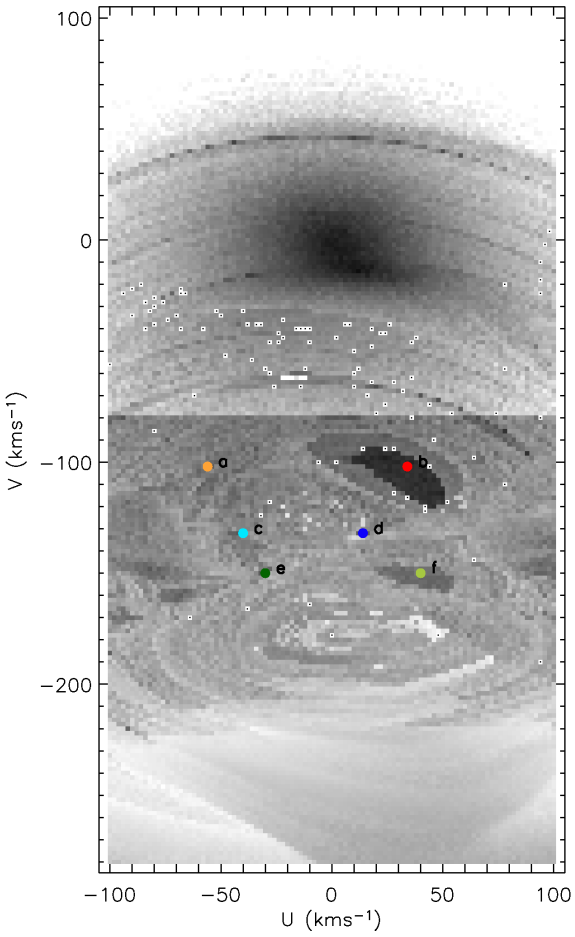

Figure 15.12: **Orbital regularity of the prolate bar model at low angular momentum for** $Omega_b = 47.5\,\mathrm{km\,s^{-1}kpc^{-1}}$**.** U–V plane at low angular momentum coloured as the periodicity of the corresponding orbits for the prolate bar with $Omega_b = 47.5\,\mathrm{km\,s^{-1}kpc^{-1}}$ at $\phi = 0°$ and $R = 8.5\,\mathrm{kpc}$. The points corresponding to orbits in Figure 15.13 are marked with coloured circles.

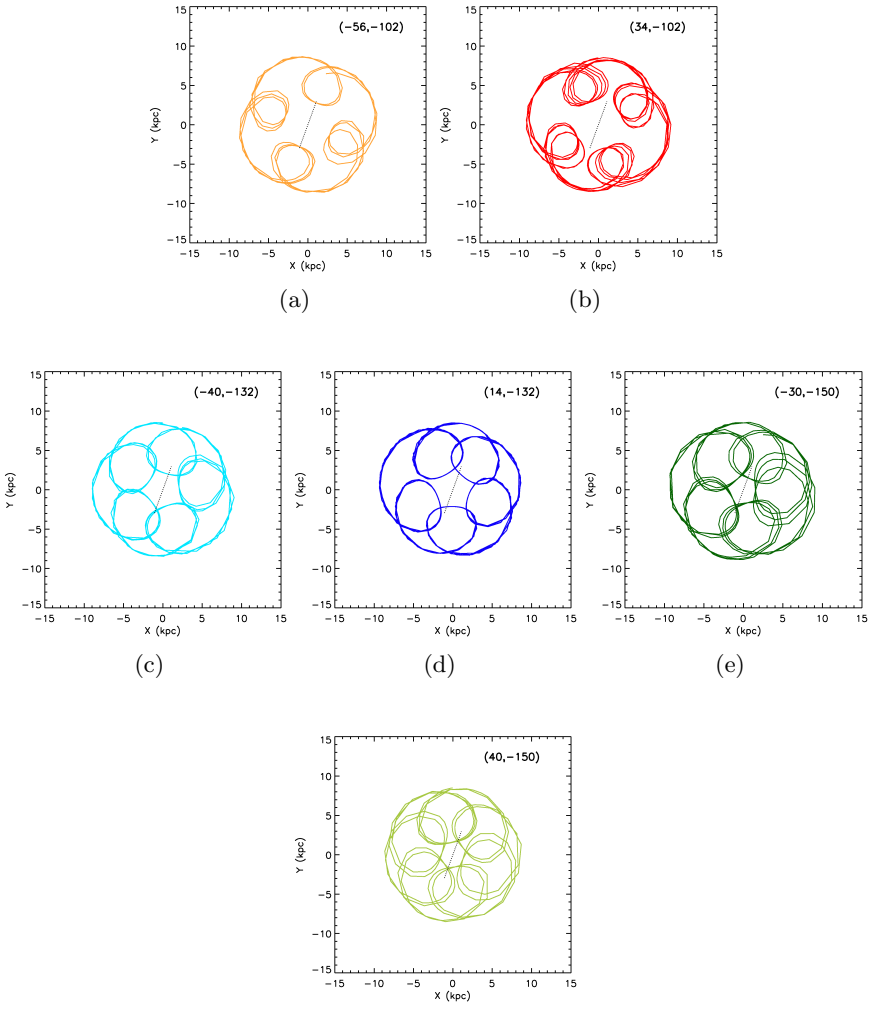

Figure 15.13: **Bar-induced regular orbits at low angular momentum.** Orbits of the U–V points indicated in Figure 15.12.

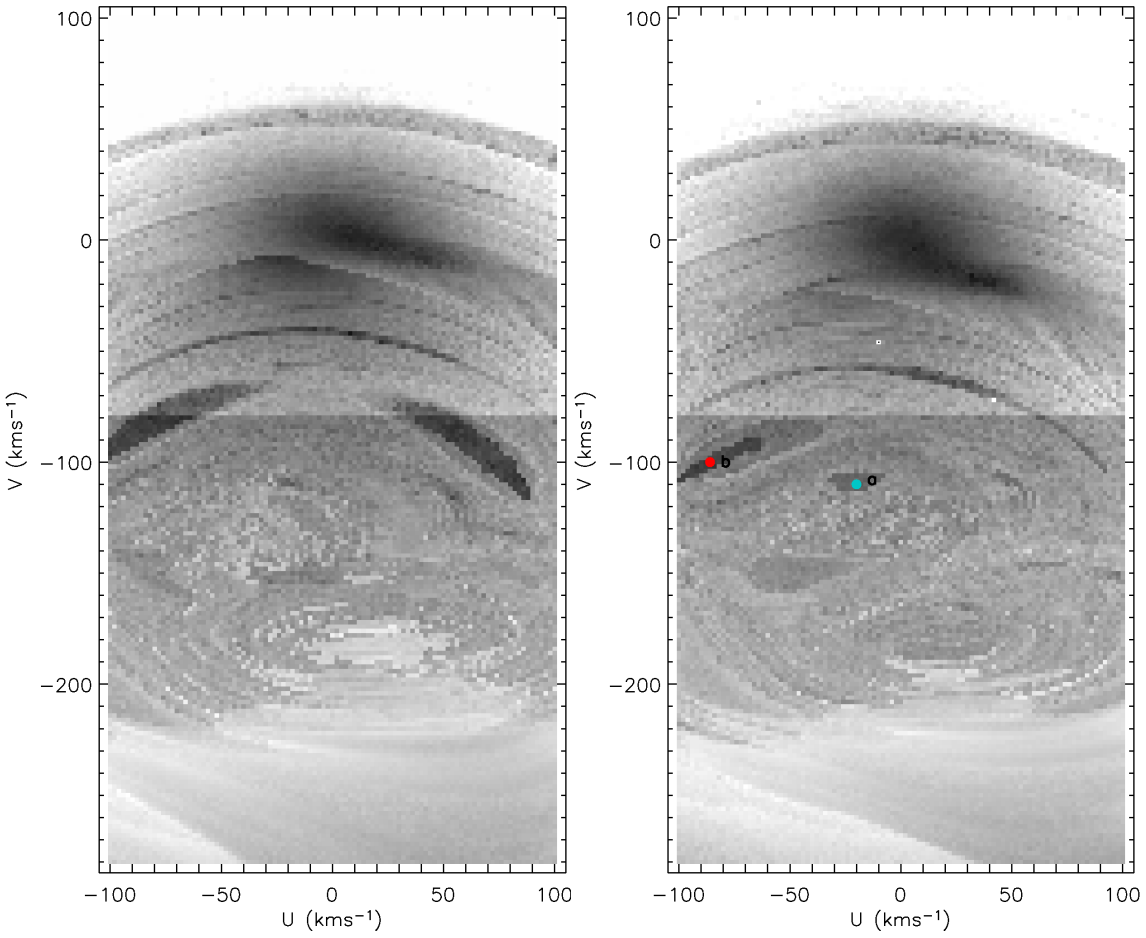

(a) Default

(b) $\Omega_b = 47.5\,\mathrm{km\,s^{-1}kpc^{-1}}$

Figure 15.14: **Orbital regularity of the prolate bar model at low angular momentum for a bar orientation of** 40°**.** U–V plane coloured according to the periodicity of the corresponding orbits for the prolate default bar and with $\Omega_b = 47.5\,\mathrm{km\,s^{-1}kpc^{-1}}$ at $\phi = 160°$ ($\phi_{0b} = 40°$) and $R = 8.5\,\mathrm{kpc}$.

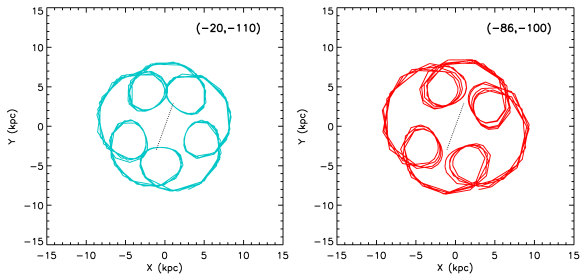

(a) (b)

Figure 15.15: **Bar-induced regular orbits at low angular momentum for a bar orientation of 40°.** Orbits of the U–V points indicated in Figure 15.14b.

15.5 Summary and discussion

We have found two alternative plausible origins of the groups at low angular momentum such as Arcturus, different from the origin associated with the remnants of past accretion events of satellite galaxies. These are found when the bar acts on a relatively hot stellar disc.

We have studied a disc where there have been a certain perturbation such as a recnet interaction with an orbiting satellite that has caused it to experience a relaxation process. We consider this as a plausible situation for the MW as current scenarios of galaxy formation and evolution have shown that both external and internal perturbation mechanisms perturb galaxies. In this case, as a product of the ongoing phase mixing arch-shaped structures in the velocity distributions at solar radius appear. These arches are open towards negative V in the U–V plane and they are transient structures that progressively gather together and eventually blur. We have explored the effects of the bar and the spiral arms on the local velocity distribution of this special disc. We have found that our default spiral arms do not have a noticeable influence on these structures of low angular momentum. By contrast, the bar modify the position of the arches making them to depend clearly on azimuth. Moreover, different bar pattern speeds produce different modifications on the arches and even make some of them disappear in several cases. All these are evidence that, as expected, the bar influences significantly the orbits with inner guiding centres that at solar radius achieve so negative V.

In particular, for short bar exposure times (400 Myr) and a bar pattern speed of $\Omega_b = 45\,\mathrm{km\,s^{-1}kpc^{-1}}$ the velocity distribution at solar radius exhibits a clear arch at $V \sim -100\,\mathrm{km\,s^{-1}}$ which is close to the Arcturus V component. Moreover, this simulated structure covers a wide range of U but for realistic bar orientations it is slightly shifted to towards negative U like the observed structure. However, as we have not carried out an exhaustive exploration of the

influence of the bar pattern speed on the arches at low angular momentum nor an thorough exploration of the time dependence of these arches, this result should be considered for the moment only as evidence of sensitivity to the model but not necessarily as favouring a particular Ω_b value or time since the perturbing agent. It is risky to use other observed moving groups at low angular momentum to fit the time since the perturbing event that caused the transient arches using an axisymmetric model (Minchev et al. 2009): some of these groups have a mean U component different from 0, which the axisymmetric model can not account for, and some groups have low chemical and age scattering in contrast to this formation scenario.

Our results support an internal disc origin for structures such as Arcturus. We find that the dynamics of the bar has a strong influence on these low angular momentum kinematic groups that have been generated due to the phase mixing in the disc caused by a given perturbation, suggesting that both kinematic initial conditions and Galactic structure contribute to create these kinematic groups. The fact that the bar is able to shift the arches to the left or to the right depending on the properties of the bar and the position studied is also promising in the sense that the positions of the real structures at low V can help to constrain the properties of the bar.

On the other hand, we found that the bar also creates steady kinematic structures at low angular momentum that maybe associated with its induced resonant effects on the U–V plane. We have studied this in relaxed discs obtained following several approaches, leading all of them to similar conclusions. When we extend the integration time in order to stabilise the possible transient kinematic features we found very promising results. For instance, if the quadrupole bar is studied, it creates three conspicuous and stable structures in the U–V plane for many bar orientations. The two first groups are the ones of the bimodality discussed in Chapter 14. The third one is located at more negative V and it mean U component depends on the bar orientation which is a clear imprint of the bar influence. In particular for an orientation of $\phi_{0b} = 40^\circ$ which is consistent with the recently discovered long bar of the MW and a bar pattern speed around $47.5\,\mathrm{km\,s^{-1}kpc^{-1}}$ the first two arches are consistent with the central mode at low peculiar velocities and the Hercules structure whereas the third arch is consistent with the $V \sim -100\,\mathrm{km\,s^{-1}}$ of the Arcturus moving group and also its mean negative U. However, we must be careful in interpreting these results as the particles that form this structure have large radial excursions that arrive to very inner regions that can even enter through the bar itself for which the quadrupole potential do not give a proper description.

For the case of the prolate bar which gives a potential model derived from an observationally constrained density distribution we do observed kinematic structures at around $V \sim -100\,\mathrm{km\,s^{-1}}$ but they are weaker probably because it is a less strong bar. For the realistic bar orientations of $\phi_{0b} = 20^\circ$ and $\phi_{0b} = 40^\circ$ the created branches are titled $\sim 16^\circ$ similarly to the observed

branches. When these kinematic structures are studied in more detail using the projection of the U and V velocities to an axis perpendicular to the structures we observe 4 overdensities for the two realistic bar orientations. Two of them are located below $V \sim -50\,\mathrm{km\,s^{-1}}$ and the other two are the ones of the bimodality discussed in Chapter 14. It is very tentative to associate these structures with observed moving groups such as Arcturus. However, we must emphasise that the positions of the previous peaks are very sensitive to the parameters of the model which are still very uncertain. Using a more massive prolate bar, higher velocity dispersions or higher density of test particles in the inner regions allowing more particles to populate these groups at low angular momentum and this would help in deriving definitive conclusions about these two kinematic structures at low angular momentum.

Our very preliminary orbital analysis points the fact that, assuming a pattern speed that links the Hercules structure to the 2:1 OLR, the region at $V \sim -100\,\mathrm{km\,s^{-1}}$ seems to be influenced by the resonances 4:1 and/or 5:1. Also the 3:1 resonance seem to produce a region or regularity around $V \sim -65\,\mathrm{km\,s^{-1}}$ which could take part in the shaping of some structures at low angular momentum. However, we do not find evidence that these regions of regular orbits corresponding to these resonances are equivalent to overdensities in the our test particle simulations.

On the other hand, two key points related to this issue must be stressed. First, we have found promising results for the bar orientations corresponding to the Galactic bar and to the long bar separately. We expect that if the bars rotate at similar pattern speed we will have an approximate combination of the previous panels at $\phi = 0^\circ$ and $\phi = 160^\circ$ but if not, the results can vary significantly. The relative strength of these two bar would play an important role on the final induced effects. A definitive conclusion would require a simulation including both bars at the same time. Second, our simulations have been carried our in the disc plane under the assumption that vertical movement is decoupled from the in-plane motion. This assumption is valid for nearly circular orbits and that do not take larger heights above the plane (see e.g. Binney & Tremaine 2008). Therefore the results of these chapter which deals with hot initial discs are subject to a 3D experiment that recover also the arches at low angular momentum confirming that at least a certain fraction of particles, perhaps the ones with small W and the most near-circular, give shape to these kinematic structures. Although the vertical distributions of our IC must be improved in order to carry out these final proves, the PM04–MW potential model is ready to be used in 3D simulations as it is a full 3D model which, instead of taking an ad hoc dependence on the z coordinate for the spiral arms and bar, it considers directly a three-dimensional mass distribution. The possibility that the resonances of the bar affect also the stars in the thick disc, which groups such as Arcturus are assigned to belong to, is a very intriguing issue.

Originally, the Arcturus moving group was introduced to be a thick disc moving group

remnant of a dissolved open cluster (Eggen 1996b). Later, this kinematic group was proposed to have arisen from a past accretion event (Navarro et al. 2004, Villalobos & Helmi 2009) based on its kinematic and metal abundance pattern. Alternatively Williams et al. (2009) recently discussed a possible disc-dynamical origin of Arcturus based on stellar population evidence, and postulated the bar 6:1 OLR as the triggering mechanism from an extrapolation of the 2:1 being the cause of the Hercules group. On the other hand, Minchev et al. (2009) was the first to suggest that Arcturus and other groups at low angular momentum could have an origin related to non-relaxed initial conditions. Here we have seen that first, the dynamics of the bar has a strong influence on the low angular momentum kinematic groups that have been generated due to the phase mixing in the disc that could have been caused by a given perturbation. We wonder also if the some moving groups that can be remnants of past accretion events of satellite galaxies are in fact influenced by the bar resonances which give them certain shapes or certain mean U. We also have found that the bar itself creates steady kinematic structures at low angular momentum that maybe associated with its induced resonant effects. The possibility that these groups can be influenced and indeed caused by the resonances of the bar is a very promising subject of study that, however, needs further investigation.

An additional encouraging consequence of the analysis with the hot disc is the possible resonance influence on the particles in the dark disc predicted in cosmological simulations of galaxy formation. These particle may indeed follow similar behaviour to the stellar particles. This issue is discussed in Appendix C.

Chapter 16

Combining spiral arms & bar

In this chapter the kinematic structure developed by the spiral-bar PM04–MW potential model, that is a model that includes the prolate bar and the self-gravitating spiral arms, is presented. First in Section 16.1 the results of the simulations with the spiral-bar PM04–MW potential model (parameters of Table 11.2 for the axisymmetric component, Table 11.3 for the spiral arms and Table 11.4 for the bar) are presented for IC1 and for IC2 (default values of Table 10.1). Afterwards, the effect of the variation of some default parameters is shown.In Section 16.2 we study the regularity of the orbits on the U–V plane for the spiral-bar model. At the end, Section 16.3 shows a summary and a discussion of the results of this chapter.

16.1 How do they act together?

The complexity of these simulations is higher not only because the the total number of free parameters of the potential is larger. First, the relative phase between the spiral arms and the bar varies with time due to the different pattern speed of the bar and the spiral in the default model. This require that the velocity distributions must be studied only at fixed times when the desired relative phase is achieved. Second, the spiral-bar PM04–MW potential model depends on time and the analysis comes to be clearly time-depending. We expect that the final distributions depend on the final relative phase and also on the history of the combined influence of the bar and the spiral arms.

The aim of this chapter is not to find the set of parameters of the spiral-bar model that best fits the observed moving groups. This would require a large number of high CPU time

simulations. The first affordable step is to analyse whether the groups generated by the spiral arms or the bar separately are maintained or modified when the spiral-bar model is used. This will tell us if the simulations with the individual non-axisymmetric components can be used to constrain the properties of the bar and the spiral arms. It would be interesting to see in which conditions or in which regions of the U–V plane it is the bar or t he spiral influence which dominates on the kinematic structures or if the action of the two MW components or the resonance superposition create new kinematic structures. The results of these simulations can prove the speculations of other authors about the influence of the bar or the spiral arms in a particular region of the U–V plane (see details in Page 230 and subsequent pages). Moreover it will be interesting to compare the present results with the simulations of Chakrabarty (2007) with a model that, despite including the two non-axisymmetric components at the same time, studied the case of 4 weak spiral arms (see Section 11.5).

It has been seen in Chapter 15 that the spiral arms do not show significant influence on the region of low angular momentum of the U–V plane which is explored using the IC3 disc. For this reason the results that we show in this chapter are restricted to IC1 and IC2. The CPU cost of the present simulations is high compared with the simulations of previous chapters. This complicates the scanning of the model parameter space and for this reason show only a few examples of the influence of several parameters.

IC1– Figure 16.1 shows the results for the spiral-bar PM04–MW potential model with the default parameters used with IC1 at several azimuths ϕ of the solar radius $R = 8.5\,\mathrm{kpc}$. From this panels we can see that the kinematic structure at $V \sim -40\,\mathrm{km\,s^{-1}}$ created by the spiral arms (Figure 13.1) appears again for almost every azimuth.

On the other hand, in the central part of the distribution several features that we can identify with the effects of the bar (Figure 14.1) or with the effects of the spiral arms (Figure 13.1) are also differentiated depending on the azimuth ϕ. For instance, at $\phi = 0^\circ$ we see an elongation through positive U at $V \sim 0\,\mathrm{km\,s^{-1}}$ that is observed also for the simulations with the bar. Besides, as in the results for the spiral arms, there is a bifurcation at $U \sim -20\,\mathrm{km\,s^{-1}}$ and $V \sim 0\,\mathrm{km\,s^{-1}}$. Therefore at this position where the orientation of the bar is $\phi_{0b} = 20^\circ$ and the one for the spiral arms is $\phi_{0sp} = 88^\circ$ we might identify effects of both non-axisymmetric components.

In the case for $\phi = 100^\circ$ the orientation of the bar is $\phi_{0b} = -80^\circ$ (or 100°) and the one for the spiral arms is $\phi_{0sp} = -12^\circ$ (or 168°), that is almost on the arm. In this position the influence of the spiral arms seems to dominate as we can observe the three central branches again. The influence of the spiral arms is also notorious at $\phi = 120^\circ$.

For positions in the ranges $20 - 60^\circ$ and $140 - 160^\circ$ the central parts of the distributions are

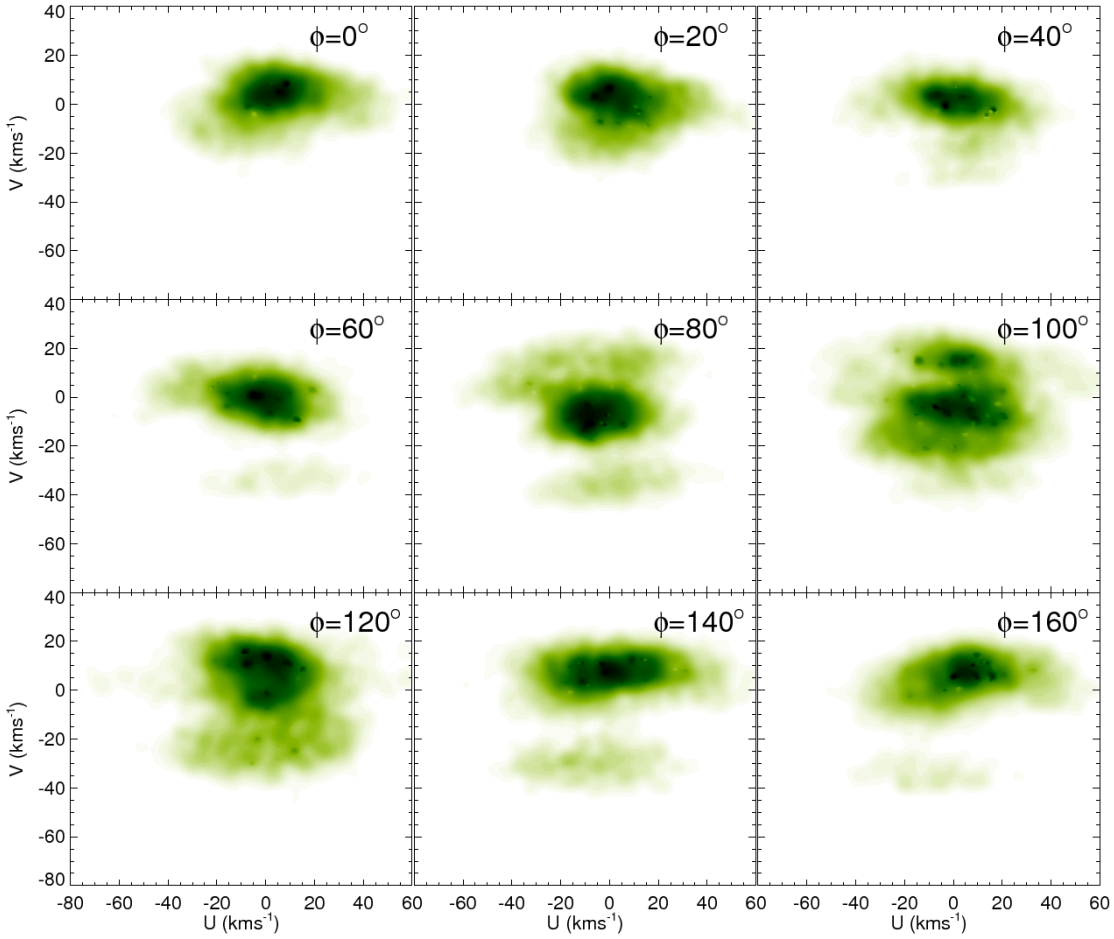

Figure 16.1: **Kinematic effects of the bar and the spiral arms on a cold disc.** U–V velocity distributions after WD at $R = 8.5\,\mathrm{kpc}$ and at different azimuths ϕ for the simulations with the spiral-bar PM04–MW potential model (bar and spiral arms) and IC1.

almost identical that the case with only the prolate bar. This positions correspond to orientations of $\phi_{0b} = [-40°, 0°]$ and $\phi_{0b} = [40°, 60°]$ for the bar and $\phi_{0sp} = [28°, 68°]$ and $\phi_{0sp} = [-52°, -72°]$ for the spiral arms. Remarkably, at $\phi = 80°$, $\phi = 100°$ and $\phi = 120°$ we notice a band or stripe at the highest V that was only slightly discerned for the simulations with only the bar but at lower V. This constitutes an example of joined action of the two non-axisymmetric components.

IC2– Figure 16.2 shows the results for the spiral-bar PM04–MW potential model with the default parameters used with IC2 at several azimuths ϕ of the solar radius $R = 8.5\,\mathrm{kpc}$. Again tracers of the bar and the spiral arm influence can be seen in certain azimuths ϕ. For instance, at $\phi = 0°$ we see again an elongation through positive U at $V \sim 0\,\mathrm{km\,s^{-1}}$ that is observed also for the simulations with the bar. Also we see the tendency of the particles with negative V to be shifted towards negative U as in the bimodality caused by the bar alone. For $\phi = 120°$ and $\phi = 140°$ the two groups are very similar to the groups created by the spiral arms alone.

Varying the default parameters– As explained at the beginning of the chapter, for the spiral-bar PM04–MW potential model the space parameter has become very extensive and in addition to the complexity of being time-dependent simulations. Next we present a few examples of interesting simulations when some default parameters are modified.

- **Orientation of the spiral arms:** Now we explore the velocity distributions of a simulation where we change only the orientation of the spiral arms. These are rotated counterclockwise as indicated in Figure 16.3. The new orientation of the spiral arms with respect to $\phi = 0°$ is $\phi_{0sp} = 39°$ (the default value is 88°) and now the outer arm is nearer the supposed position of the Sun. We use IC2. The results are shown in Figure 16.4. As compared to Figure 16.2, we see that the velocity distributions that shown two groups due to the spiral arms at $\phi = 120°$ and $\phi = 140°$ that were maintained in the spiral-bar model are now observed at $\phi = 80°$ and $\phi = 100°$ due to new orientation of the spiral arms. It is interesting that the group at negative V appears now shifted to positive U whereas it was approximately centred in U in the previous simulations. This may be attributed to the effects of the bar.

- **Bar pattern speed:** Now we repeat the simulation of the previous item that has a new orientation for the spiral arms ($\phi_{0sp} = 39°$) but in addition we change the default bar pattern speed to $\Omega_b = 60\,\mathrm{km\,s^{-1}kpc^{-1}}$ (Figure 16.5). It is surprising the richness and clearness of the kinematic structures that are generated in these simulations. Again tracers of the bar and the spiral arms are identified. For instance, the group at $V \sim -60\,\mathrm{km\,s^{-1}}$ was also seen in the simulations of the prolate bar with $\Omega_b = 60\,\mathrm{km\,s^{-1}kpc^{-1}}$. The two

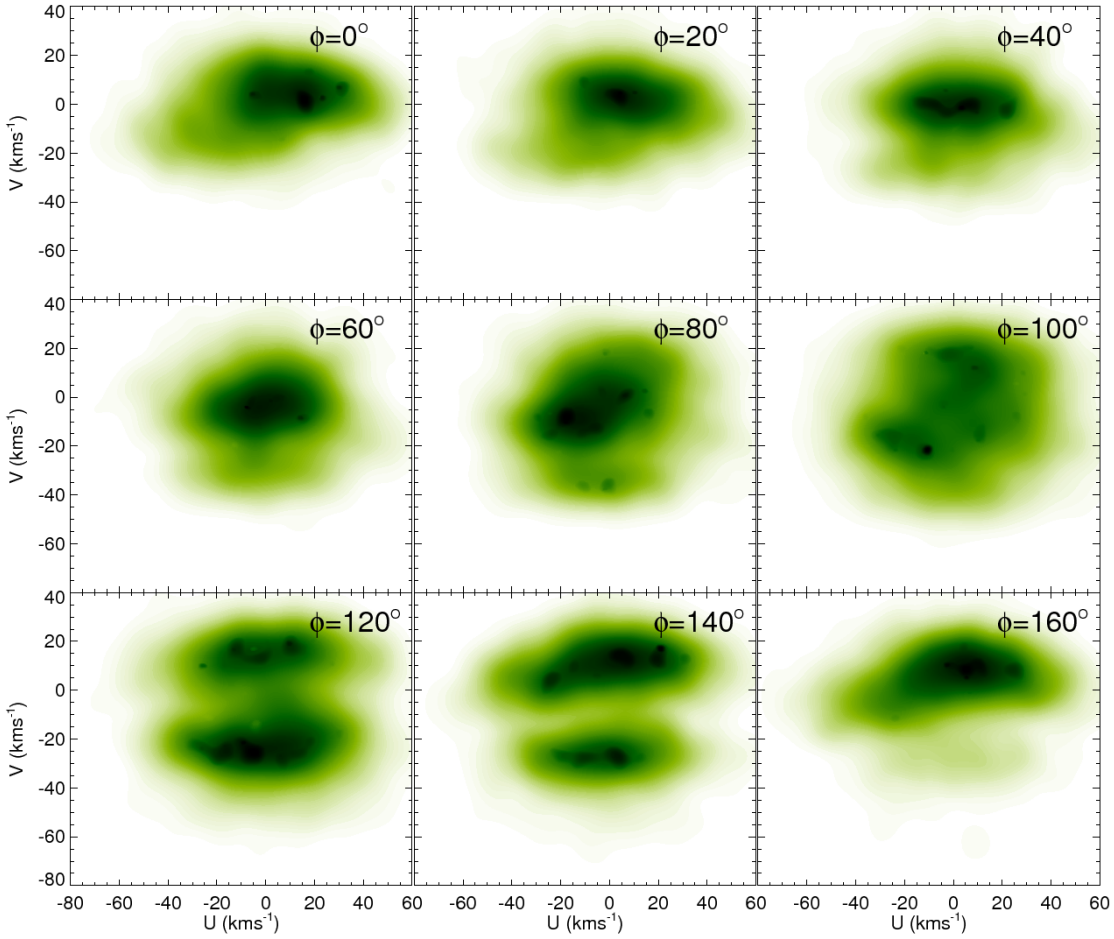

Figure 16.2: **Kinematic effects of the bar and the spiral arms on an intermediate disc.** U–V velocity distributions after WD at $R = 8.5\,\mathrm{kpc}$ and at different azimuths ϕ for the simulations with the spiral-bar PM04–MW potential model (bar and spiral arms) and IC2.

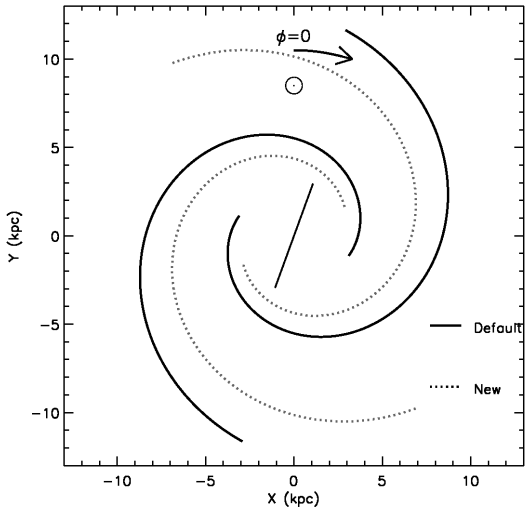

Figure 16.3: **Different orientations of the spiral arms.**Comparison between the default spiral arms and the spiral arms oriented with $\phi_{0sp} = 39°$.

central groups at $\phi = 80°$ and $\phi = 100°$, which were produced by the spiral arms, are again observed.

- **Integration time:** With additional simulations that are shown in Figures B.24 and B.25 in Appendix B, we also state that the time variation of the structures can be very significant.

Although Chakrabarty (2007) is the only study prior to the present one that have analysed the problem of the moving groups using a model that includes the spiral arms and the bar at the same time, other authors have speculated about the combined effects of both non-axisymmetric components. For instance in Dehnen (2000), it is argued that stars should have epicycles smaller than the interarm separation to be affected by the spiral arms. This lead him to conclude that the bimodality (Hercules) was unlike to be produced by the spiral arms (see Chapter 13). This discussion applied perfectly for the interarm distance that he considered. However, we have seen that in the PM04–MW potential model this can be as large as $5.5 - 7\,\mathrm{kpc}$ and the stars of a structure located at $V \sim -40\,\mathrm{km\,s^{-1}}$ have epicycles of $\sim 3\,\mathrm{kpc}$. Therefore, we can not avoid the effects of the spiral arms at the regions of negative V of the U–V plane, as we have confirmed with our test particle simulations with the spiral-bar model. Following the same argument, Dehnen (2000) concluded that the effects of the bar on the central part of the U–V plane, which correspond to orbits of low eccentricity and small epicycles, are little conclusive as these kind of

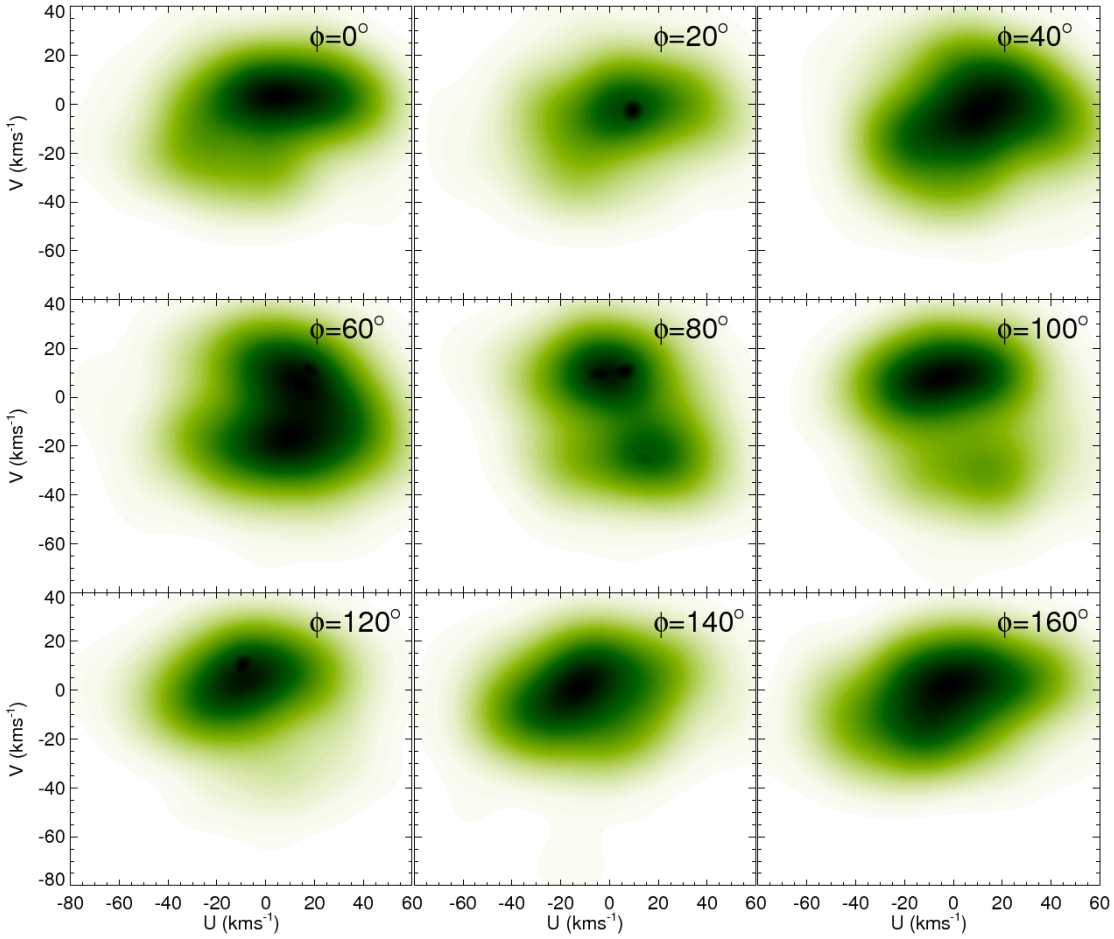

Figure 16.4: **Kinematic effects of the bar and differently oriented spiral arms on.** U–V velocity distributions after WD at $R = 8.5\,\mathrm{kpc}$ and at different azimuths ϕ for the simulations with the spiral-bar PM04–MW potential model (bar and spiral arms) with $\phi_{0sp} = 39°$ and IC2.

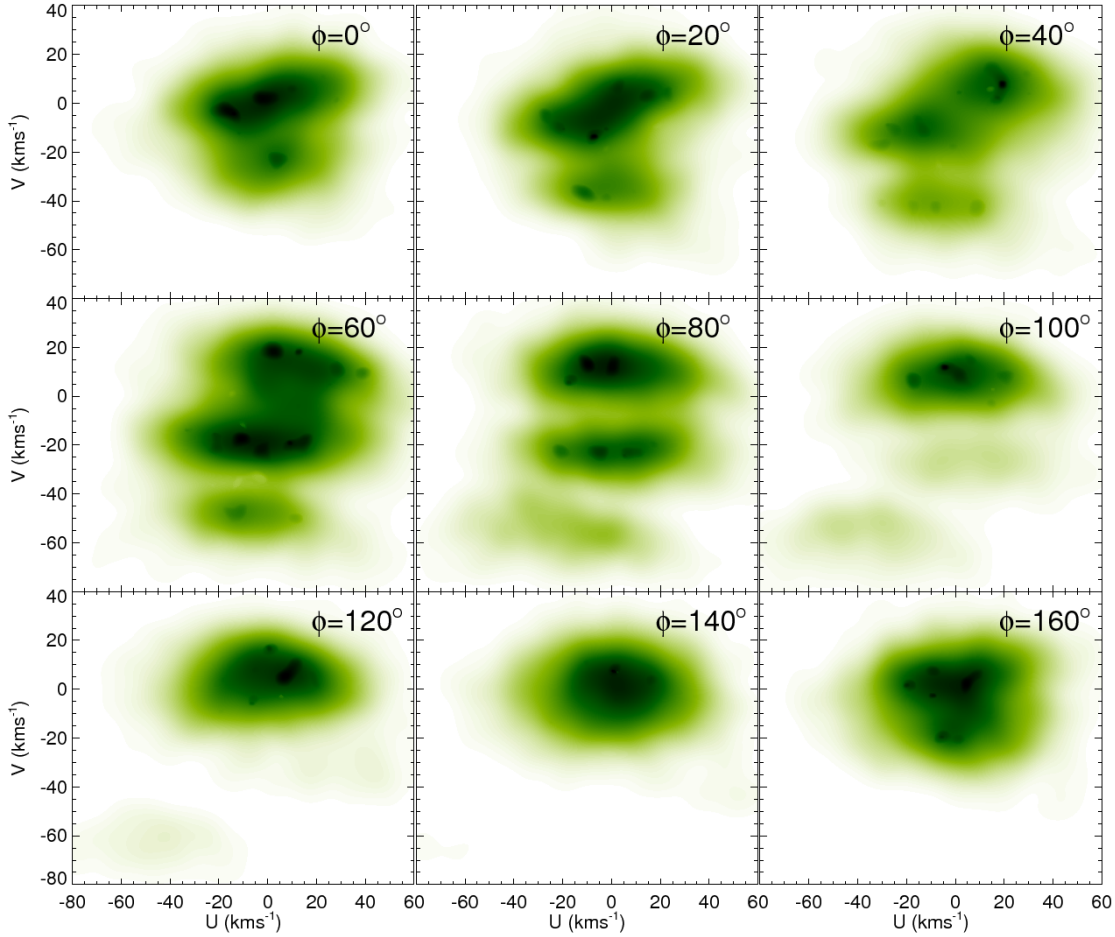

Figure 16.5: **Kinematic effects of a rapid bar and differently oriented spiral arms.** U–V velocity distributions after WD at $R = 8.5\,\mathrm{kpc}$ and at different azimuths ϕ for the simulations with the spiral-bar PM04–MW potential model (bar and spiral arms) with $\phi_{0sp} = 39°$, $\Omega_b = 60\,\mathrm{km\,s^{-1}kpc^{-1}}$ and IC2.

orbits would now have been highly influenced by the spiral structure. We have confirmed with our simulations that in the central parts of the U–V plane both non-axisymmetric components have important influence. But we have seen that the influence of these components in this central parts of the U–V plane depends on the particular parameters of the model and on the studied position on the disc. In this sense, we agree with the reasoning of Chakrabarty (2007): from considerations of the average epicyclic amplitude of the orbits and the interarm separation, the effects of the spiral arms can not be ruled out neither can be the effects of the bar that will be strong near the OLR. In fact we have seen that for the vast majority of our simulations with the default spiral-bar model, the influence of the spiral arms is great (except for IC3). However, we have also seen that under several conditions and positions on the disc, the spiral arms or the bar can have only minor influence.

According to Quillen & Minchev (2005), only stars that are affected by a Lindblad resonance from a certain perturbation are strongly affected by this perturbation. Away from a resonance, the orbital kinematics can be treated with low-order perturbation theory and the orbits are only weakly influenced. The effects of the bar should be noticed only in stars of negative V of the Hercules stream by means of the influence of the bar's 2:1 Lindblad resonance. And the orbits of stars with low values of $|U|$ and $|V|$ which are very close to the solar radius should be distant and so unaffected by Lindblad resonances with the Galactic bar. With this argument, they conclude that the periodic orbits induced by the spiral arms in the central parts of the U–V plane are weakly affected by the bar. We have shown how the bar can have great influence on the central parts of the distribution in contrast with this argumentation.

It was seen in Chakrabarty (2007) that the inclusion of the spiral pattern reduces the boldness of the features created in the U–V plane and the action of the two perturbers produces numerous small clumps in the central parts of the velocity distributions at many locations as a consequence of the presence of a relatively greater variety of families of stellar orbits in these simulations. We do not particularly observe such trends although it must be stressed that in that study weak and 4 arms were used. Here the influence of the spiral arms is great and and they can create large and conspicuous kinematic structures when they act together with the bar.

16.2 Orbital regularity in the simulations with the spiral-bar model

Although there exist no periodic orbits when a time-dependent potential is used (there is no possible reference frame where the potential is fixed), the quantification of how regular the orbits are when the two non-axisymmetric components are included in the potential model is

still possible and indeed very interesting. Moreover, the computing time of this method makes easier the scan of the parameter space which in this case is very time expensive with the test particle simulations. It is worth mentioning that this kind of regularity maps can depend on time or on the reference system of study is needed. As a first approach we keep the time integration fixed as in the original design of the method (see Section 10.3) and establish the reference system to be the one than moves with the bar. This first approximation is equivalent to considering how the orbital structure of the bar is distorted or changed by the effects of the spiral arms. Further research will be needed o study the reverse case and establish definitive conclusions.

We begin this study by comparing the results for the default spiral-bar PM04–MW potential model with the results obtained from the individual non-axisymmetric components (Figure 16.6). As expected due to the above discussion about the reference frame of the method, Figure 16.6alooks more similar to Figure 16.6c. From this Figure we see that the valley of the bimodality that is created by the bar (see Section 14.2) still appears but now is clearly distorted due to the effects of the spiral arms. The same happens with the oval dark feature at positive U and negative V. Between the valley and this oval feature complex shapes appear. Also we can see tracers of the oval feature which was formed for the spiral arms at large positive V. The central splitting into two groups for the spiral arms case that creates an approximately horizontal valley at $V \sim 0\,\mathrm{km\,s^{-1}}$ is still observed for the spiral-bar case despite being more diluted.

Next we present the analysis of regularity for several variations of the parameters. We have explored the changes in mass, pattern speed and orientation of the spiral arms and the bar. Among all these case we want to emphasise some interesting aspects. We see for instance that when the mass of the bar is increased (Figure 16.7b) the regularity map has not changed essentially but it seems a little more distorted. By contrast, we can notice that when the mass of the spiral arms is decreased (Figure 16.7c) the resonant arches at negative V are less distorted.

Figure 16.7d corresponds to a case where the 4:1 ILR of the spiral arms and the 2:1 OLR of the bar are very close and located just in the solar radius. This corresponds to pattern speeds of $\Omega_{sp} = 16.7\,\mathrm{km\,s^{-1}kpc^{-1}}$ and $\Omega_b = 44.1\,\mathrm{km\,s^{-1}kpc^{-1}}$. It has been suggested in Quillen (2003) that when the resonances of the bar and the spiral arms overlap the fraction of chaotic orbits is larger that for individual perturbations. (Chakrabarty 2007) corroborated it and noticed the impossibility to use this method to constrain the bar characteristics in that case, which could be an important drawback if there is some dynamical mechanism that couple the bar and the spiral like this. With our results we see that in this case this map is very irregular in the central part of the U–V plane and even the two clear groups of the bimodality appear here highly blurred. Nevertheless some features of this maps can still be identified with the effects of the bar or the spiral arms.

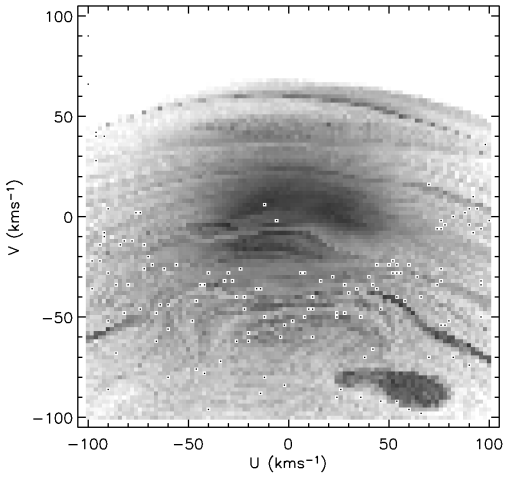

(a) Default spiral-bar model

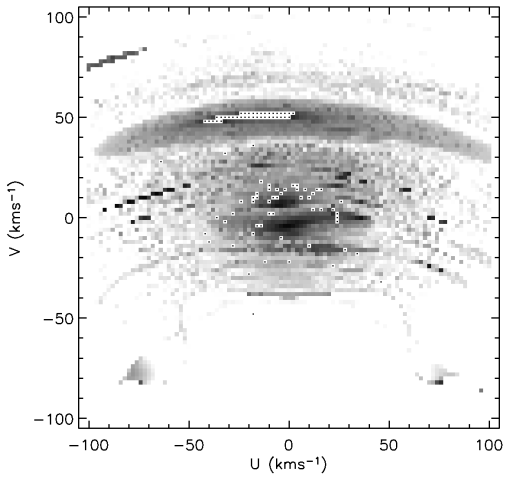

(b) Default self-gravitating spiral arms

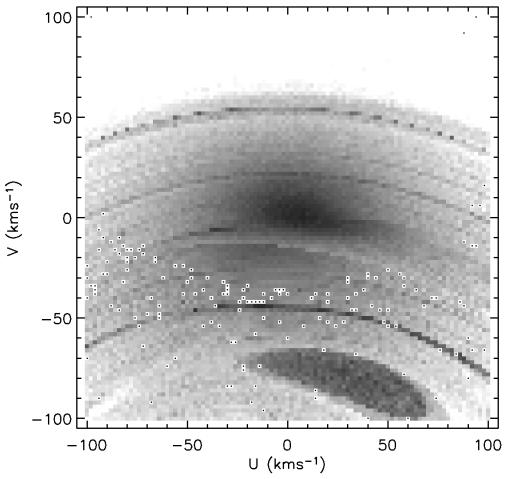

(c) Default prolate bar

Figure 16.6: **Orbital regularity of the prolate bar and the self-gravitating spiral arms.** U–V plane coloured according to the periodicity of the corresponding orbits at $\phi = 0°$ and $R = 8.5\,\mathrm{kpc}$ for the default spiral-bar PM04–MW potential model (bar and spiral arms), the model including only the self-gravitating spiral arms and for the model including only the prolate bar. The darker the region is, the more periodic or closed the corresponding orbit is.

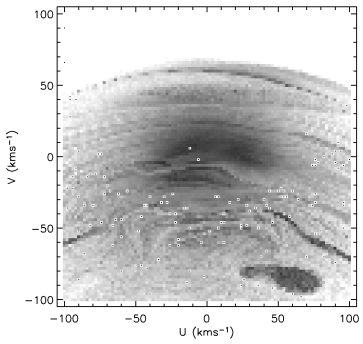

(a) Default

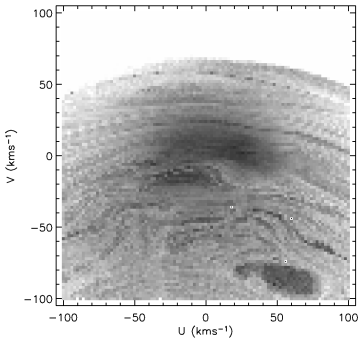

(b) $M_b = 14 \cdot 10^9 \mathrm{M}_\odot$

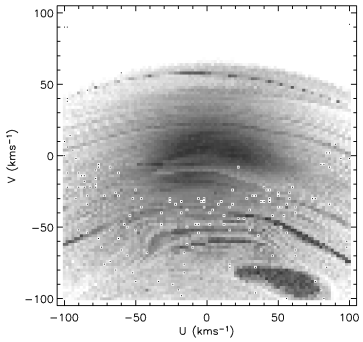

(c) $M_{sp} = 0.03 M_d$

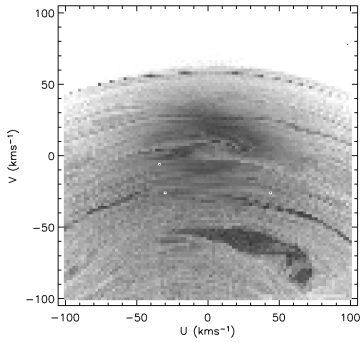

(d) Resonances overlapping

Figure 16.7: **Orbital regularity of the prolate bar and the self-gravitating spiral arms with different properties.** U–V plane coloured as the periodicity of the corresponding orbits for several variations of the parameters of the default spiral-bar PM04–MW potential model (bar and spiral arms).

16.3 Summary and discussion

In this chapter we have analysed whether the groups generated by the spiral arms or the bar separately are maintained or modified when the spiral-bar model is used. This gives us clues about whether the results of our models that use only bar or only spiral arms can be extrapolated for the spiral-bar model. The complexity of the simulations that include bar and spiral arms is very high because of the number of free parameters of the potential and also because the spiral-bar PM04–MW potential model depends on time.

Some previous speculations in the literature about the effects of the bar and the spirals arms pointed to the conclusion that the central region of the U–V plane is more affected by the spiral arms whereas regions at V around $V \sim -40\,\mathrm{km\,s^{-1}}$ (the velocity of the Hercules moving group) and below would be mainly affected by the bar (Dehnen 2000, Quillen & Minchev 2005). In contrast with this argumentation, we see that the bar can have large influence on the central parts of the distribution and the spiral arms create groups at $V \sim -40\,\mathrm{km\,s^{-1}}$. That is, in general, the two non-axisymmetric components have important influence on both the central parts of the U–V plane and in the regions moderate negative V.

For the vast majority of the obtained velocity distributions under the spiral-bar model the influence of the spiral arms is great and and they can create large and conspicuous kinematic structures. This is in contrast to the studies of Chakrabarty (2007) where the weak arms in her spiral-bar model only contributed to more subtle effects such as reducing the boldness of the kinematic structures or increasing the number of small kinematic clumps in the U–V plane.

For our spiral-bar PM04–MW potential model, in general we see that the velocity distributions show separated imprints of the bar and the spiral arms, that is some kinematic structures are maintained. The detailed imprints depend on the particular parameters of the model and on the studied position on the disc. In some positions we identify separated effects of both non-axisymmetric components whereas sometimes the effects of one of the components seem to dominate. For example, the intermediate disc the bimodality that is produced by the bar is still observed if the spiral arms are also acting on the disc. Besides, the kinematic structure at $V \sim -40\,\mathrm{km\,s^{-1}}$ that is created by the spiral arms appears again if the bar acts together with the spiral arms on the cold disc. In particular, in positions near the arms the imprints of the spiral arms seems to be more significant. We have found a particular kinematic structure which was created by the spiral arms alone that appears now shifted in the U–V plane due to effects of the bar. But we do not find cases where the U–V plane is distorted so as to present completely different kinematic structures.

Due to the fact the test particle simulations with the spiral-bar model are very expensive in CPU time, we do not have carried out an exhaustive exploration of the parameters space. On

the other hand, we see that the final distributions depend on the final relative phase and on the history of the combined influence of the bar and the spiral arms. However, our first simulations and the fact that it is still possible to identify tracers of the bar and the spiral arms separately shows that our studies with only spiral arms or only bar are a valid way to understand the effects of each component and eventually be used to constrain the characteristics of the bar and the spiral arms. Assuming that each moving groups is an imprints of the bar or of the spiral arms, if the structures are seen to be distorted with time we could even obtain limits on the joint action of the spiral arms and the bar.

Although strictly there are no periodic orbits for a time-dependent potential, the quantification of how regular the orbits is still possible. An exploration of how this kind of regularity maps would depend on time or on the reference system of study is needed. For the moment, the study of regularity of the regions on the U–V plane leads to conclusions that are equivalent to our test particle simulations. In general we see how the main regular regions and resonant features are maintained but they can be distorted by the additional non-axisymmetric component for some combinations of the model parameters. For instance the valley that creates the bimodality in the bar only case appears in almost all our experiments with the spiral-bar model but it is distorted in some occasions. We see that when the 4:1 ILR of the spiral arms and the 2:1 OLR of the bar overlaps we see that distortion is high. The maintenance of at least some orbital properties due to the bar or due to the spiral arms supports the hypothesis that moving groups are due to the orbital structure and resonances of the non-axisymmetric components of the MW.

Part VI

CONCLUSION

Chapter 17

Summary, conclusions & perspectives

In this chapter Section 17.1 summarises the main outcomes of the whole thesis, Section 17.2 brings out the general conclusions of the study and, finally, Section 17.1 examines the required improvements and perspectives for future studies of moving groups.

17.1 Summary

One of the most intriguing features of the stellar velocity distribution in the solar neighbourhood is the existence of moving groups. At present, the origin of these kinematic structures is far from completely understood although it is more than 140 years since they were discovered. Nowadays, several explanations for their origin are considered: cluster disruption, dynamical effects induced by the non-axisymmetric components of the MW (i.e. spiral arms and bar), remnants of past accretion events and external dynamical effects on the disc resulting from interaction events. This thesis has dealt with the origin of the moving groups, with particular reference to the possibility that moving groups are imprints of the bar and spiral arms of the MW, which would mean that they could be used to constrain the large-scale structure of our Galaxy.

It has already been shown that the effects of the non-axisymmetric components can induce kinematic groups in the local stellar velocity distribution. The most compelling evidence is the demonstration that the effects of the Galactic bar resonances can trigger a kinematic group similar to the observed Hercules group (Dehnen 2000, Fux 2001). But despite the efforts made in these recent studies, there is a long list of unresolved questions that are still a matter of debate or that have not yet been addressed (some of them are detailed in Chapter 1). This

shows that further research is required. In this thesis we have attempted to answer some of these questions. This study had two specific goals, undertaken via different approaches. First, we aimed to analyse and characterise the observed moving groups, establishing observational insights into their origin. Second, we aimed to explore the extent to which we can use the kinematic imprints to constrain the large-scale structure of the MW and its recent evolution.

Observations Results

To undertake the observational study we have compiled an extensive compendium with the best available astrometric and photometric data for more than 24000 stars in the solar neighbourhood. We have applied the WD multiscale technique to this sample to characterise and analyse the moving groups in the U–V–age–$[Fe/H]$ space. The main outcomes of the observational analysis are the following:

- The dominant kinematic structures in the U–V plane are the branches of Sirius, Coma Berenices, Hyades-Pleiades and Hercules. They all present a negative slope of $\sim 16^{\circ}$ in the U–V plane.
- A new kinematic group centred at $(35, -20)\,\mathrm{km\,s^{-1}}$ is identified, which may be considered as part of the elongation of the Sirius or Coma Berenices branch.
- The geometrical structure of the branches and the observed density drops in the kinematic space rule out the classic idea of a smooth velocity distribution.
- The branches are significant for all ages, except for stars younger than 100 Myr.
- The four branches are present in all spatial regions studied, but there is a dependence of the kinematic branches on Galactic position. The shape of the Hercules branch changes from one region to another. It is more conspicuous in the region of inner galactocentric radius, and for a region near the Sun in comparison to a region that is located further in the direction of rotation. A significant change of contrast among kinematic substructures inside the branches depending on the spatial region has also been identified.
- There is a large spread of ages inside each branch. This suggests ruling out those models that propose that these kinematic structures are remnants of disc star clusters.
- While the Hyades-Pleiades and Coma Berenices branches have an important fraction of very young stars, Sirius has its first main peak for slightly older stars at ~ 400 Myr. The extended branch-like shape of Hercules is detected in all subsamples with ages > 2 Gyr.
- There is a periodicity in age of about 500-600 Myr in the Hyades-Pleiades branch although the large errors in ages compared to this period require more investigation. For the other branches only an outline of the shape of the whole age distribution is observed.

- A wide range of metallicity is found for each branch, especially for Hercules with a higher metallicity dispersion.
- The three branches of Hyades-Pleiades, Coma Berenices and Sirius show a kinematic-metallicity correlation: the more negative the V component of the branch, the higher the mean metallicity. However, the Hercules branch does not follow this pattern of the three main branches.
- The Hyades and Pleiades kinematic substructures inside the branch show distinctive metallicity, the former being more metallic.
- The age-metallicity relations of all the branches exhibit the same general tendency as the whole sample.

Simulation results

We have performed test particle simulations with the PM04–MW potential model to explore the phase space available to the local stellar distribution. This is a specific potential model for the MW which is very flexible and has been tuned to reproduce some recent observational constraints. We have also considered a great variety of initial conditions and integration procedures. This methodology has allowed to study the imprints of the spiral arms and the bar on the velocity distribution at different disc positions. We have also used a method to ascertain the regularity of the orbits in the U–V plane. The main results of our simulations are:

- Contrary to common speculations, the spiral arms influence the kinematic velocity distribution at moderate negative V (apart from its influence in the central parts of the U–V plane) and the bar has a large influence on the central parts of the distribution (apart from its well-established influence on groups at more negative V).
- In our simulations where both the spiral arms and the bar are included, individual imprints of the bar and the spiral arms can still be identified in the final velocity distributions throughout the solar radius.
- The self-gravitating spiral arms by themselves create significant strong imprints on the velocity plane. The imprints are particularly intense at positions near the arms.
- The arms can induce slightly tilted kinematic branches that resemble some of the observed central kinematic structures.
- We identify several resonant orbits that cross the solar neighbourhood. In particular, the spiral arms are able to carve the regular orbital structure in the central region of the U–V plane, which is mainly influenced by the 6:1 ILR, following similar shapes to the observed branches.

- The spiral arms can crowd the region of the Hercules moving group in the velocity plane ($V \sim -40\,\mathrm{km\,s^{-1}}$) and not only the bar, as traditionally believed. These orbits oscillate around a square orbit due to the 4:1 ILR.
- The velocity distributions induced by the arms change significantly with variations of pattern speed. Pattern speeds that locate the Sun near the 4:1 ILR produce different strong kinematic structures. For several relative orientations of the arms, the upper part of the distribution on the U–V plane is shifted to $U > 0$, as for the observed Sirius moving group.
- Spiral arms that act for short times on the disc produce transient but strong kinematic structures. A clear split into two groups appears at most azimuths in this case.
- The prolate bar with realistic orientation and density profile triggers a bimodality in the velocity distribution: one kinematic group at negative V and another in the central part of U–V plane. This is caused by a thin region of irregular orbits that are probably related to the bar 2:1 OLR. This region is inclined in the U–V plane, which makes the group at negative V slightly tilted, as in the observations.
- For realistic bar orientations the group at negative V has mean negative radial motion U, as the Hercules branch does. But for some pattern speeds this group could be better related to Hyades-Pleiades.
- The central mode of the bimodality is distorted through positive U, which is created by elliptic orbits aligned with the bar and also related to the bar 2:1 OLR. This distortion could be associated with the new observed group found here at $(U, V) = (35, -20)\,\mathrm{km\,s^{-1}}$ and with the elongation of the Coma Berenices branch. However, in the simulations, the relative density of particles in this region is higher than that in the observed velocity field.
- Orbits close to the antialigned orbital family are found to cross the solar neighbourhood in a position on the U–V plane that may be coincident with the Hyades group.
- The low angular momentum moving groups, including Arcturus, could have two distinct viable origins related to the bar acting on a relatively hot stellar disc.
- As a first possibility, the dynamics of the bar could have a strong influence on the transient kinematic groups at low angular momentum that are products of the ongoing phase mixing in an un-relaxed disc. The bar makes these transient arches depend clearly on azimuth and bar pattern speed.
- For particular conditions, the velocity distribution exhibits a clear arch at $V \sim -100\,\mathrm{km\,s^{-1}}$ which covers a wide range of U but for realistic bar orientations it is slightly shifted towards negative U. This could be associated with the Arcturus moving group.

- The second possibility is that the bar also creates steady kinematic structures at low angular momentum that may be associated entirely with its induced resonant effects on the U–V plane. For the realistic bar orientations of $\phi_{0b} = 20°$ (consistent with the Galactic bar) and $\phi_{0b} = 40°$ (consistent with the long bar), two overdensities at low angular momentum are seen, apart from the two of the above-mentioned bimodality.
- The bar resonances 3:1, 4:1 and/or 5:1 could be responsible for these kinematic groups at low angular momentum.

17.2 Capabilities of the kinematic imprints to constrain the MW structure and recent evolution

Our analysis of the observational sample and the simulations indicates that it is very feasible that some of the moving groups observed in the solar neighbourhood have a dynamical origin related with the effects induced by the spiral arms and the bar. Our test particle simulations approach has shown that non-axisymmetric Galactic components that are consistent with several observational constraints induce strong imprints on the local stellar kinematics. The imprints are mainly sensitive to the orientation and pattern speed of the spiral arms and the bar. We have confirmed this with our study of the orbital regularity on the U–V plane. In contrast, the strength of the non-axisymmetric components, the time of exposure to the non-axisymmetric components, or the characteristics of the discs used to trace the phase space DF such as its velocity dispersion, influence mainly the way that kinematic groups are populated. The dependence of the stellar kinematic groups on the structure and dynamics of the model and on the initial conditions of our experiments show that kinematic groups may provide useful constraints on non-axisymmetric MW components.

In the case of the spiral arms, there is currently a great deal of observational ambiguity surrounding, e.g., their pattern speed, strength, orientation, number of arms and lifetime. The strong imprints of the self-gravitating spiral arms on the velocity distributions at solar radius and the sensitivity of our results to the properties of the arms indicate that kinematics could be used as one of the constraints on this current uncertainty. We find strong but different imprints when the spiral arms are a long-lived or a short-lived non-axisymmetric component. To our knowledge, the effects of self-gravitating spiral arms on the velocity distribution have not been studied before. Furthermore, we find significant differences between the effects produced by the self-gravitating spiral arms and the TWA arms due to the important differences between the force-field shape of a TWA model and that derived from a mass distribution. We have also seen that the self-gravitating spiral arms create stronger substructure than the TWA arms. This could help to establish whether the arms of the MW are weak and tightly wound following the

TWA or whether they are strong self-gravitating arms.

In particular for the bar of the MW, its orientation with respect to the Sun is currently rather tightly constrained. However, its pattern speed has been determined using independent methods that yield similar results but still contain considerable uncertainty. The kinematic groups can help in the determination of this parameter as well as in constraining the properties of the recently discovered long bar of the MW. Only minor differences between the induced effects of the quadrupole model and of the prolate bar are observed for similar force amplitude when they are applied to discs that are not very hot. Therefore, we conclude that in contrast to the case of the spiral arms, where important differences were found between models, it seems more difficult to discriminate between bar models. However, we have seen that the force profiles are indeed very different at inner regions of the disc or in the bar itself. As with hotter initial conditions there can be orbits that have large radial excursions that can even enter the bar itself, we expect more accurate results with the prolate model which is more realistic for these regions. By contrast, the quadrupole bar model is probably only a good approximation at larger radii.

There are some examples of revealing results from our simulation study. First, the spiral arms and the bar can have an influence on regions on the U–V plane that was unexpected according to other authors. For instance, contrary to common conjecture, the spiral arms, and not only the bar, can crowd the region of the Hercules moving group. It is compelling that this moving group can help to constrain both the spiral arms and the bar. Also, we see that the observed branches and moving groups in the central part of the U–V plane can be produced not only by the spiral arms but also influenced by the bar. Secondly, the bimodality induced by the bar could explain the existence of Hyades-Pleiades. This would change the restrictions on the bar pattern speed that are usually obtained by fitting the Hercules moving group.

Finally, the possibility that the kinematic groups of low angular momentum can be influenced and indeed caused by the resonances of the bar introduces a new perspective into the recent interpretation of its extragalactic origin. Although our observational sample does not include low angular momentum moving groups, other observational studies have pointed out that this group is more likely to have a disc-dynamical origin based mainly on stellar chemical abundances. Our simulations have demonstrated this by relating them to the bar influence. It is very promising that kinematic groups such as Arcturus can help to constrain properties of the bar, such as the pattern speed or the orientation. Moreover, as the stars in these kinematic structures can originate at very small Galactic radii, they can provide information regarding the processes that takes place in the central regions of the Galaxy or near the bar itself. If they finally turn out to be transient kinematic groups, they could also offer information about the evolution of the MW. Moreover, the Hercules moving group could be consistent with one these transient groups.

In our simulations where both the spiral arms and the bar are included, individual imprints

of the bar and the arms can still be identified in the final velocity distributions throughout the solar radius. The detailed imprints depend on the particular parameters of the model and on the position on the disc studied. This shows that in most cases, studies with only spiral arms or only the bar are a valid way to understand the effects of each component, and eventually they could be used to constrain the characteristics of the bar and the spiral arms. Moreover, in the case with both non-axisymmetric components, as the structures are seen to be distorted with time, we could even obtain temporal limits on the joint action of the components. The maintenance of at least some orbital properties due to the bar or due to the spiral arms supports the hypothesis that moving groups are due to the orbital structure and resonances of the non-axisymmetric components of the MW.

17.3 Improvements & future perspectives

In this section we first present the main limitations and required improvements in our particular approach to the study of moving groups. We end up with a list of some examples of future research lines and perspectives for the study.

The results of this thesis are encouraging in that they show that the moving groups could be used to constrain spiral arms and bar characteristics. This study represents a significant advance in the field, especially concerning the statistical method used to analyse the observed and simulated data, the large observational sample, the flexibility of the MW potential and its consistency with some recent observational constraints, the variety of initial conditions of the simulations and the different simulation strategies. However, several improvements are needed in the field in order to definitively disentangle the origin of the different kinematic groups in the solar neighbourhood and finally constrain some properties of the MW and its evolution.

(i). ***Observational sample.*** Whereas the accuracy in the kinematic data of our observational sample is unprecedented, metallicities and especially ages, lack the desired precision, despite being key parameters in this study. At the cost of having relatively imprecise ages and metallicities, the sample provides us with an exceptional number of stars with these physical parameters. In general, the photometric metallicities have been sufficient for our general purposes but for the moment they are available only for part of the FGK-type stars of our sample and only the [Fe/H] parameter. The ages have large error determinations. A cut-off by error for this parameter has been necessary to work with the more reliable ages. The near spatial limits of the sample provide us with accurate kinematic measurements but do not allow us to study the observed moving groups in other disc positions. The

sample of KM giant stars is more extended but this subsample only includes stars from the northern hemisphere and, therefore, it has a non-uniform sky coverage. The limits of completeness of the sample make it difficult to estimate the relative density of stars in each kinematic branch. For instance, the limit of volume completeness is only 40 pc. On the other hand, our sample does not contain many stars with low angular momentum or low metallicities, so new sample selection criteria must be planned.

(ii). ***Potential model.*** The potential of the MW used in this thesis is a significant improvement upon other studies in the field. Its main advantages are that it is very flexible, it has been tuned following several observational constraints, and it is a 3D model. However, its self-consistency has been proved formally only for the periodic orbital structure which may not be representative of all other orbits. Also, this and all other models need continuous updating to incorporate the contributions of the scientific community to increased knowledge about the Galaxy. New findings must be incorporated and explored (e.g. two bars, and their respective masses and pattern speeds).

(iii). ***Simulation method and initial conditions.*** Our variety of initial conditions and different integration times improve significantly on previous studies. However, here and in all similar studies in the field, the main limitations of the method probably come from the idealised initial conditions. We have shown that the results can depend significantly on the properties of initial discs, which is revealing of the complexity of the real MW case. Due to this dependence, comparison between the observed velocity distribution and the results of test particle simulations is not straightforward. Besides, our simulations have been carried our in the disc plane under the assumption that vertical movement is decoupled from the in-plane motion, which is valid for nearly circular orbits that do not involve large heights above the plane. This may not be correct for hot discs. The PM04–MW potential model is ready to be used in 3D simulations, which can help us to deal with this issue.

(iv). ***Method of determining the orbital regularity.*** Whereas the test particle simulations can depend on the initial conditions that for the moment are very idealised, the study of regular orbits does not show which orbital features are populated or how. It is not straightforward to directly ascribe moving groups to periodic (or chaotic) orbits. First, we see that there are very clear regions of regularity which are not seen as a significant overdensity in the test particle simulations. Second, the coincidence in position on the U–V plane of a periodic orbit with some observed kinematic group is not sufficient proof that the observed structure has a dynamical or resonant origin. On the other hand, the method does not deal with the stability of these orbits, which would help us to determine whether stars could be trapped around these orbits. This method, together with the test

particle simulations, has provided some clues to the resonant origin of moving groups. In some cases we have seen a clear correspondence between regions of regular orbits in the U–V plane and groups created by our potential model in the test particle simulations. In other cases, the groups seem to be due to regions delineated by empty regions of irregular chaotic orbits.

(v). ***Degeneracy.*** With our simulations we are been able to examine the degeneracy inherent in this field. This means that for a given moving group there can be several interpretations that relate it to effects of the MW non-axisymmetric components (e.g. Hercules, Hyades, Arcturus). Unfortunately, it is currently difficult to decide which is the most appropriate. Moreover, a unique interpretation is no proof that the group has this orbital origin. To reduce this ambiguity we are currently planning strategies that involve both simulations and observations concerning chemical and age tagging, moving groups in other disc regions or relative density contrast in the U–V plane of the kinematic structures.

(vi). ***Best fit of the MW structure.*** A large systematic scan of the parameter space of the model will be required in order to constrain some properties of the MW and its history. The exploration of the influence of each parameter carried out in this thesis has not been exhaustive. We have not used a goodness-of-fit parameter or an equivalent quantification to evaluate how well the simulated distributions fit the observed one, which would be useful for the fit of the best model parameters. However, due to the mentioned current degeneracy and to the fact that other processes will influence and sculpt the real velocity distributions, we should not expect an exact mathematical equivalence between simulations and observations. For instance, the fit will be highly biased if some of the observed moving groups have not been induced by the bar or the spiral arms or if some of them have additional influences such as dispersion by giant molecular clouds or additional transient effects. An additional limitation to constrain the parameters of the potential comes from the uncertainty in the solar motion that makes it difficult to determine with exactitude the peculiar velocity of the observed moving groups. The problem is complex as the presence of kinematic substructure due to resonant effects in the nearby velocity field calls into question some of the methods for determining the solar movement. For the moment, we have chosen a simple exploration of the parameter in order to study qualitatively the effects of each particular component and parameter.

(vii). ***Phenomena simplification.*** With the increase of knowledge about the structure and the evolution of the MW, we have to cope with a more complex scenario and a variety of processes that can play a role in the formation of the moving groups. We have not considered external processes like past accretion events or tidal interactions, or internal

disc processes like star formation bursts. We have hardly addressed the bar or spiral arm evolution and we have not taken into account the possible evolution of the disc which can change its kinematic properties or mass. Our short integration times can partially allow for some of these latter phenomena, but the evolution must be taken into more consideration. Although some of these mechanisms were initially considered mutually exclusive, they are all natural in current galaxy formation models. The observed velocity field may be the result of the combined action of several Galactic and external processes.

We have seen that the kinematic groups can very plausibly be created by the effects of the bar and the spiral arms. However, we cannot reject the possibility that some moving groups could indeed have other origins such as being remnants of clusters or past accretion events in the disc. It will be interesting to study how all these Galactic and external mechanisms interact. For instance, we wonder whether some of these remnants of satellite galaxies are influenced by the bar resonances which give them certain shapes or certain mean U. It is also possible that some dispersed star clusters, which in fact experience the same resonant influence as other stars, also appear as part of a moving group.

In view of all the improvements required in the study of moving groups, we can identify several scientific challenges for the coming years as far as moving groups are concerned. We consider that a combination of chemical tagging, improved large-scale Galactic dynamics studies and cosmological simulations applied to the MW are required in order to disentangle the origin of the kinematic structures in the Galactic disc. These may lead to more reliable use of the moving groups to trace the structure of the MW and its formation and evolution. New theoretical and observational strategies to approach the problem are needed in preparation for the upcoming Gaia and other surveys. Some examples of future research lines and perspectives are:

- **Study of the velocity distribution at different Galactic positions on the disc.** Our simulations can be studied from the point of view of the whole disc and we have already seen that the particles that belong to a given kinematic group have distinctive final spatial distribution. The spatial study of the observed moving groups is limited by the extension and precision of the current observational samples. The comparisons between observed and simulated velocity distributions in several regions of the disc may establish additional constraints on the MW potential. We expect an improvement in the characterisation of the spatial distribution of the stars in each moving group and of velocity distributions in other disc regions. Future (and current) surveys (USNO, UCAC3, 2MASS, RAVE, SEGUE, PanStars, LAMOST, GAIA) are required.

  Recently we have carried out a preliminary evaluation of the Gaia capabilities to provide

new insights into the study of moving groups. We have calculated the accuracies in U, V, W velocities using the Gaia Universe Model Snapshot (GUMS), based on the Besançon Galaxy Model, and the current estimations of the Gaia errors[1]. We have found, for instance, that even using the relatively inaccurate radial velocities offered by Gaia for stars up to V=16 we may be able to perform robust statistical analysis of the disc velocity distribution (with accuracies better than$2\,\mathrm{km\,s^{-1}}$) up to $\sim 3\,\mathrm{kpc}$ from the Sun.

- **Metallicity and age characterisation of the disc kinematic structures.** Although the available ages and metallicities for our observational sample lack the desired precision, they are key parameters in this study. Our simulations have shown that the particles of a kinematic group can have distinctive initial spatial distribution and distinctive time exposure to the non-axisymmetric components. When our method is complemented with chemical models of galaxy evolution which refine the relation between age, chemical abundances and migration, these distributions can be used as tracers of the chemistry or the age of those particles. They may eventually be able to be compared with the distinctive metallicities and ages of the observed moving groups. In the observational domain, new IR photometric and spectroscopic surveys will play an important role in this context. The inclusion of all these additional elements in the comparison between observed and simulated moving groups are mandatory. This will also allow us to investigate and perhaps confirm, for instance, the periodicity found in the age distribution of the Hyades-Pleiades observed branch. Although several recent studies have begun to obtain high-resolution spectra that have led to accurate and complete chemical determinations, our methodology requires metallicity and α-element abundances for larger samples. The future systematic use of multi-spectrographs may contribute significantly to this.

- **Study of the resonant streams in N-body simulations developing bar and/or spiral arms.** Up to now moving groups have been studied theoretically mainly through test-particle simulations. The goals of using N-body simulations as a new type of modelling are the following. First, to model the temporal evolution of the MW self-consistently (evolution of the bar and the spirals). Second, to use cosmological simulations that include gas and star formation which will allow simulated stellar ages and metallicities to be obtained that can be compared to our observational data. Future N-body simulations with larger numbers of particles in the Galactic disc, improved initial conditions and better spatial and temporal resolution are required (massive parallel computation).

- **Inclusion of Galactic evolution.** Up to now, moving groups have been used mainly

[1]For more information see Antoja et al. 2009,
http://www.ari.uni-heidelberg.de/meetings/milkyway2009/talks/index.html

as tracers of the current structure of the MW (properties of bar and the spiral arms). In the future the time evolution of MW must be included in our test-particle simulations, adding complexity to the problem but also realism. The first step is the inclusion of time-dependent bar and spiral arms. The fact that the evolution of the non-axisymmetric components of the disc (e.g. slowing down of the bar or transient spirals) also creates imprints on the local velocity distribution leads to the possibility of using the moving groups to constrain the MW evolution and not only its present structure. As a result of new perspectives, the study of moving groups has grown to be more complex. It is now becoming progressively integrated with galaxy formation and evolution, thus establishing a link between cosmology and near-field cosmology

- **Extension to all kinds of moving groups.** As the resonant moving groups are used to constrain the properties of the bar and the spiral arms, other kinds of moving groups (e.g. remnants of accreted satellites) can also help in the study of other large-scale properties of the MW (e.g. shape of the halo). The extension of our study to other types of moving groups and the application of the same but adapted techniques (denoising methods of data treatment, analysis through simulations) are a natural step. For example, WD techniques could be used to detect streams in the MW halo.

- **Study of the "dark moving groups".** As a result of our dynamical studies, we have been recently interested in the effects of the resonances on the possible dark disc of the MW predicted by recent studies of galaxy formation in the Λ-CDM Universe. In this thesis we have suggested that the particles in this possible dark disc are also influenced by the resonances, as stars are. The motivation is to examine whether the "dark moving groups" generated could influence direct dark matter detection. A deep study of this should begin with the analysis of the cosmological simulations to establish proper initial conditions for the dark disc that will be the input for simulations including bar and spiral arms. This will allow an analysis of the conditions of resonant trapping of dark matter and the triggered dark matter currents.

To conclude, this thesis has involved statistical data analysis (multiscale techniques), scientific exploitation of astronomical catalogues (kinematics, photometric ages, metallicities), rigorous treatment of observational errors and biases, galactic dynamics, analytical models for the potential of the MW, test particle orbit simulations, programming and running simulations in multi-processing systems, and knowledge of the data simulation in the preparation tasks of the Gaia mission and of the accuracies expected for this mission. All this technical and methodological background sets us at a good starting point to address the Gaia scientific challenge in the next decade.

Bibliography

Abadi, M.G., Navarro, J.F., Steinmetz, M., et al. 2003, AJ, 597, 21 21
Aguilar, L., Hoogerwerf, R. 2001, RMxAC, 11, 99 44
Allen, C., Santillán, A. 1991, Rev. Mexicana Astron. Astrofis., 22, 255 120, 121, 125, 126, 130, 139, 140, 141, 142, 143, 158, 178, 268, 306, 308, 309, 313, 318
Anscombe, F.J. 1948, *Biometrika*, 15, 245 35
Arenou, F., Luri, X. et al. 1999, ASPC 167, 13 56
Arifyanto, M.I., Fuchs, B. 2006, A&A, 449, 533 21, 203
Asiain, R., Figueras, F., Torra, J. et al. 1999, A&A, 341, 427 x, 7, 10, 16, 46, 51, 53, 55, 58
Asiain, R., Figueras, F., Torra, J. 1999, A&A, 350, 434 17, 82, 155
Athanassoula, E., Bienaymé, O., Martinet, & L., et al. 1983, A& A, 127, 349 130
Athanassoula, E. 2002, ApJ, 569, 83 301
Athanassoula, E. 2003, MNRAS, 341, 1179 209, 301
Athanassoula, E. 2005, New York Academy Sciences Annals, 1045, 168 301
Aumer, M., Binney, J.J. 2009, MNRAS, 397, 1286 103
Baba, J., Asaki, Y., Makino, J., et al. 2009, ApJ, 706, 471 110
Baiesi Pillastrini, G.C., 2009, MNRAS, 397, 1990 121
Barbanis, B. 1976, A&A, 46, 269 117, 163, 166
Benjamin, R.A., Churchwell, E., Babler, B.L., et al. 2005, ApJ, 630, 149 122, 123, 128, 129, 138
Bensby, T., Feltzing, S., Lunström, I. 2007a, A&A, 410, 527 108
Bensby, T., Oey, M.S., Feltzing, S., et al. 2007b, ApJ, 655, 89 22
Binney, J.J., Dehnen, W., Houk, N. et al. 1997, ESA SP-402, 473 56
Binney, J. and Tremaine, S., 2008, *Galactic Dynamics*, Princeton University Press Princeton, New Jersey 102, 106, 109, 131, 132, 149, 223
Binney, J.J. 2010, MNRAS, 401, 2318 106, 150
Bissantz, N., Gerhard, O. 2002, MNRAS, 330, 591 127
Bissantz, N., Englmaier, P., Gerhard, O. 2003, MNRAS, 340, 949 129
Block, D.L., Puerari, I., Elmegreen, B.G. et al. 2009, AJ, 694, 115 22
Block, D.L., Buta, R., Knapen, J.H, et al. 2004, AJ, 128, 183 130, 131, 137, 142
Bobylev, V.V., Bajkova, A.T. 2007, ARep, 51, 372 46, 82
Bochanski, J.J., Hawley, S.L., Reid, I.N. et al. 2005, AJ, 130, 1871 x, 7, 51, 54, 55, 56, 58, 74
Bochanski, J.J., Munn, J.A., Hawley, S.L. et al. 2007, AJ, 134, 2418 82
Bok, B.J. 1934, HarCi, 384, 1 15
Bovy, J., Hogg, D.W., Roweis, S.T. 2009, ApJ, 700, 1794 46
Buta, R. 1986, ApJS, 61, 631 18
Buta, R., Block, D.L. 2001, ApJ, 550, 243 130, 142
Brown, A. G. A., Arenou, F., van Leeuwen, F. et al. 1997, ESA SP-402, 63 56
Bruch, T., Read, J., Baudis, L., & Lake, G. 2008, 804, arXiv:0804.2896 108, 301

Ceverino, D. & Klypin, A. 2007, MNRAS, 379, 1155 301
Chakrabarty, D. 2004, MNRAS, 352, 427 114
Chakrabarty, D. 2007, A&A, 467, 145 19, 109, 114, 115, 116, 137, 142, 160, 174, 181, 182, 183, 226, 230, 233, 234, 237
Chakrabarty, D., Sideris, I.V. 2008, A&A, 488, 161 20
Chen, B., Asiain, R., Figueras, F., et al 1997, A&A, 318, 29 46
Chereul, E., Creze, M., Bienayme, O. 1998, A&A, 340, 384 16, 44, 46, 47
Chereul, E., Creze, M., Bienayme, O. 1999, A&AS, 135, 5 47
Churchwell, E., Babler, B.L., Meade, M.R., et al. 2009, PASP, 121, 213 122, 128
Colín, P., Valenzuela, O., & Klypin, A. 2006, ApJ, 644, 687 301
Contopoulos, G., Grosbol, P. 1986, A&A, 155, 11 132
Contopoulos, G., Grosbol, P. 1989, A&ARv, 1, 261 182
Debattista, V. P., Gerhard, O., Sevenster, M. N. 2002, MNRAS, 334, 355 182
Dehnen, W. 1998, AJ, 115, 2384 16, 17, 44, 61, 63, 64, 71, 92, 317
Dehnen, W., Binney, J. 1998, MNRAS, 298, 387 150
Dehnen, W. 1999, AJ, 118, 1201 19, 105, 109
Dehnen, W. 2000, AJ, 119, 800 19, 82, 109, 113, 114, 115, 117, 138, 139, 141, 142, 143, 154, 155, 162, 173, 174, 179, 181, 182, 183, 186, 189, 190, 191, 192, 193, 209, 230, 237, 241, 310
Delfosse, X., Forveille, T., Beuzit, J.-L. et al., 1999, A&A, 344, 897 54
De Lorenzi, F., Debattista, V.P., Gerhard, O., et al. 2007, MNRAS, 376, 71 109
De Silva, G.M., Freeman, K.C., Bland-Hawthorn, J. et al. 2007, AJ, 133, 694 22, 205
De Simone, R.S., Wu, X., Tremaine, S. 2004, MNRAS, 350, 627 19, 93
Drimmel, R., Spergel, D.N. 2001, ApJ556, 181 122, 123, 138, 154
Dwek, E., Arendt, R. G., Hauser, M. G., et al. 1995, ApJ, 445, 716 127
Eddington, A.S. 1906, MNRAS, 67, 34 13
Efremov Y. N. 1988, Soviet Sientific Reviews E. Astrophysics and Space Physics Reviews 7, 105 17
Eggen, O.J. 1958, MNRAS, 118, 154 15, 317
Eggen, O.J. 1971, PASP, 83, 251 15, 61, 64, 66, 317
Eggen, O.J. 1996a, ApJ, 111, 1615 15, 317
Eggen, O.J. 1996b, ApJ, 112, 1595 viii, 4, 15, 20, 61, 64, 224, 317
Evans, N.W., Read, J.C.A. 1998, MNRAS, 300, 83 109
Famaey, B., Jorissen, A., Luri, X., et al. 2005, A&A, 430, 165 x, 7, 17, 44, 51, 54, 55, 56, 71, 72
Famaey, B., Pont, F., Luri, X., et al. 2007, A&A, 461, 957 17, 88
Famaey, B., Siebert, A., Jorissen, A. 2008, A&A, 483, 453 17
Feast, M., Whitelock, P. 1997, MNRAS, 291, 683 56
Fehrenbach, Ch., Burnage, R., Duflot, M., et al. 1987, A&AS, 71, 263 53, 58

Feltzing, S., Holmberg 2000, A&A, 357, 153 22, 205
Ferrers, N.M. 1877, Q.J. Pure Appl. Math., 14, 1 130
Figueras, F., Gomez, A.E., Asiain, R., et al. 1997, ESASP, 402, 519 46
Franco, J., Martos, M., Pichardo, B., et al. 2002, ASPC, 275, 343 136
Freeman, K.C. 1970, ApJ, 160, 811 102
Freeman, K., Bland-Hawthorn, J. 2002, ARA&A, 40, 487 vii, 3
Freudenreich, H.T. 1998 ApJ, 492, 495 102, 125, 127
Fuchs, B., Dettbarn, C., Rix, H-W., et al. 2009, AJ, 137, 4149 108, 109
Fux, R. 1997, A&A, 327, 983 18
Fux, R. 2000, *Galactic Dynamics from the Early Universe to the present*, eds. Combes, F., Mamon, G.A. and Charmandaris, V., ASP Conference Series Vol 197, 27 18, 142, 193
Fux, R. 2001, ApJ, 373, 511 18, 19, 71, 111, 114, 115, 116, 117, 142, 143, 162, 173, 179, 182, 183, 191, 198, 209, 216, 217, 241
Georgelin, Y.M., Georgelin, Y.P. 1976, A&A, 49, 57 123
Gerhard, O. 2002, ASPC, 273, 73 128
Gizis, J.E., Reid, I. N., Hawley, S.L. 2002,AJ, 123, 3356 54
Gomez, F.A., Helmi, A. 2009, arxiv:0904.1377G 21
Grenier, S., Baylac, M.-O., Rolland, L., et al. 1999, A&AS, 137, 451 53
Hammersley, P.L., Garzón, F., Mahoney, T. J., et al. 2000, MNRAS, 317, 45 128, 129
Haywood, M. 2006, MNRAS, 371, 1760 60, 87, 88
Helmi, A., White, S.D.M 1999a, MNRAS, 307, 495 20
Helmi, A., White, S.D.M., de Zeeuw, P.T. et al. 1999b, Natur, 402, 53 20
Helmi, A., de Zeeuw, P.T. 2000, MNRAS, 319, 657 20
Helmi, A., Navarro, J.F., Nordström, B., et al. 2006, MNRAS, 365, 1309 21, 87, 89, 317
Hernandez, X., Valls-Gabaud, D. Gilmore, G. 2000, MNRAS, 316, 605 85, 93
Hernquist, L. 1993, ApJS, 86, 389 102, 105, 108
Holmberg, J., Nordström, B., Andersen, J. 2007, A&A, 475, 519 60, 107, 108
Ibata, R.A., Gilmore,G., Irwin, M.J. 1994, Natur 370, 194 20
Jeans, J.H. 1922a, MNRAS, 82, 122 14
Jeans, J.H. 1922b, MNRAS, 82, 132 15
Jørgensen, B.R., Lindegren, L. 2005, A&A, 436, 127 54
Jurić, M., Ivezić, E., Brooks, A., et al. 2008, ApJ, 673, 864 102, 107, 108
Kalnajs, A. J. 1991, *Dynamics of Disk Galaxies*, eds. B. Sundelius, 323 18, 183
Kapteyn, J.C. 1905, *Reports of the British Association for the Advancement. of Science*, 264, 257 13
Kim, W.-T. 2009, IAUS, 254, 313 103
Klement, R., Fuchs, R., Rix, H.W. 2008, ApJ, 685, 261 21, 203

Klement, R., Rix, H.W., Flynn, C., et al. 2009, ApJ, 698, 865 21
Klypin, A., Valenzuela, O., Colin, P., et al. 2009, MNRAS, 398, 102 101, 116
Lega, E., Scholl, H., Alimi, J.M., et al. 1995, ParC, 21, 265 27
Lewis, J.R., Freeman, K.C. 1989, AJ, 97, 139 106
Lin, C.C., Theory of the spiral structure. In *Highlights of Astronomy 4*, by Jager (Reidel Publ. Co., Dordrecht, Holland 1971), p.441 18, 131
Lindblad, B. 1923, ApJ, 59, 37 14
Lindblad, B. 1925a, ApJ, 62, 191 14
Lindblad, B. 1925b, Archiv für Mathematik, 19, 21 14
López-Corredoira, M., Cabrera-Lavers, A., Garzón, F., et al. 2002, A&A, 394, 883 105
López-Corredoira, M., Cabrera-Lavers, A., Mahoney, T. J., et al. 2007, AJ, 133, 154 129
López-Santiago, J., Montes, D., Crespo-Chacón, I., et al. 2006, ApJ, 643, 1160 61
Luri, X., Mennessier, M.O., Torra, J., et al. 1996, A&AS, 117, 405 44, 54, 72
Mädler, J.H. 1846, AN, 24,213viii, 4, 12, 15
Martínez, V. J., Starck, J.L., Saar, Enn. et al. 2005, ApJ, 634, 744 35, 46
Martinez-Delgado, D., Aparicio, A., Gómez-Flechoso, M.A. 2001, ApSSS, 277, 425 20
Martos, M.A., Cox, D.P. 1998, ApJ, 509, 703 125
Martos, M., Yañez, M., Hernandez, X., et al. 2004, JKAS, 37, 199 123
Mayor, M. 1972, A&A, 6, 60 18
McMillan, P.J., Binney, J.J 2010, MNRAS, 402, 934 121
Meillon, L., Crifo, F., Gómez, A.E., et al. 1997, Hipparcos - Venice'97', ESA SP-402, 591 56
Minchev, I., Quillen, A. C., Williams, M., Freeman, K. C., Nordhaus, J., Siebert, A., & Bienayme, O. 2009, MNRAS396, 56 22, 197, 198, 203, 222, 224, 267
Minchev, I., Boily, C., Siebert, A., et al. 2010, arXiv:0909.3516 22, 116, 142
Miyamoto, M., Nagai, R. PASJ, 27, 533 121
Monet, D.G., Levine, S.E., Canzian, B., et al. 2003, AJ, 125, 984 54
Montes, D. 2001, ASPC, 223, 1471 61
Murtagh, F., Starck, J.-L., Bijaoui, A. 1995, A&AS, 112, 179 27
Navarro, J. F., Helmi, A., & Freeman, K. C. 2004, ApJ, 601, L43 21, 201, 224
Nordström, B., Mayor, M., Andersen, J., et al. 2004, A&A, 418, 989 x, 7, 17, 21, 51, 54, 55, 56, 58, 60, 87
Patsis, P.A., Contopoulos, G., Grosbol, P. 1991, A&A, 243, 373 119, 132, 137
Patsis, P. A., Kaufmann, D. E., Gottesman, S. T., Boonyasait, V. 2009, MNRAS, 394, 142 129
Pichardo, B.2003a, UNAM, PhD Thesis 119, 125, 129, 159, 306
Pichardo, B., Martos, M., Moreno, E., et al. 2003b, ApJ, 582, 230 xi, 7, 97, 119, 120, 122, 123, 132, 133, 318
Pichardo, B., Martos, M., & Moreno, E. 2004, ApJ, 609, 144 xi, 7, 97, 119, 120, 127, 128, 318

Press, W.H., Teukolsky, S.A., Vetterling, W.T. et al. 1992, Numeric al Recipes in Fortran 77: The Art of Scientific Computing, 2nd. ed. (Cambridge University Press: Cambridge) 99
Pont F., Eyer L., 2004, MNRAS, 351, 487 60
Proctor, R.A., 1869, R. 1995, Proceedings of the Royal Society of London, Vol. 18, p. 169-171 viii, 4, 12, 13, 15
Quillen, A.C. 2003, AJ, 125, 785 234
Quillen, A.C., & Minchev, I. 2005, ApJ, 130,576 19, 111, 113, 117, 138, 160, 167, 233, 237
Quillen, A.C., Minchev, I., Bland-Hawthorn, J., et al. 2009, MNRAS397, 1599 22
Raboud, D., Grenon, M., Martinet, L., et al. 1998, A&A, 335, 61 18
Read, J. I., Lake, G., Agertz, O., & Debattista, V. P. 2008, MNRAS, 389, 1041 108, 301
Read, J. I., Mayer, L., Brooks, A. M., Governato, F., & Lake, G. 2009, arXiv:0902.0009 301
Reid, I.N., Gizis, J.E., Hawley, S.L. 2002,AJ, 124, 2721 x, 7, 51, 54, 55, 56, 58, 74
Reid, I.N., Turner, E.L., Turnbull, M.C., et al. 2007, ApJ, 665, 76760
Reid, M.J., Menten, K.M., Zheng, X.W., et al. 2009, ApJ, 700, 137 121
Roberts, W.W., Jr., Huntley, J.M., van Albada, G.D. 1979, ApJ, 233, 67 122
Robin, A., Reylé, C., Derrierè, S. et al. 2003, A&A, 409, 523 102, 107, 108, 125
Schoenrich, R., Binney, J., Dehnen, W. 2009, arXiv:0912.3693 150
Schuster, W.J., Moitinho, A., Márquez, A., et al. 2006, A&A, 445, 939 203
Schwarzschild, K. 1907, Gottingen Nachrichten, 1907, 614 13
Seabroke, G.M., & Gilmore, G. 2007, MNRAS, 380, 1348 23, 61, 71
Seabroke, G.M., Gilmore, G., Siebert, A., et al. 2008, MNRAS, 384, 11 21
Schmidt, M. 1956, Bull. Astron. Inst. Neth. 13, 468, 15 125
Skuljan, J., Hearnshaw, J. B., Cottrell, P. L. 1999, MNRAS, 308, 731 17, 19, 46, 47, 56, 61, 63, 66, 71, 91
Soubiran, C., Bienaymé, O., Siebert, A. 2003, A&A, 398, 141 108
Soubiran, C., Bienaymé, O., Mishenina, T. V., et al. 2008, A&A, 480, 91 107, 108
Starck, J.L., Bijaoui, A. 1994, Signal Processing, 35, 195 27, 34, 35, 36
Starck, J.L., Murtagh, F., Bijaoui, A. 1998, *Image Processing and Data Analysis* (Cambridge University Press) 27, 34
Starck, J.L., Murtagh, F. 2002, *Astronomical Image and data Analysis* (Springer) 27, 32, 34, 36
Stromberg, G. 1925, ApJ, 61, 363 14
Tabachnick, B.G., Fidell, L.S. 1996, *Using multivariate statistics*, HarperCollins College Publishers, New York, NY 266
Takeda, Y. 2007, PASJ, 59, 33560
Thomasson, M., Donner, K.J., Elmegreen, B.G. 1991, A&A, 250, 316 103
Torra, J., Fernández, D., Figueras, F. 2000, A&A, 359, 82 x, 7, 51, 53, 55, 58
Tremaine, S., Weinberg, M.D. 1984, ApJ, 282, 5 182

Turner, H.H. 1912, MNRAS, 72, 387 14
Turon, C., Primas, F., Binney, J., et al. 2008, Report n°4, ESA-ESO Working Group, Galactic Populations, Chemistry and Dynamics vii, 3
Vallée, J.P. 2008, ApJ, 135, 1301 123
van der Kruit, P.C., Searle, L. 1981, A&A, 95, 105 105
van der Kruit, P.C., Searle, L. 1982, A&A, 110, 61 106
Villalobos, A., & Helmi, A. 2009, arXiv:0902.1624 21, 224
Vorobyov, E.I., Theis, C. 2008, MNRAS383, 817 23
Weidemann, V., Jordan, S., Iben, I. Jr., et al. 1992, ApJ, 104, 1876 16
Weinberg, M.D. 1994, ApJ, 420, 597 18
Williams, M.E.K., Freeman, K.C., Helmi, A. 2009, IAUS, 254, 139 22, 203, 217, 224
Wilson, R.E. 1932, AJ, 42, 49 15
Yanny, B., Newberg, H.J., Kent, S., et al. 2000, ApJ, 540, 825 20
Zhao, H., Mao, S. 1996, MNRAS, 283, 1197 127
Zhao, J., Zhao, G., Chen, Y. 2009, ApJ, 692, 113 47
Zhu, Z. 2009, RAA, 9, 1285 103

Appendixes

Appendix A

Considerations about the initial conditions

As we have discussed in Section 10.2, several assumptions and approximations in our method of IC building have been taken. These are: i) exponential approximation of the radial density distribution of the disc in contrast to the density of the PM04–MW potential model (Miyamoto-Nagai disc), ii) truncation of the collisionless Boltzmann equation at certain order and iii) epicyclic approximation. In this appendix we evaluate if these approximations mean a limitation for our study.

A.1 Phase mixing due to the initial conditions

In this section we evaluate the behaviour of our three types of IC: IC1, IC2 and specially IC3 for being the more extreme case. In short, we study how all these IC evolve under the PM04–MW potential model using only the axisymmetric part. Regarding the spatial distribution of the disc, in Figure A.1 we show the initial surface density of the disc (imposed exponential) compared to the final distribution with R after evolving for 400 Myr and 5000 Myr for the three types of IC. In the left panels of this figure we see how the initial density distribution fits the exponential curve with scale length of 2.5 kpc (see Section 10.2). After the longer time, the final density profile is stabilised. For IC1 and IC2 (Figures A.1a and A.1b) the final density profile do not change significantly. However, for IC3 (Figure A.1c) the final density distribution differs notably from the imposed at the beginning. The difference is noticed even for 400 Myr of integration. Globally, a migration of particles from the inner to the outer parts of the disc has occur.

Concerning the velocity distributions, we now study them after an integration of 5000 Myr.

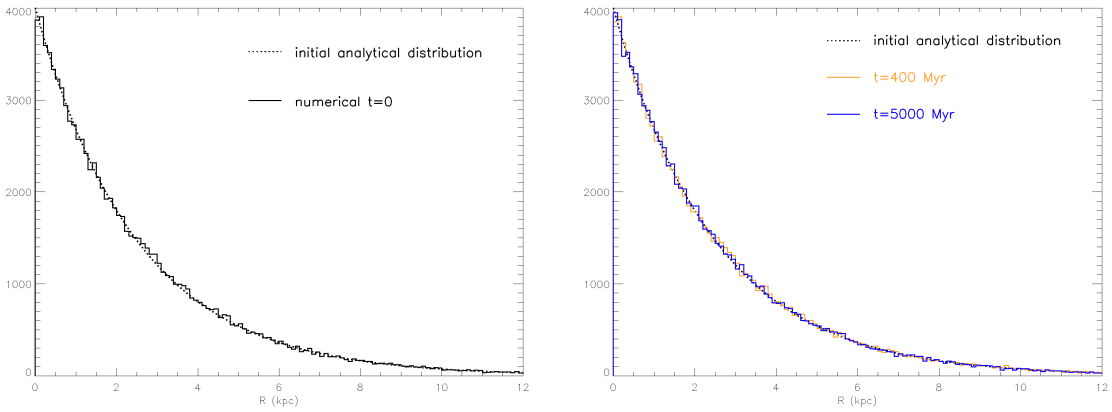

(a) IC1

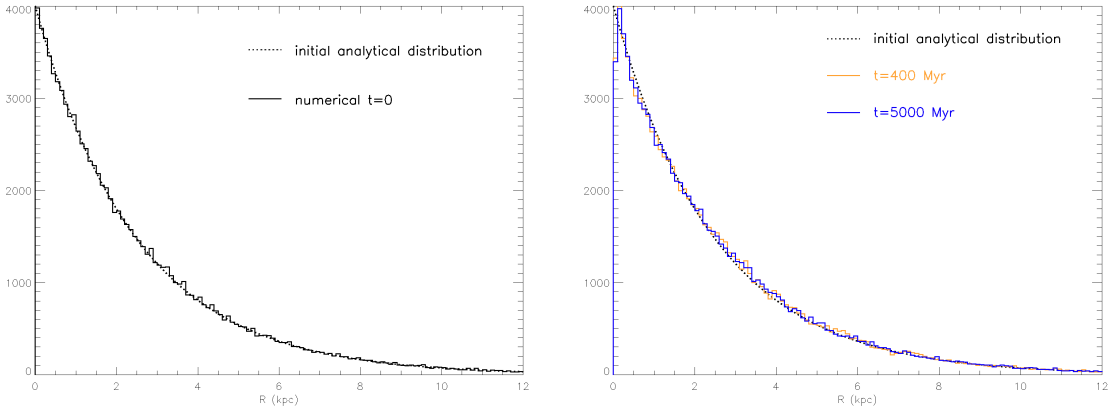

(b) IC2

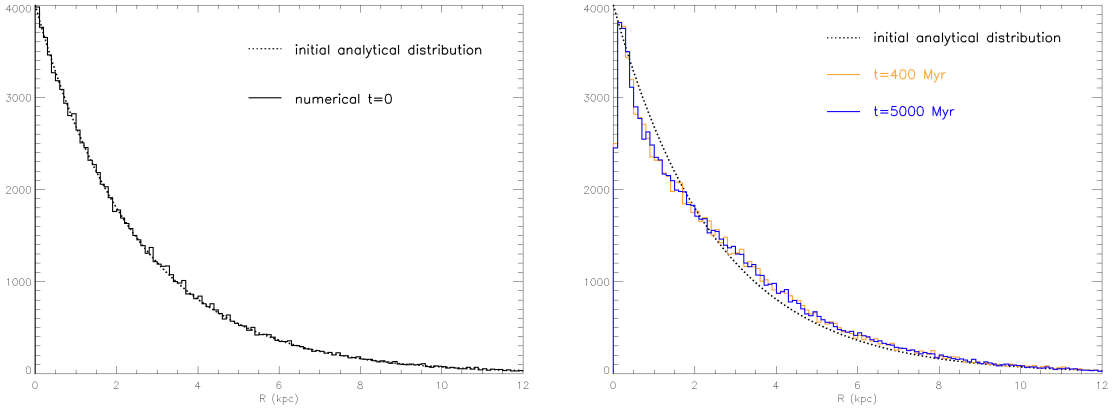

(c) IC3

Figure A.1: **Initial and final density distributions.** Comparison between the initial analytical density distribution with the numerical initial distribution (left column) and with the distributions after 400 Myr and 5000 Myr of evolution under the axisymmetric part of the PM04–MW potential model (right column) for IC1, IC2 and IC3. The analysis is done with 100000 particles of the disc.

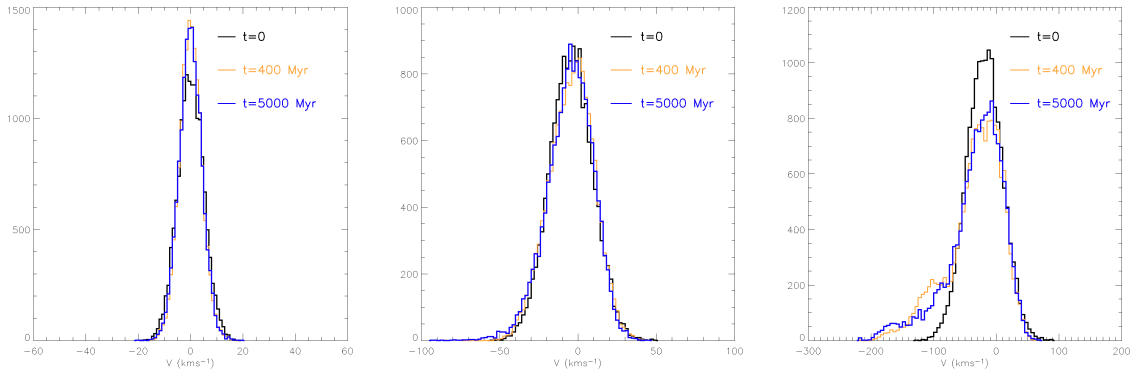

(a) IC1 (b) IC2 (c) IC3

Figure A.2: **Initial and final velocity distributions.** Comparison between the initial V velocity distribution of 15000 particles in the solar ring (8-9 kpc) with the distributions after 400 Myr and 5000 Myr of evolution under the axisymmetric part of the PM04–MW potential model for IC1, IC2 and IC3.

Table A.1: **Moments of the initial and final U distribution.** Some moments of the initial and final U distribution for the 15000 particles in the solar ring (8-9 kpc) with 5000 Myr of evolution under the axisymmetric part of the PM04–MW potential model for IC1, IC2 and IC3. For IC3 we also indicate in brackets the same statistical parameters but only considering particles with initial radius $R > 2.5$ kpc.

	IC1		IC2		IC3		
	$t = 0$	$t = 5000$ Myr	$t = 0$	$t = 5000$ Myr	$t = 0$	$t = 5000$ Myr	
mean ($\mathrm{km\,s^{-1}}$)	-0.06	-0.02	-0.03	0.05	-0.2	0.2	(-0.1)
standard deviation ($\mathrm{km\,s^{-1}}$)	5.0	6.1	19.0	20.0	40.0	49.0	(46.0)
skewness	-0.002	-0.031	-0.026	-0.005	-0.020	-0.005	(-0.021)
kurtosis	-0.02	0.16	0.07	0.18	0.1	1.6	(0.8)

Table A.2: **Moments of the initial and final V distribution.** The same as Table A.2 but for eh V component.

	IC1		IC2		IC3		
	$t = 0$	$t = 5000$ Myr	$t = 0$	$t = 5000$ Myr	$t = 0$	$t = 5000$ Myr	
mean ($\mathrm{km\,s^{-1}}$)	0.03	-0.08	-4.4	-5.3	-19.0	-33.0	(-28.0)
standard deviation ($\mathrm{km\,s^{-1}}$)	5.0	4.4	14.0	15.0	29.0	46.0	(37.0)
skewness	0.02	0.02	0.0	-0.5	0.0	-1.1	(-0.7)
kurtosis	0.0	0.3	0.0	0.8	0.0	1.3	(0.3)

Figure A.2 shows the initial and final V distributions for IC1, IC2 and IC3 at solar radius. Similarly to what we conclude for the studies of the density, the distribution is almost invariable for IC1 and IC2. But for IC3 it has became clearly asymmetric. To quantify the degree of similarity or difference between initial and final U and V distributions we present in Tables A.1 and A.2 some statistical parameters concerning these distributions. In particular we present the mean, standard deviation, skewness and kurtosis for the initial and final velocity distributions in the solar ring (8-9 kpc) with 5000 Myr of evolution under the axisymmetric part of the PM04–MW potential model for IC1, IC2 and IC3. For IC3 we also show in brackets the same statistical parameters but only considering particles with initial radius $R > 2.5$ kpc. With this we avoid the central parts of the disc where the presence of the bulge in the PM04–MW potential model is significant and where the velocity dispersions are most uncertain. The main outcomes of these calculations are the following. The final average in V, i.e. the asymmetric drift, has become significantly larger for IC3, even if the more inner particles are rejected. The dispersions in both components of the velocity have grown also significantly for IC3. We see from these calculations that the mean and velocity dispersions for IC1 and IC2 have varied less than $1\,\mathrm{km\,s^{-1}}$. To establish the significance of the skewness and the kurtosis we use approximate formulae to calculate their standard errors following Tabachnick & Fidell (1996): they can be estimated roughly with $\sqrt{6/N}$ for the skewness and with $\sqrt{24/N}$ for the kurtosis, where N is the number of points in the sample. For our samples with 15000 points these are 0.02 and 0.04 respectively. Taking into account these values, we conclude that all discs (IC1, IC2, IC3), which initially had null kurtosis and null skewness as they are Gaussian distributions, have changed these parameters. They have all gained a significant positive kurtosis both in U and in V. Significant negative skewness has been found in the final distributions only in the V component for IC2 (which is noticed in the weak tail of particles at negative V in Figure A.2b) and for IC3 (perfectly noticeable in Figure A.2c).

With these tests we conclude that strictly all discs (IC1, IC2, IC3) suffer from phase mixing processes due to the approximations made in their construction. We see that for IC1 and IC2 the effects of this process are minor or at least, it is not necessary to take them into consideration in the time scales of relevance in our simulations. However, the hottest disc IC3 experiences conspicuous effects that can have consequences on our results. In particular, the phase mixing causes transient effects on the velocity plane until the final relaxation is reached. We see in Chapter 15 that the velocity distributions exhibit arch-shaped structures specially at lower V which successively disappear with time leading to the smooth velocity distribution when the complete phase mixing has been achieved. In other words, the initial non-homogeneous coverage of the phase space due to the followed approximations triggers a process of phase-mixing that becomes apparent in the formation of these transient arches. With the use of IC3 as a tracer of

the final DF we are probably biasing the DF through inner and very eccentric orbits that tend to reach the solar radius. Neither IC1 nor IC2 exhibit these arches.

We have generated a new set of IC with a density profile consistent with a Miyamoto-Nagai disc following the same process and normalisation as in IC3 detailed in Section 10.2. Repeating the above tests using these new IC, we see that similar phase-mixing processes occur and, therefore, the approximation in the density (i) is not the cause, or at least the unique cause, of the mentioned transient effects in the disc. This is discussed in Section A.2. Besides, the significant skewness and kurtosis in the final the velocity distributions of IC3 points to the fact that probably higher order moments in the collisionless Boltzmann equation (ii) should have been considered. On the other hand, the invalidity of the epicyclic approximations (iii) for high velocity dispersion such as the one of IC3 and specially at the inner parts of the disc should not be forgotten either. Examining carefully which approximation has the maximum contribution to these transient effects and establishing a new set of IC without these approximations are out of the scope of this thesis although it is a point that can be dealt with in our future work.

Whatever it is the exact cause of the transient features in the disc, we take advantage of IC3 to study the effects of the bar and the spiral arms on a disc that experiences strong phase mixing at the same time that experiences the influence of the non-axisymmetric components of the potential. The use of IC3 is therefore consistent with simulating a disc which is not in perfect relaxed equivalently to what a galaxy would experience if an certain phenomena perturbed it (e.g. a passage of an orbiting satellite or if a bar develops and evolves). This methodology of using unevenly distributed in phase space initial conditions as a proxy for studying an unrelaxed population was first used in Minchev et al. (2009). Traditionally the choice of IC is motivated by self-consistency with the present stage of the Galactic disc structure. However, current scenarios of galaxy formation and evolution predict that both external and internal perturbation mechanisms affect the disc kinematics. Therefore, we want also to consider as plausible the possibility that a recent perturbation on the MW disc has changed the overall potential that governs it.

A.2 Exponential density approximation

In this section we evaluate the effects of the exponential approximation in the initial density profile. This approximation helped us to simplify considerably Equation 10.7 in the IC derivation but differs from the density of the PM04–MW potential model which includes a Miyamoto-Nagai disc and a bulge. In particular, the bulge exceeds the 1% of the disc density, i.e. begin to contribute importantly, for $R < 2.2\,\mathrm{kpc}$. The comparison between both densities is shown in Figure A.3. The normalisation of the density has been chosen to give equal density at

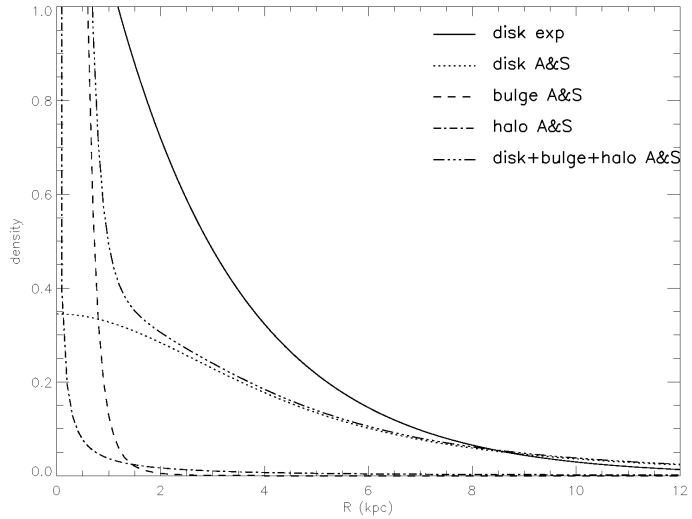

Figure A.3: **Different density profiles.** Density profile of an exponential disc with the scale length of $R_\Sigma = 2.5\,\mathrm{kpc}$ (as in all our IC) and density profiles of the components and full axisymmetric model by Allen & Santillán (1991). The density of the discs have been matched at solar radius $R = 8.5\,\mathrm{kpc}$.

$R = 8.5\,\mathrm{kpc}$. The exponential profile is steeper than the Miyamoto-Nagai disc and it is, therefore, equivalent to considering a shorter scale length.

As we deal with test particles, we consider that the exponential density profile approximation would not cause significant alterations with respect to a Miyamoto-Nagai profile. In principle for not very different density distributions the only expected changes in the final velocity distribution are minor differences in the relative crowding of the kinematic groups. This is due to the fact that in general the particles that crowd a specific group come from a certain initial ranges of radius and the different slope of the density profiles causes differences in the relative density in these ranges. In any case we have undertaken some tests to evaluate the importance of the exponential density profile approximation generating a new set of IC with a density profile consistent with a Miyamoto-Nagai disc following the same process as in IC2 detailed in Section 10.2. We have evaluated the effect of the new density profile on the kinematic structures created by the bar and the spiral arms by comparing equal simulations with these two different discs. With these tests we conclude that the results are not significantly sensitive to this different initial distribution. For instance in Figure A.4 we show the same simulation as in Figure 13.7 but using a Miyamoto-Nagai profile. This simulation uses the PM04–MW potential model including only spiral arms and is described in the corresponding Section 13.1. We show also an example of a simulation with only bar (Figure A.5) that must be compared with Figure 14.2. Mo significant changes are noticed between the two figures of each pair.

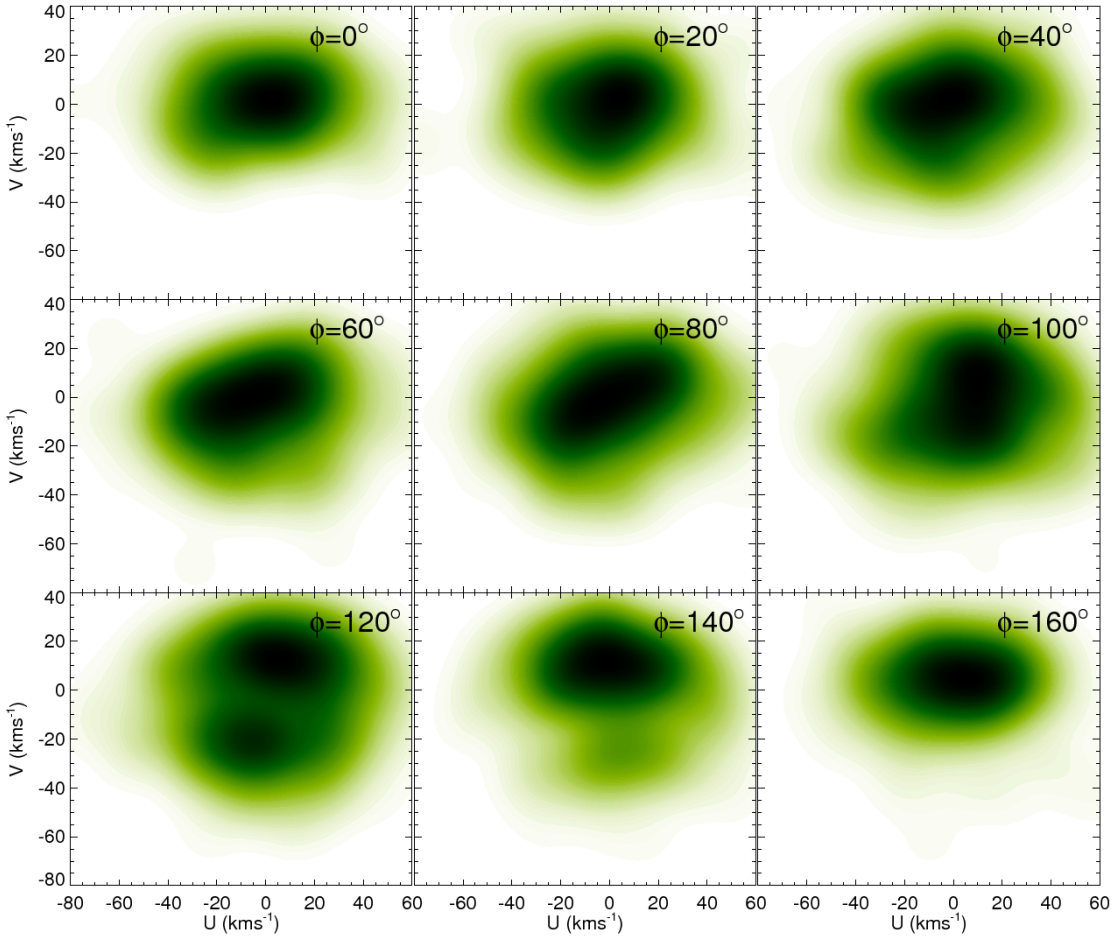

Figure A.4: **Kinematic effects of the spiral arms on a Miyamoto-Nagai disc.** U–V velocity distributions after WD at $R = 8.5\,\mathrm{kpc}$ and at different azimuths ϕ for the simulations with the PM04–MW potential model using only spiral arms and IC consistent with a Miyamoto-Nagai disc.

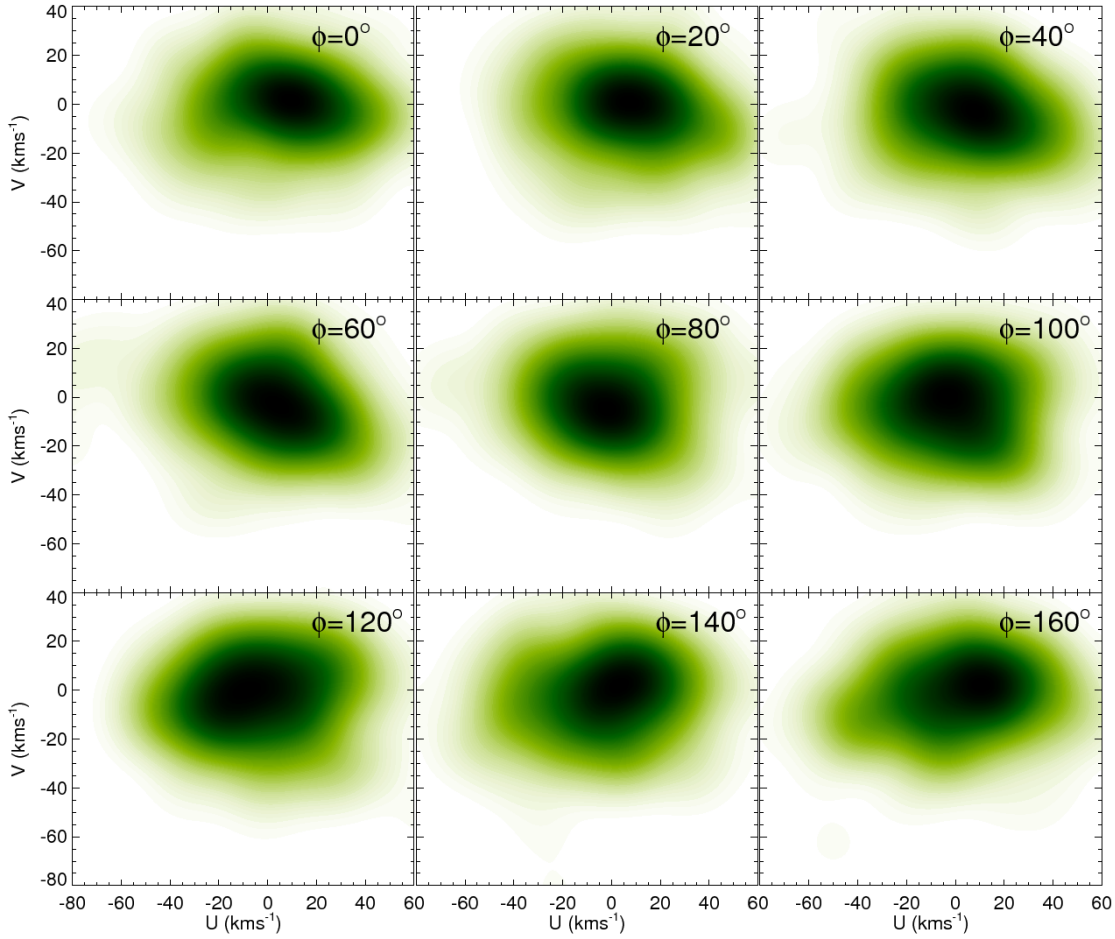

Figure A.5: **Kinematic effects of the bar on a Miyamoto-Nagai disc.** U–V velocity distributions after WD at $R = 8.5\,\mathrm{kpc}$ and at different azimuths ϕ for the simulations with the PM04–MW potential model using only bar and IC consistent with a Miyamoto-Nagai disc.

We have followed the evolution of IC that are as hot as IC3 and consistent with a Miyamoto-Nagai disc. As it is seen in Appendix A.1 and in Section 15.1 the use of the hot disc IC3 produces several arches in the velocity distributions when they are integrated with the axisymmetric part of the PM04–MW potential model. These arches are eventually mixed up and dissolved. We check that exactly the same arches appear when these IC are used and integrated for 400 Myr (compare Figure A.6 with Figure 15.1 where we used IC3 that have exponential density profile). To be more consistent, we can consider only particles with initial radius $R > 2.5\,\mathrm{kpc}$, where the density of the bulge is smaller than 0.7% of the disc. In this case Figure A.6 is turned into Figure A.7. Although we have cut out the arches at lowest part of the panels still some arches and transient features appear in this case.

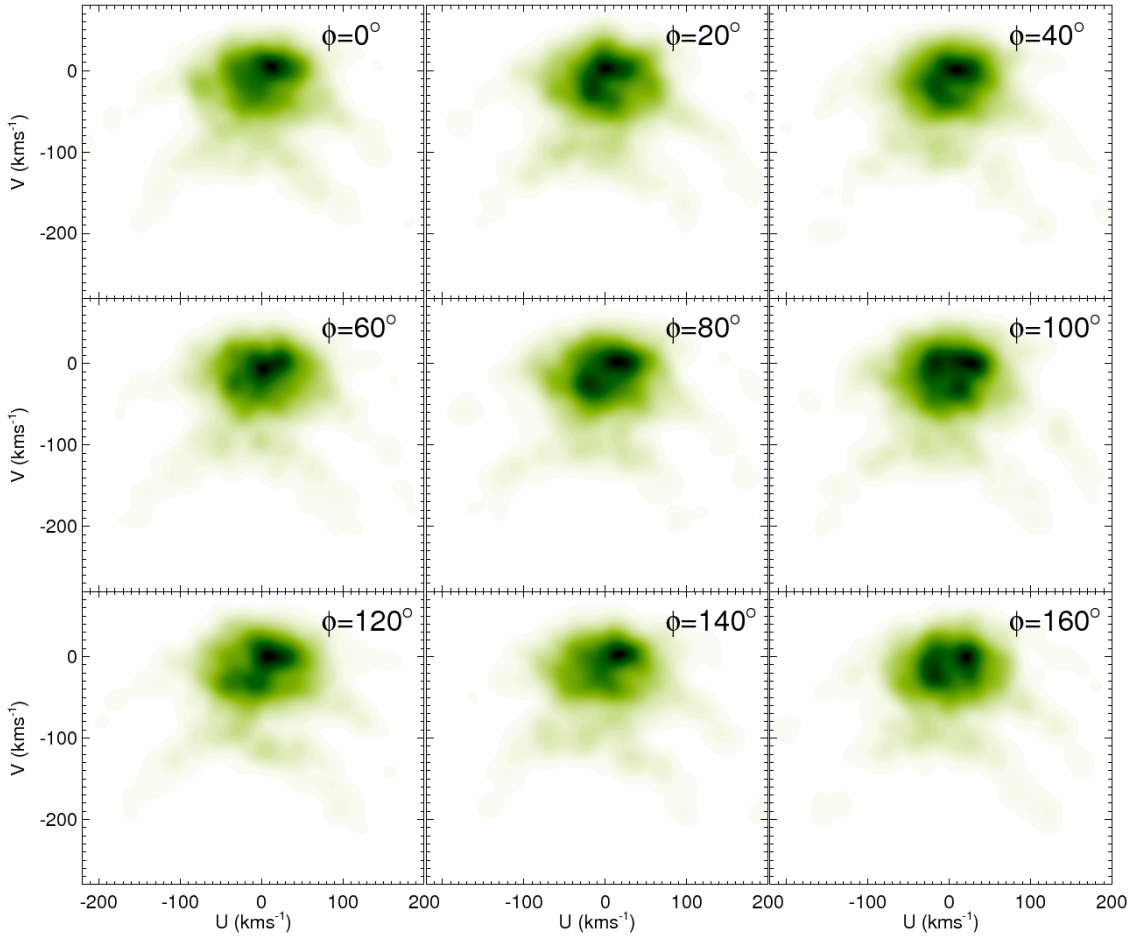

Figure A.6: **Velocity distribution of a hot Miyamoto-Nagai disc for the axisymmetric part of the potential model.** U–V velocity distributions after WD at $R = 8.5\,\mathrm{kpc}$ and at different azimuths ϕ for the simulations with the PM04–MW potential model with only the axisymmetric part and the IC consistent with a Miyamoto-Nagai disc.

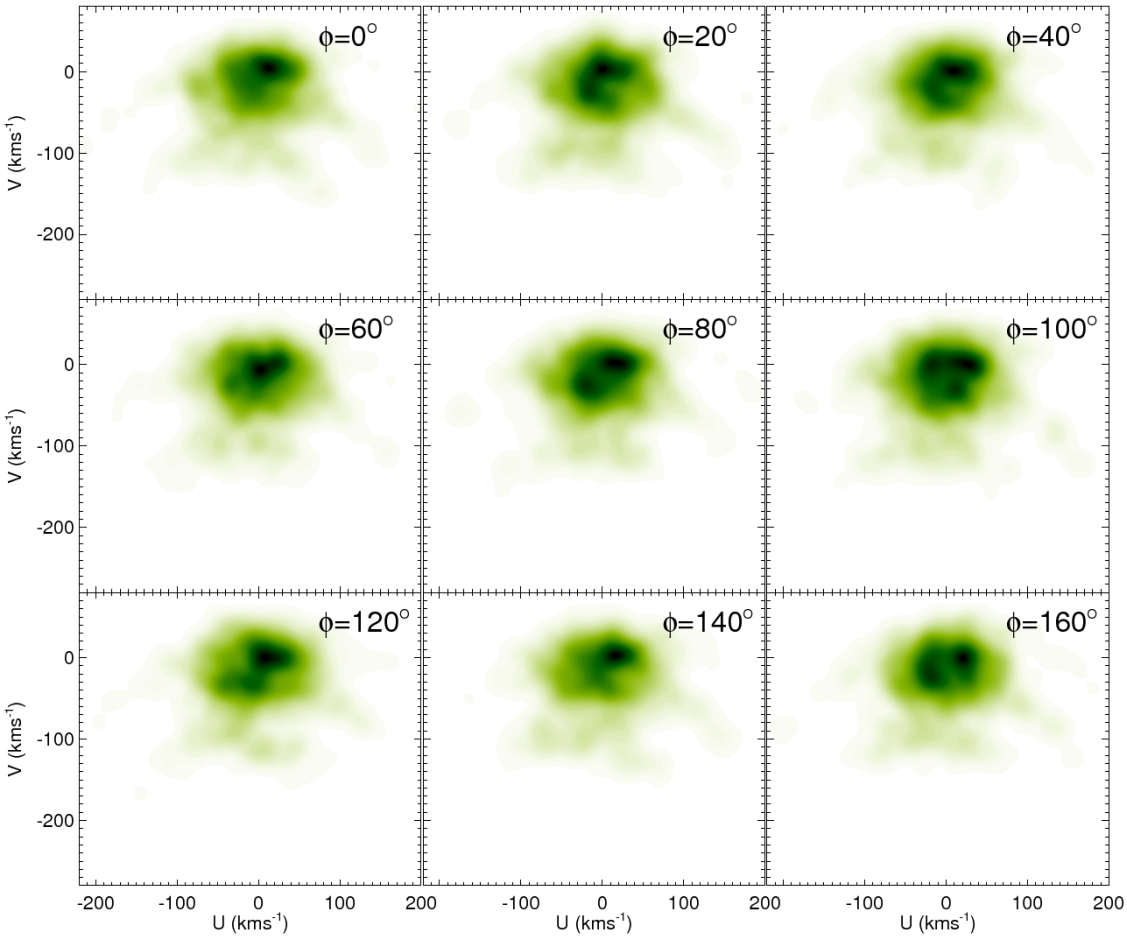

Figure A.7: **Velocity distribution of a hot Miyamoto-Nagai disc for the axisymmetric part of the potential model without the inner particles.** The same as FigureA.6 but only considering particles with initial radius $R > 2.5\,\mathrm{kpc}$.

Appendix B

Additional materials

B.1 Method figures

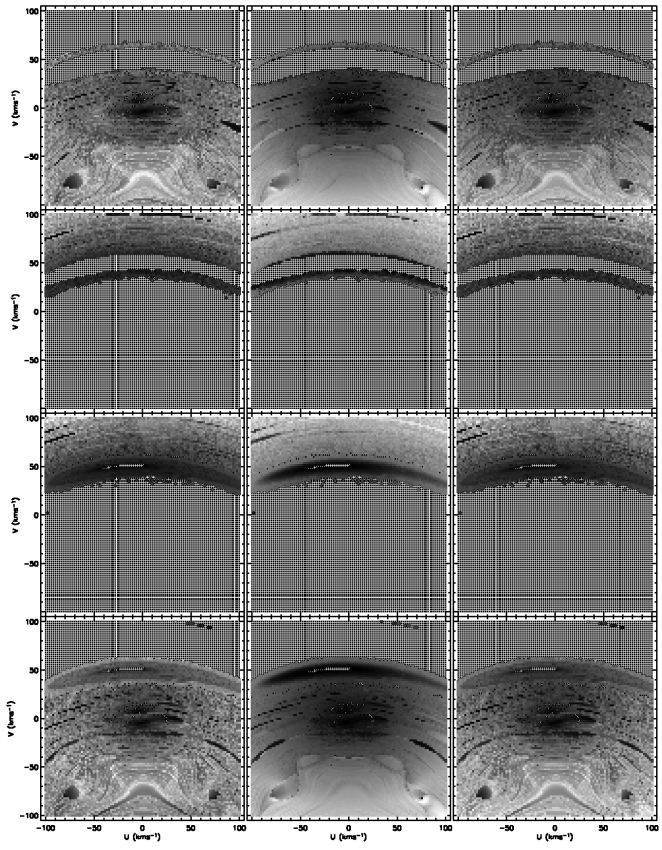

Figure B.1: U–V plane coloured as the periodicity of the corresponding orbits calculated for the 12 variables following the order of Table 10.2 for the model of spiral arms.

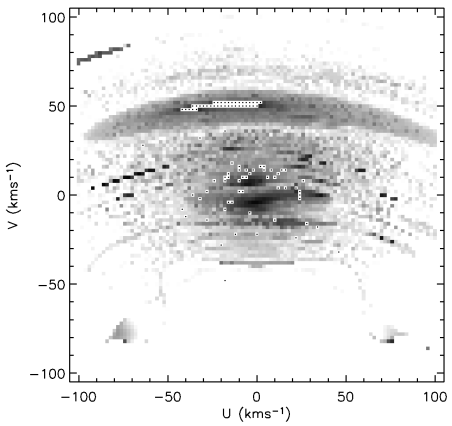

Figure B.2: U–V plane coloured as the periodicity of the corresponding orbits for the default model of spiral arms.

B.2 Simulations with the axisymmetric part of the potential

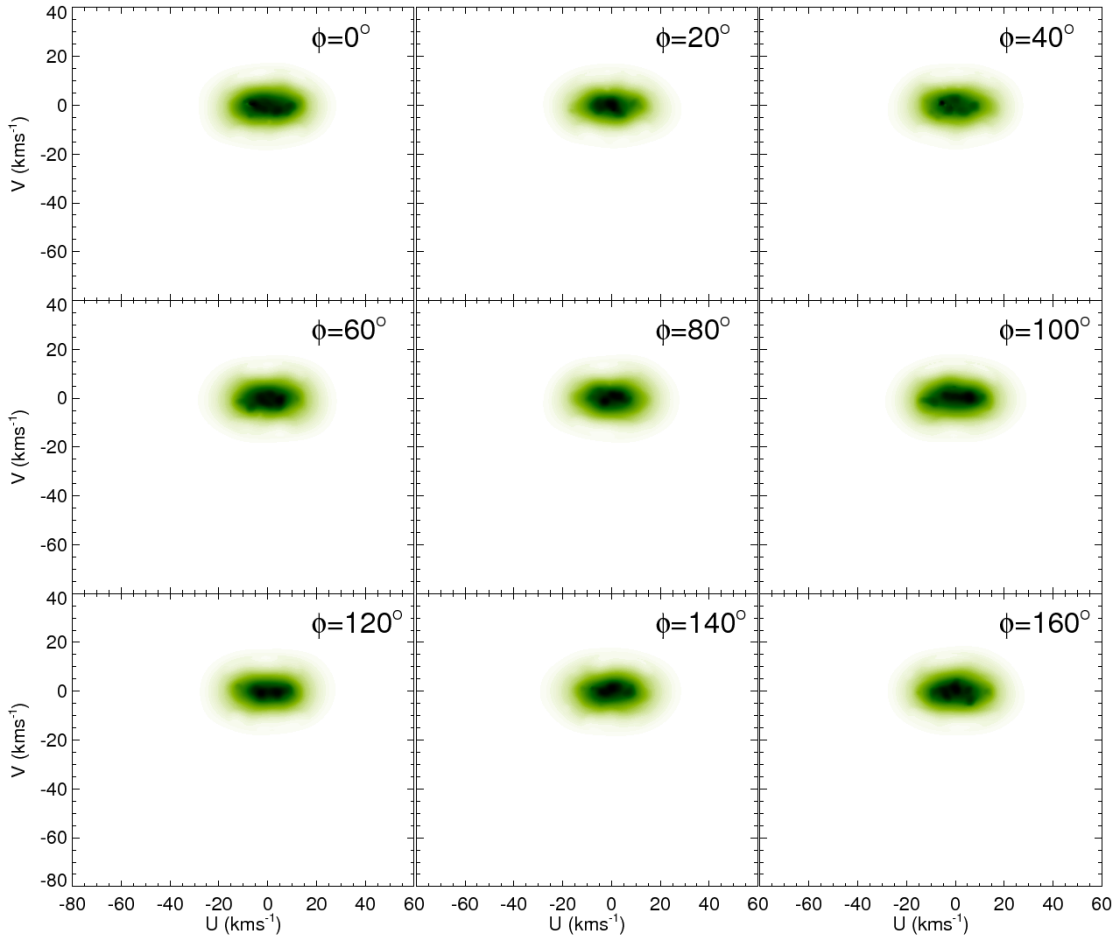

Figure B.3: **Velocity distribution of the cold disc for the axisymmetric part of the potential model.** U–V velocity distributions after WD at $R = 8.5\,\mathrm{kpc}$ and at different azimuths ϕ for the simulations with the PM04–MW potential model with only the axisymmetric part and IC1.

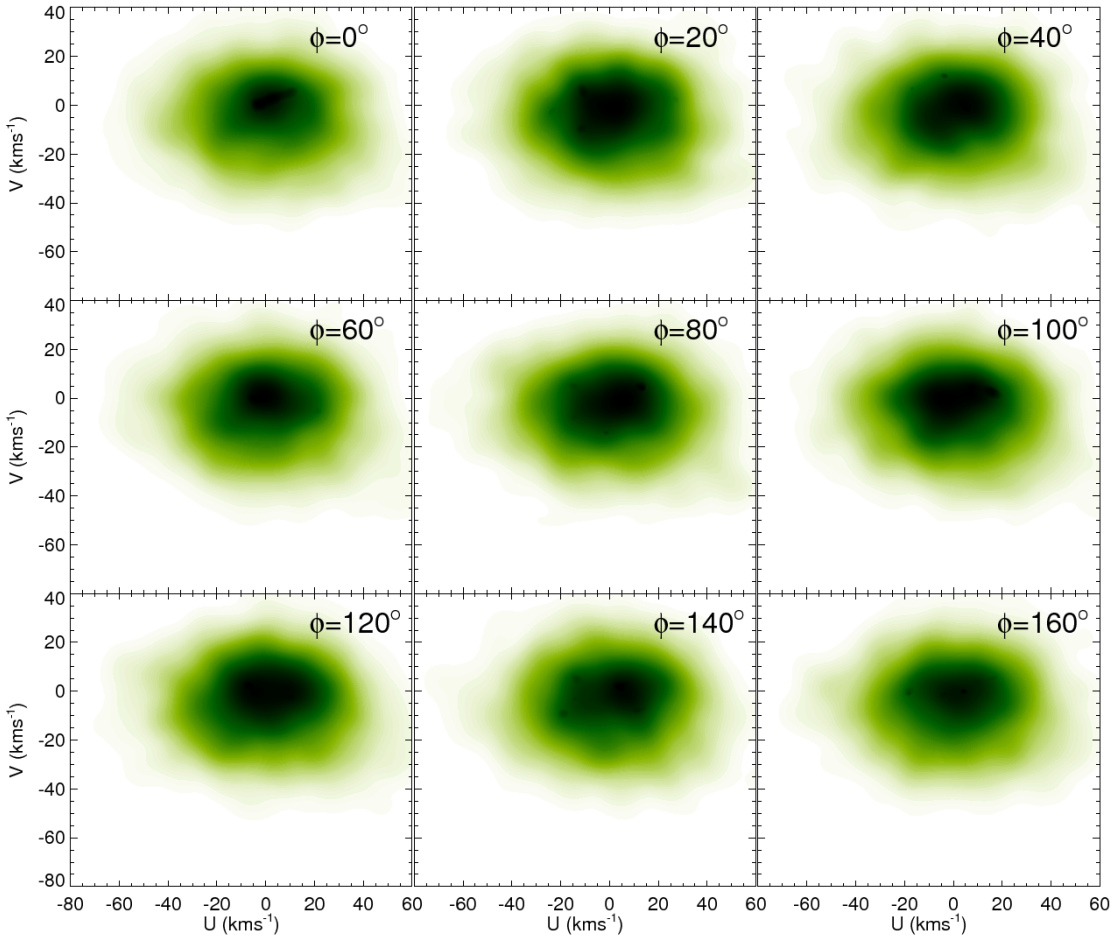

Figure B.4: **Velocity distribution of the intermediate disc for the axisymmetric part of the potential model.** U–V velocity distributions after WD at $R = 8.5\,\mathrm{kpc}$ and at different azimuths ϕ for the simulations with the PM04–MW potential model with only the axisymmetric part and IC2.

B.3 Simulations with the spiral arms

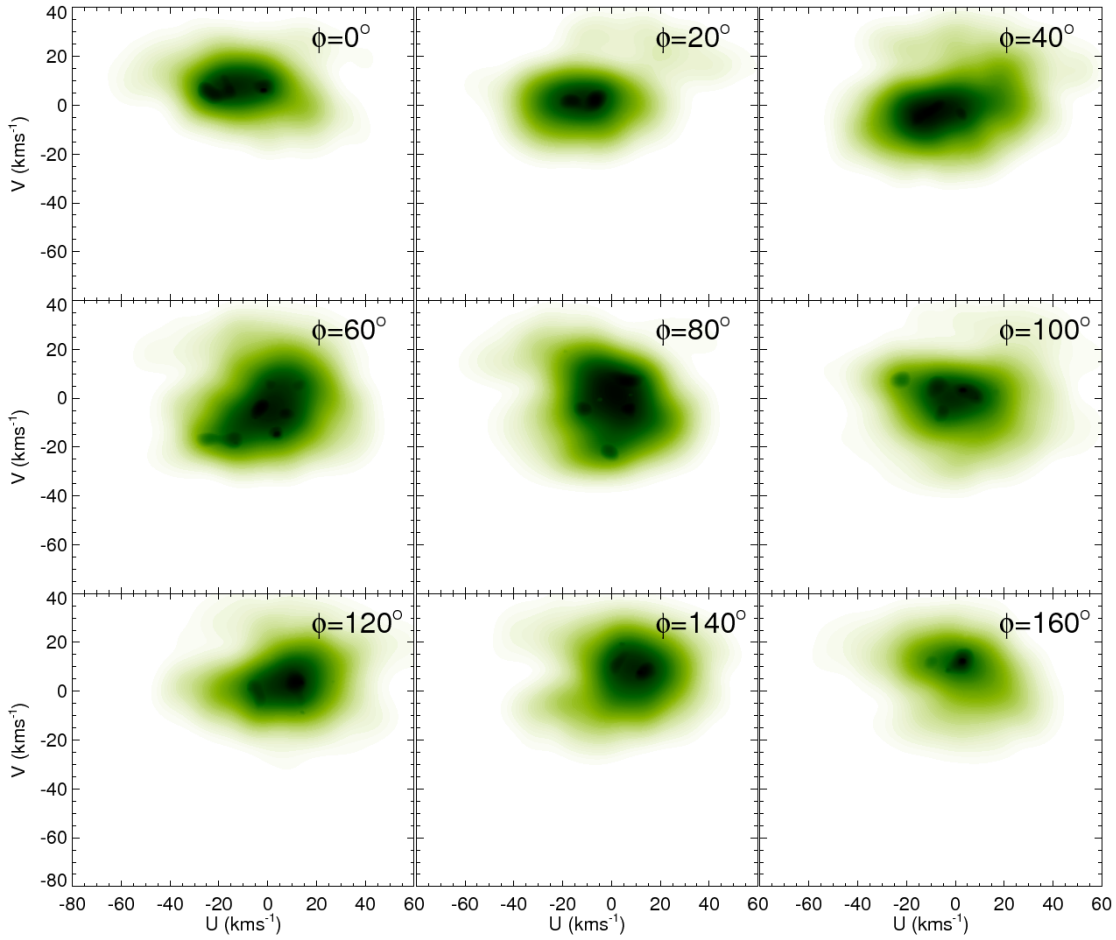

Figure B.5: **Kinematic effects of spiral arms with $\Omega_{sp} = 15\,\mathrm{km\,s^{-1}kpc^{-1}}$ on a cold disc.** U–V velocity distributions after WD at $R = 8.5\,\mathrm{kpc}$ and at different azimuths ϕ for the simulations with the PM04–MW potential model using only spiral arms with $\Omega_{sp} = 15\,\mathrm{km\,s^{-1}kpc^{-1}}$ and IC1.

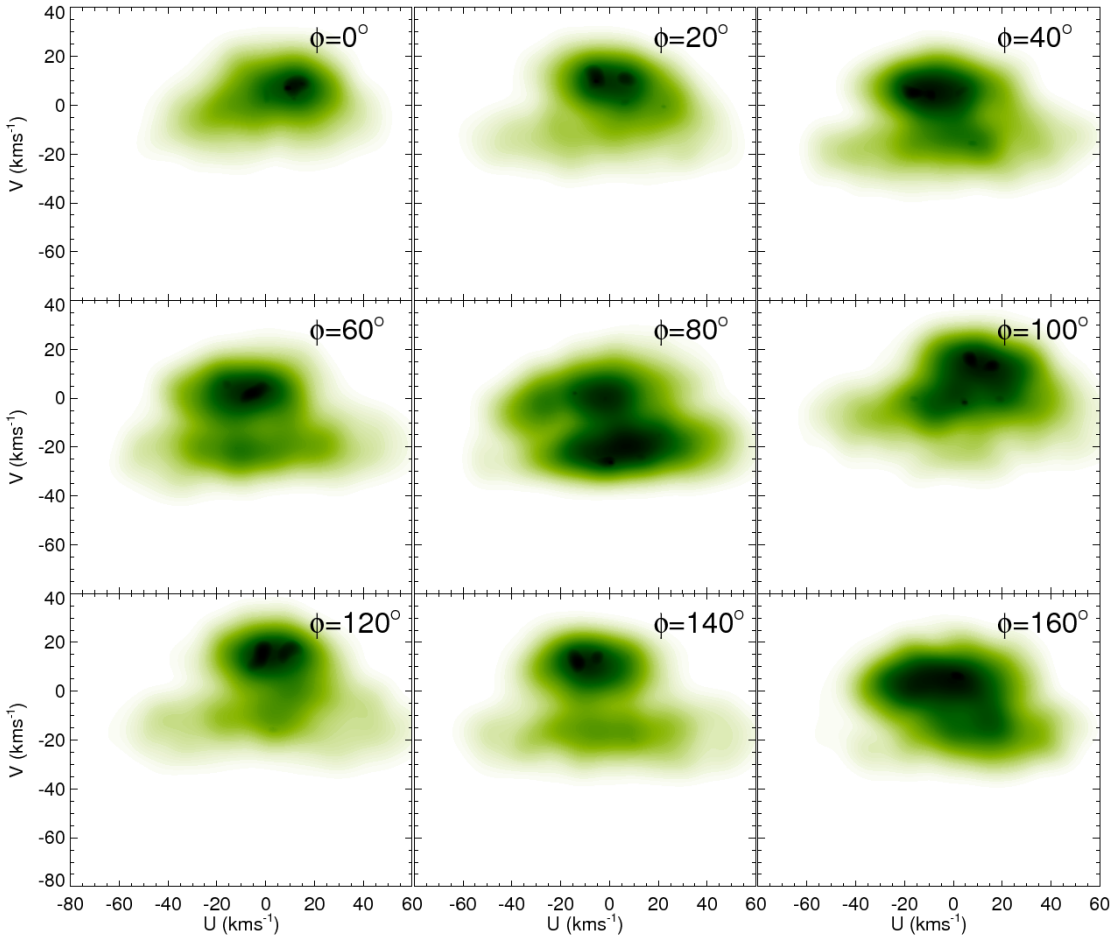

Figure B.6: **Kinematic effects of spiral arms with $\Omega_{sp} = 18\,\mathrm{km\,s^{-1}kpc^{-1}}$ on a cold disc.** U–V velocity distributions after WD at $R = 8.5\,\mathrm{kpc}$ and at different azimuths ϕ for the simulations with the PM04–MW potential model using only spiral arms with $\Omega_{sp} = 18\,\mathrm{km\,s^{-1}kpc^{-1}}$ and IC1.

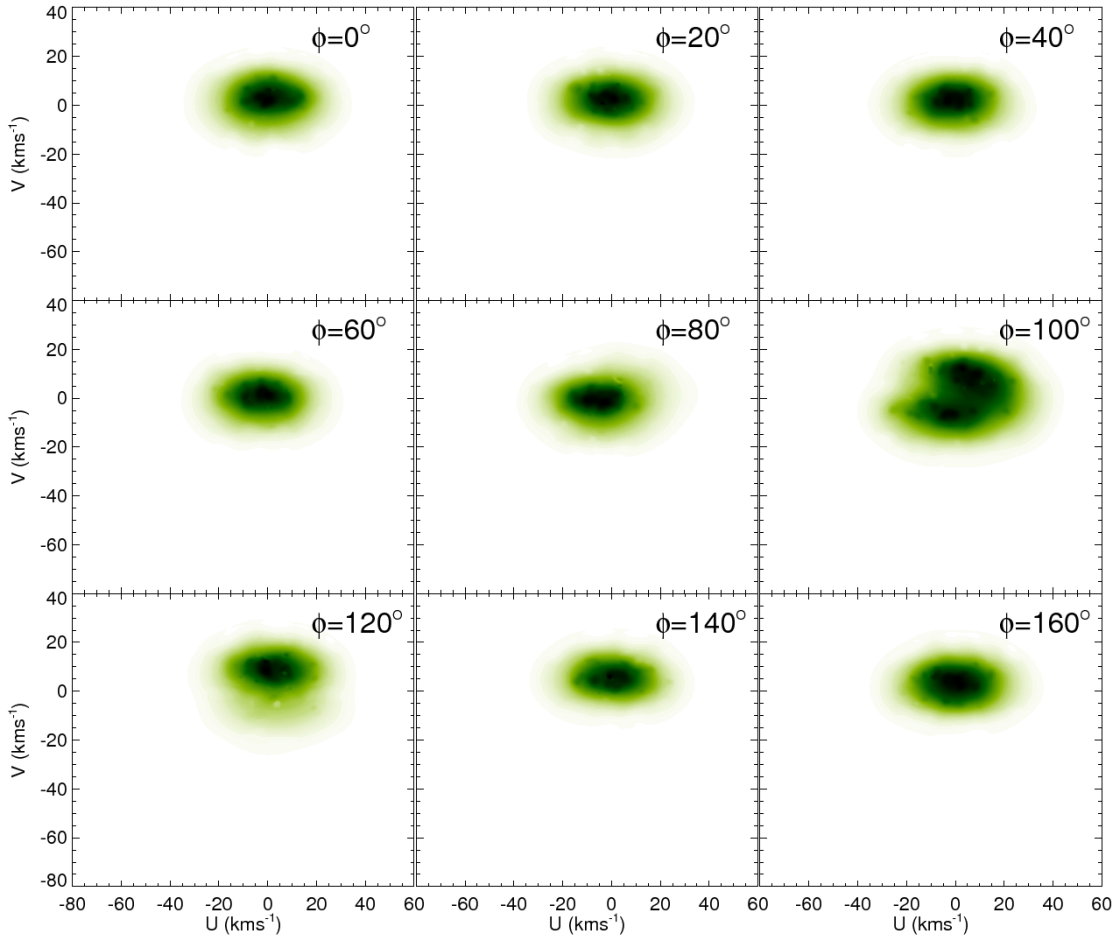

Figure B.7: **Kinematic effects of spiral arms with $\Omega_{sp} = 22\,\mathrm{km\,s^{-1}kpc^{-1}}$ on a cold disc.** U–V velocity distributions after WD at $R = 8.5\,\mathrm{kpc}$ and at different azimuths ϕ for the simulations with the PM04–MW potential model using only spiral arms with $\Omega_{sp} = 22\,\mathrm{km\,s^{-1}kpc^{-1}}$ and IC1.

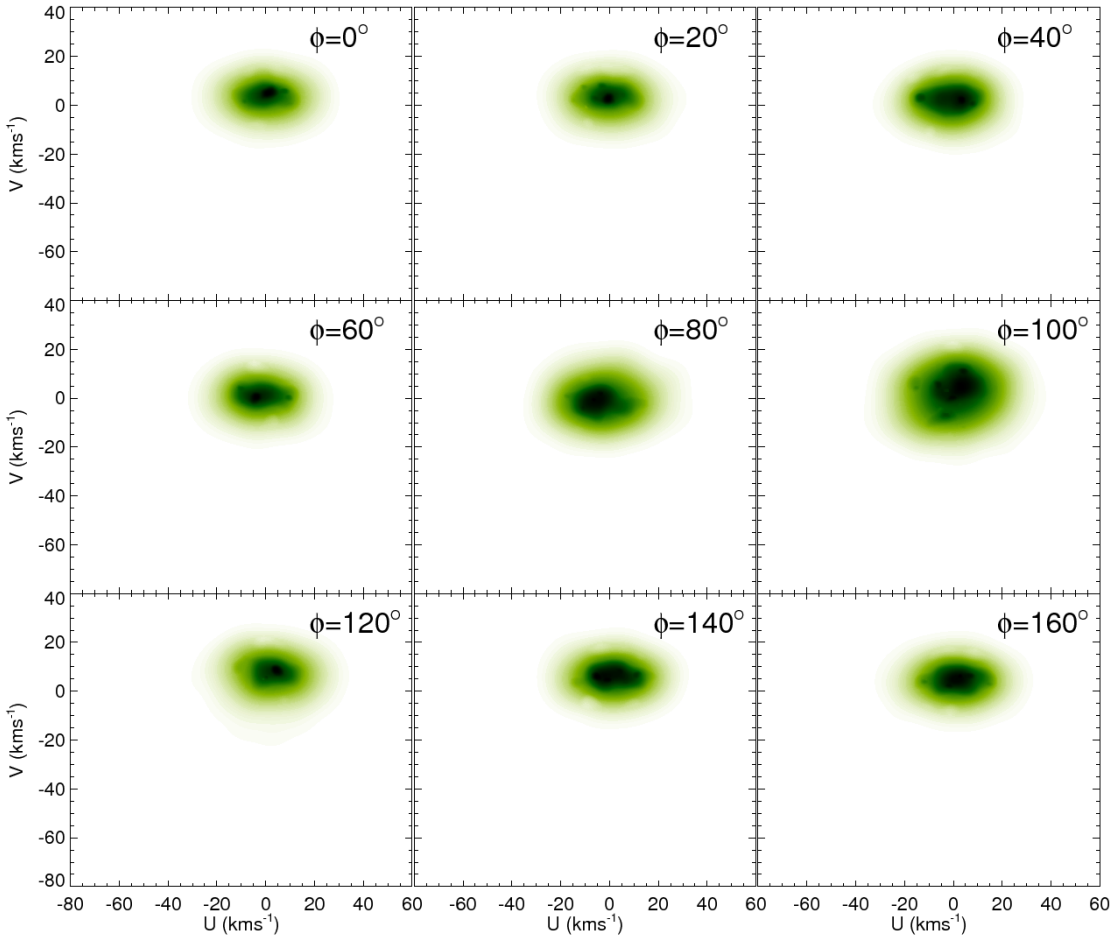

Figure B.8: **Kinematic effects of spiral arms with $\Omega_{sp} = 25\,\mathrm{km\,s^{-1}kpc^{-1}}$ on a cold disc.** U–V velocity distributions after WD at $R = 8.5\,\mathrm{kpc}$ and at different azimuths ϕ for the simulations with the PM04–MW potential model using only spiral arms with $\Omega_{sp} = 25\,\mathrm{km\,s^{-1}kpc^{-1}}$ and IC1.

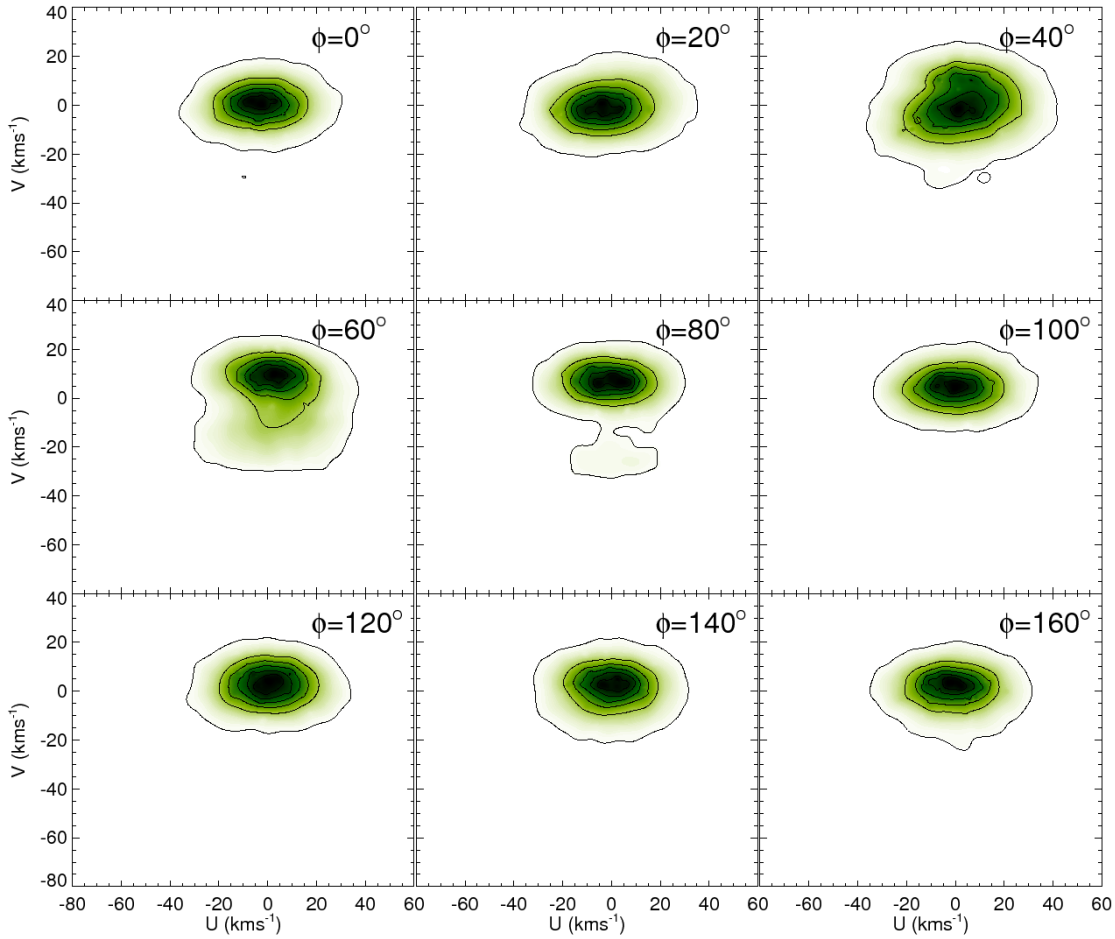

Figure B.9: **Kinematic effects of wounder spiral arms on a cold disc.** U–V velocity distributions after WD at $R = 8.5\,\mathrm{kpc}$ and at different azimuths ϕ for the simulations with the PM04–MW potential model using only spiral arms with $i = 12°$ and IC1.

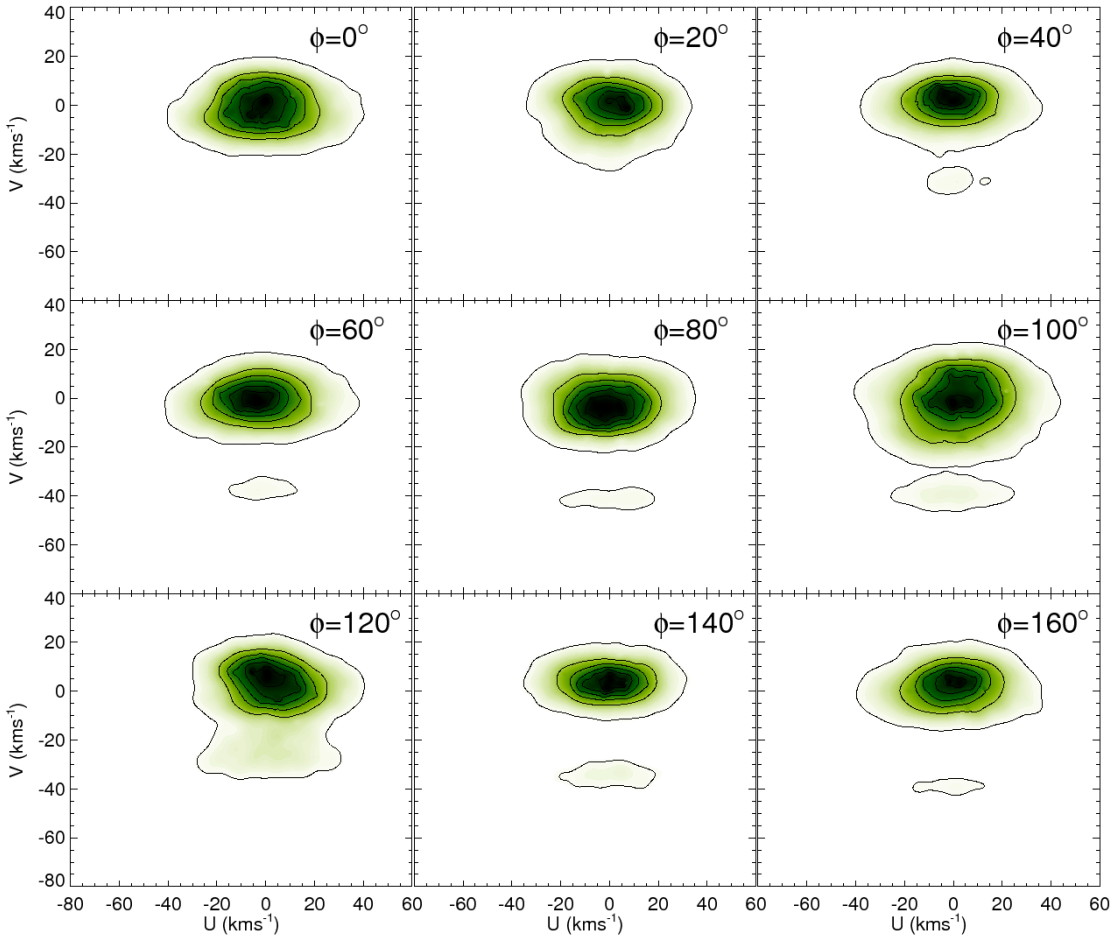

Figure B.10: **Kinematic effects of less massive spiral arms on a cold disc.** U–V velocity distributions after WD at $R = 8.5\,\mathrm{kpc}$ and at different azimuths ϕ for the simulations with the PM04–MW potential model using only spiral arms with $M_{sp} = 0.03 M_D$ and IC1.

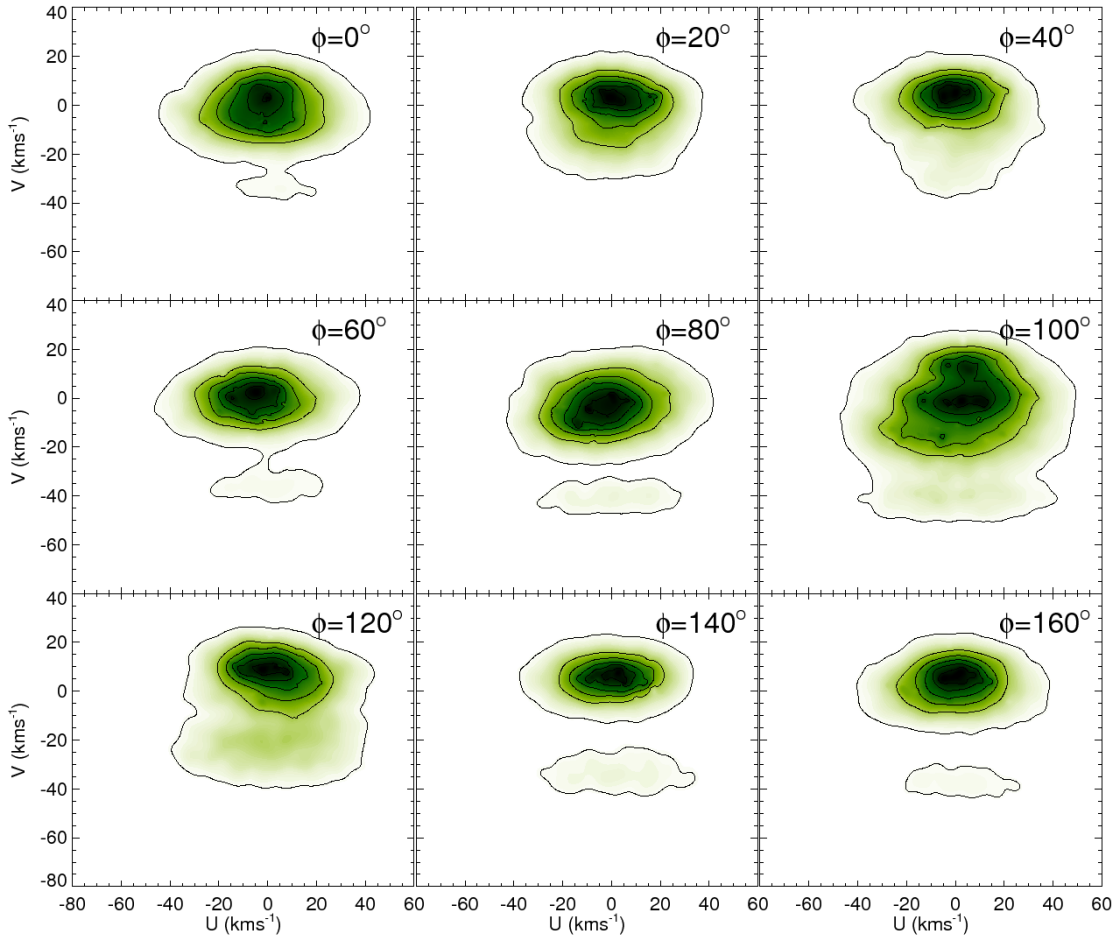

Figure B.11: **Kinematic effects of spiral arms acting on a cold disc for longer times.** U–V velocity distributions after WD at $R = 8.5\,\mathrm{kpc}$ and at different azimuths ϕ for the simulations with the PM04–MW potential model using only spiral arms and IC1 with maximum integration time of 3000 Myr.

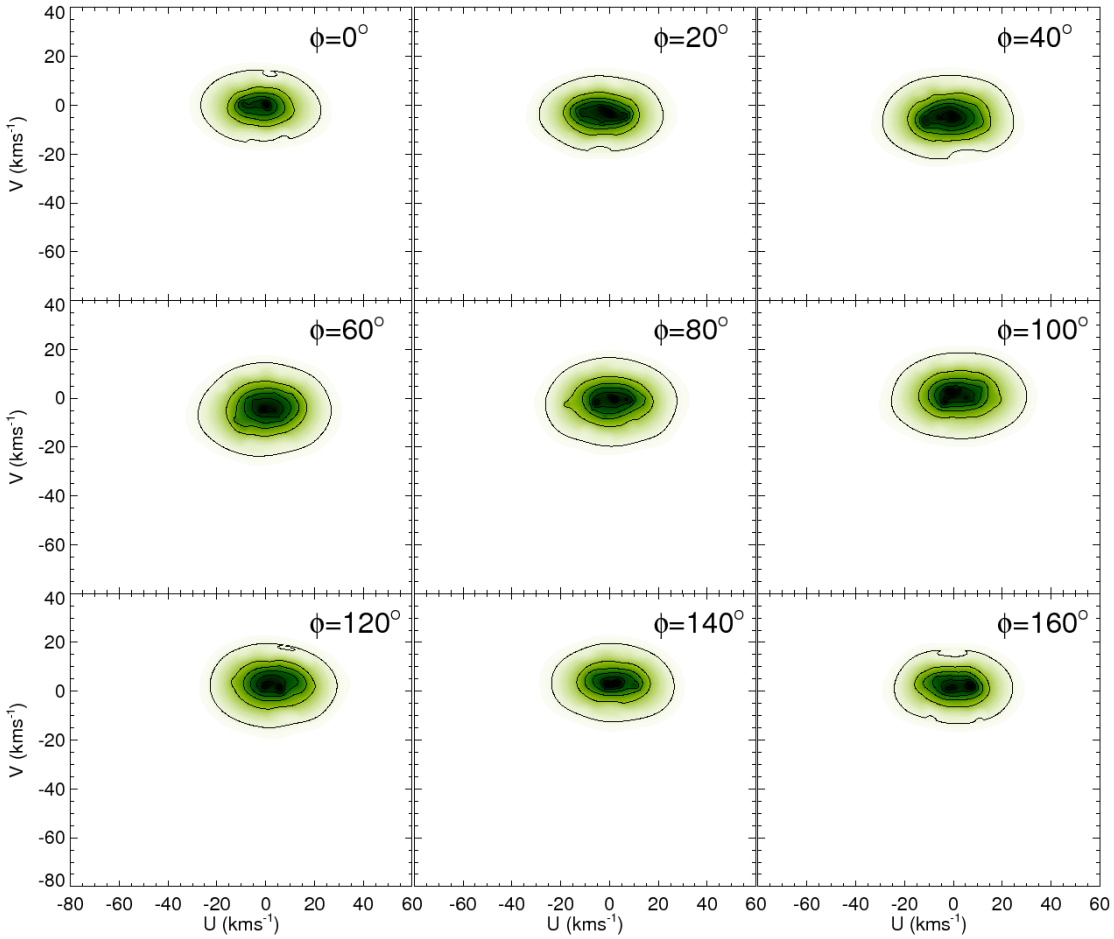

Figure B.12: **Kinematic effects of the TWA spiral arms on a cold disc.** U–V velocity distributions after WD at $R = 8.5\,\mathrm{kpc}$ and at different azimuths ϕ for the simulations with the TWA model for the spiral arms and IC1.

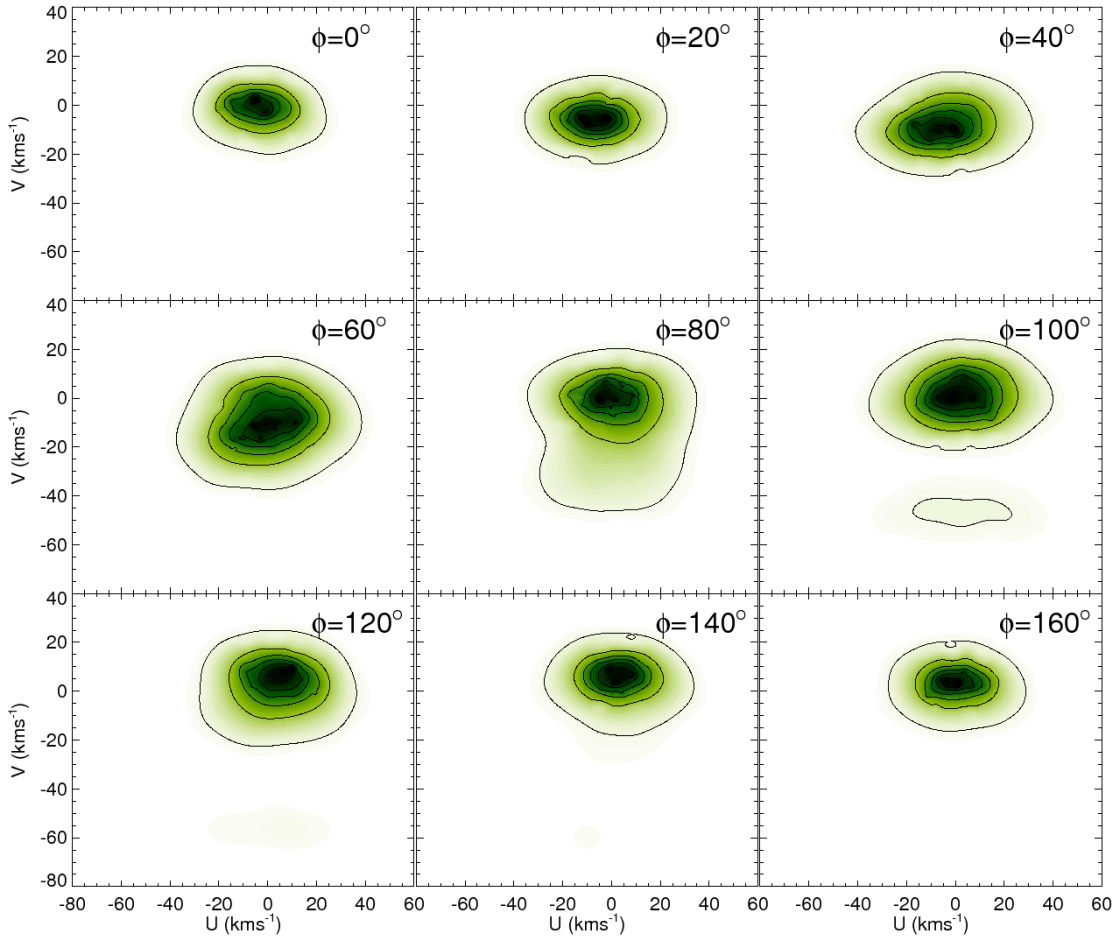

Figure B.13: **Kinematic effects of stronger TWA spiral arms on a cold disc.** U–V velocity distributions after WD at $R = 8.5\,\mathrm{kpc}$ and at different azimuths ϕ for the simulations with the TWA model for the spiral arms with approximately double amplitude $A_{sp} = 1500(\,\mathrm{km\,s^{-1}})^2\,\mathrm{kpc}^{-1}$ compared to Figure B.12 and IC1.

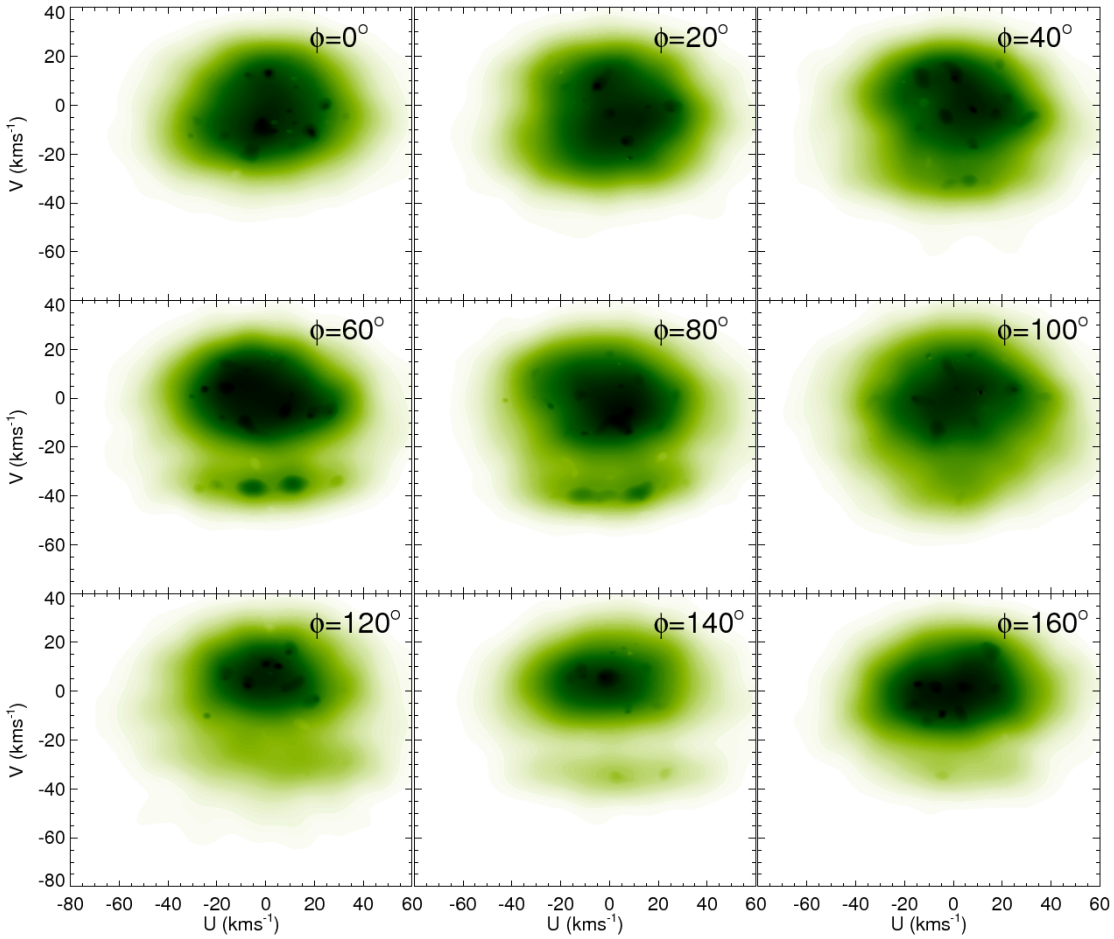

Figure B.14: **Kinematic effects of spiral arms acting on an intermediate disc for a longer time.** U–V velocity distributions after WD at $R = 8.5\,\mathrm{kpc}$ and at different azimuths ϕ for the simulations with the PM04–MW potential model using only spiral arms and IC2 with total integration time of 1000 Myr.

B.4 Simulations with the bar

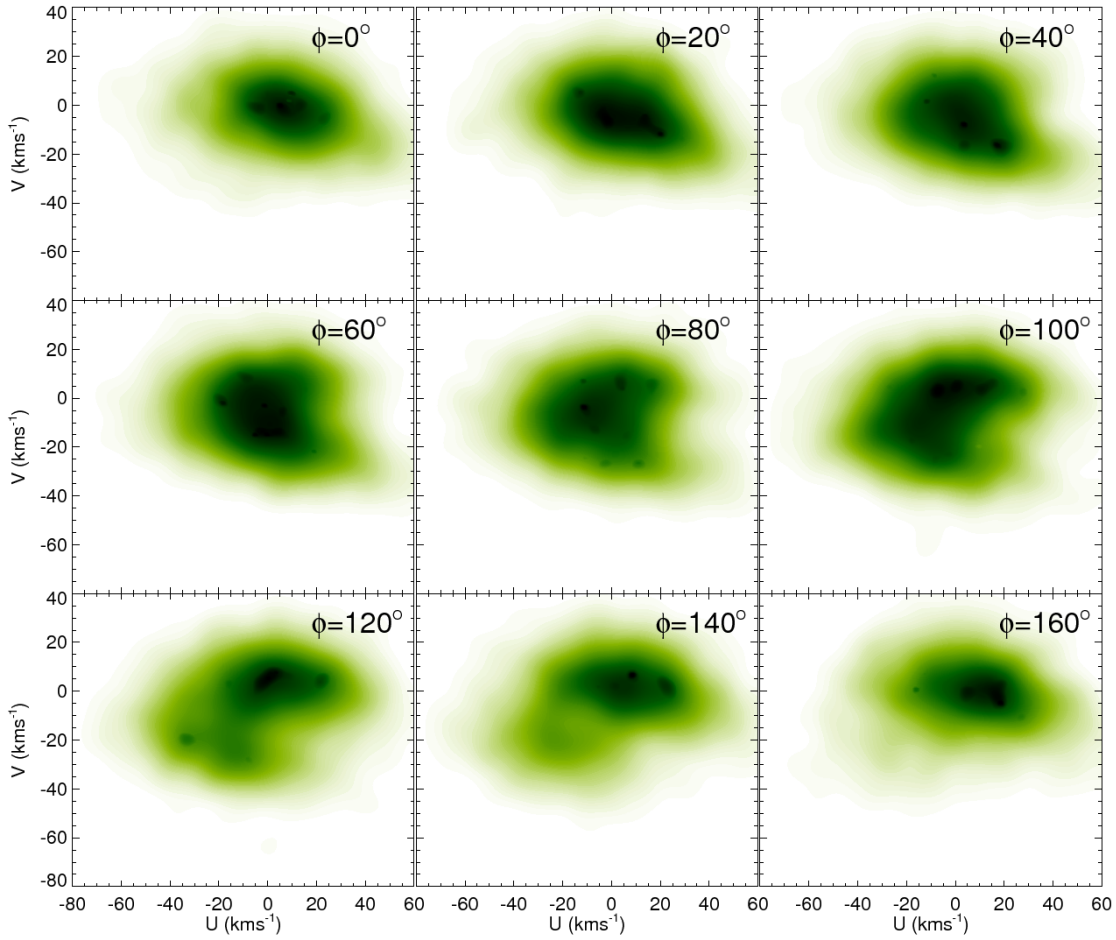

Figure B.15: **Kinematic effects of the bar with $\Omega_b = 48\,\mathrm{km\,s^{-1}kpc^{-1}}$ on an intermediate disc.** U–V velocity distributions after WD at $R = 8.5\,\mathrm{kpc}$ and at different azimuths ϕ for the simulations with the PM04–MW potential model using only a bar with $\Omega_b = 48\,\mathrm{km\,s^{-1}kpc^{-1}}$ and IC2.

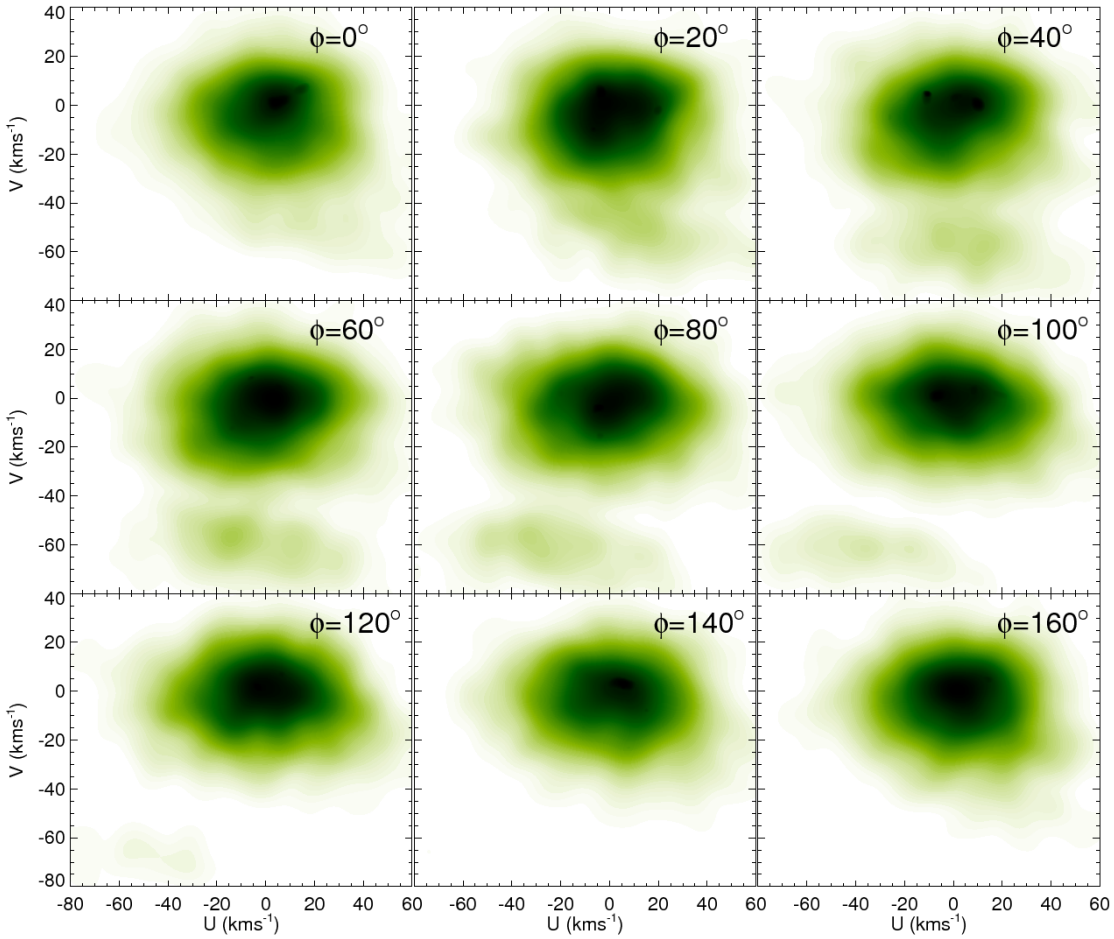

Figure B.16: **Kinematic effects of the bar with $\Omega_b = 60\,\mathrm{km\,s^{-1}kpc^{-1}}$ on an intermediate disc.** U–V velocity distributions after WD at $R = 8.5\,\mathrm{kpc}$ and at different azimuths ϕ for the simulations with the PM04–MW potential model using only a bar with $\Omega_b = 60\,\mathrm{km\,s^{-1}kpc^{-1}}$ and IC2.

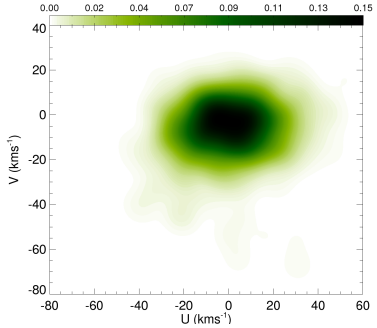

(a) $R = 10.5\,\mathrm{kpc}$

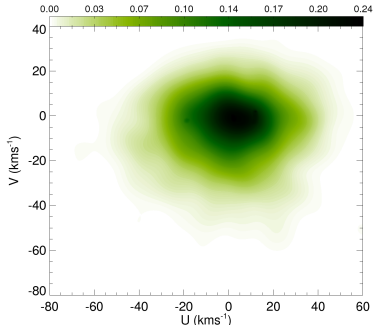

(b) $R = 9.5\,\mathrm{kpc}$

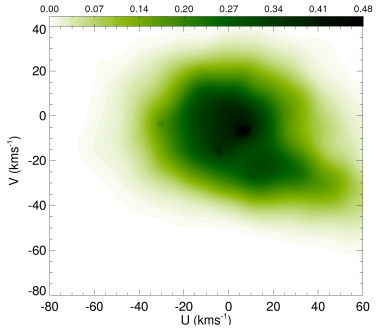

(c) $R = 7.5\,\mathrm{kpc}$

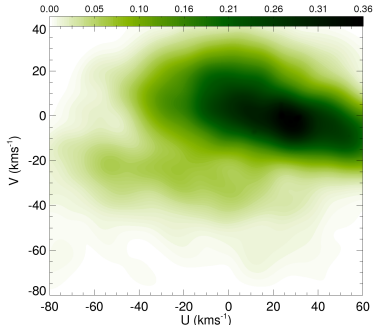

(d) $R = 6.5\,\mathrm{kpc}$

Figure B.17: **Kinematic effects of the bar at different radius.** U–V velocity distributions after WD at $\phi = 0°$ and at different radius R for the simulations with the PM04–MW potential model using only bar with $\Omega_b = 60\,\mathrm{km\,s^{-1}kpc^{-1}}$ and IC2.

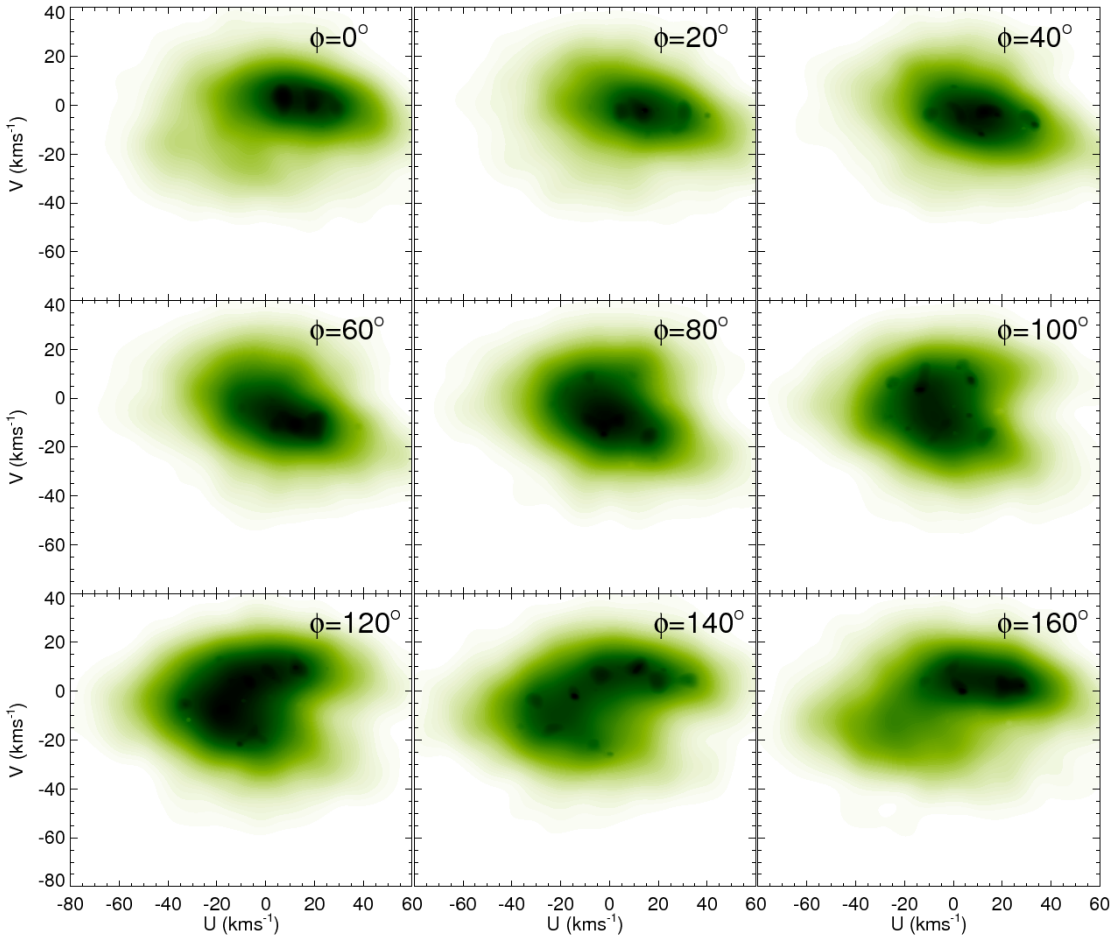

Figure B.18: **Kinematic effects of a more massive bar on an intermediate disc.** U–V velocity distributions after WD at $R = 8.5\,\mathrm{kpc}$ and at different azimuths ϕ for the simulations with the PM04–MW potential model using only the bar with a mass $M = 1.4 \times 10^{10}\mathrm{M}_{\odot}$ and IC2.

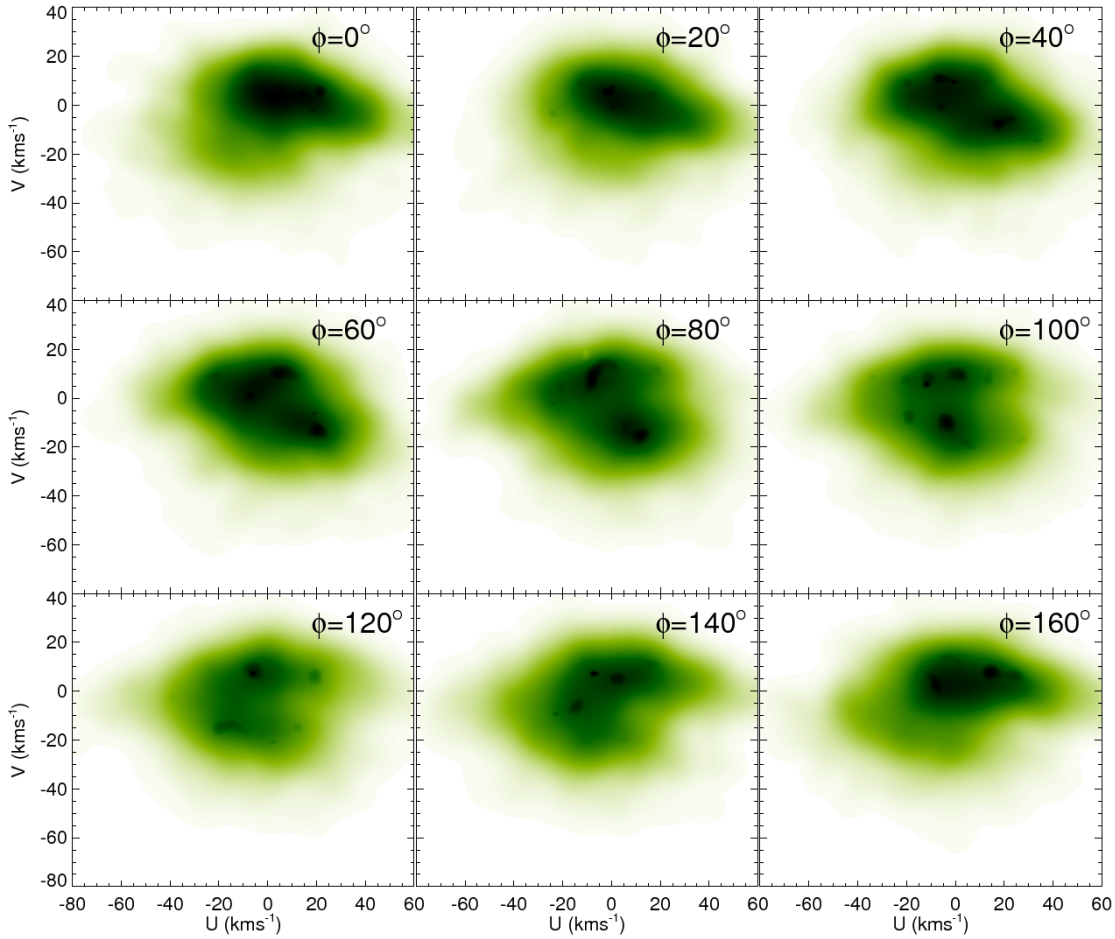

Figure B.19: **Kinematic effects of a more massive bar acting on an intermediate disc for a longer time.** U–V velocity distributions after WD at $R = 8.5\,\mathrm{kpc}$ and at different azimuths ϕ for the simulations with the PM04–MW potential model using only the bar and IC2 with integration time $t = 1000\,\mathrm{Myr}$.

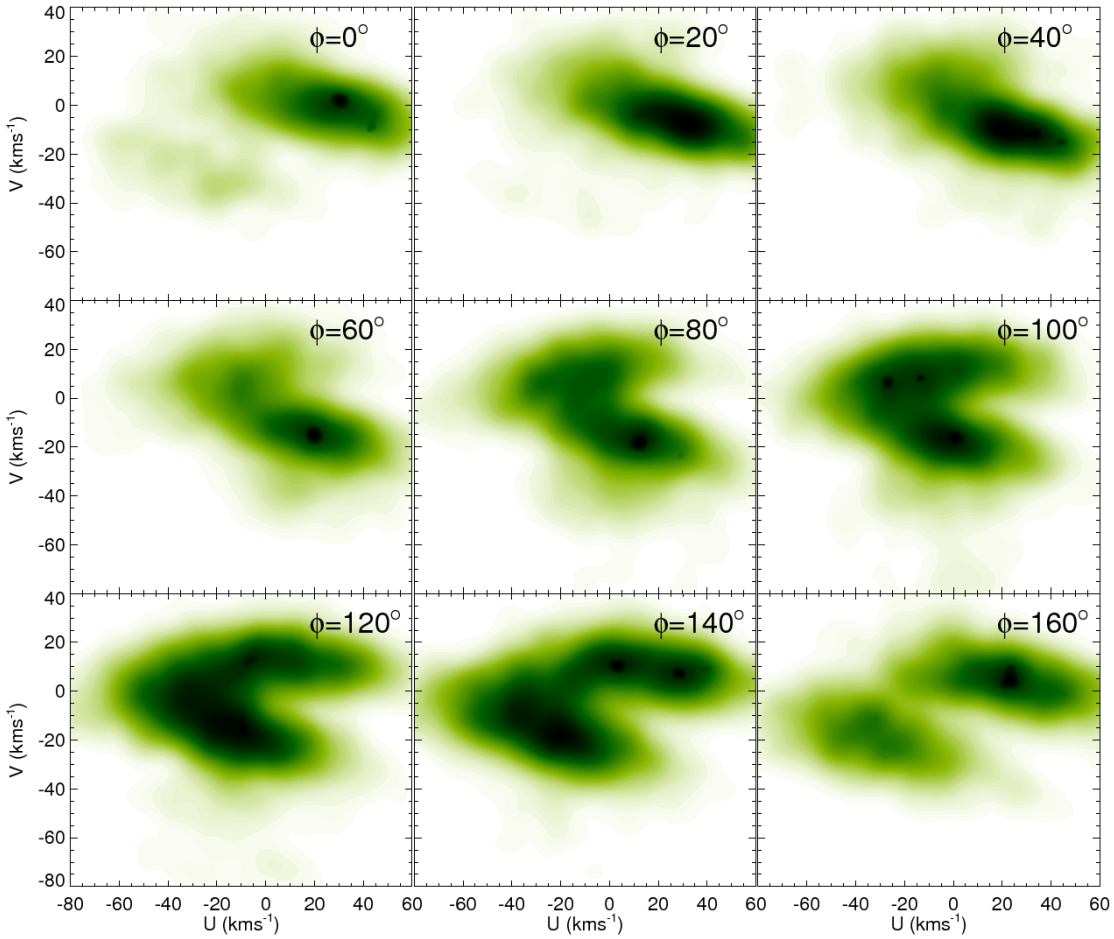

Figure B.20: **Kinematic effects of the quadrupole bar on an intermediate disc.** U–V velocity distributions after WD at $R = 8.5\,\mathrm{kpc}$ and at different azimuths ϕ for the simulations with the quadrupole bar model $\Omega_b = 45\,\mathrm{km\,s^{-1}kpc^{-1}}$ and IC2.

B.5 Simulations for the hot disc

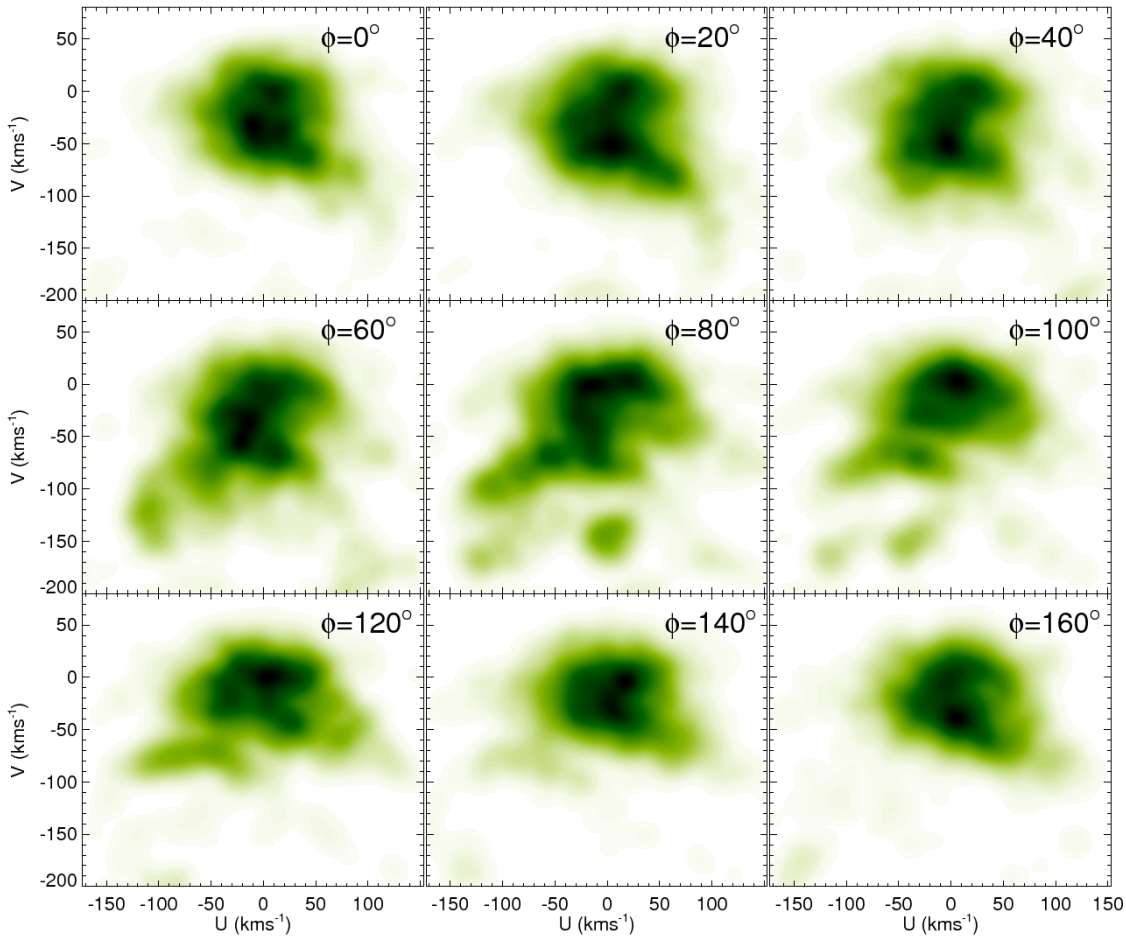

Figure B.21: **Kinematic effects of the bar with $\Omega_b = 60\,\mathrm{km\,s^{-1}kpc^{-1}}$ on a hot disc.** U–V velocity distributions after WD at $R = 8.5\,\mathrm{kpc}$ and at different azimuths ϕ for the simulations with the PM04–MW potential model using only a bar with $\Omega_b = 60\,\mathrm{km\,s^{-1}kpc^{-1}}$ and IC3.

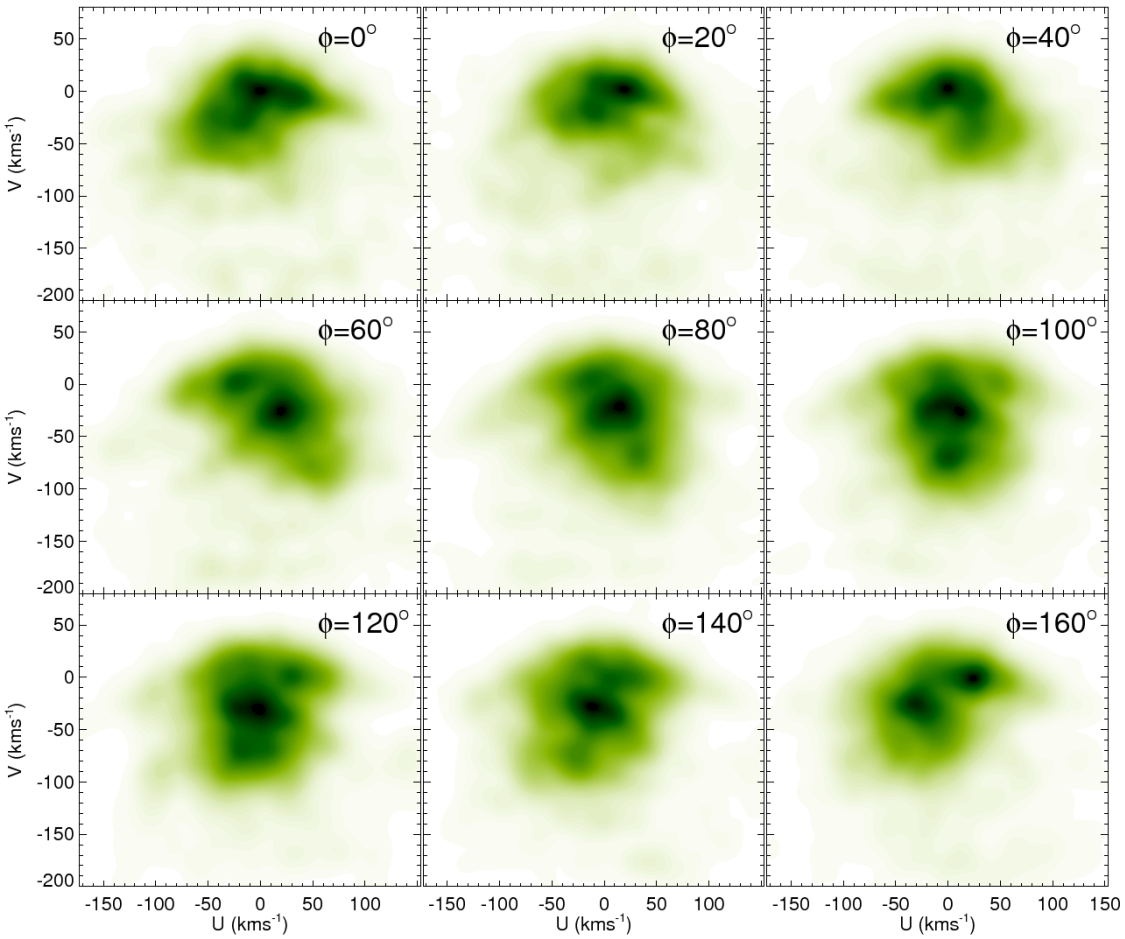

Figure B.22: **Kinematic effects of the quadrupole bar acting on a hot disc for longer times.** U–V velocity distributions after WD at $R = 8.5\,\mathrm{kpc}$ and at different azimuths ϕ for the simulations with the quadrupole bar model and IC3 with integration time of 5500 Gyr.

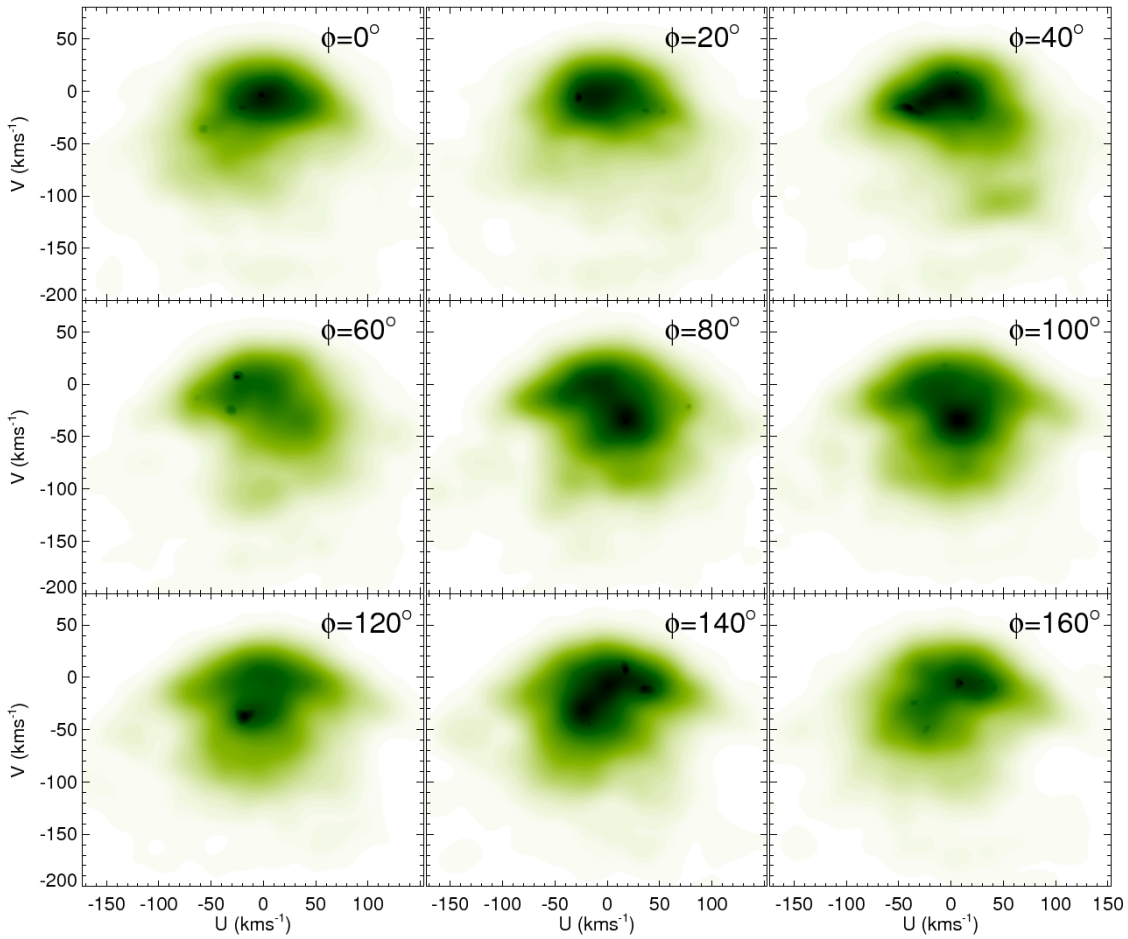

Figure B.23: **Kinematic effects of the faster quadrupole bar acting on a hot disc for longer times.** U–V velocity distributions after WD at $R = 8.5\,\mathrm{kpc}$ and at different azimuths ϕ for the simulations with the quadrupole bar model with $\Omega_b = 47.5\,\mathrm{km\,s^{-1}kpc^{-1}}$ and IC3 with integration time of 5000 Gyr.

B.6 Simulations with the bar and the spiral arms

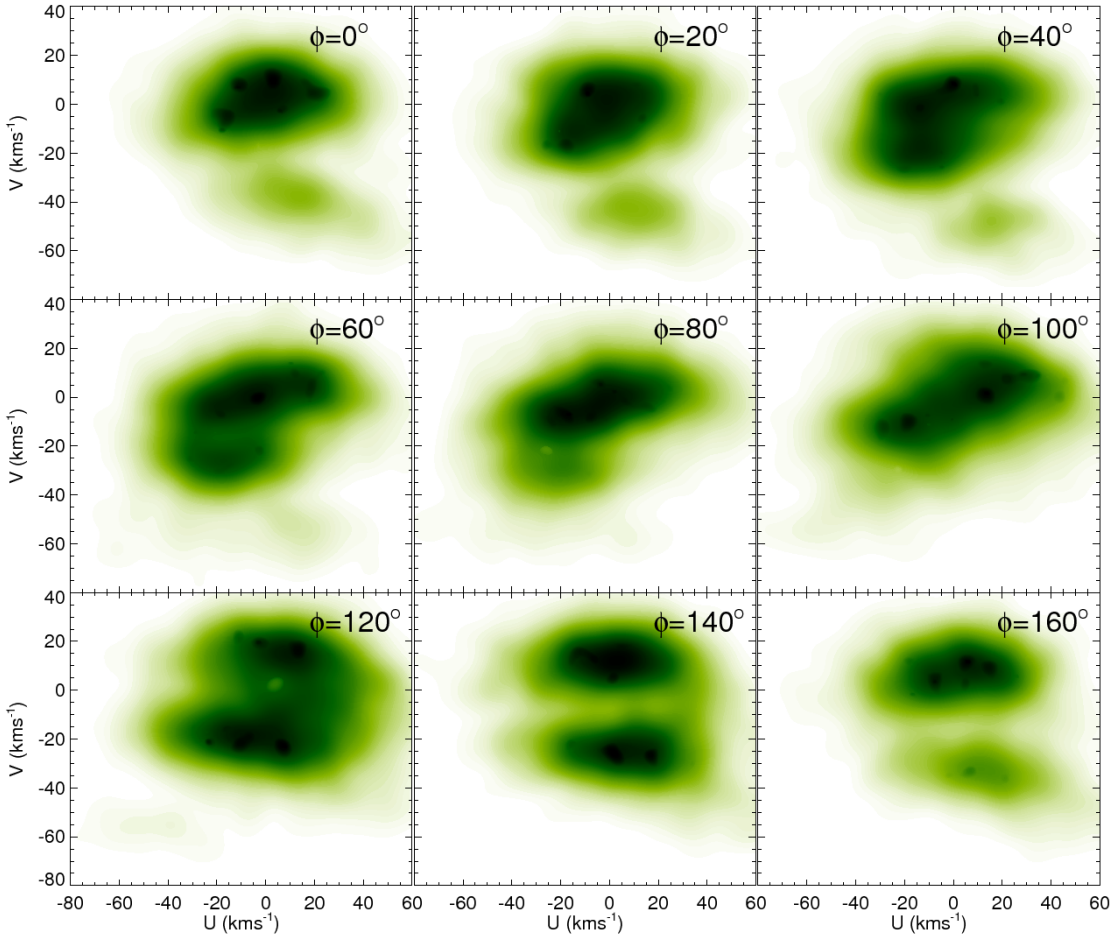

Figure B.24: **Kinematic effects of the bar and the spiral arms on a cold disc.** U–V velocity distributions after WD at $R = 8.5\,\mathrm{kpc}$ and at different azimuths ϕ for the simulations with the spiral-bar PM04–MW potential model (bar and spiral arms) with $\Omega_b = 60\,\mathrm{km\,s^{-1}kpc^{-1}}$ and IC2.

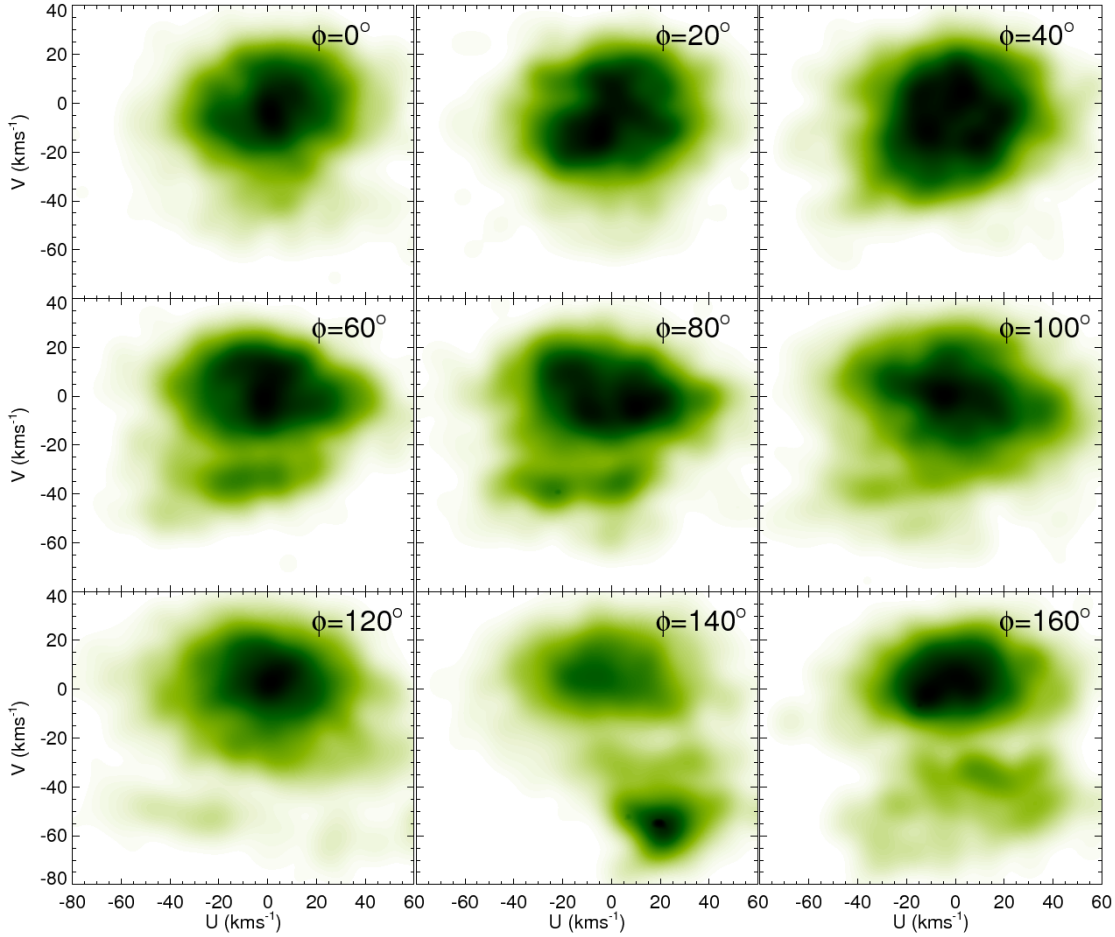

Figure B.25: **Kinematic effects of the bar and the spiral arms on a cold disc.** U–V velocity distributions after WD at $R = 8.5\,\mathrm{kpc}$ and at different azimuths ϕ for the simulations with the spiral-bar PM04–MW potential model (bar and spiral arms) with $\Omega_b = 60\,\mathrm{km\,s^{-1}kpc^{-1}}$ and IC2 with total integration time of 1000 Myr.

Appendix C

Local dark matter kinematics

Another unexpected aspect of the bar- and spiral arm-induced phase space structure is the effect on the local dark matter kinematics. Particles in a possible dark matter bar (Colín et al. 2006) and even in the dark matter halo (Athanassoula 2005) are trapped/scattered in the same resonances as stars are. It has been shown that different bar-induced resonances can be populated by disc-like and halo particles (Athanassoula 2002, 2003, Ceverino & Klypin 2007). For instance, Ceverino & Klypin (2007) shown in their figures 9 and 11 that different bar-induced resonances can be populated by disc-like and halo particles. Recent studies of galaxy formation of MW mass predict that a flattened dark matter component mirroring the stellar thick disc structural and kinematic properties will form in a Λ-CDM Universe (Bruch et al. 2008, Read et al. 2008). We suggest that the particles in this possible dark disc are also influenced by the resonances as stars are.

Following (Read et al. 2009) we assume that our hottest initial conditions (IC3) are the ones that more closely represent the dark particles in the dark thick disc. As discussed in Section 10.2, the thick disc would be even hotter and have more rotational lag. However, these IC3 are a first approximation for the particles in the dark disc. With this approach, the results of Chapter 15 are extrapolated to the dark disc and their Figures could also reproduce the local dark matter kinematics induced by the PM04–MW potential model, mainly the bar. The main conclusion is that some "dark groups" at low angular momentum could be influenced and indeed caused by the resonances of the bar.

This is a very promising subject of study that, however, needs further investigation and it is subject to all the mentioned restrictions such as the validity of the 2D approximation. Moreover, the characteristics of the dark disc are poorly constrained, which makes it difficult to build proper IC to represent this MW component. This issue has never been addressed before and these dark-matter currents would be independent of the Galactic assembly history or the

dark substructure abundance. The dynamical history of the Galaxy and its detailed large-scale structure may help to establish whether the amplitude of the dark matter kinematic structure is detectable by planned dark matter detection experiments.

List of Figures

List of Tables